Theoretical models of hybrid light-matter systems and their applications

Kevin C. Smith

A dissertation
submitted in partial fulfillment of the
requirements for the degree of

Doctor of Philosophy

University of Washington

2021

Reading Committee:

David J. Masiello, Chair

Arka Majumdar

Marcel den Nijs

Program Authorized to Offer Degree:
Physics

University of Washington

Abstract

Theoretical models of hybrid light-matter systems and their applications

Kevin C. Smith

Chair of the Supervisory Committee:
Professor David J. Masiello
Department of Chemistry

Controllable light-matter interactions are of central importance to a broad range of problems at the heart of modern theoretical, experimental, and applied physics, particularly in the rapidly expanding areas of nanoscale and quantum science. The past few decades have seen incredible advances in this area, heralding a new era in quantum optics and cavity quantum electrodynamics (QED) characterized by chip-scale, hybrid light-matter platforms with engineered properties. In tandem to providing a rich platform for fundamental study of quantum physics, such systems have been shown to support an incredible variety of applications ranging from quantum communication and quantum information science to biomolecular sensing and cavity-controlled chemistry. This thesis compiles a diverse set of theoretical work involving first-principles mathematical modeling of cavity QED and nanophotonic platforms both for fundamental study and for application. In some cases, a classical description is sufficient. In others, quantum effects are considered. Part I of this dissertation contains introductory material which underpins the published works appearing in Parts II and III. Topics discussed in these four preliminary chapters include a Lagrangian-based approach to modeling light-matter interactions (Chapter 1), oscillator model descriptions of photonic cavities, plasmonic nanoresonators, and quantized light-matter interactions (Chapter 2), theoretical modeling of experimental observables (Chapter 3), and, finally, a survey of phenomena in various parameter regimes realizable in cavity QED and nanophotonic platforms (Chapter 4). Parts II and III enclose six chapters of mostly published work, each focus-

ing on a particular platform realizable in a laboratory setting. Chapters 5 and 6 detail collaborative, joint experimental-theoretical work on hybrid photonic-plasmonic resonators, while Chapter 7 follows with a theoretical analysis of an experimentally probed coupled plasmonic dimer supporting infrared Fano resonances. Chapter 8 extends this work with a theoretical treatment of coupled dielectric cavities, followed by collaborative application to a heterogeneous photonic molecule in Chapter 9. We conclude in Chapter 10 with an in-depth analysis of effective photon-photon interactions in cavity and circuit QED systems, with a particular focus on the realization of quantum many-body phenomena in these platforms. Taken together, the chapters herein comprise a set of varied approaches for theoretically modeling and understanding a diverse range of nanophotonic and cavity QED platforms for the fundamental study, control, and technological application of light-matter interactions.

TABLE OF CONTENTS

LIST OF FIGURES

LIST OF TABLES

GLOSSARY

QED: Quantum cavity electrodynamics

LSP: Localized surface plasmon

$\mathcal{PT}$: Parity-time

EP: Exceptional point

WGM: Whispering gallery mode

NR: Nanorod

AUNR: Gold nanorod

QHM: Quasi-hybrid modes

EEL: Electron energy-loss

FP: Fabry-Pérot

CMT: Coupled mode theory

TLS: Two-level system

JCH: Jaynes-Cummings-Hubbard

ACKNOWLEDGMENTS

First and foremost, I'd like to acknowledge my advisor Professor David Masiello for his constant support over the years. It's been an absolute pleasure working with him, and I'll forever be grateful to have had a mentor who is interested not just in teaching students, but also learning from them. Since day one, he has given me the freedom to pursue research topics I am interested in, even when they fall outside of the group's expertise. He has taught me to efficiently collaborate with both experimentalists and theorists, write proposals, and, above all, conduct research at a high level. Under his guidance, I have undoubtedly grown as a scientist and researcher, and will continue to do so using the skills he has taught me. For all of this, I am extremely grateful, and it's been a great pleasure having David as both a mentor and a collaborator throughout this journey.

I would next like to give my sincerest thanks to both my reading and exam committee. Since we began collaborating, Professor Arka Majumdar has challenged me to always relate my mathematical derivations to experimental reality, and for that I am grateful. He has also provided me with terrific and fruitful advice over the years, and his continued mentorship has been extremely meaningful for my growth as a researcher. Professor Marcel den Nijs was a last-minute addition to my committee, and I greatly appreciate his willingness give his time to read and provide feeback on this dissertation. I also thank Professors Boris Blinov, Mo Li, and Karl Böhringer for their time, and have appreciated their feedback and advice over the years.

I've been incredibly fortunate to work with a terrific group of collaborators throughout my graduate career, including Professors Arka Majumdar, Randy Goldsmith, Nathan Wiebe, and Jon Camden. All have contributed significantly to my academic growth across many research projects, and for that I am extremely grateful. I'd also like to acknowledge Dr. Charles Cherqui and Dr. Niket Thakkar, both of whom left the Masiello group long ago but

undoubtedly shaped the way I approach science. Charles has also remained a good friend to this day, and I look forward to our continued discussion of all things vinyl records and hip-hop. I have been lucky to have worked alongside so many incredible people over the last five years – I'll always look back fondly at my time with my group-mates Jake Busche, Elliot Buetler, Claire West and Dr. Harrison Goldwyn. I'm extremely grateful to have had all four of them as friends throughout this process, and I thank each and every one of them for our discussions over the years, scientific and otherwise.

I've also very much enjoyed mentoring younger students in the group – it's been incredible to watch Praise Anyanwu's growth over the years, and I've long been impressed by his work ethic and drive to learn new material. It's also been a pleasure to watch Austin Nixon grow as a researcher, and I thank him for his willingness to dive head-first into working out unitary transformations for me in detail, no matter how ugly the math gets. While Siamak Khorasani and I did not have much of a chance to collaborate, his friendliness and sense of humor has been infectious over the last couple of years, and I wish him the best in his future endeavors. As for the postdoctoral scholars in the group, I'd like to first and foremost thank Dr. Aniruddha Bhattacharya for his tremendous impact on my work over the last year. His work ethic has been nothing short of inspirational since the day he arrived in the group, and I am incredibly grateful for all of his advice, support, and collaborative efforts over the last year. While our time together was brief, Dr. Marc Bourgeois has been guiding and motivating presence since joining the group, and I hope to emulate his creativity and expertise as I embark on my own postdoctoral journey. Last but not least, getting to know the younger students in the group over the course of this year has been a great joy, even if our encounters were mostly confined to Zoom. I cannot begin to imagine how difficult an entirely remote first year of graduate school is, but all three of Nicole Panek, Andrew Rossi, and Matthieu Chalifour have shown incredible resilience and progress, and all have inspired me to do better in my own work by asking terrific questions. While my time in the group is at its end, it's comforting to know its future is in such good hands with those three.

Entering my Senior year of high school, I had no idea what Physics even was. For

setting me on this path, I would like to acknowledge my high school Physics teacher, Mr. Miller. While his teaching methods were at times somewhat extreme, something about the systematic way he approached problem-solving has stuck with me to this day, and I often find myself returning to those early lessons when stuck on a problem. I was always a decent student, but never stood out in any particular subject aside from math. Mr. Miller helped me realize I had a talent for Physics and, as he put it, I soon after "caught the bug".

The last six years have been both thrilling and exhausting, and I'm extremely appreciative of all of the support I've received from my family and friends that have sustained me throughout this phase of my life. While it's clear that both of my parents are somewhat unsure of exactly what it is that I'm doing and why, they've never once urged me to question my passions and have been supportive since day one, and for that I am grateful. I'm fortunate to have two siblings that I am incredibly close with, and I thank Mike and Kim for all of their love and support. In addition, I've had an incredible network of friends throughout this journey, and I'm thankful for each and every one of them. Finally, words cannot express how helpful it has been to having a loving and supportive partner at my side throughout the last six years. This journey would have order-of-magnitude more difficult without Adriana. Her support has never faltered, despite the many, many late nights I spent working, and I'm especially grateful for her insistence that I take a break every once in a while.

PREFACE

This dissertation compiles the notes, writings, and first/co-first authored publications of Kevin C. Smith. It is broken into three distinct Parts, each of which begins with a detailed, introductory description of its content. A summary in brief:

- Part I contains background information and mathematical derivations pertinent to the published portions of this dissertation. Topics covered include the light-matter Lagrangian (Chapter 1), modeling of photonic cavities, plasmonic nanoresonators and light-matter interactions (Chapter 2), analytic calculation of experimental observables (Chapter 3), and a survey of parameter regimes in cavity quantuam electrodynamics and nanophotonics experiments (Chapter 4).

- Part II includes three published manuscripts, each composing a single chapter. All concern the common theme of observation and theoretical modeling of Fano resonances in nanophotonic platforms. In the first two Chapters, the platform of interest is a hybrid photonic-plasmonic resonator. The first details the utility of such a platform for realizing large Purcell enhancements (Chapter 5), while the second describes a detailed accounting of energy flow in the system via simultaneous measurement of observables (Chapter 6). Part II concludes with the first observation of Fano resonances in an all-plasmonic system using electron energy-loss spectroscopy (Chapter 7).

- Part III includes two manuscripts (one published and one under review), each of which is a single Chapter, as well as a set of notes which serves as the basis for a third manuscript currently in preparation. All three concern physical phenemena in which light, roughly speaking, behaves like matter. Part III begins with a theoretical framework for describing strongly coupled photonic molecules – systems of two or more dielectric cavities in close proximity which hybridize (Chapter 8). This is followed by an account of this theoretical framework's application to a heterogeneous photonic

molecule composed of a photonic crystal nanobeam cavity coupled to a ring resonator, illustrating potential for controllable light-matter interactions (Chapter 9). Part III then concludes with an exposition of the many-body character underlying the Jaynes-Cummings Hamiltonian with a particular focus on application to analog quantum simulation of many-body phenomena using interacting photons (Chapter 10).

Below is a list of publications pertinent to this dissertation, with those enclosed herein noted explicitly. For a complete list of publications, see Kevin C. Smith's Google Scholar page.

7. **Smith, K. C.**, Masiello, D. J. Coupled dielectric cavities beyond standard coupled mode theory. *In preparation*. (Basis for this work is Chapter 8)

6. **Smith, K. C.**, Bhattacharya, A., Masiello, D. J. Exact k-body representation of the Jaynes-Cummings interaction in the dressed basis: Insight into many-body phenomena with light. *Under review*. arXiv:2103.07571 (Chapter 10)

5. ⋆**Smith, K. C.**, ⋆Chen, Y., Majumdar, A. Masiello, D. J. Active tuning of hybridized modes in a heterogeneous photonic molecule. *Physical Review Applied* 13, 044041. (2020). DOI: 10.1103/PhysRevApplied.13.044041 (Chapter 9)

4. **Smith, K. C.**, Olafsson, A., Hu, X., Quillin, S. C., Idrobo, J. C., Collette, R., Rack, P. D., Camden, J. P., Masiello, D. J. Direct Observation of Infrared Plasmonic Fano Antiresonances by a Nanoscale Electron Probe. *Physical Review Letters* 123, 177401. (2019). DOI: 10.1103/PhysRevLett.123.177401 (Chapter 7)
   ⋆ Selected for Editor's Suggestion. Press coverage: Phys.org, Nanowerk, UW News

3. ⋆Pan, F., ⋆**Smith, K. C.**, Nguyen, H. L., Knapper, K. A., Masiello, D. J., Goldsmith, R. H. Elucidating Energy Pathways through Simultaneous Measurement of Absorption and Transmission in a Coupled Plasmonic–Photonic Cavity. *Nano Letters* 20, 50-58. (2019). DOI: 10.1021/acs.nanolett.9b02796 (Chapter 6)
   ⋆ Selected for the January 2020 cover of Nano Letters.

2. Goldwyn, H.J., **Smith, K. C.**, Busche, J. A., Masiello, D. J. Mislocalization in plasmon-enhanced single-molecule fluorescence microscopy as a dynamical Young's interferometer. *ACS Photonics* 5, 3141-3151. (2018). DOI: 10.1021/acsphotonics.8b00372

1. ⋆Thakkar, N., ⋆Rea, M. T., ⋆**Smith, K. C.**, ⋆Heylman, K. D., Quillin, S. C., Knapper, K. A., Horak, E. H., Masiello, D. J., Goldsmith, R. H. Sculpting Fano resonances to control photonic-plasmonic hybridization. *Nano Letters* 17, 6927-6934. (2017). DOI: 10.1021/acs.nanolett.7b03332 (Chapter 5)

⋆ indicates co-first authorship

Part I

CONFINING LIGHT: CAVITY QED, NANOPHOTONICS, AND THE HARMONIC OSCILLATOR AS A BUILDING BLOCK FOR REDUCED ORDER MODELING

A brief history of light. The pursuit to understand and manipulate light spans much of recent human history, with crafted optical artifacts such as mirrors and burning lenses first appearing in antiquity over 3,000 years ago [1]. These early tools long predate the first documented attempts to understand the physical nature of light by Greek and Indian philosophers in the sixth century BC, yet convey basic understanding of a fundamental feature of modern optics: Light and matter interact, and the latter can influence the behavior of the former.

It would take thousands of years for these ideas to be formalized. The mathematical foundation for geometric optics appeared in the influential writings of Euclid in the third century BC [2], followed by a millenium of refinement by Greek and Islamic scholars. This culminated with Ibn al-Haytham's seminal *Book of Optics* in the 11th century AD [3], containing explanations of reflection and refraction of light via mirrors and lenses as well as a working theory of vision and color – contributions so monumental that today al-Haytham is considered both the father of modern optics and an early pioneer of the scientific method.

In time it became clear that certain phenomena such as diffraction and interference could not be explained with geometric optics, leading to the emergence of an improved description known as physical optics. Particularly influential works during this period include particle and wave theories contributed by Isaac Newton and Christiaan Huygens and the formative experiments by Francesco Grimaldi and Thomas Young investigating diffraction and two-slit interference, respectively [1]. Our understanding of light was again revolutionized in 1865 when James Clerk Maxwell published his famous Maxwell's equations, leading to the unification of electromagnetism and optics [4]. Perhaps most notably, Maxwell illustrated that these equations suggest the existence of electromagnetic waves propagating at the speed of

light and therefore proposed that these solutions and light are one in the same, later proven to be true by the pioneering experiments of Heinrich Hertz between 1886 and 1889. Quite comically, when asked of the possible applications of this discovery, Hertz simply replied "Nothing, I guess" [5]. Today, electromagnetic waves (particularly at radio frequencies) are the backbone of the entire global telecommunication industry, facilitating wireless communication for a wide array of historically momentous technologies from radio and television to cellular networks and the wireless internet.

By the 20th century, it was generally (and quite incorrectly) agreed upon that the fundamental laws of physics were established and only minor details remained incomplete. However, it was noticed that certain phenomena – the energy spectrum of blackbody radiation and the photoelectric effect, in particular – could not be explained by Maxwell's equations, and our understanding of light (and electromagnetic radiation, in general) was once again in question. The fallout of these inconsistencies is well-chronicled [6] – Max Planck put forth a basic quantum theory in 1900 and in 1905 Einstein demonstrated that it explained the photoelectric effect [7], illustrating that light is composed of particles called *photons*. The success of this quantum theory soon evolved into quantum electrodynamics – a quantum field theoretic description introduced by Paul Dirac, whereby light-matter interactions are understood through exchange of quanta between matter and the quantized electromagnetic field [8]. This work resulted in the notion of the quantum vaccuum field and furthermore explained phenomena such as spontaneous emission. The quantum theory of electrodynamics was later generalized to its relativistic form in large part through the efforts of Tomonaga, Schwinger, and Feynman who shared the Nobel Prize in 1965 for their contributions [9]. Today, quantum electroynamics is considered one of the most successful theories in all of physics, having been repeatedly tested via precision measurements of various quantities such as the fine-structure constant [10, 11] and the Lamb shift [12, 13], and serves as a foundation upon which other quantum field theories are constructed. Quantum optics, the term typically applied to the nonrelativistic, optical frequency limit of quantum electrodynamics, remains an extremely active field of experimental and theoretical research today, in large part due to the outsized role of optical systems in the burgeoning areas of nanoscale and quantum science [14].

Engineering the photonic environment. One of the most import discoveries of the quantum era is the existence of the quantum radiation field, capable of populating and depopulating upon emission and absorption of photons by individual atoms. Similar to the realization of early civilizations that the behavior of light could be altered by engineering objects to reflect and refract in a particular way, in 1946 Edward Purcell published a seminal American Physical Society abstract which suggested the opposite effect was true in the quantum world. In particular, he showed that the lifetime of a single magnetic spin could be reduced through coupling to a resonant circuit [15]. It was soon realized that this result was quite general for various quantum systems, suggesting the possibility to alter the lifetime of an emissive atom by engineering its photonic environment. This discovery heralded a new era of studying light-matter interactions in a controllable context and marked the birth of cavity quantum electrodynamics (CQED), the study of light-matter interactions between individual atoms and the spatially confined resonances of an electromagentic cavity [14].

In years since, advances on multiple fronts have broadened CQED to encompass various subdisciplines which involve a diversity of electromagnetic resonators and so-called "artificial atoms". Notable examples of active research include circuit QED in the microwave domain, involving superconducting cavities and Josephson-junction enabled superconducting qubits [16, 17], and optical frequency solid-state QED, entailing the study of interactions between solid-state quantum emitters (such as quantum dots) and dielectric optical microcavities [14]. In parallel, the study of nanophotonics – involving interactions between light and matter at the nanoscale – has evolved into a thriving adjacent field of research [18, 19], with plasmonic nanoresonators gaining particular interest for their ability to confine light to the nanoscale and facilitate strong light-matter interactions [20, 21]. In all, these rapidly advancing areas of research offer a rich diversity of exciting applications that range from advanced optical sensing [22, 23, 24, 25] and cavity-controlled chemistry [26, 27, 28, 29, 30, 31] to the realization of scalable quantum computers, such as those based upon circuit QED systems [32, 33, 34] currently in development at IBM and elsewhere. CQED systems additionally provide an ideal setting for studying quantum physics at a fundamental level [14, 16], the forefront of which now involves (i) using CQED platforms to study quantum many-body phenomena [35, 36, 37], and (ii) studying light matter interactions in extreme

parameter regimes, such as ultrastrong and deep ultrastrong coupling [38].

A Summary of content ahead. Crucial to all of the aforementioned applications is an extensive theoretical understanding of the underlying experimental platform. Theoretical modeling is thus an important element for development and application of hybrid light-matter systems, both for the purpose of interpreting experiment and informing future avenues. The first part of this dissertation includes a presentation of the basic building blocks for modeling CQED and nanophotonic systems. The techniques introduced here are used throughout Parts II and III, the former focusing on hybrid photonic-plasmonic resonators for large Purcell enhancements and the emergence of Fano resonances in a plasmonic dimer, and the latter concerning hybridization of photonic modes in coupled dielectric cavities and photon-photon interactions in cavity QED platforms.

In Chapter 1, we present the standard procedure for deriving a Lagrangian-based description of coupled light-matter systems starting from Maxwell's equations. The general approach closely follows standard techniques in cavity quantum electrodynamics, but here is generalized for arbitrary, non-dispersive dielectric environments. The final Lagrangian of this Chapter serves as a substrate for all hybrid light-matter systems considered throughout this dissertation.

In Chapter 2, we demonstrate how the field theoretic description of light-matter interactions can be mapped onto simplified models through analogy to simple mechanical systems. Particular focus will be given to optical frequency platforms comprising photonic cavities and/or plasmonic nanoresonators, as both appear as components of complex nanophotonic systems in Part II. As will be shown, the equations which govern the behavior of these systems are identical to those of a harmonic oscillator. Consequently, the presented analysis is applicable to a wide array of resonant systems displaying oscillatory behavior and, wherever possible, the specifics of the underlying system will be left general. Chapter 2 concludes with a discussion on modeling quantized light-matter interactions.

Chapter 3 focuses on the connection between dissipation and spectral observables, building upon the theoretical models of Chapter 2. In particular, we present a unified framework for computing absorption, scattering, and extinction spectra for a driven, damped oscil-

lating dipole using a classical description. We extend this framework to coupled systems, and furthermore illustrate how radiative interference effects can be modeled by introducing a complex coupling strength. We then follow this with a brief introduction to input-output theory, a theoretical formalism used to compute one- and two-sided sided transmission through resonant cavities. Both of these techniques are used in Part II.

In Chapter 4, we present a survey of several parameter regimes of interest in nanophotonic and cavity QED experiments. Focusing first on weakly coupled systems, we introduce an original derivation of Purcell enhancement using only classical arguments. This is followed by a discussion of the Fano lineshape, of central importance to all three publications enclosed in Part II. We then continue on to strong coupling and introduce the concept of hybridization. We conclude with an introduction to $\mathcal{PT}$-symmetric physics.

Taken together, these first four Chapters introduce many of the core concepts and techniques which underpin the published work appearing in Parts II and III. While many of the derivations contained herein follow standard techniques in cavity quantum electrodynamics and quantum optics used throughout the literature, several results (particularly the modeling of radiative interference and the classical derivation of Purcell enhancement) constitute original derivations presented here for the first time.

Chapter 1

THE ELECTROMAGNETIC LAGRANGIAN: A BOTTOM-UP APPROACH

The goal of this first chapter is to construct a general theory which is capable of describing systems of atoms interacting with the electromagnetic field. Ideally, this construction will be adaptable to various nanophotonic platforms comprising electromagnetic and material degrees of freedom, without specifying the underlying details *a priori*, and can facilitate either a classical or quantum mechanical description depending on the particular problem of interest. The approach presented here draws inspiration from several textbooks, most notably Refs. [39, 40]. However, the focus herein will be on light-matter interactions in optical microcavities composed of dielectric media, whereas the aforementioned references are primarily concerned with light-matter interactions between individual molecules and the free-space radiation field. As a result, several important generalizations will need to be introduced to account for the polarizable media which supports the cavities, and to facilitate quantization of the electromagnetic fields in a dielectric environment.

1.1 Maxwell's equations and the Newton-Lorentz force law

As with any electromagnetic theory, we begin with Maxwell's equations. Defining $\mathbf{E}$ and $\mathbf{B}$ to be the electric and magnetic fields, they may be written, in Gaussian units, as

$$\begin{aligned} \nabla \cdot \mathbf{B} &= 0 \\ \nabla \times \mathbf{E} + \frac{1}{c}\frac{\partial \mathbf{B}}{\partial t} &= 0 \\ \nabla \cdot \mathbf{E} &= 4\pi\rho \\ \nabla \times \mathbf{B} - \frac{1}{c}\frac{\partial \mathbf{E}}{\partial t} &= \frac{4\pi}{c}\mathbf{j}, \end{aligned} \tag{1.1}$$

where ρ and $\mathbf{j}$ are charge and current densities, and c the speed of light. Following Refs. [41, 42] Let us now imagine that the matter which sources Gauss's and Ampere's laws

(third and fourth equations, above) can be partitioned into two distinct subsets, the first corresponding to the bound charges and currents of a macroscopic, dielectric medium and the second comprising independent, freely moving charged particles. In particular, we define

$$\begin{aligned} \rho &= \rho_f + \rho_b \\ \mathbf{j} &= \mathbf{j}_f + \mathbf{j}_b \end{aligned} \tag{1.2}$$

where the subscripts f and b denote the free and bound charge/current density. The former may be written in terms of the charge q_i and position r_i of its constituent particles as

$$\begin{aligned} \rho_f(\mathbf{r}) &= \sum_i q_i \mathbf{r}_i \delta(\mathbf{r} - \mathbf{r}_i) \\ \mathbf{j}_f(\mathbf{r}) &= \sum_i q_i \dot{\mathbf{r}}_i \delta(\mathbf{r} - \mathbf{r}_i). \end{aligned} \tag{1.3}$$

Defining the macroscopic polarization density $\mathbf{P}$, the bound charge density may be written in the usual way as

$$\rho_b = \nabla \cdot \mathbf{P}. \tag{1.4}$$

As the temporal variations in the bound charge density are related to the current density, we would therefore expect $\mathbf{j}_b$ to be related to $\dot{\mathbf{P}}$ in some way. This can be seen most clearly by appealing to the continuity equation

$$\nabla \cdot \mathbf{j}_b + \frac{\partial \rho_b}{\partial t} = 0. \tag{1.5}$$

Rewriting the second term in terms of the polarization density $\mathbf{P}$, we find

$$\nabla \cdot (\mathbf{j}_b - \dot{\mathbf{P}}) = 0. \tag{1.6}$$

Thus $\mathbf{j}_b$ may be broken into two pieces, one with nonzero divergence equal to $\dot{\mathbf{P}}$ (i.e., the polarization current), and the second a divergenceless contribution known as the magnetization current. For simplicity, we will specialize to nonmagnetic materials with relative permeability $\mu = 1$, in which case it may be shown that this second contribution vanishes [4], leading to

$$\mathbf{j}_b = \dot{\mathbf{P}}. \tag{1.7}$$

We can now rewrite Maxwell's equations to reflect the separation of matter into free and dielectric contributions. Starting with Gauss's law, the right-hand side can be broken into two pieces and rearranged such that

$$\nabla \cdot (\mathbf{E} - 4\pi\mathbf{P}) = 4\pi\rho_f. \tag{1.8}$$

Assuming our dielectric medium is isotropic and linear (i.e., $\mathbf{P} = \chi(\mathbf{r})\mathbf{E}$ where χ is the linear susceptibility, here a scalar function of space), Gauss's law may be further rewritten as

$$\nabla \cdot \varepsilon(\mathbf{r})\mathbf{E} = 4\pi\rho_f, \tag{1.9}$$

where $\varepsilon(\mathbf{r})$ is an inhomogeneous dielectric function defined by $\varepsilon(\mathbf{r}) = 1 + 4\pi\chi(\mathbf{r})$. In a similar fashion, Ampere's law may be rearranged using the fact that $\mathbf{j} = \mathbf{j}_f + \dot{\mathbf{P}}$ to find

$$\nabla \times \mathbf{B} - \frac{\varepsilon(\mathbf{r})}{c}\frac{\partial \mathbf{E}}{\partial t} = \frac{4\pi}{c}\mathbf{j}_f. \tag{1.10}$$

Thus we have arrived at the *macroscopic* form of Maxwell's equations,

$$\begin{aligned} &\nabla \cdot \mathbf{B} = 0 \\ &\nabla \times \mathbf{E} + \frac{1}{c}\frac{\partial \mathbf{B}}{\partial t} = 0 \\ &\nabla \cdot \varepsilon(\mathbf{r})\mathbf{E} = 4\pi\rho_f \\ &\nabla \times \mathbf{B} - \frac{\varepsilon(\mathbf{r})}{c}\frac{\partial \mathbf{E}}{\partial t} = \frac{4\pi}{c}\mathbf{j}_f, \end{aligned} \tag{1.11}$$

albeit with the restriction $\mu = 1$. These equations, along with the Newton-Lorentz equations for the free matter (accurate only in the nonrelativistic limit $\dot{\mathbf{r}}_i/c \ll 1$),

$$m_i \frac{\mathrm{d}^2\mathbf{r}_i}{\mathrm{d}t^2} = q_i\mathbf{E}(\mathbf{r}_i, t) + q_i\frac{\dot{\mathbf{r}}_i}{c} \times \mathbf{B}(\mathbf{r}_i, t), \tag{1.12}$$

fully describe the interacting matter-field system. In this form, however, it is not readily apparent how to quantize the system – following Dirac's procedure [8], this is typically achieved by (i) identifying the distinct degrees of freedom and corresponding pairs of canonical variable pairs, and (ii) replacing Poisson brackets by canonical commutation relations, steps which are typically carried out in the Lagrangian and Hamiltonian formalism, the latter deriving from the former through Legendre transform. Thus it is apparent that we must first cast the physics described by Eqs. (1.11 – 1.12) into a Lagrangian framework.

1.2 The matter-field Lagrangian

The most obvious initial obstacle toward writing a Lagrangian consistent with Eqs. (1.11 – 1.12) is the fact that the Euler-Lagrange equations provide equations of motion which are second order in time [43], while Maxwell's equations contain only first order time derivatives of the fields. This is resolved by rewriting the fields in terms of the scalar and vector potentials,

$$\begin{aligned} \mathbf{E} &= -\nabla\Phi - \frac{\dot{\mathbf{A}}}{c} \\ \mathbf{B} &= \nabla \times \mathbf{A}. \end{aligned} \tag{1.13}$$

It is important to note that these relations define Φ and $\mathbf{A}$ only up to some arbitrary gauge function ψ such that the replacement

$$\begin{aligned} \Phi &\to \Phi - \frac{1}{c}\dot{\psi} \\ \mathbf{A} &\to \mathbf{A} + \nabla\psi, \end{aligned} \tag{1.14}$$

leaves the fields (and by extension, Maxwell's equations), unchanged. This is remedied by fixing to a particular gauge, a choice which we will leave unspecified until the next section.

One advantage of introducing the potentials is that the definitions in Eq. (1.13) automatically satisfy the two sourceless Maxwell's equations. Thus we have reduced four equations to two:

$$-\nabla\cdot\varepsilon(\mathbf{r})\nabla\Phi - \frac{1}{c}\nabla\cdot\varepsilon(\mathbf{r})\dot{\mathbf{A}} = 4\pi\rho_f \tag{1.15a}$$

$$\nabla\times\nabla\times\mathbf{A} + \frac{\varepsilon(\mathbf{r})}{c^2}\ddot{\mathbf{A}} = \frac{4\pi}{c}\mathbf{j}_f - \frac{\varepsilon(\mathbf{r})}{c}\nabla\dot{\Phi}. \tag{1.15b}$$

Eqs. (1.15a) and (1.15b), together with the Newton-Lorentz equation (Eq. (1.12)), constitute the three equations which govern the dynamics of our system. Paired with them are the dynamical variables Φ, $\mathbf{A}$ and $\mathbf{r}_i$ and their time derivatives, all together forming the necessary ingredients for a Lagrangian description of the system dynamics.

It can be shown that the Lagrangian

$$L = \sum_i \frac{1}{2}m_i\dot{\mathbf{r}}_i^2 + \int\frac{d^3r}{8\pi}\left[\varepsilon(\mathbf{r})\mathbf{E}^2 - \mathbf{B}^2\right] + \int d^3r\left[\frac{\mathbf{j}_f}{c}\cdot\mathbf{A} - \rho_f\Phi\right] \tag{1.16}$$

yields the three requisite equations upon application of the Euler-Lagrange equations for each of the three dynamical coordinates. In particular, application of the principle of least action with respect to $\mathbf{r}$, Φ, and $\mathbf{A}$ leads to Eq. (1.12), Eq. (1.15a), and Eq. (1.15b), respectively. For explicit calculations see Ref. [39], there carried out for $\varepsilon(\mathbf{r}) = 1$ but proceeding in the exact same way as the more general case.

While Eq. (1.16) satisfies our goal of finding a Lagrangian which describes the dynamics of a system of charged particles coupled to the electromagnetic field, it is readily obvious that by introducing the potentials, we have introduced additional degrees of freedom – at each point in space, the field variables and their time derivatives $\{\mathbf{A}, \dot{\mathbf{A}}, \Phi, \dot{\Phi}\}$ comprise eight total degrees of freedom while the electric and magnetic fields are described by just six.

Removing these redundancies is achieved through two steps. First, because $\dot{\Phi}$ does not appear in the Lagrangian it can be removed [43]. This is evident through application of the Euler-Lagrange equations as Eq. (1.15a) is not a dynamical equation of motion, but rather a constraint between Φ, the longitudinal part of $\varepsilon(\mathbf{r})\dot{\mathbf{A}}$, and the free charge ρ_f. Second, Φ and the longitudinal part of $\mathbf{A}$ are interrelated via gauge freedom (see Refs. [39, 40] for a more in-depth discussion on this). A particularly natural gauge choice which cleanly separates field and matter degrees of freedom is defined by the condition

$$\nabla \cdot \varepsilon(\mathbf{r})\mathbf{A} = 0, \tag{1.17}$$

often termed the *generalized Coulomb gauge* [44, 41] due to its close relation to the Coulomb gauge (also called the transverse or radiation gauge) defined by the same condition with $\varepsilon(\mathbf{r}) \to 1$ [39].

In the generalized Coulomb gauge, Gauss's law (Eq. (1.15a)), becomes

$$\nabla \cdot \varepsilon(\mathbf{r})\nabla\Phi = -4\pi\rho_f, \tag{1.18}$$

a generalized form of Poisson's equation which accounts for the polarization of bound matter characterized by the inhomogeneous dielectric function $\varepsilon(\mathbf{r})$. Thus the generalized Coulomb gauge serves to decouple Φ and $\mathbf{A}$, such that the dynamics of Φ are determined by the dynamics of the *free* matter, and the field degrees of freedom are entirely contained in

the contributions of the vector potential which satisfy $\nabla \cdot \varepsilon(\mathbf{r})\mathbf{A} = 0$. This choice is a natural generalization of the regular Coulomb gauge, whereby the scalar potential becomes dependent on the total matter in the system and the transverse components of $\mathbf{A}$ encode the field degrees of freedom.

We now aim to remove Φ entirely from the Lagrangian, leaving in its place quantities which depend explicitly on matter coordinates. To that end, we first focus on the contribution to the second term due to the electric field. Rewriting in terms of potentials and integrating by parts (discarding surface terms as the fields/potentials vanish at infinity),

$$\begin{aligned}\int \frac{d^3r}{8\pi}\varepsilon(\mathbf{r})\mathbf{E}^2 &= \int \frac{d^3r}{8\pi}\varepsilon(\mathbf{r})\frac{\dot{\mathbf{A}}^2}{c^2} + \int \frac{d^3r}{8\pi}\varepsilon(\mathbf{r})(\nabla\Phi)^2 + \int \frac{d^3r}{4\pi}\varepsilon(\mathbf{r})\mathbf{A}\cdot\nabla\Phi \\ &= \int \frac{d^3r}{8\pi}\varepsilon(\mathbf{r})\frac{\dot{\mathbf{A}}^2}{c^2} - \int \frac{d^3r}{8\pi}(\nabla\varepsilon(\mathbf{r})\nabla\Phi)\Phi - \int \frac{d^3r}{4\pi}(\nabla\cdot\varepsilon(\mathbf{r})\mathbf{A})\Phi \\ &= \int \frac{d^3r}{8\pi}\varepsilon(\mathbf{r})\frac{\dot{\mathbf{A}}^2}{c^2} - \frac{1}{2}\int d^3r\rho_f\Phi,\end{aligned} \tag{1.19}$$

where we have applied the generalized Poisson equation to simplify the second term and used the generalized Coulomb gauge condition to show that the third term vanishes. Inserting this rearranged form back into the Lagrangian, we now find

$$L = L_{\text{matter}} + L_{\text{field}} + L_{\text{int}} \tag{1.20}$$

where

$$\begin{aligned}L_{\text{matter}} &= \sum_i \frac{1}{2}m_i\dot{\mathbf{r}}_i^{\,2} - V_{\text{Coul}} \\ L_{\text{field}} &= \int \frac{d^3r}{8\pi}\left[\varepsilon(\mathbf{r})\frac{\dot{\mathbf{A}}^2}{c^2} - (\nabla\times\mathbf{A})^2\right] \\ L_{\text{int}} &= \frac{1}{c}\int d^3r\,\mathbf{j}_f\cdot\mathbf{A}.\end{aligned} \tag{1.21}$$

Here,

$$V_{\text{Coul}} = \frac{1}{2}\int d^3x\rho_f\Phi \tag{1.22}$$

is the Coulomb potential energy of the system of charges defined by ρ_f [4]. Thus the generalized Coulomb gauge has led to an electromagnetic matter-field Lagrangian which cleanly separates into three contributions describing the matter, dielectric-dressed field and matter-field interactions. The matter degrees of freedom are described by the generalized

coordinates $\mathbf{r}_i$ and their time derivatives, related to the free charge density via Eq. (1.3). Separately, the field degrees of freedom are tied to the vector potential $\mathbf{A}$ and its time derivative.

1.3 The minimal coupling Hamiltonian

With the scalar potential removed entirely from the Lagrangian and a gauge chosen, it is now straightforward to compute the system Hamiltonian. Noting that the interaction term of the Lagrangian may alternatively be written in the form

$$L_{\text{int}} = \frac{1}{c}\sum_i q_i \dot{\mathbf{r}}_i \cdot \mathbf{A}(\mathbf{r}_i), \tag{1.23}$$

it can be seen that the kth component of the momenta conjugate to $\mathbf{r}_i$ and $\mathbf{A}$ are given by

$$\begin{aligned} p_{ik} &= \frac{\partial L}{\partial \dot{r}_{ik}} = m_i \dot{r}_{ik} + q_i A_k(r_i)/c \\ \Pi_k &= \frac{\partial \mathscr{L}}{\partial \dot{A}_k} = \frac{\varepsilon(\mathbf{r})}{4\pi c^2}\dot{A}_k \end{aligned} \tag{1.24}$$

where $\mathscr{L}$ is the Lagrangian density defined by $L = \int d^3r \mathscr{L}$. Following Legendre transform of the Lagrangian, we arrive at the matter-field Hamiltonian

$$H = \sum_i \frac{1}{2m_i}(\mathbf{p}_i - q_i \mathbf{A}(\mathbf{r}_i)/c)^2 + V_{\text{Coul}} + \int \frac{d^3r}{8\pi}\left[\frac{(4\pi c)^2}{\varepsilon(\mathbf{r})}\mathbf{\Pi}^2 + (\nabla \times \mathbf{A})^2\right]. \tag{1.25}$$

Notably, the momentum conjugate to $\mathbf{r}_i$ is not the mechanical momentum, but rather includes an additional contribution from the field. In contrast, the field momentum depends only upon the first time derivative of the vector potential. As will be discussed in the next section, gauge freedom of the potentials allows for these roles to be reversed, such that the field momentum depends upon the matter (leading to concept of the displacement field), and the particle momenta become $\mathbf{p}_i^{\text{mech}} = m_i \dot{\mathbf{r}}_i$. The present framework is referred to as the *minimal coupling* formalism, named as such due to the minimal terms needed in the starting Lagrangian Eq. (1.16) needed to reproduce the Maxwell-Lorentz equations.

At this stage, it is feasible to quantize the Hamiltonian in Eq. (1.25), most easily achieved [39] by transforming into k-space and enforcing the commutation relations

$$\begin{aligned} [r_{ik}, p_{jm}] &= i\hbar\delta_{ij}\delta_{km} \\ [\mathcal{A}_\varepsilon(\mathbf{k}), \pi^\dagger_{\varepsilon'}(\mathbf{k}')] &= i\hbar\delta_{\varepsilon\varepsilon'}\delta(\mathbf{k}-\mathbf{k}'), \end{aligned} \tag{1.26}$$

where $\{k,\, m\}$ label vector components and $\{\varepsilon,\, \varepsilon'\}$ index the two independent polarizations of the field. Alternatively, quantization can be directly carried out in coordinate-space by introducing the transverse delta function [39, 40, 44]

$$\delta_{ij}^{\perp}(\mathbf{r}) = \frac{2}{3}\delta_{ij}\delta(\mathbf{r}) - \frac{1}{4\pi r^3}\left(\delta_{ij} - \frac{3r_i r_j}{r^2}\right) \tag{1.27}$$

and imposing the field commutation relation

$$[A_i(\mathbf{r}), \Pi_j(\mathbf{r}')] = i\hbar\delta_{ij}^{\perp}(\mathbf{r} - \mathbf{r}'). \tag{1.28}$$

In later sections, we will pursue an alternate approach to quantization. This involves a rewriting of the fields as a sum over orthogonal modes, each scaling with a dynamical coordinate which determines the overall field amplitude. Canonical commutation relations are then imposed on the dynamical coordinates rather than on the fields at each point in space. This "mode centric" approach is particularly useful in systems which involve a discrete set of field modes, as is the case for an electromagnetic cavity, and will be further discussed in Chapter 2. At present, we will hold off on carrying out quantization in an explicit manner to first discuss alternate representations of the matter-field Lagrangian and Hamiltonian.

1.4 Alternate descriptions of the matter-field Lagrangian

While the Lagrangian in Eqs. (1.20–1.21) (and the corresponding Hamiltonian in Eq. (1.25)) ultimately provide a complete and general description of the matter-field interactions in an arbitrary system (assuming $\mu = 1$), it is not by any means a unique description. We have thus far seen that the minimal coupling framework provides a straightforward path toward forming an initial description. However, gauge freedom ensures that alternate formulations exist and, depending on the particular system of interest, they can be significantly simpler to analyze and leverage for application.

Separately, we have thus far treated the free matter as an arbitrary collection of charged particles. For most systems of interest, however, these charged particles are not completely unstructured, and instead involve a localized distribution comprising an atom, nanoparticle or quantum dot, for example. It is therefore advantageous to repackage the matter degrees

of freedom into a formulation which capitalizes on the collective behavior of the particles, in lieu of the particle-by-particle approach considered thus far.

In this section, we will describe a simplified version of what is more generally known as the *multipolar* formalism of electrodynamics. Whereas the minimal coupling formulation yields a description where the conjugate momenta associated with the matter depend upon field variables and conjugate fields which are independent of the matter, the multipolar formalism leads to the opposite: conjugate momenta for the matter equivalent to the mechanical momenta, and conjugate field variables which depend on matter coordinates. Most often, the free matter is then decomposed into its multipole expansion, and matter-field interactions appear as a sum over multipole-field interactions which may be truncated at the desired order. The general procedure for arriving at this alternate description is known as the Power–Zienau–Woolley (PZW) transformation, and we defer to existing literature for a detailed discussion of its application and consequences both in free space [45, 46, 39, 40, 47] and its generalization for dielectric media [41].

Here, we present the simplest limit of this theory where only the dipolar term is retained via the long-wavelength approximation. First, let us assume that the system of charges is globally neutral

$$\sum_i q_i = 0 \tag{1.29}$$

and is clustered around some central location $\mathbf{r}_0$. In addition, we assume that the spatial extent of the charges, characterized by some length scale a, is much less than the wavelengths of the electromagnetic field considered ($\lambda \gg a$). Then, to first approximation,

$$L_{\text{int}} = \frac{1}{c}\sum_i q_i \dot{\mathbf{r}}_i \cdot \mathbf{A}(\mathbf{r}_i) \;\approx \frac{1}{c}\sum_i q_i \dot{\mathbf{r}}_i \cdot \mathbf{A}(\mathbf{r}_0), \tag{1.30}$$

where we have approximated the field "felt" by each individual particle by its value at the center of the distribution. The vector potential may now be factored out of the sum, and we find that

$$L_{\text{int}} = \frac{1}{c}\dot{\mathbf{d}} \cdot \mathbf{A}(\mathbf{r}_0), \tag{1.31}$$

where

$$\mathbf{d} = \sum_i q_i \mathbf{r}_i \tag{1.32}$$

is the dipole moment about the central coordinate $\mathbf{r}_0$. Separately, we recall that one may always add a total time derivative to the Lagrangian, leaving the equations of motion unaffected according to the principle of least action [43]. Adding to the above Lagrangian the total time derivative of $-\mathbf{d}\cdot\mathbf{A}(\mathbf{r}_0)/c$, we find

$$\begin{aligned} L_{\text{int}} &= \frac{1}{c}\dot{\mathbf{d}}\cdot\mathbf{A} - \frac{1}{c}\frac{\mathrm{d}}{\mathrm{d}t}(\mathbf{d}\cdot\mathbf{A}(\mathbf{r}_0)) \\ &= -\mathbf{d}\cdot\dot{\mathbf{A}}/c. \end{aligned} \tag{1.33}$$

Writing the full Lagrangian, we have

$$L = \sum_i \frac{1}{2} m_i \dot{\mathbf{r}}_i{}^2 - V_{\text{Coul}} + \int \frac{d^3r}{8\pi}\left[\varepsilon(\mathbf{r})\frac{\dot{\mathbf{A}}^2}{c^2} - (\nabla\times\mathbf{A})^2\right] + \mathbf{d}\cdot\mathbf{E}_\perp(\mathbf{r}_0), \tag{1.34}$$

where the subscript $\perp$ designates the "transverse" portion of the electric field $\mathbf{E}_\perp = -\dot{\mathbf{A}}/c$, here in quotes as it obeys the generalized transversality condition

$$\nabla\cdot\varepsilon(\mathbf{r})\mathbf{E}_\perp = 0, \tag{1.35}$$

rather than the true transversality condition

$$\nabla\cdot\mathbf{E}_\perp = 0, \tag{1.36}$$

thus generalizing the usual result [39, 40] to allow for an inhomogeneous dielectric background other than vaccuum. Regardless of the specific condition obeyed by $\mathbf{E}_\perp$, its physical significance remains the same for $\varepsilon(\mathbf{r}) \neq 1$ or otherwise – it contains the portion of the electric field which is entirely independent of the (free) matter, and thus encodes the true, independent degrees of freedom of the (dielectric-dressed) field.

With the multipolar Lagrangian of Eq. (1.34) in hand, we now have at our disposal an alternate description of the matter-field interaction that involves the first time derivative of the field variable rather than that of the matter coordinates. To that end, computing the momenta conjugate to matter and field coordinates now yields

$$\begin{aligned} p_{ik} &= m_i \dot{r}_{ik} \\ \Pi_k &= \frac{\varepsilon(\mathbf{r})}{4\pi c^2}\dot{A}_k - (d_k/c)\delta(\mathbf{r}-\mathbf{r}_0), \end{aligned} \tag{1.37}$$

thus verifying that the conjugate momenta for the matter are now equivalent to the mechanical momenta, and the field momentum picks up contributions from the matter. While the

minimal coupling and multipolar frameworks are equivalent in that both produce identical measurable quantities [39], the latter picture, where the field is dressed by the matter rather than the opposite, is often simpler to interpret as the Hamiltonian can be entirely written in terms of the transverse electric and magnetic fields, in place of the vector potential which plays a featured role in the minimal coupling framework [39, 40, 47]. In addition, canonical quantization yields an easily interpretable description of the matter unplagued by additional terms contributed by the fields, and it is therefore simplest to model interactions between distant dipoles mediated by the fields in the multipolar framework (see, for example, Ref. [40]).

For much of the remainder of this thesis, the Lagrangian in Eq. (1.34), either in full or certain portions thereof, will be the starting point for modeling various cavity QED and nanophotonic systems. In the next chapter, we will take a closer look at the field and matter portions of the Lagrangian independently. Central to our analysis will be the harmonic oscillator. In particular, we will show that the modes of a simple Fabry Pérot cavity may be mapped onto a set of harmonic oscillators. Similarly, we will also show that a metal nanoparticle can support a dipolar resonance which also behaves as a harmonic oscillator. This duality between material and photonic resonances and oscillator modes is much more general than just these two examples, and we thus follow with two additional Chapters entirely dedicated to techniques and analysis pertaining to coupled oscillator models in nanophotonic systems, before moving onto the main scientific accomplishments detailed in Parts II and III.

Chapter 2

MODELING NANOPHOTONIC COMPONENTS WITH OSCILLATORS: PHOTONIC CAVITIES, PLASMONIC NANOPARTICLES, AND LIGHT-MATTER COUPLING

Central to modern nanophotonic systems and applications is the ability to confine light to the nanoscale at optical frequencies. Fueled in part by developments in fabrication techniques, the last few decades has seen an explosion of micro- and nano-scale structures of varying geometries and materials that provide unprecented ability to control and locally enhance light-matter interactions for a wide array of applications. In this Chapter, we develop theory for both photonic and plasmonic cavities. Each has its own particular advantages – photonic cavities support long-lived resonances with lifetimes that can exceed hundreds of microseconds at optical frequencies. Plasmonic nanoresonators, on the other hand, support resonances which typically live on the order of tens of femtoseconds, yet can confine light to sub-diffraction limit length scales unattainable with conventional photonic cavities. Today, photonic and plasmonic resonators play a complementary role in modern cavity QED experiments, encompassing two distinct strategies for achieving enhancement of light-matter interactions – the former involving long-lived photons, and the latter involving short-lived excitations with exceptionally large fields confined to sub-wavelength length scales.

In the first half of this chapter, we present a general theory of a three-dimensional cavity composed of perfectly conducting walls enclosing vacuum. This formalism serves as a foundation for the extension to optical microresonators composed of dielectric media, a problem further discussed in Chapters 8 and 9, the former containing a formal treatment and the latter an application to an experimentally realized system. In the back half of this Chapter, we develop a basic theoretical understanding of the dipolar plasmonic resonance of a spherical metal nanoparticle. Here, the general aim is not to present a rigorous, all-encompassing theoretical treatment, but rather motivate one of the primary theoretical tools in modeling the optical response of plasmonic nanoparticles: the harmonic oscillator.

We then conclude with a discussion on quantized light-matter interactions, leading to two extremely important models for cavity QED: quantum coupled oscillators and the Jaynes-Cummings Hamiltonian.

2.1 An ideal photonic cavity

In the previous Chapter, we briefly described (without actually carrying out the procedure to completion) how one can quantize the electromagnetic field at the level of field operators. Here, we will demonstrate an alternate route using the concept of a mode expansion. Ultimately, this will allow us to integrate out the spatial information in the field and arrive at a dynamical description in terms of field amplitudes which is significantly simpler than that which centers on the field operators.

For simplicity, we will carry out this calculation for a three-dimensional cavity with perfectly conducting walls. The more general case of a dielectric microresonator, characterized by a piecewise dielectric function $\varepsilon(\mathbf{r})$, is detailed in Chapter 8. In addition, we will assume no free charge in the system and therefore the only degrees of freedom are those of the field. Then, drawing upon our discussion in Chapter 1, the Lagrangian for the system is

$$L = \int \frac{d^3r}{8\pi} \left[\frac{\dot{\mathbf{A}}^2}{c^2} - (\nabla \times \mathbf{A})^2 \right]. \tag{2.1}$$

Working in the Coulomb gauge $\nabla \cdot \mathbf{A} = 0$, absence of free charge allows us to take the scalar potential as vanishing without loss of generality. Then the electric field is related to the vector potential by

$$\mathbf{E} = -\dot{\mathbf{A}}/c, \tag{2.2}$$

and the fundamental equations of the system become the wave equation (i.e., the equation of motion for $\mathbf{A}$),

$$\nabla^2 \mathbf{A} - \frac{\ddot{\mathbf{A}}}{c^2} = 0 \tag{2.3}$$

and the corresponding boundary conditions at the conducting walls of the cavity,

$$\begin{aligned} \mathbf{n} \times \mathbf{E}|_S &= 0 \\ \mathbf{n} \cdot \mathbf{B}|_S &= 0, \end{aligned} \tag{2.4}$$

where $\mathbf{n}$ labels the unit vector normal to the surface.

2.1.1 The mode expansion

Let us now decompose the vector potential $\mathbf{A}$ into a set of orthogonal modes which individually satisfy Eq. (2.3). To that end, we write

$$\mathbf{A}(\mathbf{r},t) = \sum_m \frac{c\sqrt{4\pi}}{V_m} q_m(t)\mathbf{f}_m(\mathbf{r}) \tag{2.5}$$

where $q_m(t)$ is a time-dependent dynamical amplitude, $\mathbf{f}_m(\mathbf{r})$ the mode function which characterizes the spatial profile of each mode, and V_m is the mode volume of the mth mode, defined by [48, 49, 50]

$$V_m = \frac{\int d^3r|\mathbf{f}_m(\mathbf{r})|^2)}{\max\{|\mathbf{f}_m(\mathbf{r})|^2\}}. \tag{2.6}$$

The electric and magnetic fields may also be written in terms of this mode expansion as

$$\begin{aligned} \mathbf{E}(\mathbf{r},t) &= -\sum_m \frac{\sqrt{4\pi}}{V_m}\dot{q}_m(t)\mathbf{f}_m(\mathbf{r}) \\ \mathbf{B}(\mathbf{r},t) &= \sum_m \frac{c\sqrt{4\pi}}{V_m} q_m(t)\nabla\times\mathbf{f}_m(\mathbf{r}). \end{aligned} \tag{2.7}$$

We note that the mode functions $\mathbf{f}_m(\mathbf{r})$ and dynamical coordinates $q_m(t)$ may be arbitrarily rescaled at the expense of one another, without loss of generality. For simplicity, we will proceed with the convention

$$\max\{|\mathbf{f}_m(\mathbf{r})|^2\} = 1, \tag{2.8}$$

leading to the simplified form of the mode volume,

$$V_m = \int d^3r|\mathbf{f}_m(\mathbf{r})|^2. \tag{2.9}$$

This constitutes a deviation from the usual choice in the literature, where the mode volume itself is normalized to unity [14, 51] (i.e., $\int d^3r|\mathbf{f}_m(\mathbf{r})|^2 = 1$). We will soon see, however, that this alternate choice brings the physical importance of the mode volume V_m to the forefront, both in the present example as well as for the extension to dielectric microresonators in Chapter 8.

Substituting the mth term of Eq. (2.5) into Eq. (2.3), we find

$$c^2 q_m(t)\nabla^2\mathbf{f}_m(\mathbf{r}) = \ddot{q}_m(t)\mathbf{f}_m(\mathbf{r}), \tag{2.10}$$

implying

$$\begin{aligned} \ddot{q}_m(t) &= \alpha_m c^2 q_m(t) \\ \nabla^2 \mathbf{f}_m(\mathbf{r}) &= \alpha_m \mathbf{f}_m(\mathbf{r}) \end{aligned} \tag{2.11}$$

where α_m is some to-be-determined separation constant. The differential equation for $q_m(t)$ admits two qualitatively distinct types of solutions: oscillatory and exponential growth/decay. The former class corresponds to $\alpha_m < 0$, while the latter corresponds to $\alpha_m > 0$. We now aim to show that only oscillatory solutions are physical. Appealing to the definition of the mode volume in Eq. (2.9), we can use the second line in Eq. (2.11) to write

$$\begin{aligned} V_m &= \frac{1}{\alpha_m} \int d^3r \, \mathbf{f}_m^*(\mathbf{r}) \cdot \nabla^2 \mathbf{f}_m(\mathbf{r}) \\ &= -\frac{1}{\alpha_m} \int d^3r \, \mathbf{f}_m^*(\mathbf{r}) \cdot (\nabla \times \nabla \times \mathbf{f}_m(\mathbf{r})) \\ &= -\frac{1}{\alpha_m} \int d^3r \, \nabla \cdot (\mathbf{f}_m^*(\mathbf{r}) \times \nabla \times \mathbf{f}_m(\mathbf{r}))) - \frac{1}{\alpha_m} \int d^3r |\nabla \times \mathbf{f}_m(\mathbf{r})|^2 \end{aligned} \tag{2.12}$$

where in the last step we integrated by parts. Applying Gauss's theorem and invoking boundary conditions, we find

$$\begin{aligned} V_m &= \frac{1}{\alpha_m} \oint d\mathbf{S} \cdot (\mathbf{f}_m^*(\mathbf{r}) \times \nabla \times \mathbf{f}_m(\mathbf{r})) - \frac{1}{\alpha_m} \int d^3r |\nabla \times \mathbf{f}_m(\mathbf{r})|^2 \\ &= \frac{1}{\alpha_m} \oint (\nabla \times \mathbf{f}_m(\mathbf{r})) \cdot (d\mathbf{S} \times \mathbf{f}_m^*(\mathbf{r})) - \frac{1}{\alpha_m} \int d^3r |\nabla \times \mathbf{f}_m(\mathbf{r})|^2 \\ &= -\frac{1}{\alpha_m} \int d^3r |\nabla \times \mathbf{f}_m(\mathbf{r})|^2. \end{aligned} \tag{2.13}$$

According the definition of the mode volume in Eq. (2.9), V_m is positive. Likewise, the integrand in the final form of the above equation is positive. Consequently, it must be true that $\alpha_m < 0$ and we may therefore assign it the value

$$\alpha_m = -k_m^2 \tag{2.14}$$

where k_m is real-valued. Substituting into the two equations in Eq. (2.11) leads to

$$\begin{aligned} \ddot{q}_m(t) &= -\omega_m^2 q_m(t) \\ \nabla^2 \mathbf{f}_m(\mathbf{r}) &= -k_m^2 \mathbf{f}_m(\mathbf{r}). \end{aligned} \tag{2.15}$$

Thus we see that each individual cavity mode behaves dynamically as a harmonic oscillator with resonant frequency $\omega_m = ck_m$, and is further characterized by a spatial mode profile

obeying the Helmholtz equation. For simplicity, we can assume the mode functions $\mathbf{f}_m(\mathbf{r})$ to be completely real. No generality is lost in enforcing this, as Eq. (2.15), paired with the fact that k_m is real, implies that the complex conjugate of any solution to the Helmholtz equation is also a solution. As a result, completely real solutions may always be formed through linear combination of complex conjugate pairs.

The mode functions obeying the Helmholtz equation are mutually orthogonal, as can be seen through the following argument. Using the fact that $\nabla^2\mathbf{f}_m(\mathbf{r}) = -k_m^2\mathbf{f}_m(\mathbf{r})$, the overlap integral between two mode functions $\mathbf{f}_m(\mathbf{r})$ and $\mathbf{f}_n(\mathbf{r})$ can be rewritten as

$$\begin{aligned}\int d^3r\, \mathbf{f}_m(\mathbf{r})\cdot\mathbf{f}_n(\mathbf{r}) &= -\frac{1}{k_n^2}\int d^3r\, \mathbf{f}_m(\mathbf{r})\cdot\nabla^2\mathbf{f}_n(\mathbf{r}) \\ &= -\frac{1}{k_n^2}\int d^3r\, \nabla^2\mathbf{f}_m(\mathbf{r})\cdot\mathbf{f}_n(\mathbf{r}) \\ &= \frac{k_m^2}{k_n^2}\int d^3r\, \mathbf{f}_m(\mathbf{r})\cdot\mathbf{f}_n(\mathbf{r}),\end{aligned} \tag{2.16}$$

where we have integrated by parts twice to arrive at the second line, and applied the Helmholtz equation in simplifying to the third. Comparing this final expression to the original, it is clear that, unless $k_m = k_n$ (and, by extension, $\mathbf{f}_m(\mathbf{r}) = \mathbf{f}_n(\mathbf{r})$), it must be true that the starting integral vanishes. Thus the distinct modes of the cavity are mutually orthogonal,

$$\int d^3r\, \mathbf{f}_m(\mathbf{r})\cdot\mathbf{f}_n(\mathbf{r}) = V_m\delta_{mn}. \tag{2.17}$$

2.1.2 Canonical quantization of the cavity fields

As previously discussed, there are two commonly used strategies to quantize the electromagnetic field. The first involves direct quantization of the field variables, while the second is achieved through mode expansion of the fields and quantization of the mode amplitudes. In this section, we will carry out the latter procedure.

To begin, we recall the form of the electromagnetic Lagrangian,

$$L = \int \frac{d^3}{8\pi}\left[\frac{\dot{\mathbf{A}}^2}{c^2} - (\nabla\times\mathbf{A})^2\right]. \tag{2.18}$$

Substituting in the mode expansion for the vector potential in Eq. (2.5), we find

$$\begin{aligned} L &= \sum_{mn} \left[\frac{1}{2V_m V_n} \dot{q}_m \dot{q}_n \int d^3r\, \mathbf{f}_m(\mathbf{r}) \cdot \mathbf{f}_n(\mathbf{r}) - \frac{c^2}{2V_m V_n} q_m q_n \int d^3r\, (\nabla \times \mathbf{f}_m(\mathbf{r})) \cdot (\nabla \times \mathbf{f}_n(\mathbf{r})) \right] \\ &= \sum_{mn} \left[\frac{1}{2V_m V_n} \dot{q}_m \dot{q}_n - \frac{c^2 k_m^2}{2V_m V_n} q_m q_n \right] \int d^3r\, \mathbf{f}_m(\mathbf{r}) \cdot \mathbf{f}_n(\mathbf{r}) \\ &= \sum_{mn} \left[\frac{1}{2V_m V_n} \dot{q}_m \dot{q}_n - \frac{c^2 k_m^2}{2V_m V_n} q_m q_n \right] V_m \delta_{mn}, \end{aligned} \tag{2.19}$$

where the second line was obtained through integration by parts and application of the Helmholtz equation in Eq. (2.15), and the orthogonality relation in Eq. (2.17) was used in arriving at the final expression. Applying the Kronecker delta, we find

$$L = \sum_m \left[\frac{1}{2V_m} \dot{q}_m^2 - \frac{\omega_m^2}{2V_m} q_m^2 \right], \tag{2.20}$$

thus illustrating that the dynamics of the electromagnetic modes of a cavity are isomorphic to a set of independent, harmonic oscillators of resonant frequency ω_m and effective mass $1/V_m$.

We now turn our attention to computation of the Hamiltonian. The momenta conjugate to the generalized coordinates q_m are given by

$$p_m = \dot{q}_m / V_m. \tag{2.21}$$

Interestingly, we see that p_m determines the scaling of the electric field, just as the vector potential scales with q_m,

$$\begin{aligned} \mathbf{A}(\mathbf{r}, t) &= \frac{c\sqrt{4\pi}}{V_m} q_m(t) \mathbf{f}_m(\mathbf{r}) \\ \mathbf{E}(\mathbf{r}, t) &= -\sqrt{4\pi}\, p_m(t) \mathbf{f}_m(\mathbf{r}), \end{aligned} \tag{2.22}$$

confirming what is otherwise found through direct quantization at the level of the fields: the vector potential $\mathbf{A}$ and electric field $\mathbf{E}$ are, up to some prefactors, dynamically conjugate to one another. As we will see in Chapter 8, a similar relation is found for dielectric microresonators, except there it is the displacement field $\mathbf{D} = \varepsilon(\mathbf{r})\mathbf{E}$ which is conjugate to $\mathbf{A}$.

Computing the Legendre transform of Eq. (2.20), we find the Hamiltonian governing the system dynamics to be exactly that of a set of independent harmonic oscillators,

$$H = \sum_m \frac{V_m}{2} p_m^2 + \frac{1}{2V_m} \omega_m^2 q_m^2. \tag{2.23}$$

Following the procedure set forth by Dirac [8], quantization is achieved by promoting the dynamical variables q_m and p_m to operators obeying the canonical commutation relation $[q_m, p_n] = i\hbar\delta_{mn}$. For simplicity, we will not introduce any additional notation (such as a hat) to distinguish operators from classical variables, and will instead rely on context for when the distinction is needed.

In place of Hamilton's classical equations, the dynamics of the system are encoded by Heisenberg's equations of motion, yielding

$$\begin{aligned} \dot{q}_m &= \frac{i}{\hbar}[H, q_m] = V_m p_m \\ \dot{p}_m &= \frac{i}{\hbar}[H, p_m] = -\frac{\omega_m^2}{V_m} q_m. \end{aligned} \tag{2.24}$$

These two coupled first order equations can be rewritten as two uncoupled second order equations through substitution, yielding equations identical to those expected of a classical harmonic oscillator, albeit in terms of operators,

$$\begin{aligned} \ddot{q}_m &= -\omega_m^2 q_m \\ \ddot{p}_m &= -\omega_m^2 p_m \end{aligned} \tag{2.25}$$

with the initial conditions

$$q_m(0) = q_m \qquad \dot{q}_m(0) = V_m p_m \tag{2.26}$$

$$p_m(0) = p_m \qquad \dot{p}_m(0) = -\frac{1}{V_m} \omega_m^2 q_m, \tag{2.27}$$

where all expressions on the right-hand side refer to the static, Schrödinger picture operators. Unless otherwise stated, any operator with an explicit time dependence (e.g., $q_m(t)$, $p_m(t)$) denotes an operator in the Heisenberg picture. The current representation of the system in terms of conjugate pairs $\{q_m, p_m\}$, while correct, is not unique. In particular, the first-order equations supplied by Heisenberg's equations of motion are not diagonal, suggesting the possibility for a different basis in which Heisenberg's equations *are* diagonal, constructed

by casting the Hamiltonian in terms of particular linear combinations of q_m and p_m (or, at the level of the fields, $\mathbf{A}$ and $\mathbf{E}$). This leads to the well-known concept of creation and annihilation operators and, by extension, the photon. For completeness, we will briefly sketch a typical strategy for computing the creation and annihilation operators.

The most direct route toward computing the correct linear combination of q_m and p_m which decouples Heisenberg's equations involves analyzing the solutions to Eq. (2.25) which, taking into account the corresponding initial conditions in Eq. (2.27), yields

$$\begin{aligned} q_m(t) &= q_m \cos(\omega_m t) + \frac{V_m}{\omega_m} p_m \sin(\omega_m t) \\ &= \frac{1}{2}\left[q_m - i\frac{V_m}{\omega_m}p_m\right] e^{i\omega_m t} + \left[q_m + i\frac{V_m}{\omega_m}p_m\right] e^{-i\omega_m t} \\ p_m(t) &= -q_m \frac{\omega_m}{V_m} \sin(\omega_m t) + p_m \cos(\omega_m t) \\ &= i\frac{\omega_m}{2V_m}\left[q_m - i\frac{V_m}{\omega_m}p_m\right] e^{i\omega_m t} - i\frac{\omega_m}{2V_m}\left[q_m + i\frac{V_m}{\omega_m}p_m\right] e^{-i\omega_m t}, \end{aligned} \tag{2.28}$$

where we have rewritten trigonometric functions as linear combinations of complex exponentials and grouped terms accordingly. Next, we define the operator

$$a_m = \frac{1}{2\alpha_m}\left[q_m + i\frac{V_m}{\omega_m}p_m\right], \tag{2.29}$$

where α_m is some constant that will be chosen such that the operators a_m obey the commutation relation

$$[a_m, a_n^\dagger] = \delta_{mn}, \tag{2.30}$$

allowing us to identify a_m and $a_m^\dagger$ as bosonic annihilation and creation operators. The generalized coordinates and momenta can then be expressed in terms of a_m and $a_m^\dagger$ as

$$\begin{aligned} q_m(t) &= \alpha_m^* a_m^\dagger e^{i\omega_m t} + \alpha_m a_m e^{-i\omega_m t} \\ p_m(t) &= i\frac{\omega_m}{V_m}\alpha_m^* a_m^\dagger e^{i\omega_m t} - i\frac{\omega_m}{V_m}\alpha_m a_m e^{-i\omega_m t}. \end{aligned} \tag{2.31}$$

Crucially, the commutation relations imposed on the creation and annihilation operators must be consistent with the canonical commutation relations obeyed by $q_m(t)$ and $p_n(t)$ for which we find, after some algebra,

$$[q_m(t), p_n(t)] = i\frac{2\omega_m}{V_m}\mathrm{Re}\{\alpha_m^* \alpha_n e^{i(\omega_m - \omega_n)t}\}\delta_{mn}. \tag{2.32}$$

Thus we find that in order to have preserve $[q_m(t), q_n(t)] = i\hbar\delta_{mn}$ for all times, we require $\alpha_m = \sqrt{\frac{\hbar V_m}{2\omega_m}}e^{-i\phi}$, where ϕ encodes an arbitrary phase which we are free to choose. The standard definitions of a_m and $a_m^\dagger$ (for example, those found in Ref. [52]) derive from the choice $\phi = 0$. However, it is often convenient to keep in mind the more general solution with arbitrary ϕ, as in certain situations another choice can facilitate freedom in choosing the light-matter coupling strength to be real-valued. This will be shown more explicitly in Section 2.3.

We conclude by writing some general expressions for the generalized coordinates, momenta, and fields in terms of creation and annihilation operators. As expected, the Hamiltonian may be shown to equal the well-known result

$$H = \sum_m \hbar\omega_m \left[a_m^\dagger a_m + \frac{1}{2}\right], \tag{2.33}$$

with time-dependent generalized coordinates and momenta given by

$$\begin{aligned} q_m(t) &= \sqrt{\frac{\hbar V_m}{2\omega_m}}\left[a_m^\dagger e^{i(\omega_m t+\phi)} + a_m e^{-i(\omega_m t+\phi)}\right] \\ p_m(t) &= i\sqrt{\frac{\hbar\omega_m}{2V_m}}\left[a_m^\dagger e^{i(\omega_m t+\phi)} - a_m e^{-i(\omega_m t+\phi)}\right] \end{aligned} \tag{2.34}$$

and corresponding annihilation operators

$$a_m = \sqrt{\frac{\omega_m}{2\hbar V_m}}\left[q_m + i\frac{V_m}{\omega_m}p_m\right]e^{i\phi}, \tag{2.35}$$

with creation operators defined as the Hermitian conjugate of a_m. Extrapolating to the fields, we find

$$\begin{aligned} \mathbf{A}(\mathbf{x},t) &= \sum_m \sqrt{\frac{2\pi\hbar c}{k_m V_m}}\left[a_m e^{-i(\omega_m t+\phi)} + a_m^\dagger e^{i(\omega_m t+\phi)}\right]\mathbf{f}_m(\mathbf{r}) \\ \mathbf{E}(\mathbf{x},t) &= i\sum_m \sqrt{\frac{2\pi\hbar c k_m}{V_m}}\left[a_m e^{-i(\omega_m t+\phi)} - a_m^\dagger e^{i(\omega_m t+\phi)}\right]\mathbf{f}_m(\mathbf{r}) \\ \mathbf{B}(\mathbf{x},t) &= \sum_m \sqrt{\frac{2\pi\hbar c}{k_m V_m}}\left[a_m e^{-i(\omega_m t+\phi)} + a_m^\dagger e^{i(\omega_m t+\phi)}\right]\nabla\times\mathbf{f}_m(\mathbf{r}). \end{aligned} \tag{2.36}$$

2.2 A plasmonic nanoresonator

When subjected to an electric field, the conduction band electrons of a metal nanoparticle will become displaced relative to the ionic background, screening the applied field as a

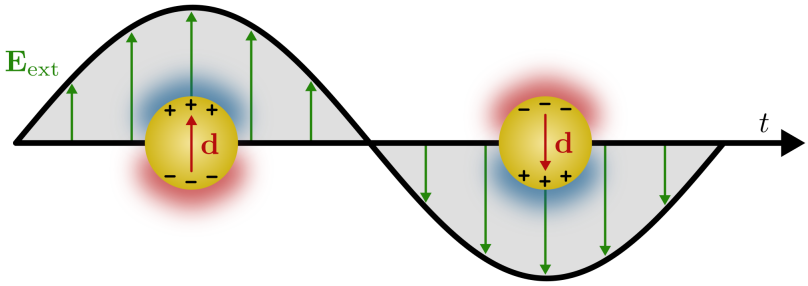

Figure 2.1: The dipolar localized surface plasmon mode of a metallic sphere driven by an oscillating external field $\mathbf{E}_{\text{ext}}$. The conduction band electrons of the sphere medium respond to the applied field, setting up an an induced dipole moment $\mathbf{d}$. The relative displacement between the electrons and the ionic background produces a restoring force, causing the electrons to accelerate toward their equilibrium positions once the sphere is at the node of the applied field. At steady-state, oscillatory evolution of the dipole ensues, mirroring the mechanical motion of a damped harmonic oscillator.

result. If the incident field is then turned off, the restoring force exerted by the ionic background will cause those displaced electrons to accelerate toward, and possibly overshoot, their equilibrium positions, provoking continued oscillation until all energy is dissipated due to electron-ion collisions. Alternatively, applying an oscillatory electric field of wavelength λ much larger than the dimensions of the nanoparticle, as illustrated in Fig. 2.1, can, depending on the morphology and material of the nanoparticle, create sustained, steady-state oscillations encapsulated by the time dependent evolution of the net dipole moment $\mathbf{d}$. The dynamics described above hint at a qualitative similarity between the collective response of the conduction band electrons of a metal nanoparticle – known as a localized surface plasmon (LSP) [53] – and a damped harmonic oscillator upon application of an external applied force. The goal of this section is to make this connection more quantitative using simple mathematical and physical arguments.

Let us imagine that we have a perfectly spherical metal nanoparticle of radius a, subjected to an oscillatory electric field of frequency ω. In the limit where the wavelength of the applied field is much larger than the particle radius ($\lambda = 2\pi c/\omega \gg a$), the dominant contribution to

the induced response is that of an electric dipole [54, 55]

$$\mathbf{d} = \alpha(\omega)\mathbf{E} \tag{2.37}$$

characterized by the Clausius-Mossotti polarizability [4]

$$\alpha(\omega) = \left(\frac{\varepsilon(\omega) - 1}{\varepsilon(\omega) + 2}\right) a^3, \tag{2.38}$$

where $\varepsilon(\omega)$ is the dielectric function which characterizes the nanoparticle material. Here, we assume the nanoparticle is metallic and thus invoke Drude theory [56], leading to the dipersive dielectric function

$$\varepsilon(\omega) = \varepsilon_\infty - \frac{\omega_p^2}{\omega^2 + i\omega\gamma}, \tag{2.39}$$

where ω_p and γ are the material dependent plasma frequency and characteristic scattering frequency, and ε_∞ incorporates the instantaneous response of high-frequency core electrons.

Substituting Eq. (2.39) into Eq. (2.38), we find

$$\begin{aligned}
\alpha(\omega) &= \frac{\varepsilon_\infty - \omega_p^2/(\omega^2 - i\omega\gamma) - 1}{\varepsilon_\infty - \omega_p^2/(\omega^2 + i\omega\gamma) + 2} a^3 \\
&= \frac{(\varepsilon_\infty - 1)(\omega^2 - i\omega\gamma) - \omega_p^2}{(\varepsilon_\infty + 2)(\omega^2 - i\omega\gamma) - \omega_p^2} a^3 \\
&= \frac{\frac{\varepsilon_\infty - 1}{\varepsilon_\infty + 2}(\omega^2 + i\omega\gamma) - \omega_0^2}{\omega^2 - \omega_0^2 + i\omega\gamma} a^3,
\end{aligned} \tag{2.40}$$

where we have made the definition

$$\omega_0^2 = \frac{\omega_p^2}{\varepsilon_\infty + 2}. \tag{2.41}$$

We now aim to separate the instantaneous (i.e., frequency-independent) portion of $\alpha(\omega)$ from the dynamical (i.e., frequency-dependent) contribution. To achieve this, we add and subtract $\omega_0^2(\varepsilon_\infty - 1)/(\varepsilon_\infty + 2)$ to the numerator, yielding (after some simplification)

$$\begin{aligned}
\alpha(\omega) &= \frac{\varepsilon_\infty - 1}{\varepsilon_\infty + 2} a^3 + \frac{e^2/m}{-\omega^2 + \omega_0^2 - i\omega\gamma} \\
&= \alpha_{\text{static}} + \alpha_{\text{LSP}}(\omega)
\end{aligned} \tag{2.42}$$

where the effective mass m is defined by

$$m = \frac{e^2(\varepsilon_\infty + 2)}{3\omega_0^2 a^3}. \tag{2.43}$$

Eq. (2.42) demonstrates that the response of the metal nanoparticle to an external field can be broken into two distinct contributions: one which is instantaneous and furthermore vanishing in the limit where the interband transitions are neglected (i.e., $\varepsilon_\infty \to 1$), and one describing an inertial, frequency-dependent response. This latter contribution is known as the the dipolar localized surface plasmon (LSP) [53].

2.2.1 Modeling the dipolar LSP as a harmonic oscillator

The analytic form of $\alpha_{\text{LSP}}(\omega)$ demonstrates that the response of the dipolar LSP of a spherical metal nanoparticle is identical to that of a damped harmonic oscillator. To illustrate this more explicitly, we imagine harmonically driving a dipole resonance characterized by effective mass m, resonant frequency ω_0, and damping rate γ. For simplicity, let us define the applied external field as $\mathbf{E}_{\text{ext}} = E_0 e^{-i\omega t}\hat{\mathbf{z}}$ such that the dynamics of the induced dipole are described by the one-dimensional equation of motion

$$m\ddot{x} + m\gamma\dot{x} + m\omega_0^2 x = eE_0 e^{-i\omega t}, \tag{2.44}$$

where x is the generalized coordinate related to the dipole moment by $\mathbf{d} = ex\hat{\mathbf{z}}$.

Seeking a steady-state solution of the form $x(t) = x(\omega)e^{-i\omega t}$, substituting $x(t)$ into Eq. (2.44) and solving for $x(\omega)$ yields

$$x(\omega) = \frac{eE_0/m}{-\omega^2 + \omega_0^2 - i\omega\gamma}. \tag{2.45}$$

Recasting this solution in terms of the polarizability $\alpha(\omega) = ex/E_0$, we arrive at an expression identical to α_{LSP},

$$\alpha(\omega) = \frac{e^2/m}{-\omega^2 + \omega_0^2 - i\omega\gamma}, \tag{2.46}$$

thus demonstrating the equivalence between the dipolar plasmonic response of a metal nanoparticle and a damped, harmonic oscillator with effective parameters m, γ, and ω_0 informed by the nanoparticle material and size.

While we have specialized to the ideal case of a spherical nanoparticle, it is worth noting that the derived result Eq. (2.46) is general for any dipolar resonance driven by an external electric field, including those describing the LSP response of nonspherical nanoparticles.

However, the analytic forms presented for ω_0 and m in Eqs. (2.41) and (2.41) are specific to a spherical morphology, though generalizations can be derived for oblate and prolate spheroidal particles [57, 58, 59] – particularly useful for approximate modeling of metallic nanorods and nanodisks. Separately, it is possible to construct oscillator models for the higher order multipole plasmon resonances. Such a procedure is beyond the scope of the simple arguments presented here, however, and we thus defer to the existing literature [60, 61] for a more complete discussion.

2.2.2 Inclusion of radiation losses

Central to the above derivation is the Rayleigh (or long-wavelength) approximation $\lambda \gg a$, allowing us to apply the Clausius-Mossotti polarizability in Eq. (2.38) which, strictly speaking, is a solution to Maxwell's equations in the so-called quasistatic approximation defined by the limit $c \to \infty$ [54], in effect ignoring retardation effects resulting from the finite speed of light. In this limit, the field of the induced dipole is given by

$$\mathbf{E}_{\text{dip}}(\mathbf{r}, t) = \frac{1}{r^3}(3\hat{\mathbf{r}}\hat{\mathbf{r}} - 1) \cdot \mathbf{d}(t). \tag{2.47}$$

However, it is clear from Eq. (2.44) that the induced dipole is not static, but rather oscillates at a frequency corresponding to that of the applied harmonic field. From classical electrodynamics, we know that the field of an oscillating dipole is given by

$$\mathbf{E}_{\text{dip}}(\mathbf{r}, t) = \left[\frac{1}{r^3}(3\hat{\mathbf{r}}\hat{\mathbf{r}} - 1) - \frac{ik}{r^2}(3\hat{\mathbf{r}}\hat{\mathbf{r}} - 1) - \frac{k^2}{r}(\hat{\mathbf{r}}\hat{\mathbf{r}} - 1)\right] e^{ikr} \cdot \mathbf{d}(t), \tag{2.48}$$

where the first, second, and third terms correspond to the near, intermediate, and far fields.

Crucially, the far field is entirely transverse and therefore represents a transfer of energy from the dipole oscillator to the free radiation field [4]. From the viewpoint of the dipole dynamics, this indicates that the oscillating dipole radiates energy, suggesting the presence of an additional dissipative pathway not previously included in Eq. (2.44). Its absence is a consequence of taking the quasistatic limit where $c \to \infty$, causing the intermediate and far fields to vanish, leaving just the near field portion in agreement with Eq. (2.47). For large enough particles (which still obey the Rayleigh limit $\lambda \gg a$), such radiative or scattering losses can become important [54]. We thus wish to "patch up" the dynamical equation Eq.

(2.44) with the aim of constructing a more accurate description which accounts for radiation losses, but otherwise neglects retardation effects that can influence, for example, the exact value of LSP resonant frequency ω_0 [54].

To achieve this, we rely on the arguments presented in Ref. [4]. In particular, it may be shown that the instantaneous power radiated by a oscillating dipole is given by the Larmor power,

$$P_{\text{rad}} = \frac{2}{3}\frac{e^2}{c^3}\ddot{\mathbf{x}}^2. \tag{2.49}$$

Over the course of a single period of oscillation τ, the average power radiated is equal to

$$\langle P_{\text{rad}} \rangle = \frac{1}{\tau}\int_{-\tau/2}^{\tau/2} \frac{2}{3}\frac{e^2}{c^3}\ddot{\mathbf{x}}^2 dt. \tag{2.50}$$

To account for this, we introduce the radiation reaction force $\mathbf{F}_{\text{rad}}$ which, over the course of an oscillation cycle, does work on the dipole at a rate equal to

$$\frac{dW}{dt} = -\frac{1}{\tau}\int_{-\tau/2}^{\tau/2} \mathbf{F}_{\text{rad}} \cdot \dot{\mathbf{x}}\, dt. \tag{2.51}$$

Equating Eqs. (2.50) and (2.51),

$$\begin{aligned} \frac{1}{\tau}\int_{-\tau/2}^{\tau/2} \mathbf{F}_{\text{rad}} \cdot \dot{\mathbf{x}}\, dt &= -\frac{1}{\tau}\int_{-\tau/2}^{\tau/2} \frac{2}{3}\frac{e^2}{c^3}\ddot{\mathbf{x}}^2\, dt \\ &= -\frac{1}{\tau}\int_{-\tau/2}^{\tau/2} \frac{2}{3}\frac{e^2}{c^3}\dddot{\mathbf{x}} \cdot \dot{\mathbf{x}}\, dt, \end{aligned} \tag{2.52}$$

where we have integrated by parts in arriving at the second line, using the fact that $x(\tau/2) = x(-\tau/2)$ to eliminate the boundary terms. Thus we see that the appropriate choice for $\mathbf{F}_{\text{rad}}$ is

$$\mathbf{F}_{\text{rad}} = -\frac{2}{3}\frac{e^2}{c^3}\dddot{\mathbf{x}}. \tag{2.53}$$

Inserting this force into Eq. (2.44) and relabeling the nonradiative Drude damping rate by γ_{nr}, the equation of motion for the oscillator becomes

$$m\ddot{x} + m\gamma_{\text{nr}}\dot{x} + m\omega_0^2 x = -\frac{2}{3}\frac{e^2}{c^3}\dddot{x} + eE_0 e^{-i\omega t}. \tag{2.54}$$

In this form, the role of $\mathbf{F}_{\text{rad}}$ is somewhat mysterious, particularly due to the presence of the third time derivative of x. To that end, it is helpful to specialize to a steady-state scenario such that $\dddot{x} = -\omega^2\dot{x}$, allowing us to write

$$m\ddot{x} + m\gamma_{\text{tot}}\dot{x} + m\omega_0^2 x = eE_0 e^{-i\omega t}, \tag{2.55}$$

where

$$\gamma_{\text{tot}} = \gamma_{\text{nr}} + \gamma_{\text{rad}}. \tag{2.56}$$

Here, γ_{rad} is the effective frequency-dependent radiative damping rate

$$\gamma_{\text{rad}}(\omega) = \frac{2}{3}\frac{e^2\omega^2}{mc^3} \tag{2.57}$$

which takes into account the size of the nanoparticle via the effective mass m, indicating that smaller nanoparticles (larger m) radiate comparatively less than larger nanoparticles (smaller m). Importantly, the size dependence of m and the form of γ_{rad} together ensure that in the extreme end of the Rayleigh limit where $a/\lambda \to 0$, γ_{rad} also tends towards zero, deeming the radiative corrections negligible.

Conservation of energy has allowed us to write an effective equation of motion which accounts for the radiation reaction force, but it is not obvious at present the underlying mechanism which causes it. We thus conclude this Section with a brief discussion regarding an alternate, more physical interpretation of Eq. (2.53). Introducing the dyadic Green's function $\mathbf{\Lambda}(\mathbf{r})$ (also known as the dipole relay tensor), we can write the full electric field of the dipole as $\mathbf{E}_{\text{dip}}(\mathbf{r}, t) = \mathbf{\Lambda}(\mathbf{r}) \cdot \mathbf{d}(t)$, where

$$\mathbf{\Lambda}(\mathbf{r}) = k^3 \left[\frac{1}{(kr)^3}(3\hat{\mathbf{r}}\hat{\mathbf{r}} - 1) - \frac{i}{(kr)^2}(3\hat{\mathbf{r}}\hat{\mathbf{r}} - 1) - \frac{1}{kr}(\hat{\mathbf{r}}\hat{\mathbf{r}} - 1) \right] e^{ikr}. \tag{2.58}$$

While prior expressions were derived using the fact that the dipole feels only the external field $\mathbf{E}_{\text{ext}}$, in reality the dipole is subjected to the *total* field $\mathbf{E}_{\text{tot}} = \mathbf{E}_{\text{ext}} + \mathbf{E}_{\text{dip}}$, including both external contributions and the self-field of the dipole, evaluated at the origin where the dipole is located. At first glance, this suggests trouble – in the limit where $r \to 0$, $\mathbf{\Lambda}(\mathbf{r})$ (and by extension $\mathbf{E}_{\text{dip}}$) diverges. This may be remedied by breaking the force $\mathbf{F}_{\text{rad}} = e\mathbf{E}_{\text{dip}}$ into two phase-orthogonal contributions,

$$\mathbf{F}_{\text{rad}} = e^2 \text{Re}\{\mathbf{\Lambda}(\mathbf{r})\} \cdot \mathbf{x} + e^2 \text{Im}\{\mathbf{\Lambda}(\mathbf{r})\} \cdot \mathbf{x}, \tag{2.59}$$

where we have used the fact that $\mathbf{d} = e\mathbf{x}$. At steady-state, $\mathbf{x}(t)$ and $\dot{\mathbf{x}}(t)$ are $\pi/2$ out-of-phase. The divergent contribution to $\mathbf{F}_{\text{rad}}$ proportional to $\text{Re}\{\mathbf{\Lambda}(\mathbf{r})\}$ is therefore also $\pi/2$ out-of-phase with $\dot{\mathbf{x}}$ and thus does zero net work on the dipole over the course of a complete cycle. In contrast, the second term proportional to $\text{Im}\{\mathbf{\Lambda}(\mathbf{r})\}$ does do work on the dipole

and therefore must be included in the equation of motion. Computing the appropriate limit, we find

$$\mathbf{F}_{\text{rad}} = \lim_{\mathbf{r}\to\mathbf{0}} e^2 \text{Im}\{\mathbf{\Lambda}(\mathbf{r})\} \cdot \mathbf{x} = \frac{2e^2}{3c^3}\omega^3 \mathbf{x}, \tag{2.60}$$

agreeing exactly with Eq. (2.53) upon application of the steady-state limit and use of the identity $k = \omega/c$. Thus we see that the radiation reaction force may be interpreted as the work done on the dipole by its own self-field.

Finally, we note that revisiting the radiation reaction force through this lens facilitates a valuable gain in intuition regarding the oscillator polarizability. At first glance, it appears that the Clausius-Mossotti relation used at the outset of the section was unable to capture the alteration of the dynamics due to the radiation reaction force. However, this is not the case – instead, it is clear that a distinction must be made between the bare polarizability and the radiation dressed polarizability, the former relating to the total field and the latter to the external field alone. In other words, we can write

$$\mathbf{d} = \alpha_0 \mathbf{E}_{\text{tot}} \tag{2.61}$$

and, separately,

$$\mathbf{d} = \alpha \mathbf{E}_{\text{ext}}, \tag{2.62}$$

where α_0 is the Claussius-Mossotti polarizability, and α is the radiation dressed polarizability. Using the previously derived relations, one can show that the dressed polarizability is related to the bare form by

$$\alpha = \frac{\alpha_0}{1 - i\frac{2}{3}k^3\alpha_0}, \tag{2.63}$$

effectively allowing us to renormalize the dipole response to take into account interactions with the free radiation field. This idea of a dressed polarizability is incredibly powerful, and will be further utilized in Section 4.2 to gain an understanding of Fano resonances in coupled oscillator systems.

2.3 Quantized light-matter interactions

In Chapter 1, we showed that the Lagrangian of a hybrid light-matter system consisting of a set of charges coupled a photonic cavity (in the long-wavelength approximation) is given

by

$$L = L_{\text{matter}} + L_{\text{cav}} + L_{\text{int}} \tag{2.64}$$

where

$$\begin{aligned} L_{\text{matter}} &= \sum_i \frac{1}{2} m_i \dot{\mathbf{r}}_i^2 - V_{\text{coul}} \\ L_{\text{cav}} &= \int \frac{d^3 r}{8\pi} \left[\varepsilon(\mathbf{r}) \frac{\dot{\mathbf{A}}^2}{c^2} - (\nabla \times \mathbf{A}) \right] \\ L_{\text{int}} &= -\mathbf{d} \cdot \frac{\dot{\mathbf{A}}(\mathbf{r}_0)}{c}. \end{aligned} \tag{2.65}$$

While, at its most general, L_{matter} describes an arbitrary set of charges confined to a spatial region much smaller than a wavelength, for most problems of interest these individual charges support a particular resonance of interest. It is often advantageous to "zoom out" and replace the microscopic degrees of freedom of L_{matter} by a description at the level of the *collective* degrees of freedom which play a role in the particular problem of interest. One example of this is the localized surface plasmon of Section 2.2 – if we wished to model an LSP mode interacting with the photonic modes of a resonant cavity, this would amount to making the replacement $L_{\text{matter}} \to L_{\text{LSP}}$ where L_{LSP} is just that of a harmonic oscillator, describing the collective oscillation of the conduction band electrons.

Through similar arguments, modeling light-matter interactions in quantum optical and cavity QED systems often involves reducing the material degrees of freedom to one of two idealized descriptions: the harmonic oscillator and the two-level system. The former approach is most often taken to describe behavior which involves resonant, near-equilibrium phenomena involving acceptance of multiple quanta of energy – e.g., vibrational modes of a molecule or the phononic modes of a crytalline solid. In the Thomson-Lorentz approximation, atoms themselves are modeled as harmonic oscillators, successfully explaining phenomena such as the scattering of light [14]. In the theory of superradiance, a large number of identical two-level atoms interacting with a single cavity mode are modeled as a "super oscillator" describing the collective in-phase behavior of the constituent atoms [62]. For many of these cases, however, faithful agreement with harmonic oscillator behavior begins to break down when the system is subjected to a strong driving field. In this case, the atom must be imbued

with some nonlinearity, often achieved (to good approximation [14]) by modeling the atomic resonance of interest as a two-level system.

In this section, we will demonstrate how the Lagrangian in Eq. (2.65) may be used to arrive at a general system Hamiltonian capable of describing quantized light-matter interactions with the matter degrees of freedom mapped onto either a harmonic oscillator or a two-level system. For simplicity, we will take $\varepsilon(\mathbf{r}) \to 1$ so that the results of Section 2.1 can be directly applied. Extension to the case of an inhomogeneous dielectric function is straightforward using the generalized mode expansion presented in Chapter 8. In addition, let us imagine that the system consists of a just a single mode. Following the setup of Section 2.2, the vector potential may therefore be written as

$$\mathbf{A}(\mathbf{r}, t) = \frac{c\sqrt{4\pi}}{V} q(t)\mathbf{f}(\mathbf{r}) \tag{2.66}$$

Turning now to the matter, let us assume that the Coulomb potential in Eq. (2.65) is well-approximated by the harmonic potential

$$V_{\text{coul}} = \frac{1}{2}\omega_a^2 x^2 \tag{2.67}$$

where $\mathbf{d} = e\mathbf{x}$ is the dipole moment defined in Eq. (1.32), $\mathbf{x}$ a generalized coordinate, and ω_a the transition frequency. Furthermore, let us replace the kinetic energy term by

$$\sum_i \frac{1}{2} m_i \dot{\mathbf{r}}_i^2 \to \frac{1}{2} m \dot{x}^2 \tag{2.68}$$

where m is some effective mass characterizing the oscillator strength of the transition.

Combining these approximations and carrying out the Legendre transform, the resulting Hamiltonian may be written as

$$H = \frac{p^2}{2m} + \frac{1}{2} m\omega_a^2 x^2 + \frac{V_c}{2} p_c^2 + \frac{1}{2V_c}\omega_c^2 q_c^2 + \sqrt{mV_c}\lambda x p_c, \tag{2.69}$$

where all cavity parameters include a subscript c and the constant λ is defined as

$$\lambda = e\sqrt{\frac{4\pi}{mV_c}}\mathbf{f}(\mathbf{r}_0) \cdot \hat{\mathbf{x}}, \tag{2.70}$$

not to be confused with the wavelength of the cavity mode. In arriving at Eq. (2.69), we have made the assumption that $\lambda \ll \{\omega_0, \omega_a\}$, neglecting an additional perturbative term

proportional to $\lambda^2 x^2$ which shifts the resonance frequency of the atom. Neglect of this term is analogous to the usual procedure of discarding the diamagnetic $\mathbf{A}^2$ term in the minimal coupling framework [14].

Next, we promote the generalized coordinates and corresponding momenta to canonically conjugate pairs obeying the commutation relations

$$\begin{aligned} [q_c, p_c] &= i\hbar \\ [x, p] &= i\hbar \end{aligned} \tag{2.71}$$

and reexpress in terms of creation and annihilation operators as

$$\begin{aligned} q_c &= \sqrt{\frac{\hbar V_c}{2\omega_c}} \left[c^\dagger e^{i\phi} + c e^{-i\phi} \right] \\ p_c &= i\sqrt{\frac{\hbar \omega_m}{2V_c}} \left[c^\dagger e^{i\phi} - c e^{-i\phi} \right] \\ x &= \sqrt{\frac{\hbar}{2m\omega_a}} \left[a^\dagger + a \right] \\ p &= i\sqrt{\frac{\hbar m \omega_a}{2}} \left[a^\dagger - a \right], \end{aligned} \tag{2.72}$$

where, as discussed in the text surrounding Eq. (2.34), we have left the phase ϕ arbitrary for the cavity modes and have adopted the usual definitons for the dipole oscillator – the reason for the generality of ϕ will be made clear shortly. Substituting these expressions into the Hamiltonian, we find

$$H = \hbar\omega_a a^\dagger a + \hbar\omega_c c^\dagger c + i\hbar\sqrt{\omega_c/\omega_a}(c^\dagger e^{i\phi} - c e^{-i\phi})(a^\dagger + a) \tag{2.73}$$

The two counter-rotating terms proportional to $c^\dagger a^\dagger$ and ca oscillate at a frequency $\omega_c + \omega_a$ much faster than the time-scale of light-matter interactions, and thus contribute negligibly and may be discarded via the so-called "rotating wave approximation" [39] as long as $\lambda \ll \omega_a, \omega_b$ is satisfied. Then the Hamiltonian becomes

$$H = \hbar\omega_a a^\dagger a + \hbar\omega_c c^\dagger c + (g c^\dagger a + g^* c a^\dagger) \tag{2.74}$$

where the light-matter interaction strength g is given by

$$g = i e^{-i\phi} \hbar \sqrt{\frac{\pi e^2 \omega_c}{m\omega_a V_c}} \mathbf{f}(\mathbf{r}_0) \cdot \hat{\mathbf{x}}. \tag{2.75}$$

We can now see that it is advantageous to choose a phase other than zero. In particular, the choice $\phi = \pi/2$ ensures that the coupling strength is real, simplifying calculations and allowing us to express the Hamiltonian in the simplified form

$$H = \hbar\omega_a a^\dagger a + \hbar\omega_c c^\dagger c + g(c^\dagger a + c a^\dagger) \tag{2.76}$$

where

$$g = \hbar\sqrt{\frac{\pi e^2 \omega_c}{m\omega_a V_c}}\mathbf{f}(\mathbf{r}_0)\cdot\hat{\mathbf{x}}. \tag{2.77}$$

While the above analysis specialized to consideration of the matter as a quantum harmonic oscillator, the two-level approximation follows the same exact strategy, albeit with the modification

$$\begin{aligned} x &= \sqrt{\frac{\hbar}{2m\omega_a}}\,[\sigma_+ + \sigma_-] \\ p &= i\sqrt{\frac{\hbar m\omega_a}{2}}\,[\sigma_+ - \sigma_-] \end{aligned} \tag{2.78}$$

in place of the expressions in Eq. (2.72), where

$$\begin{aligned} \sigma_+ &= \sigma_x + i\sigma_y \\ \sigma_- &= \sigma_x - i\sigma_y \end{aligned} \tag{2.79}$$

are two-level analogues of raising and lowering operators constructed from Pauli matrices. With this modification, the system Hamiltonian becomes

$$H = \hbar\omega_c c^\dagger c + \frac{1}{2}\hbar\omega_a\sigma_z + \hbar g(c^\dagger\sigma_- + c\sigma_+) \tag{2.80}$$

Thus we have arrived at the Jaynes-Cummings Hamiltonian, one of the most important models in all of quantum optics and cavity QED. We will return to a detailed analysis of this Hamiltonian and its utility for analog quantum simulation of many-body phenomena in Chapter 10.

Chapter 3

LINKING THEORY WITH EXPERIMENT: USING OSCILLATOR MODELS TO COMPUTE OBSERVABLES

In the previous chapter, we illustrated how one can reduce complicated equations describing photonic cavities and plasmonic nanoresonators to those of simple harmonic oscillators. The advantages of such a procedure are numerous. For one, harmonic oscillator equations are often simpler to analyze and manipulate compared to Maxwell's equations. This is especially true for coupled systems – it is fairly straightforward to decouple coupled oscillator equations of motion, whereas coupled partial differential equations are comparatively more complex to interpret. Second, reduction of dynamical systems to harmonic oscillator equations facilitates a clear pathway to canonical quantization and analysis of quantum phenomena. The importance of quantum harmonic oscillators permeates many subdisciplines of physics and, as a result, a rich and varied toolbox (e.g. creation and annihilation operators, coherent states, quasiprobability distributions, etc.) can be leveraged to study cavity QED and quantum nanophotonic platforms through this lens. Lastly, oscillator models provide an intuitive, reduced physical picture which can be used to understand core behavior underlying experimental measurements. Most often, quantitative exactness is less desirable than a qualitative, physical understanding. Oscillator models are especially impactful at offering the latter, allowing for interpretation of complicated physical systems through analogy to simple mechanical models. For all of these reasons, oscillator models have become a popular and versatile tool to understand complex phenomena in nanophotonic [63, 64, 65], cavity QED [66, 67, 68], and optomechanical systems [69, 70, 71, 72].

In this Chapter, we will develop simple methods for relating oscillator models to various observables. As will become clear, inextricably linked to these observables is dissipation, as detection of a photon, for example, requires energy to leave the system in question via coupling to the environment.

Section 3.1 introduces a basic and intuitive method for computing common optical observables (absorption, scattering and extinction) for a single oscillating dipole. In large part, the resulting expressions are well-known, but here presented in a unique, simple, and unified manner. We then extend these calculations in Section 3.2 to a coupled system comprising two coupled dipoles interacting through the electromagnetic field. We emphasize, however, that the presented methods are fairly general, and can be adapted to describe any system well-modeled as coupled oscillators such as those appearing in cavity QED, optomechanics, etc. For one example, see Chapter 6 where these methods are applied toward analysis of a hybrid plasmonic-photonic resonator. In Section 3.3 we introduce input-output theory, used to compute transmission through systems involving photonic cavities. As this framework commonly leverages a quantum mechanical description, we will also make some brief remarks on different approaches to modeling open quantum systems.

3.1 Optical observables for a single dipole oscillator

We start with the equation of motion for a single dipole $\mathbf{d} = ex\hat{\mathbf{z}}$ with natural frequency ω_0, effective mass m, and nonradiative damping γ_{nr}, driven by the external field $E_{\mathrm{ext}} = E_0 e^{-i\omega t}\hat{\mathbf{z}}$,

$$m\ddot{x} = -m\omega_0^2 x - m\gamma_{\mathrm{nr}}\dot{x} + \frac{2}{3}\frac{e^2}{c^3}\dddot{x} + eE_0 e^{-i\omega t}. \tag{3.1}$$

As before, let us specialize to a steady-state scenario where $x(t) = x(\omega)e^{-i\omega t}$. In total, the oscillating dipole experiences four unique forces: the restoring force $F_{\mathrm{res}} = -m\omega_0^2 x$, the nonradiative damping force $F_{\mathrm{nr}} = -m\gamma_{\mathrm{nr}}\dot{x}$, the radiation reaction force $F_{\mathrm{rad}} = -m\gamma_{\mathrm{rad}}\dot{x}$, and the external, optical driving force $F_{\mathrm{ext}} = eE_0 e^{-i\omega t}$.

At steady-state, the average power contributed to the system by each of these forces over the course of a single period τ is given by

$$\langle P_i \rangle = \frac{1}{\tau}\int_{-\tau/2}^{\tau/2} \mathbf{F}_i \cdot \dot{\mathbf{x}}\, dt. \tag{3.2}$$

Imagine we now wish to experimentally probe the dynamics of the system. One strategy for achieving this involves detection and spectral analysis of the energy which is dissipated into the environment. For the toy system modeled by Eq. (3.1), two dissipative pathways exist: nonradiative absorption and radiation, as illustrated in Fig. 3.1. Each of these pathways is

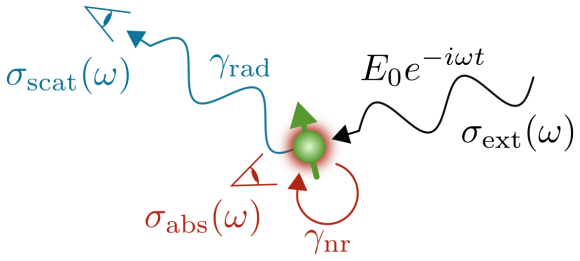

Figure 3.1: The flow of energy at steady-state for an oscillating dipole. Power input by the harmonic driving field $E_0 e^{-i\omega t}$ is equally matched by the total radiative and nonradiative outflow of energy, each characterized by the rates γ_{rad} and γ_{nr}. Measurement of the scattering and absorption cross-sections requires direct or indirect detection of energy decayed through radiative and nonradiative channels, respectively. Conservation of energy dictates that the sum of σ_{abs} and σ_{scat}, i.e., the extinction cross-section σ_{ext}, corresponds to both the total extinguished power and the (normalized) rate at which work is done on the dipole by the external driving field. All three cross-sections depend upon the polarizability and are therefore useful experimental tools for probing spectrally-dependent system dynamics.

associated with a particular observable – detection of radiation probes the scattered power, while nonradiative decay corresponds to loss of energy which is ultimately dissipated as heat via absorption of the composing matter (via plasmon-phonon coupling, for example).

Eq. (3.2) provides a means for computing the impact of each of these pathways, with the ultimate goal of relating the dipole dynamics back to measurable quantities. As an example, we explicitly compute the average absorbed power (i.e., the power dissipated via nonradiative decay) by substituting $\mathbf{F}_{\mathrm{nr}}$ into Eq. (3.2). As the integrand contains a product of complex time dependent variables, care must be taken in first taking the real part of both

$\mathbf{F}_{\rm nr}$ and $\dot{\mathbf{x}}$, yielding

$$\begin{aligned}
\langle P_{\rm abs}\rangle &= \frac{1}{\tau}\int_{-\tau/2}^{\tau/2} \mathrm{Re}\{\mathbf{F}_{\rm nr}\}\cdot\mathrm{Re}\{\dot{\mathbf{x}}\}\,dt \\
&= -\frac{1}{\tau}\int_{-\tau/2}^{\tau/2} m\gamma_{\rm nr}\mathrm{Re}\{-i\omega x(\omega)e^{-i\omega t}\}^2\,dt \\
&= -\frac{1}{\tau}\int_{-\tau/2}^{\tau/2} m\omega^2\gamma_{\rm nr}\left[\mathrm{Im}\{x(\omega)\}\cos(\omega t) - \mathrm{Re}\{x(\omega)\}\sin(\omega t)\right]^2\,dt \\
&= -\frac{1}{\tau}\int_{-\tau/2}^{\tau/2} m\omega^2\gamma_{\rm nr}\left[\mathrm{Im}\{x(\omega)\}^2\cos^2(\omega t) + \mathrm{Re}\{x(\omega)\}^2\sin^2(\omega t)\right]\,dt \\
&= -\frac{1}{2}m\omega^2\gamma_{\rm nr}(E_0/e)^2|\alpha(\omega)|^2,
\end{aligned} \tag{3.3}$$

where we have cast the final form in terms of the oscillator polarizability

$$\alpha(\omega) = \frac{e^2/m}{-\omega^2+\omega_0^2 - i\omega\gamma_{\rm tot}} \tag{3.4}$$

with the total damping rate defined as $\gamma_{\rm tot} = \gamma_{\rm nr} + \gamma_{\rm rad}$. Somewhat inconvenient (but unsurprising) is the fact that $\langle P_{\rm abs}\rangle$ depends upon the intensity of the incident field. To remedy this, we define the absorption cross-section, computed by normalizing $\langle P_{\rm abs}\rangle$ to the incoming energy flux defined by the time-averaged Poynting vector $\langle S\rangle = cE_0^2/8\pi$. Intuitively, the absorption cross-section characterizes the fraction of the total incoming power absorbed and dissipated into heat, reported as an area which may be much larger (or smaller) than the physical dimensions of the dipole. Computing this, we find

$$\sigma_{\rm abs}(\omega) = \frac{\langle P_{\rm abs}\rangle}{\langle S\rangle} = \frac{4\pi\omega^2}{c}(m/e^2)\gamma_{\rm nr}|\alpha(\omega)|^2. \tag{3.5}$$

Following a similar calculation (with the substitution $\mathbf{F}_{\rm nr}\rightarrow\mathbf{F}_{\rm rad}$), it may be shown that the scattering cross-section is given by

$$\sigma_{\rm scat}(\omega) = \frac{4\pi\omega^2}{c}(m/e^2)\gamma_{\rm rad}|\alpha(\omega)|^2. \tag{3.6}$$

Finally, we turn to the extinction cross-section, characterizing the total power extinguished by the dipole. Because the total energy is conserved at steady-state, the rate of work done on the dipole by the external driving field must be equal to the rate at which energy is dissipated. This is most easily seen by substituting Eq. (3.1) for $\mathbf{F}_i$ in full into Eq. (3.2).

As both the net force F_{net} and the restoring force F_{res} are $\pi/2$ out-of-phase with the velocity $\dot{x}$, the integrals associated with each of these terms vanishes. Remaining is the equality

$$\langle P_{\text{ext}} \rangle = \langle P_{\text{abs}} \rangle + \langle P_{\text{scat}} \rangle \tag{3.7}$$

which is simply a statement of conservation of energy. Normalizing to the incident flux leads to the corresponding relation in terms of cross-sections,

$$\sigma_{\text{ext}} = \sigma_{\text{abs}} + \sigma_{\text{scat}}, \tag{3.8}$$

which, combining Eqs. (3.5) and (3.6), provides the analytic form for the extinction cross-section

$$\sigma_{\text{ext}}(\omega) = \frac{4\pi\omega^2}{c}(m/e^2)\gamma_{\text{tot}}|\alpha(\omega)|^2. \tag{3.9}$$

Separately, we could have computed σ_{ext} directly from Eq. (3.2) with the substitution $\mathbf{F}_i \to \mathbf{F}_{\text{ext}}$. This leads to the more familiar form for the extinction cross-section [54]

$$\sigma_{\text{ext}}(\omega) = \frac{4\pi\omega}{c}\text{Im}\{\alpha(\omega)\} \tag{3.10}$$

which, using the fact that $|\alpha(\omega)|^2 = (e^2/m\omega\gamma_{\text{tot}})\text{Im}\{\alpha(\omega)\}$ for the polarizability defined in Eq. (3.4), suggests the alternate forms for the absorption and scattering cross-sections,

$$\begin{aligned} \sigma_{\text{abs}} &= \frac{4\pi\omega}{c}\left(\frac{\gamma_{\text{nr}}}{\gamma_{\text{tot}}}\right)\text{Im}\{\alpha(\omega)\} \\ \sigma_{\text{scat}} &= \frac{4\pi\omega}{c}\left(\frac{\gamma_{\text{rad}}}{\gamma_{\text{tot}}}\right)\text{Im}\{\alpha(\omega)\}. \end{aligned} \tag{3.11}$$

We note that caution must be exercised in applying Eq. (3.11) to systems with a polarizability more complicated than that of a simple oscillator – one such example being the sphere polarizability Eq. (2.40) in the limit where the static term is non-negligible and ultimately contributes to the scattered fields. Still, for the simple oscillating dipole considered at present, these alternate definitions provide an additional degree of physical intuition and clarity not afforded by the forms derived prior: the imaginary part of $\alpha(\omega)$ encodes the component of the oscillator that is $\pi/2$ out-of-phase with the driving force, and the rate at which work is done by the driving field therefore scales with $\text{Im}\{\alpha(\omega)\}$. Combining this with

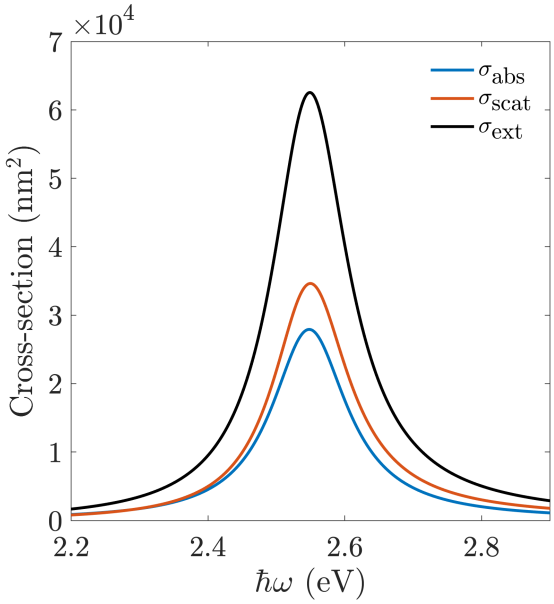

Figure 3.2: Absorption (blue), scattering (red), and extinction cross-sections of an oscillating dipole. All parameters are consistent with the dipole plasmon mode of a 40 nm gold sphere [73]. Parameters: $\hbar\omega_0 = 2.55$ eV, $\hbar\gamma_{\mathrm{nr}} = 60$ meV, $m = 8.31 \times 10^{-7}\ m_e$ where m_e is the mass of the electron.

the prefactor ω and assuming that the oscillator is driven close enough to resonance such that $\omega + \omega_0 \approx 2\omega$, we see that each cross section is proportional to

$$\begin{aligned} \omega \mathrm{Im}\{\alpha(\omega)\} &= (e^2/m)\frac{\omega^2\gamma_{\mathrm{tot}}}{(\omega^2-\omega_0^2)^2+\omega^2\gamma_{\mathrm{tot}}^2} \\ &\approx (e^2/2m)\frac{\gamma_{\mathrm{tot}}/2}{(\omega-\omega_0)^2+(\gamma_{\mathrm{tot}}/2)^2}, \end{aligned} \tag{3.12}$$

characterizing a Lorentzian centered at ω_0 with a linewidth (i.e., full width at half maximum) of γ_{tot} and overall amplitude inversely proportional to the effective mass m. Finally, σ_{abs} and σ_{scat} scale with the corresponding fractions $\gamma_{\mathrm{nr}}/\gamma_{\mathrm{tot}}$ and $\gamma_{\mathrm{rad}}/\gamma_{\mathrm{tot}}$, encoding the proportion of the total extinguished energy that is then ultimately absorbed and converted into heat vs. rerouted to the radiation field.

While the exhaustive treatment presented here is perhaps somewhat excessive for such a simple system, the physical insight gained and mathematical tricks employed lays the

groundwork for more complicated analyses of the more complex, hybrid photonic-plasmonic and all-plasmonic systems studied in Part II of this dissertation.

3.2 Optical observables for two electromagnetically coupled dipole oscillators

We now wish to extend the methods of the previous section to two electromagnetically coupled dipoles. To that end, we begin by writing the general equations of motion

$$\begin{aligned} m_1\ddot{\mathbf{x}}_1 + m_1\gamma_{1,\mathrm{nr}}\dot{\mathbf{x}}_1 + m_1\omega_1^2\mathbf{x}_1 &= e\mathbf{E}(\mathbf{r}_1,t) \\ m_2\ddot{\mathbf{x}}_2 + m_2\gamma_{2,\mathrm{nr}}\dot{\mathbf{x}}_2 + m_2\omega_2^2\mathbf{x}_2 &= e\mathbf{E}(\mathbf{r}_2,t) \end{aligned} \tag{3.13}$$

where each dipole is related to its corresponding generalized coordinate by $\mathbf{d}_i = e\mathbf{x}_i$ and $\mathbf{E}(\mathbf{r}_i,t)$ is the *total* field incident on the ith dipole located at $\mathbf{r}_i$. Summing all individual contributions, this total field may be written as

$$\mathbf{E}(\mathbf{r},t) = \mathbf{E}_{\mathrm{ext}}e^{-i\omega t} + \mathbf{E}_{1,\mathrm{dip}}(\mathbf{r},t) + \mathbf{E}_{2,\mathrm{dip}}(\mathbf{r},t) \tag{3.14}$$

where, as in Eq. (2.58), and $\mathbf{E}_{i,\mathrm{dip}}(\mathbf{r},t) = \boldsymbol{\Lambda}(\mathbf{r}-\mathbf{r}_i)\cdot\mathbf{d}_i(t)$ where

$$\boldsymbol{\Lambda}(\mathbf{r}) = k^3\left[\frac{1}{(kr)^3}(3\hat{\mathbf{r}}\hat{\mathbf{r}}-1) - \frac{i}{(kr)^2}(3\hat{\mathbf{r}}\hat{\mathbf{r}}-1) - \frac{1}{kr}(\hat{\mathbf{r}}\hat{\mathbf{r}}-1)\right]e^{ikr}. \tag{3.15}$$

For simplicity, let us define the dipole-dipole separation vector $\mathbf{R} = \mathbf{r}_2 - \mathbf{r}_1$. Following the discussion in Section 2.2.2, the real part of the self-field does zero work on the ith dipole and need not be included in the equation of motion. Given these considerations and noting that $\Lambda(\mathbf{R}) = \Lambda(-\mathbf{R})$, Eq. (3.13) can be rewritten as

$$\begin{aligned} m_1\ddot{\mathbf{x}}_1 + m_1\gamma_{1,\mathrm{nr}}\dot{\mathbf{x}}_1 + m_1\omega_1^2\mathbf{x}_1 &= e\mathbf{E}_{\mathrm{ext}}(\mathbf{r}_1,t) + \lim_{\mathbf{r}\to\mathbf{0}} e^2\mathrm{Im}\{\boldsymbol{\Lambda}(\mathbf{r},t)\}\cdot\mathbf{x}_1 + e^2\boldsymbol{\Lambda}(\mathbf{R},t)\cdot\mathbf{x}_2 \\ m_2\ddot{\mathbf{x}}_2 + m_2\gamma_{2,\mathrm{nr}}\dot{\mathbf{x}}_2 + m_2\omega_2^2\mathbf{x}_2 &= e\mathbf{E}_{\mathrm{ext}}(\mathbf{r}_2,t) + \lim_{\mathbf{r}\to\mathbf{0}} e^2\mathrm{Im}\{\boldsymbol{\Lambda}(\mathbf{r},t)\}\cdot\mathbf{x}_2 + e^2\boldsymbol{\Lambda}(\mathbf{R},t)\cdot\mathbf{x}_1. \end{aligned} \tag{3.16}$$

Let us now imagine that we drive the system with a plane wave polarized in the z-direction and that both dipoles are closely spaced enough such that they experience the same applied field $\mathbf{E}_{\mathrm{ext}}(\mathbf{r},t) = E_0e^{-i\omega t}\hat{\mathbf{e}}_z$. Projecting the ith equation onto the axis along the dipole orientation $\hat{\mathbf{x}}_i$ and assuming a steady-state scenario, we find

$$\begin{aligned} m_1\ddot{x}_1 + m_1\gamma_{1,\mathrm{tot}}\dot{x}_1 + m_1\omega_1^2x_1 - gx_2 &= eE_0\cos(\phi_1)e^{-i\omega t} \\ m_2\ddot{x}_1 + m_2\gamma_{2,\mathrm{tot}}\dot{x}_2 + m_2\omega_2^2x_2 - gx_1 &= eE_0\cos(\phi_2)e^{-i\omega t}, \end{aligned} \tag{3.17}$$

where $g = e^2(\hat{\mathbf{x}}_1 \cdot \mathbf{\Lambda}(\mathbf{R}, t) \cdot \hat{\mathbf{x}}_2)$ defines the coupling strength between the two oscillators, $\cos(\phi_i) = (\hat{\mathbf{x}}_i \cdot \hat{\mathbf{e}}_z)$ accounts for the relative angle between the polarized incident field and the dipole, and $\gamma_{i,\text{tot}} = \gamma_{i,\text{nr}} + \gamma_{i,\text{rad}}$ labels the total dissipation rate, combining contributions from the nonradiative and nonradiative rates $\gamma_{i,\text{nr}}$ and $\gamma_{i,\text{rad}} = \frac{2}{3}\frac{e^2\omega^2}{m_i c^3}$.

3.2.1 The dressed polarizability

In the case of a single oscillator, we found that the notion of a polarizability could be generalized to internally account for coupling to the radiation field. In effect, this allowed us to reexpress the relation

$$\mathbf{x} = \alpha_0(\omega)\mathbf{E}_{\text{tot}}, \tag{3.18}$$

as

$$\mathbf{x} = \alpha(\omega)\mathbf{E}_{\text{ext}}. \tag{3.19}$$

Here, the radiation-dressed polarizability $\alpha(\omega)$ differs from its bare counterpart $\alpha_0(\omega)$ in how each accounts for the self-field – the former via the radiation reaction force and the latter explicitly on the right-hand side as a contribution to $\mathbf{E}_{\text{tot}}$. The notion of a dressed polarizability thus allows us to, in a sense, describe the *renormalized* oscillator response where the effects of radiation are accounted for as an effective linewidth broadening.

It is useful to generalize this idea even further to multiple oscillators, particularly in the scenario where they are weakly coupled and only one oscillator is driven. As an illustrative example, we return to the scenario of two coupled oscillators and orient the dipoles as $\phi_1 = 0$ and $\phi_2 = \pi/2$ such that only the first dipole is driven. Assuming a steady state scenario where $x_1(t) = x_1(\omega)e^{-i\omega t}$ and $x_2(t) = x_2(\omega)e^{-i\omega t}$, Eq. (3.17) can be reexpressed as

$$\begin{aligned}(-\omega^2 + \omega_1^2 - i\omega\gamma_{1,\text{tot}})x_1 - (g/m_1)x_2 &= eE_0 \\ (-\omega^2 + \omega_2^2 - i\omega\gamma_{2,\text{tot}})x_2 - (g/m_2)x_1 &= 0.\end{aligned} \tag{3.20}$$

Solving for x_2 using the second equation and substituting into the first, we find

$$\left(-\omega^2 + \omega_1^2 - i\omega\gamma_{1,\text{tot}} - \frac{g^2/m_1 m_2}{-\omega^2 + \omega_2^2 - i\omega\gamma_{2,\text{tot}}}\right) x_1 = eE_0. \tag{3.21}$$

Partitioning the fraction proportional to g^2/m_1m_2 into real and imaginary parts, this may be further rewritten as

$$\left(-\omega^2 + \widetilde{\omega}_1^2 - i\omega\widetilde{\gamma}_{1,\mathrm{tot}}\right) x_1 = eE_0, \tag{3.22}$$

where $\widetilde{\omega}_1$ and $\widetilde{\gamma}_2$ are the dressed resonant frequency and linewidth defined by

$$\begin{aligned} \widetilde{\omega}_1^2 &= \omega_1^2 + \frac{g^2/m_1m_2}{(\omega^2-\omega_2^2)^2 + \omega^2\gamma_{2,\mathrm{tot}}^2}(\omega^2 - \omega_2^2) \\ \widetilde{\gamma}_{1,\mathrm{tot}} &= \gamma_{1,\mathrm{tot}} + \frac{g^2/m_1m_2}{(\omega^2-\omega_2^2)^2 + \omega^2\gamma_{2,\mathrm{tot}}^2}\gamma_{2,\mathrm{tot}}. \end{aligned} \tag{3.23}$$

At first glance, the response of the driven oscillator is identical in form to a single oscillator with resonant frequency $\widetilde{\omega}_1$ and total dissipation rate $\widetilde{\gamma}_{1,\mathrm{tot}}$. However, the dressed parameters are frequency dependent and thus in general can encode complex dynamics dissimilar to that of a simple damped harmonic oscillator. However, several limits exist in which they may be treated as approximately frequency-independent: e.g., when the driving frequency ω is far-detuned from the resonance of the second oscillator ω_2 relative to the coupling strength (i.e., $|\omega^2 - \omega_2^2| \gg g/m_1m_2$), or alternatively when the coupling strength is much smaller than the dissipation rate (i.e., $g^2/m_1m_2 \ll \gamma_{2,\mathrm{tot}}$). In either of these cases, $\widetilde{\omega}_1$ and $\widetilde{\gamma}_{1,\mathrm{tot}}$ differ from their bare counterparts by perturbative corrections due to outcoupling to the second oscillator. In other words, both of these parameter regimes limit the ability for coherent energy exchange between the two oscillators, in effect ensuring that any energy that is transferred to oscillator 2 from oscillator 1 is dissipated and oscillator 2 effectively acts as an additional pathway for dissipating energy.

Ultimately, this reframing of the physical system allows us to write the dressed polarizability as

$$\widetilde{\alpha}(\omega) = \frac{e^2/m_1}{-\omega^2 - \widetilde{\omega}_1^2 - i\omega\widetilde{\gamma}_{1,\mathrm{tot}}}, \tag{3.24}$$

repackaging the impact of the second oscillator on the response of the first through the effective oscillator parameters $\widetilde{\omega}_1$ and $\widetilde{\gamma}_{1,\mathrm{tot}}$. This strategy will prove especially useful in Chapter 4, where we present a derivation of the Fano lineshape using a coupled oscillator model, and Chapter 6, where a similar analysis is applied to a hybrid photonic-plasmonic resonator.

3.2.2 Correctly modeling interference

We now turn to the problem of computing optical observables for a coupled system. While our approach largely follows that previously applied to a single oscillator in Section 3.1, interesting questions arise for the case of multiple dipole oscillators. For one, how is interference handled by the radiation reaction force? Intuition tells us that for two in-phase dipoles nearly on top of one another, the scattered fields should constructively interfere, thus necessitating a larger radiation reaction force relative to the single oscillator case to maintain steady-state evolution. Oppositely, two dipoles perfectly out-of-phase will deconstructively interfere – in this case, intuition suggests that radiation reaction forces should vanish entirely.

It is clear that interference plays an important role in the dynamics of coupled dipole oscillators, but it is not at first glance obvious how such effects should be handled. Phenomenological models have previously been introduced to account for interference effects (for example, see Ref. [74]), but often at the expense of introducing additional terms without clearly motivating their physical basis. Here we will show that the dynamical equations in Eq. (3.17) can already account for such behavior without the need for additional terms.

Following the procedure carried out in Section 3.1, we first aim to use the equations of motion to gain insight into the energy "flow" in the system at steady-state. Integrating the ith equation of Eq. (3.17) against $\dot{\mathbf{x}}_i$ and discarding terms which do zero net work, we find

$$\begin{aligned} \langle P_{\text{abs}}^{(1)} \rangle + \langle P_{\text{rad}}^{(1)} \rangle + \langle P_{\text{coup}}^{(1)} \rangle &= \langle P_{\text{ext}}^{(1)} \rangle \\ \langle P_{\text{abs}}^{(2)} \rangle + \langle P_{\text{rad}}^{(2)} \rangle + \langle P_{\text{coup}}^{(2)} \rangle &= \langle P_{\text{ext}}^{(2)} \rangle, \end{aligned} \tag{3.25}$$

where $\langle P_{\text{abs}}^{(i)} \rangle$ and $\langle P_{\text{rad}}^{(i)} \rangle$ correspond to the rate at which the nonradiative and radiative dissipative force do work on oscillator i, respectively, and $\langle P_{\text{coup}}^{(i)} \rangle$ equals the rate at which work is done on the ith oscillator by the field of the opposite dipole. The total extinguished power is then calculated by summing both equations,

$$\langle P_{\text{ext}}^{\text{tot}} \rangle = \langle P_{\text{abs}}^{(1)} \rangle + \langle P_{\text{abs}}^{(2)} \rangle + \langle P_{\text{scat}}^{(1)} \rangle + \langle P_{\text{scat}}^{(2)} \rangle + \langle P_{\text{coup}}^{(1)} \rangle + \langle P_{\text{coup}}^{(2)} \rangle \tag{3.26}$$

At first glance, it is tempting to assume the equality $\langle P_{\text{coup}}^{(2)} \rangle = -\langle P_{\text{coup}}^{(1)} \rangle$ and cancel the final two terms via (a naive application of) Newton's third law. However, one must remember

that the coupling force is not directly applied by the dipoles, but is rather mediated by the electromagnetic field which itself can carry energy. We will now show that the applied coupling forces are *not* equal and opposite, particularly when the effective coupling strength contains an imaginary part. Computing $\langle P^{(1)}_{\text{coup}}\rangle$ explicitly via Eq. (3.2), we find

$$\begin{aligned}\langle P^{(1)}_{\text{coup}}\rangle &= \frac{1}{\tau}\int_{-\tau/2}^{\tau/2}\text{Re}\{gx_2e^{-i\omega t}\}\text{Re}\{\dot{x}_1\}\\ &= -\frac{\omega}{2}\left[\text{Re}(g)\text{Im}(x_1x_2^*)-\text{Im}(g)\text{Re}(x_1x_2^*)\right].\end{aligned} \tag{3.27}$$

Through an analogous calculation, it may be shown that

$$\langle P^{(2)}_{\text{coup}}\rangle = -\frac{\omega}{2}\left[\text{Re}(g)\text{Im}(x_1^*x_2)-\text{Im}(g)\text{Re}(x_1^*x_2)\right]. \tag{3.28}$$

Noting that $\text{Im}(x_1x_2^*) = -\text{Im}(x_1^*x_2)$, it is evident that this first term of $\langle P^{(1)}_{\text{coup}}\rangle$ and its counterpart in $\langle P^{(2)}_{\text{coup}}\rangle$ describe energy transfer between the two oscillators – any energy gained by oscillator one is reciprocated by energy loss in oscillator two. In contrast, the pair of terms proportional to $\text{Im}(g)$ are not equal and opposite as $\text{Re}(x_1x_2^*) = \text{Re}(x_1^*x_2)$. As a result, Eq. (3.26) can be rewritten as

$$\langle P^{\text{tot}}_{\text{ext}}\rangle = \langle P^{(1)}_{\text{abs}}\rangle + \langle P^{(2)}_{\text{abs}}\rangle + \langle P^{(1)}_{\text{scat}}\rangle + \langle P^{(2)}_{\text{scat}}\rangle + \omega\text{Im}(g)\text{Re}(x_1^*x_2). \tag{3.29}$$

As absorption and radiation provide the only two pathways for dissipation, this final term must contribute to the total scattered power. Evaluating the individual absorption and scattering contributions independently, we find that the total absorbed, scattered and extinguished power is given by

$$\begin{aligned}\langle P^{\text{tot}}_{\text{abs}}\rangle &= \frac{1}{2}m_1\omega^2\gamma_{1,\text{nr}}|x_1(\omega)|^2+\frac{1}{2}m_2\omega^2\gamma_{2,\text{nr}}|x_2(\omega)|^2\\ \langle P^{\text{tot}}_{\text{scat}}\rangle &= \frac{1}{2}m_1\omega^2\gamma_{1,\text{rad}}|x_1(\omega)|^2+\frac{1}{2}m_2\omega^2\gamma_{2,\text{rad}}|x_2(\omega)|^2+\omega\text{Im}(g)\text{Re}(x_1^*(\omega)x_2(\omega))\\ \langle P^{\text{tot}}_{\text{ext}}\rangle &= \frac{1}{2}\omega E_0\text{Im}(x_1(\omega)+x_2(\omega)),\end{aligned} \tag{3.30}$$

where the final term of $\langle P^{\text{tot}}_{\text{scat}}\rangle$ encodes interference effects. Notably, the proportionality to $\text{Im}(g)$ suggests that it is incorrect to discard intermediate and far-field terms via the approximation

$$g = e^2(\hat{\mathbf{x}}_1\cdot\mathbf{\Lambda}(\mathbf{R})\cdot\hat{\mathbf{x}}_2)\approx\frac{e^2}{R^3}\hat{\mathbf{x}}_1\cdot(3\hat{\mathbf{R}}\hat{\mathbf{R}}-1)\cdot\hat{\mathbf{x}}_2 \tag{3.31}$$

even in the limit where the two dipoles are very close together ($kR \ll 1$) as this would imply $\mathrm{Im}(g)$ vanishes for closely spaced dipoles. Instead, care must be taken in applying the previously computed limit

$$\lim_{\mathbf{r}\to\mathbf{0}} e^2 \mathrm{Im}\{\mathbf{\Lambda}(\mathbf{r})\} = \frac{2e^2}{3c^3}\omega^3 \tag{3.32}$$

such that interference effects are correctly modeled. Naturally, this limit agrees well with intuition – for two superimposed, identical dipoles oscillating perfectly in-phase, $x_1(\omega) = x_2(\omega)$ and

$$\omega \mathrm{Im}(g)\mathrm{Re}(x_1^*(\omega)x_2^*) = \frac{1}{2}m_1\omega^2\gamma_{1,\mathrm{tot}}|x_1(\omega)|^2 + \frac{1}{2}m_2\omega^2\gamma_{2,\mathrm{tot}}|x_2(\omega)|^2, \tag{3.33}$$

leading to a classical analogue of the superradiant effect [75, 76] via an effective doubling of the radiative loss rate,

$$\langle P_{\mathrm{scat}}^{\mathrm{tot}}\rangle = \frac{1}{2}m_1\omega^2(2\gamma_{1,\mathrm{rad}})|x_1(\omega)|^2 + \frac{1}{2}m_2\omega^2(2\gamma_{2,\mathrm{rad}})|x_2(\omega)|^2 \qquad \text{(Superradiant)} \tag{3.34}$$

In contrast, for two superimposed, identical dipoles oscillating perfectly out-of-phase we find $x_1(\omega) = -x_2(\omega)$ and

$$\omega \mathrm{Im}(g)\mathrm{Re}(x_1^*(\omega)x_2^*) = -\frac{1}{2}m_1\omega^2\gamma_{1,\mathrm{tot}}|x_1(\omega)|^2 - \frac{1}{2}m_2\omega^2\gamma_{2,\mathrm{tot}}|x_2(\omega)|^2. \tag{3.35}$$

Accordingly, the total scattered power vanishes due to destructive interference,

$$\langle P_{\mathrm{scat}}^{\mathrm{tot}}\rangle = 0 \qquad \text{(Subradiant)}, \tag{3.36}$$

classically analogous to the phenomena of subradiance.

Finally, we conclude this section by noting the form of each cross-section, computed by normalizing the expressions in Eq. (3.30) to the time-averaged incident flux $\langle S\rangle = cE_0^2/8\pi$

$$\begin{aligned}
\langle \sigma_{\mathrm{abs}}^{\mathrm{tot}}\rangle &= \frac{4\pi\omega^2}{c}(m_1/e^2)\gamma_{1,\mathrm{nr}}|\widetilde{\alpha}_1(\omega)|^2 + \frac{4\pi\omega^2}{2}(m_2/e^2)\gamma_{2,\mathrm{nr}}|\widetilde{\alpha}_2(\omega)|^2 \\
\langle \sigma_{\mathrm{scat}}^{\mathrm{tot}}\rangle &= \frac{4\pi\omega^2}{c}(m_1/e^2)\gamma_{1,\mathrm{rad}}|\widetilde{\alpha}_1(\omega)|^2 + \frac{4\pi\omega^2}{c}(m_2/e^2)\gamma_{2,\mathrm{rad}}|\widetilde{\alpha}_2(\omega)|^2 + \frac{8\pi\omega}{c}\mathrm{Im}(g)\mathrm{Re}(\widetilde{\alpha}_1^*(\omega)\widetilde{\alpha}_2(\omega)) \\
\langle \sigma_{\mathrm{ext}}^{\mathrm{tot}}\rangle &= \frac{4\pi\omega}{c}\mathrm{Im}(\widetilde{\alpha}_1(\omega) + \widetilde{\alpha}_2(\omega)),
\end{aligned} \tag{3.37}$$

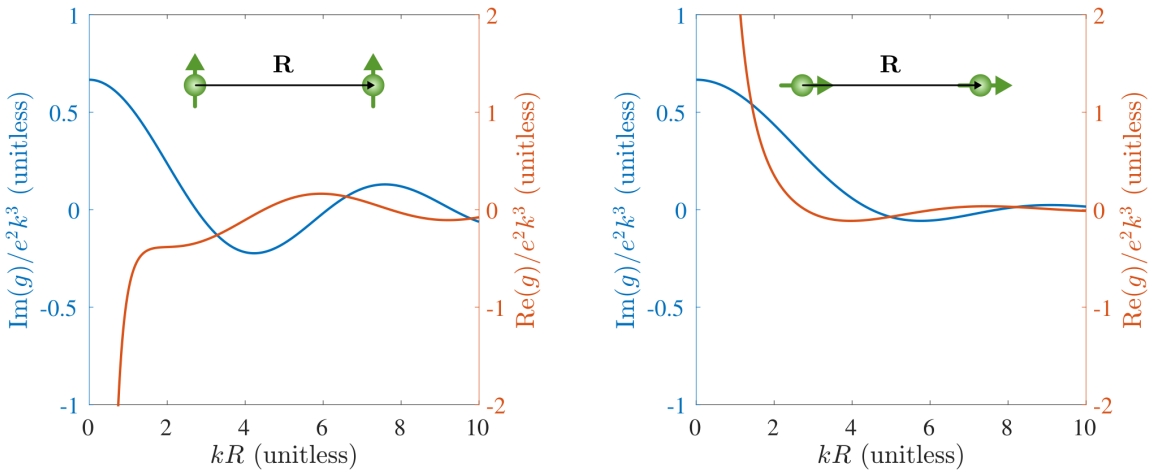

Figure 3.3: Real and imaginary parts of g as a function of dipole-dipole separation. The left panel corresponds to two coupled dipoles oriented perpendicular to the separation vector $\mathbf{R}$, while the right panel displays a colinear configuration. For $kR \ll 1$, the near field coupling dominates and the real part of g diverges, as expected. In contrast, the imaginary part asymptotes to a finite value, encoding the dynamical influence of interference in the radiated fields.

where the dressed polarizabilities are defined as

$$\begin{aligned}\widetilde{\alpha}_1 &= \frac{e^2/m_1}{-\omega^2+\widetilde{\omega}_1^2-i\omega\widetilde{\gamma}_{1,\mathrm{tot}}}\cdot\left(1+\frac{g/m_2}{-\omega^2+\omega_2^2-i\omega\gamma_{2,\mathrm{tot}}}\right)\\ \widetilde{\alpha}_2 &= \frac{e^2/m_1}{-\omega^2+\widetilde{\omega}_2^2-i\omega\widetilde{\gamma}_{2,\mathrm{tot}}}\cdot\left(1+\frac{g/m_1}{-\omega^2+\omega_1^2-i\omega\gamma_{1,\mathrm{tot}}}\right).\end{aligned} \tag{3.38}$$

Notably, these expressions differ in form from the dressed polarizability defined in Eq. (3.24) as, in the present scenario, both dipoles are driven. As a result, both $\widetilde{\alpha}_1(\omega)$ and $\widetilde{\alpha}_2(\omega)$ contain an additional multiplicative factor which accounts for an additional dressing by the external driving field acting on the opposite dipole. We can further repackage the above expressions by defining the effective, dressed masses

$$\begin{aligned}\widetilde{m}_1(\omega) &= m_1\left(1+\frac{g/m_2}{-\omega^2+\omega_2^2-i\omega\gamma_{2,\mathrm{tot}}}\right)^{-1}\\ \widetilde{m}_2(\omega) &= m_1\left(1+\frac{g/m_1}{-\omega^2+\omega_1^2-i\omega\gamma_{1,\mathrm{tot}}}\right)^{-1}\end{aligned} \tag{3.39}$$

such that the usual form of the oscillator polarizability is recovered, but care must be taken with this approach even in parameter regimes where $\widetilde{m}_1$ and $\widetilde{m}_2$ are well-approximated as constant due to the fact that the renormalizing factor is complex. Consequently, the dressed mass influences not only the amplitude of the response, but also the phase.

3.3 Input-output theory

In the previous two sections, we constructed a general framework for computing optical observables for systems composed of oscillating dipoles coupled through the electromagnetic field. As later chapters will focus on systems supporting photonic resonances, it will prove helpful (particularly for Chapters 6 and 9) to have a basic theoretical understanding of input-output theory, commonly used to model transmission through a resonant cavity. Here, we introduce the basic concepts with a simple illustrative example based upon the arguments of the classic work of Gardiner and Collett [77]. A comprehensive body of literature exists on the topic and we thus defer a more thorough treatment to Refs. [78] and [79].

Let us begin by imagining a system consisting of a photonic cavity supporting just a single mode, such that the system Hamiltonian is given by

$$H_{\mathrm{sys}} = \hbar\omega_0 a^\dagger a. \tag{3.40}$$

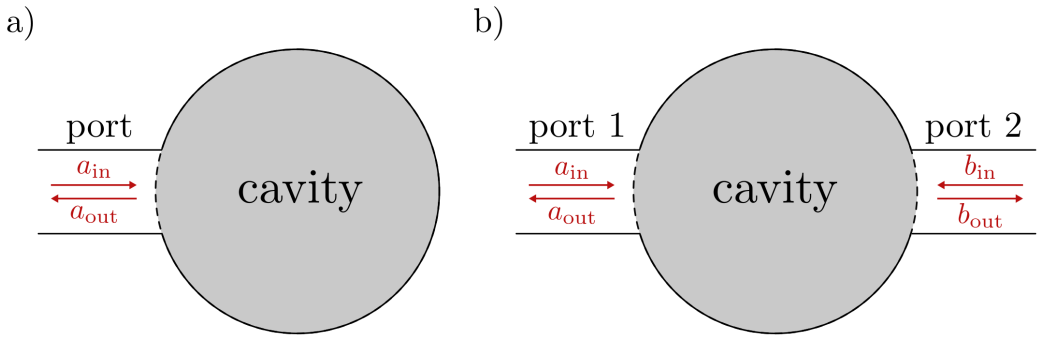

Figure 3.4: (a) A one-sided cavity, containing just a single port with incoming and outgoing fields characterized by the bosonic operators a_{in} and a_{out}. (b) A two-sided cavity, containing two ports both with incoming and outgoing fields.

Alone, this Hamiltonian describes perfectly unitary evolution in a closed system without any dissipation. We therefore must extend this description to include coupling to the environment. To that end, we assume the cavity mode interacts with the environment at a finite number of ports, facilitating both input and output of energy at each. Fig. 3.4 shows both one-sided and two-sided cavities, with the former containing just one port and the latter containing two. For simplicity, we will specialize to the one-sided case and conclude with some brief remarks on the two-sided geometry.

Open quantum systems are typically modeled using one of two strategies [80]. The first involves constructing a master equation at the level of the density operator, with the Lindblad super operator contributing both population decay and decoherence. The primary advantage of this approach is that the environmental degrees of freedom are entirely traced out, with all dissipative effects described in terms of system operators. The second is via application of Heisenberg-Langevin theory where the operator equations of motion are appended with both damping terms and noise operators, the latter introducing stochastic fluctuations. Notably, because this second approach does not rely on tracing out environmental degrees of freedom, it provides a route for computing the properties of the emitted light and is therefore well-suited for modeling experimental observations [77].

3.3.1 One-sided transmission

Using the Heisenberg-Langevin framework and assuming a single port, the equation of motion describing the dynamics of the cavity field may be extended to

$$\begin{aligned}\frac{\mathrm{d}a}{\mathrm{d}t} &= -\frac{i}{\hbar}[a, H_{\mathrm{sys}}] - \frac{\gamma}{2}a + \Gamma \\ &= -i\omega a - \frac{\gamma}{2}a + \Gamma,\end{aligned} \tag{3.41}$$

where γ is a constant describing the rate at which energy flows across the port (from cavity to environment and vice-versa), and Γ is the noise operator. Following Ref. [77], let us denote the incoming and outgoing parts of the bath field by the amplitudes a_{in} and a_{out} as shown in Fig. 3.4a. It is natural to then assume that the noise operator is proportional to the amplitude of the incoming field, i.e.,

$$\Gamma = \beta a_{\mathrm{in}}. \tag{3.42}$$

Furthermore, the field in the cavity must be proportional to the external field at steady-state with some fixed proportionality constant,

$$a = k(a_{\mathrm{in}} + a_{\mathrm{out}}). \tag{3.43}$$

We can separately consider the time-reversed situation where a_{out} represents some incoming field and the first term of Eq. (3.41) is complex-conjugated. Then, altogether we have

$$\begin{aligned}\frac{\mathrm{d}a}{\mathrm{d}t} &= -i\omega_0 a - \frac{\gamma}{2}a + \beta a_{\mathrm{in}} \\ \frac{\mathrm{d}a}{\mathrm{d}(-t)} &= i\omega_0 a - \frac{\gamma}{2}a + \beta a_{\mathrm{out}}\end{aligned} \tag{3.44}$$

along with the boundary condition in Eq. (3.43). Consistency requires that the first line is equal to the negative of the second. Enforcing this, we find

$$\gamma a = \beta(a_{\mathrm{in}} + a_{\mathrm{out}}), \tag{3.45}$$

and comparison with Eq. (3.43) then requires that $k = \beta/\gamma$. Substituting this solution back into the forward and time-reversed equations of motion, we find

$$\begin{aligned}\frac{\mathrm{d}a}{\mathrm{d}t} &= -i\omega_0 a - \frac{\gamma}{2}a + k\gamma a_{\mathrm{in}} \\ &= -i\omega_0 a + \frac{\gamma}{2}a + k\gamma a_{\mathrm{out}}.\end{aligned} \tag{3.46}$$

Just as in previous sections where we aimed to relate to dissipated power to the incident driving field, the present goal is now to relate a_{out} and a_{in} in terms of the known parameters ω_0 and γ. To do this, we must first solve for the proportionality constant k by enforcing the bosonic commutation relation $[a(t), a^\dagger(t)] = 1$.

While we cannot directly solve for $a(t)$ without specifying a_{in}, we can simplify our analysis by turning to the frequency domain. To that end, $a(t)$ is related to its Fourier transform $\widetilde{a}(\omega)$ by

$$a(t) = \int \frac{d\omega}{2\pi} e^{-i\omega t} \widetilde{a}(\omega). \tag{3.47}$$

Separately, Eq. (3.46) yields the frequency-domain solution

$$a(\omega) = \frac{-ik\gamma}{-\omega + \omega_0 - i\gamma/2} \widetilde{a}_{\text{in}(\omega)}. \tag{3.48}$$

Combining these allows us to rewrite the desired commutation relation as

$$\begin{aligned}
[a(t), a^\dagger(t')] &= \int \frac{d\omega d\omega'}{(2\pi)^2} e^{-i\omega t} e^{i\omega' t'} [\widetilde{a}(\omega), a^\dagger(\omega')] \\
&= \int \frac{d\omega d\omega'}{(2\pi)^2} e^{-i\omega t} e^{i\omega' t'} \frac{k^2\gamma^2}{[\omega - \omega_0 - i\gamma/2][\omega - \omega_0 + i\gamma/2]} [\widetilde{a}_{\text{in}}(\omega), \widetilde{a}^\dagger_{\text{in}}(\omega')] \\
&= \int \frac{d\omega}{2\pi} e^{-i\omega(t-t')} \frac{k^2\gamma^2}{[\omega - \omega_0 - i\gamma/2][\omega - \omega_0 + i\gamma/2]},
\end{aligned} \tag{3.49}$$

where we have used the input field bosonic commutation relation $[\widetilde{a}_{\text{in}}(\omega), \widetilde{a}^\dagger_{\text{in}}(\omega')] = 2\pi\delta(\omega - \omega')$ in arriving at the final line. The integrand of Eq. (3.49) contains two simple poles, easily accounted for through countour integration and application of the residue theorem. For $t > t'$ ($t < t'$) we integrate in the lower-half (upper-half) plane, enclosing one pole in each case. Ultimately, we find

$$\begin{aligned}
[a(t), a^\dagger(t')] &= k^2\gamma e^{-i\omega_0(t-t')} \left(e^{-\frac{\gamma}{2}(t-t')} \theta(t-t') + e^{-\frac{\gamma}{2}(t'-t)} \theta(t'-t) \right) \\
&= k^2\gamma e^{-\omega_0(t-t')} e^{-\frac{\gamma}{2}|t-t'|}.
\end{aligned} \tag{3.50}$$

Thus we see that enforcing $[a(t), a^\dagger(t)] = 1$ is equivalent to enforcing $k = 1/\sqrt{\gamma}$. Consequently, the noise operator may be rewritten as

$$\Gamma = \sqrt{\gamma} a_{\text{in}}, \tag{3.51}$$

and may be understood as an instance of the quantum fluctuation-dissipation theorem [78], relating the damping rate γ to the noise operator Γ. Finally, we can use this relation to

relate $\widetilde{a}_{\text{out}}(\omega)$ to the spectral content of $\widetilde{a}_{\text{in}}(\omega)$ through combination of Eqs. (3.48) and the boundary condition $a = (a_{\text{in}} + a_{\text{out}})/\sqrt{\gamma}$, yielding

$$\widetilde{a}_{\text{out}}(\omega) = -\frac{\omega - \omega_0 - i\gamma/2}{\omega - \omega_0 + i\gamma/2}\widetilde{a}_{\text{in}}(\omega). \tag{3.52}$$

We note that the ratio of outgoing to incoming energy is given by $\widetilde{a}^{\dagger}_{\text{out}}(\omega)\widetilde{a}_{\text{out}}(\omega)/\widetilde{a}^{\dagger}_{\text{in}}(\omega)\widetilde{a}_{\text{in}}(\omega) = 1$ and, accordingly, the rate at which energy enters the system is also the rate at which it exits, in accordance with steady state. Consequently, Eq. (3.52) merely describes a relative phase between the input and output field. This situation is made more interesting if we consider the cavity to have an additional intrinsic damping rate γ_{int}, which we model as a pure damping effect without consideration of quantum fluctuations. For clarity, we make the replacement $\gamma \to \gamma_{\text{out}}$ for the single port outcoupling. Carrying out the prior calculation with this additional effect leads to the one-sided transmission coefficient,

$$\begin{aligned}\mathcal{T}(\omega) &= \frac{\widetilde{a}^{\dagger}_{\text{out}}(\omega)\widetilde{a}_{\text{out}}(\omega)}{\widetilde{a}^{\dagger}_{\text{in}}(\omega)\widetilde{a}_{\text{in}}(\omega)} = \left|\frac{\omega - \omega_0 - i(\gamma_{\text{int}} - \gamma_{\text{out}})/2}{\omega - \omega_0 - i(\gamma_{\text{int}} + \gamma_{\text{out}})/2}\right|^2 \\ &= 1 - \frac{\gamma_{\text{int}}\gamma_{\text{out}}}{(\omega - \omega_0)^2 + (\gamma_{\text{tot}}/2)^2},\end{aligned} \tag{3.53}$$

describing the fraction of the input power which is output at that same port, where $\gamma_{\text{tot}} = \gamma_{\text{int}} + \gamma_{\text{out}}$ is the total cavity damping rate. We note that, depending upon the particular geometry of the port and cavity, $\mathcal{T}(\omega)$ may actually correspond more intuitively to a reflection coefficient – here, by "transmission", we simply mean that energy passes from the input to the output in an abstract, goemetry independent sense. As illustrated in Fig. (3.5)a, $\mathcal{T}(\omega)$ is simply an inverted Lorentzian with peak position ω_0, linewidth γ_{tot}, and amplitude proportional to the product $\gamma_{\text{int}}\gamma_{\text{out}}$. Interestingly, we see that on resonance (i.e., $\omega = \omega_0$), tuning $\gamma_{\text{int}} = \gamma_{\text{out}}$ ensures that $\mathcal{T}(\omega_0)$ vanishes. Physically, this corresponds to the situation of *critical coupling*, whereby the intrinsic dissipation of the cavity entirely extinguishes the incident field and all energy is "lost" within the cavity. Separately, one can have a system that is under- or over-coupled, corresponding to the situations $\gamma_{\text{out}} < \gamma_{\text{int}}$ and $\gamma_{\text{out}} > \gamma_{\text{int}}$, but it is experimentally advantageous to achieve critical coupling as this ensures the optimal signal-to-noise upon measurement of the transmitted field.

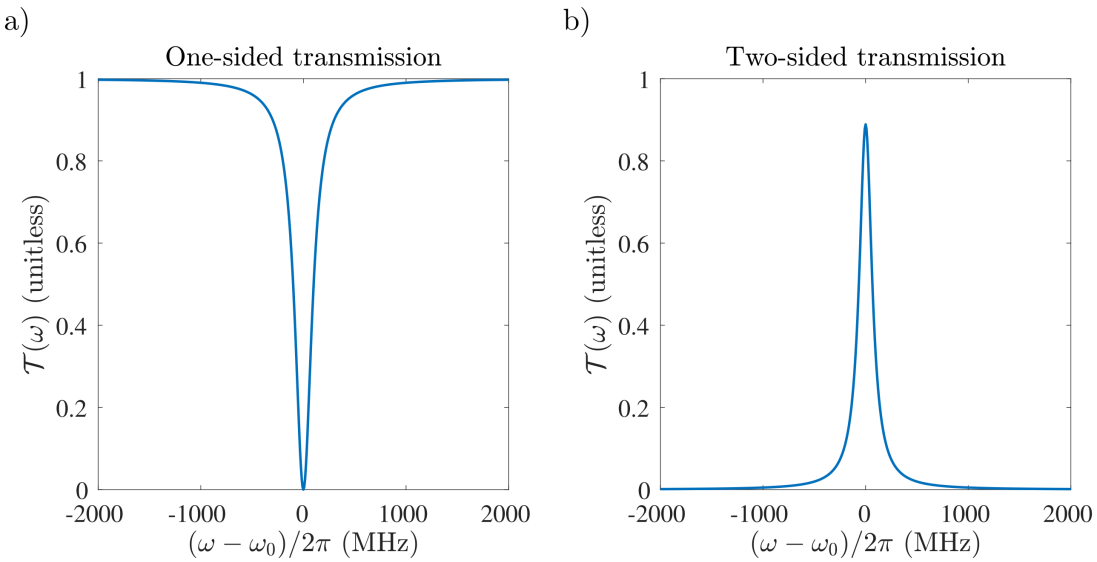

Figure 3.5: (a) One-sided transmission for a resonant cavity with intrinsic and outcoupling damping rates $\gamma_{\text{int}}/2\pi = \gamma_{\text{out}}/2\pi = 100$ MHz. Because the cavity is critically coupled to the environment, perfect transmission occurs at $\omega = \omega_0$. (b) Two-sided transmission for a resonant cavity with characteristic damping rates $\gamma_1/2\pi = 100$ MHz and $\gamma_2/2\pi = 50$ MHz. Because the two ports are asymmetric with $\gamma_1 \neq \gamma_2$, imperfect transmission occurs at $\omega = \omega_0$.

3.3.2 Two-sided transmission

We will now briefly turn to the problem of two-sided transmission, characterizing the response of a resonant cavity with two input-output ports, as shown in Fig. 3.4b. To handle this, we define a_{in} and b_{in} to be the incoming fields at the first and second port, and a_{out} and b_{out} to be the corresponding outgoing fields. Following the same strategy as in the one-sided case, we can write the Heisenberg-Langevin equation as

$$\frac{\mathrm{d}a}{\mathrm{d}t} = -i\omega_0 a - \frac{\gamma_1}{2}a - \frac{\gamma_2}{2}a + \sqrt{\gamma_1}a_{\text{in}} + \sqrt{\gamma_2}b_{\text{in}} \tag{3.54}$$

with the corresponding boundary conditions,

$$\begin{aligned} \widetilde{a}_{\text{out}}(\omega) &= \sqrt{\gamma}_1\widetilde{a}(\omega) - \widetilde{a}_{\text{in}}(\omega) \\ \widetilde{b}_{\text{out}}(\omega) &= \sqrt{\gamma}_1\widetilde{a}(\omega) - \widetilde{b}_{\text{in}}(\omega). \end{aligned} \tag{3.55}$$

Similar to before, these equations can be used together to compute, for example, two-sided transmission (e.g., conversion of input signal a_{in} to output signal b_{out}). To do this, we specify the incoming amplitude at the second port to be vanishing, i.e., $b_{\text{in}} = 0$. Using the boundary conditions together with the Eq. (3.54), this leads to

$$\mathcal{T}(\omega) = \frac{\widetilde{b}^{\dagger}_{\text{out}}(\omega)\widetilde{b}_{\text{out}}(\omega)}{\widetilde{a}^{\dagger}_{\text{in}}(\omega)\widetilde{a}_{\text{in}}(\omega)} = \frac{\gamma_1\gamma_2}{(\omega-\omega_0)^2 + (\gamma_1+\gamma_2)^2/4}, \tag{3.56}$$

yielding an upright Lorentzian spectrally centered at ω_0 with lindewidth $\gamma_1 + \gamma_2$. Intuitively, the amplitude scales with the product $\gamma_1\gamma_2$, and therefore sending either outcoupling to zero will cause the transmitted power to vanish.

Chapter 4

FROM WEAK-TO-STRONG COUPLING: PURCELL ENHANCEMENT, FANO PHYSICS, HYBRIDIZATION, AND MORE

In the half century following Purcell's discovery that the radiative properties of a spin could be altered through interaction with a resonant circuit [15], progress in cavity QED has become synonymous with the experimental realization of ever increasing light-matter coupling strengths. Early single-emitter experiments of the 1980s were confined to the *weak coupling regime*, where the light-matter coupling strength g is less than the maximum of the cavity and emitter linewidth ($g < \max\{\gamma_{\rm cav}, \gamma_{\rm em}\}$) [14, 81, 82]. In the weak coupling regime, the cavity and emitter influence one another only perturbatively, unable to coherently exchange energy prior to decay. Depending on the overlap between the cavity density of states and the frequencies at which it radiates, the emitter can experience either an enhancement or suppression of its lifetime [83].

In the *strong coupling regime*, the rate at which energy is exchanged between the cavity and emitter exceeds the maximal rate of dissipation ($g > \max\{\gamma_{\rm cav}, \gamma_{\rm em}\}$). Consequently, coherent exchange of energy occurs and the fundamental excitations of the system become polaritonic, mixing together light and matter degrees of freedom and blurring the distinction between cavity photon and emitter. Experimentally, this regime is challenging to realize – it wasn't until the invention of very high quality factor Q superconducting cavities and high Q, small V microresonators that this limit became achievable for single emitters in the microwave [84] and optical [85] frequency domains, respectively. Prior to this, realization of strong coupling depended upon the collective oscillation of N identical atoms coupled to a single cavity mode with strength g, a scenario which can be shown to be equivalent to two coupled oscillators with interaction strength $g_{\rm eff} = \sqrt{N}g$ [14], providing a pathway for experimental realization of strong coupling for sufficiently large N [86, 87]. Modern cavity QED experiments have continued the trend of increasing light-matter coupling strengths

even further. The last decade in particular has seen burgeoning interest in the so-called ultrastrong ($g \gtrsim 0.1\omega_0$) and deep ultrastrong ($g \gtrsim \omega_0$) coupling regimes, characterized by coupling strengths which approach/exceed the average resonant frequency ω_0 of the coupled cavity-emitter system. In both of these cases, the rotating wave approximation fails and, as a result, the very nature of the ground is altered and can be shown to contain virtual excitations [38].

Just as qualitatively distinct parameter regimes are achieved by tuning the ratio $g/\max\{\gamma_{\text{cav}}, \gamma_{\text{em}}\}$, physically interesting behavior has been identified in coupled nanophotonic systems with mismatched loss rates. One noteworthy limit involves a spectrally broad mode that is weakly coupled to another that is comparatively narrow (i.e., $\gamma_1 \gg \gamma_2$ and $g < \gamma_1$). This scenario resembles the limit of a discrete mode coupled to a continuum, and consequently has been shown to produce sharp, asymmetric spectral features known as Fano resonances [88, 89].

Another interesting possibility involves coupled systems with equal and opposite dissipation rates $\gamma_1 = -\gamma_2$, one describing gain and the other loss. Such a configuration – realized for example with coupled optical microresonators [90] – is a realization of an effective parity-time-symmetric ($\mathcal{PT}$-symmetric) Hamiltonian. $\mathcal{PT}$-symmetric systems are of both fundamental and applied interest, with $\mathcal{PT}$-symmetric quantum mechanics offering a fascinating extension to conventional quantum mechanics [91], and its experimental implementations having been argued to offer advantages for certain applications such as sensing [25] and nonreciprocity [92, 93].

In this Chapter, we present a brief survey of parameter space through the lens of a coupled oscillator model, with each individual section focused on a particular effect. As discussed throughout this dissertation, coupled oscillator models provide an effective means for interpreting many hybrid light-matter systems including both photonic and material (e.g. atomic, plasmonic, excitonic, phononic) components. While our approach – particularly toward weak and strong coupling – differs from the spin-oscillator model typically adopted for cavity QED, the core arguments remain intact with the advantage of significantly simplified mathematics. Aside from Section 4.1, the methods presented will be, for the most part, presented for an abstract set of coupled oscillators without specialization a particu-

lar experimental platform. As a result, the generality of the arguments presented will be evident.

Section 4.1 contains a derivation of Purcell enhancement using purely classical arguments. The strategy used is original and, in the opinion of the author, simpler to carry out analytically than methods typically used in the literature [94]. Furthermore, this method can easily be extended to coupled nanophotonic structures such as the hybrid photonic-plasmonic resonator of Chapters 5–6. Section 4.2 details an oscillator model based discussion of the Fano lineshape. Section 4.3 then moves on to the strong coupling regime, containing a brief discussion of hybridization. Section 4.4 concludes the chapter with a short introduction to effective $\mathcal{PT}$-symmetry in a coupled oscillator system.

4.1 Weak coupling: A classical derivation of Purcell enhancement

Before delving into the derivation, it is important to emphasize that spontaneous emission and, by extension, Purcell enhancement, are purely quantum mechanical phenomena. This is most easily seen by considering the light-matter interaction energy

$$H_{\text{int}} = -\mathbf{d} \cdot \mathbf{E}. \tag{4.1}$$

Classically, vacuum implies a complete absence of the radiation field ($\mathbf{E} = 0$), causing the above interaction energy to vanish. Quantum mechanically, however, the radiation field permits zero point fluctuations [80] which scale as

$$E_{\text{ZPF}} = \sqrt{\frac{2\pi\hbar\omega_0}{V}}, \tag{4.2}$$

suggesting that the interaction energy is nonvanishing even for vacuum. Interestingly, we see that decreasing the mode volume V causes a relative increase in E_{ZPF}, thus increasing the interaction energy and, as a result, the rate of spontaneous emission – this is the qualitative basis for why Purcell enhancement occurs.

While classical physics is unable to account for spontaneous emission, the radiation reaction force provides a route for computing the radiated power of an oscillating dipole via introduction of a self-interaction. This is achieved without explicit consideration of the radiation field as its own dynamic entity. To that end, it is instructive to explicitly compare

the rate of spontaneous emission in free-space with the rate at which power is radiated by a classical, oscillating dipole.

From Fermi's golden rule, the rate of spontaneous emission is given by [80]

$$\Gamma_{\text{se}} = \frac{4\omega_0^3}{3\hbar c^3}|d_{fi}|^2, \tag{4.3}$$

where f and i label some final and initial states, $\omega_0 = (E_f - E_i)/\hbar$ is the transition frequency, and $d_{fi} = \langle f|\mathbf{d}|i\rangle$ is the matrix element of the dipole operator connecting initial and final states. Modeling the transition as that of a harmonic oscillator,

$$\mathbf{d} = e\sqrt{\frac{\hbar}{2m\omega_0}}(a + a^\dagger), \tag{4.4}$$

Eq. (4.3) can be rewritten, after some manipulation, as

$$\Gamma_{\text{se}} = \frac{2e^2\omega_0}{3m\hbar c^3}\left(E - E_{\text{gnd}}\right) \tag{4.5}$$

where $E = (n + 1/2)\hbar\omega_0$ is the energy of the oscillator and E_{gnd} its ground state value. Turning now to the classical description, central to the interpretation of radiation reaction is the Larmor power (see Section 3.1) which, for an oscillating dipole at steady-state, can be expressed as

$$\langle P_{\text{rad}}\rangle = \frac{\omega^4}{3c^3}|d|^2, \tag{4.6}$$

where angle brackets indicate a time-average. To compute the rate at which photons are emitted, we normalize this to the energy of a photon resonant with the dipole frequency,

$$\Gamma_{\text{rad}} = \frac{\langle P_{\text{rad}}\rangle}{\hbar\omega_0} = \frac{e^2\omega_0^3}{3\hbar c^3}|x|^2, \tag{4.7}$$

where we have rewritten the dipole moment in terms of a generalized coordinate, i.e., $d = ex$. Assuming the dipole is oscillating at its resonant energy, the coordinate x can be reexpressed in terms of the energy of a harmonic oscillator $E = (1/2)m\dot{x}^2 + (1/2)m\omega_0^2x^2$. Using this to rewrite Γ_{rad}, we find

$$\Gamma_{\text{rad}} = \frac{2e^2\omega_0}{3m\hbar c^3}E. \tag{4.8}$$

Comparing Eqs. (4.5) and (4.8), it is evident that the only distinction is the absence of the ground state energy E_{gnd} in the latter. For a weakly coupled system, we do not expect

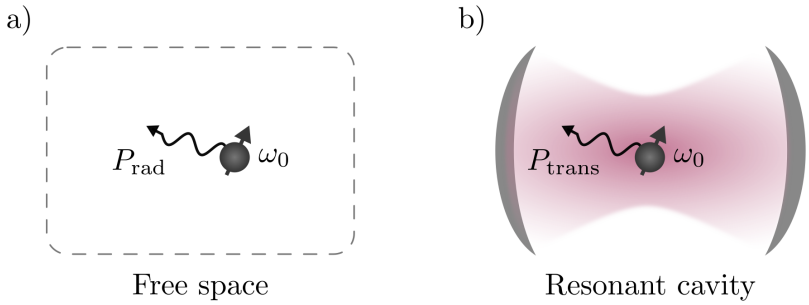

Figure 4.1: (a) A dipole oscillating at ω_0, radiating into free space at a rate P_{rad}. (b) A dipole transferring energy to an optical cavity mode at a rate oscillating P_{trans}

this ground state energy to be appreciably modified in the presence of a resonant cavity. Likewise, we assume the energy of the oscillator E to be independent of its surroundings (which certainly breaks down for strong coupling). It stands to reason, then, that this minor difference will play no role upon computation of the Purcell enhancement defined by

$$F_P = \frac{\Gamma_{\text{cav}}}{\Gamma_{\text{free}}}, \tag{4.9}$$

where Γ_{cav} is the rate at which photons are liberated into a resonant cavity and Γ_{free} into free space, suggesting a classical modeling based on the radiation reaction force is sufficient.

4.1.1 Purcell enhancement due to a resonant cavity

We will now demonstrate a method for computing the analytic expression for Purcell enhancement in the presence of a photonic cavity using methods from Chapter 3. To do this, we imagine two scenarios: (i) a resonantly driven, oscillating dipole is radiating into the free-field at steady-state and (ii) a resonantly driven, oscillating dipole is coupled to an optical cavity to which it can transfer energy, also at steady-state. Both of these scenarios are illustrated in Fig. 4.1. Importantly, in the latter case we assume the dipole cannot couple to the modes of the free-field, and therefore we do not include the radiation reaction force in our description of the dynamics. In addition, we assume weak coupling – once energy is transferred to the cavity, it has negligible probability of being reabsorbed by the emitter.

No additional calculations need to be carried out for this first scenario – the rate at which energy is liberated into the free-field is already provided by the Larmor power in Eq. (4.6). For the second scenario, we can write the system Lagrangian in terms of its individual contributions $L = L_{\text{matter}} + L_{\text{cav}} + L_{\text{int}}$, where

$$\begin{aligned} L_{\text{matter}} &= \frac{1}{2}m\dot{x}^2 - \frac{1}{2}m\omega_0^2 x^2 \\ L_{\text{cav}} &= \frac{1}{2V}\dot{q}^2 - \frac{1}{2V}\omega_c^2 q^2 \\ L_{\text{int}} &= -g\sqrt{\frac{m}{V}}x\dot{q}. \end{aligned} \tag{4.10}$$

As in Section 2.1, the vector potential of the cavity mode is given by

$$\mathbf{A}(\mathbf{r}, t) = \frac{c\sqrt{4\pi}}{V}q(t)\mathbf{f}(\mathbf{r}), \tag{4.11}$$

where the mode function $\mathbf{f}(\mathbf{r})$ is assumed to be real, and is further normalized such that

$$\begin{aligned} \max\{|\mathbf{f}(\mathbf{r})|^2\} &= 1 \\ V &= \int d^3r\, |\mathbf{f}(\mathbf{r})|^2, \end{aligned} \tag{4.12}$$

and the dipole-field coupling strength is defined as

$$g = e\sqrt{\frac{4\pi}{mV}}\mathbf{f}(\mathbf{r}_0)\cdot\hat{\mathbf{x}}. \tag{4.13}$$

Note that this notation has changed relative to Section 2.3 as λ will later be used to denote the cavity mode wavelength.

Computing the equations of motion from Eq. (4.10), we find

$$\begin{aligned} m\ddot{x} + m\gamma_{\text{nr}}\dot{x} + m\omega_0^2 x + g\sqrt{\frac{m}{V}}\dot{q} &= eEe^{-i\omega_0 t} \\ \frac{1}{V}\ddot{q} + \frac{\gamma_c}{V}\dot{q} + \frac{\omega_c^2}{V}q - g\sqrt{\frac{m}{V}}\dot{q} &= 0 \end{aligned} \tag{4.14}$$

where we have introduced a fictitious driving field acting on the dipole to force steady-state oscillation at its resonant frequency. In addition, we have added dissipation to both the cavity and dipole oscillator with damping rates γ_c and γ_{nr}, respectively. The first of these is necessary to create the situation of weak coupling – without cavity dissipation, energy

would be coherently exchanged between the dipole and cavity mode, allowing for higher-order processes beyond spontaneous emission. The added nonradiative dipole rate γ_{nr} will play no role in the following calculation, and is merely included for generality.

Following the technique of Section 3.1, the power transferred from the dipole to the cavity mode may be computed as

$$\begin{aligned}\langle P_{\text{trans}}\rangle &= -\frac{1}{\tau}\int_{\tau/2}^{\tau/2} dt\, \mathbf{F}_{\text{coup}}(t)\cdot\dot{\mathbf{x}}(t) \\ &= -\frac{1}{\tau}\int_{\tau/2}^{\tau/2} dt\, \text{Re}\left(-g\sqrt{m/V}\dot{q}(t)\right)\cdot \text{Re}\left(\dot{x}(t)\right)\end{aligned} \tag{4.15}$$

where we have assumed the steady state solutions $x(t) = xe^{-i\omega_0 t}$, $q(t) = qe^{-i\omega_0 t}$. Using the cavity mode equation of motion, q can be rewritten in terms of x as

$$q = \frac{-i\omega g\sqrt{mV}}{-\omega_0^2 + \omega_c^2 - i\omega_0\gamma_c}x. \tag{4.16}$$

Substituting this into Eq. (4.15), carrying out quite a bit of algebra and taking the integral, we find simplifies to

$$\langle P_{\text{trans}}\rangle = \frac{2\pi e^2}{V}\frac{\omega_0^4\gamma_c|\mathbf{f}(\mathbf{r}_0)\cdot\hat{\mathbf{x}}|^2}{(\omega_0^2-\omega_c^2)^2+\omega_0^2\gamma_c^2}|x|^2 \tag{4.17}$$

where we have substituted in the definition Eq. (4.13) for g.

We can now compare this to the steady-state free space radiation rate P_{rad} evaluated at the resonant frequency ω_0

$$\langle P_{\text{rad}}\rangle = \frac{e^2\omega_0^4}{3c^3}|x|^2. \tag{4.18}$$

Dividing $\langle P_{\text{trans}}\rangle$ by $\langle P_{\text{rad}}\rangle$ yields the enhancement (or suppression) factor

$$F_P = \frac{6\pi c^3}{V}\frac{\gamma_c|\mathbf{f}(\mathbf{r}_0)\cdot\hat{\mathbf{x}}|^2}{(\omega_0^2-\omega_c^2)^2+\omega_0^2\gamma_c^2}. \tag{4.19}$$

From this expression alone, it is evident that F_P can be made arbitrarily small (and the emitter lifetime arbitrarily long) by increasing the emitter-cavity detuning $\omega_0 - \omega_c$. This is unsurprising, as we have modeled the cavity as having just a single mode – a large detuning (relative to γ_c) therefore ensures a vanishing photonic density of states around ω_0, inhibiting emission as a result.

Let us now assume optimal conditions to maximize $\langle P_{\text{trans}}\rangle$. For starters, let us assume that the dipole is perfectly aligned with the field and located at its maximum. Then, using

the normalization condition in Eq. (4.12),

$$|\mathbf{f}(\mathbf{r}_0) \cdot \hat{\mathbf{x}}|^2 = 1. \tag{4.20}$$

As an aside, for the more typical normalization condition $\int d^3r|\mathbf{f}(\mathbf{r})| = 1$ this step must be combined with the definition of the mode volume (see Eq. (2.6)) to produce a factor of $1/V$. Here, our normalization condition imbued the cavity mode oscillator with an effective mass of $1/V$ and, as a result, $\langle P_{\text{trans}} \rangle$ already contains an explicit factor of $1/V$. This result is therefore entirely independent of the choice of convention for the normalization, as should be the case.

Finally, we assume the cavity mode to be resonant with the emitter $\omega_c = \omega_0$ and apply the definition of the quality factor, $Q = \omega_c/\gamma_c$ to write

$$F_P = \frac{6\pi c^3}{\omega_0^3} \frac{Q}{V} \tag{4.21}$$

Rewriting the emitter resonant frequency as the wavelength $\lambda = 2\pi c/\omega_0$, we arrive at the standard definition for the Purcell enhancement [14]

$$F_P = \frac{3\lambda^3}{4\pi} \frac{Q}{V}. \tag{4.22}$$

We will now remark on some simple generalizations to Eq. (4.22). For one, it is straightforward to extend this result to the case of a dielectric cavity. Although we have not explicitly discussed the generalization of the cavity oscillator framework for this case (see Chapter 8), the only difference pertinent here is that the squared field is multiplied by $\varepsilon(\mathbf{r})$ in the normalization condition of Eq. (4.12). Consequently, placing the cavity at the maximum of the field (approximately) corresponds to adjusting the right-hand side of Eq. (4.20) to $1/n^2$ where n is the index of refraction at the location of the emitter. Separately, the Larmor power is reduced by a factor of n for an emitter embedded in a dielectric. Combining these considerations, we find

$$F_P = \frac{3}{4\pi} \left(\frac{\lambda}{n}\right)^3 \frac{Q}{V}, \tag{4.23}$$

another common expression for the Purcell enhancement.

We can also envision a scenario where the dipole emits both into free space as well as into the cavity modes. In the approximation where the former rate is not influenced by the

presence of the cavity, we can write

$$F_P = \frac{\langle P_{\text{rad}} \rangle + \langle P_{\text{trans}} \rangle}{\langle P_{\text{rad}} \rangle} = 1 + \frac{3}{4\pi} \left(\frac{\lambda}{n} \right)^3 \frac{Q}{V}. \tag{4.24}$$

4.1.2 Purcell enhancement due to a plasmonic nanoresonator

As can be seen from Eq. (4.22), there is an obvious strategy for maximizing Purcell enhancement: simultaneously make Q as large and V as small as possible. Modern approaches to large Purcell enhancement often involve ultrahigh-Q whispering gallery mode optical resonators, with quality factors in excess of $Q > 10^8$ (and even $Q > 10^{12}$ in extreme cases) [95, 85]. However, these platforms are typically hundreds of microns in scale and thus come at the cost of a large mode volume. Separately, plasmonic nanoparticles have been extensively studied for their ability to confine light to sub-diffraction length scales, offering a complementary solution to achieve large Purcell factors. Nothing is free in Nature, however – this comes with the tradeoff of very poor Q, typically on the order of only $Q \lesssim 100$ or so for a gold nanoparticle [96].

Given this, it is instructive to apply the above procedure to the case of an emitter coupled to a plasmonic nanoparticle. For simplicity, we will specialize to a gold sphere in the dipole approximation so that the results of Section 2.2 can be used. Furthermore, we assume that (i) the plasmon mode is of small enough radius such that dissipation is dominated by nonradiative pathways and radiative decay will be neglected, (ii) the emitter feels only the near-field of the plasmon and (iii) the emitter is located at the surface of the nanoparticle (i.e., the maximum value of the field). The calculation of Purcell enhancement then follows exactly as before, with the equations of motion

$$\begin{aligned} m_0 \ddot{x}_0 + m_0 \gamma_{\text{nr}} \dot{x}_0 + m_0 \omega_0^2 - g x_0 &= eE e^{-i\omega_0 t} \\ m_1 \ddot{x}_1 + m_1 \gamma_{\text{nr}} \dot{x}_1 + m_1 \omega_1^2 - g x_1 &= 0 \end{aligned} \tag{4.25}$$

used to compute $\langle P_{\text{trans}} \rangle$, the rate at which energy is transferred from the dipole to the plasmon. Here, the subscripts 0 and 1 denote the emitter and LSP, respectively. Furthermore, the coupling strength is equal to

$$g = e^2 \, \hat{\mathbf{x}}_0 \cdot \mathbf{\Lambda}_{\text{NF}}(\mathbf{R}) \cdot \hat{\mathbf{x}}_\mathbf{1}, \tag{4.26}$$

where $\mathbf{\Lambda}_{\mathrm{NF}}(\mathbf{R})$ is the near-field contribution to the dipole relay tensor in Eq. (2.58) and $\mathbf{R}$ the vector pointing from the emitter to the nanoparticle center.

Explicit calculation of $\langle P_{\mathrm{trans}} \rangle$ and normalization to the free-space rate $\langle P_{\mathrm{rad}} \rangle$ yields the usual expression

$$F_P = \frac{3\lambda^3}{4\pi} \frac{Q}{V}, \tag{4.27}$$

where casting F_P into this form has allowed us to identify the dipole LSP mode volume as

$$V_{\mathrm{LSP}} = \frac{\pi \omega_0^2}{e^2} m_1 a^6, \tag{4.28}$$

where a is the radius of the sphere. Using the derived form of the effective mass in Section 2.2, this can be further reexpressed as

$$V_{\mathrm{LSP}} = \frac{\pi}{3} a^3 (\varepsilon_\infty + 2), \tag{4.29}$$

illustrating that the mode volume scales with the physical nanoparticle volume, differing only by a numerical prefactor. Interestingly, this result agrees with the direct calculation

$$V_{\mathrm{LSP}} = \frac{\int d^3 r \, \mathbf{D} \cdot \mathbf{E}}{\max\{\mathbf{D} \cdot \mathbf{E}\}} \tag{4.30}$$

upon substitution of the standard electrostatic expressions for $\mathbf{D}$ and $\mathbf{E}$ for a metallic sphere found in Jackson [4], adding validity to the oscillator-based approach presented here.

Finally, we emphasize that, in general, caution must be exercised in applying the standard Purcell expression to plasmonic systems as it has been previously shown that the one-mode approximation can lead to inaccurate results [96]. Still, in cases where analytic exploration is more valuable than quantitative agreement, the procedure presented here is of broad use. When quantitative accuracy is desired, numerical computation of the local density of states [94] is a more appropriate approach.

4.2 Weak coupling: The Fano resonance

In 1957, sharp asymmetric lineshapes were observed in the inelastic electron scattering spectrum of helium gas by Lassettre et al. [97]. These peculiar and puzzling features stood in distinct contrast to the Lorentzian lineshape that typically characterizes resonant phenomena. Just two years later, these observations were explained in a seminal publication by

Ugo Fano [88], demonstrating quantum interference to be the central cause. Today, Fano resonances are understood to occur in any system comprising a discrete transition weakly interacting with a continuum and have been observed in a wide breadth of optical, atomic and solid-state systems [89]. While originally considered a purely quantum mechanical effect involving interference of quantum wavefunctions, electromagnetic interference can support the Fano effect in purely classical systems to great advantage for various applications such as sensing and optical switching [98, 65].

The physics underlying the Fano resonance is remarkably straightforward and can be simply understood using a classical model of two coupled harmonic oscillators. One oscillator is assumed to describe some discrete transition (i.e., a delta function in frequency-space) and the other is taken to be describe a quasi-continuum of states (i.e., with a large spectral width). Furthermore, we will assume the coupling between the two oscillators to be weak and real-valued. Some of these assumptions are essential, while others (such as a finite linewidth for the discrete mode and complex coupling) may be relaxed – such generalizations are discussed in Part II of this dissertation, where we analyze Fano resonances appearing in the spectra of a hybrid photonic-plasmonic resonator (Chapters 5 and 6) and an infrared, plasmonic coupled nanostructure (Chapter 7). Here, we will specialize to the simplest scenario possible known to produce Fano interference.

Fig. 4.2 illustrates the system in question, with the broad, harmonically forced mode represented by the orange oscillator, and the discrete mode in blue. The equations of motion of this system can be written as

$$\begin{aligned} &m_0\ddot{x}_0 + m_0\gamma_0\dot{x}_0 + m_0\omega_0^2 x_0 + g\sqrt{m_0 m_1}x_1 = F_{\text{ext}}e^{-i\omega t} \\ &m_1\ddot{x}_1 + m_1\omega_1^2 x_1 + g\sqrt{m_0 m_1}x_2 = 0 \end{aligned} \tag{4.31}$$

Let us now compute the power absorbed via the dissipative force $F_{\text{damp}} = -m_0\gamma_0\dot{x}_0$ using the techniques of Chapter 3. As we have carried out several similar calculations up to this point, we will skip to the result

$$\langle P_{\text{abs}}\rangle = \frac{1}{2}m_0\omega^2\gamma_0|x_0(\omega)|^2, \tag{4.32}$$

where we have assumed the steady state solution $x_0(t) = x_0(\omega)e^{-i\omega t}$. While the concept of a polarizability isn't directly applicable here as we have not specialized to an electromagnet-

ically driven dipole, it is helpful to introduce an oscillator response function. In particular, let us define $\alpha(\omega)$ and $\widetilde{\alpha}(\omega)$ such that

$$x_0(\omega) = \widetilde{\alpha}(\omega) F_{\text{ext}} \qquad (g \neq 0) \tag{4.33}$$

describes the dressed quasi-continuum oscillator response when coupled to the discrete mode and

$$x_0(\omega) = \alpha(\omega) F_{\text{ext}} \qquad (g = 0) \tag{4.34}$$

defines the bare, uncoupled quasi-continuum oscillator response. From Eq. (4.31), the dressed response function can be shown to be equal to

$$\widetilde{\alpha}(\omega) = \frac{1/m_0}{-\omega^2 + \omega_0^2 - i\omega\gamma_0 - \frac{g^2}{-\omega^2+\omega_1^2}}. \tag{4.35}$$

Our goal is now to relate this back to the bare response $\alpha(\omega)$. Multiplying and dividing by $-\omega^2 + \omega_1^2$, the above result can be reexpressed as

$$\begin{aligned} \widetilde{\alpha}(\omega) &= \alpha(\omega) \left(\frac{-\omega^2 + \omega_1^2}{-\omega^2 + \omega_1^2 - \frac{g^2}{-\omega^2+\omega_0^2-i\omega\gamma_0}} \right) \\ &= \alpha(\omega) \left(\frac{-\omega^2 + \omega_1^2}{-\omega^2 + \widetilde{\omega}_1^2 - i\omega\widetilde{\gamma}_1} \right), \end{aligned} \tag{4.36}$$

where, in going from the first to the second line, we have defined the dressed frequency and damping rate of the discrete mode as

$$\begin{aligned} \widetilde{\omega}_1^2(\omega) &= \omega_1^2 + \frac{g^2(\omega^2 - \omega_0^2)}{(\omega^2 - \omega_0^2)^2 + \omega^2\gamma_0^2} \\ \widetilde{\gamma}_1(\omega) &= \frac{g^2\gamma_0}{(\omega^2 - \omega_0^2)^2 + \omega^2\gamma_0^2}. \end{aligned} \tag{4.37}$$

Note that, because the discrete mode has no inherent damping, the dressed rate $\widetilde{\gamma}_1$ includes only a contribution inherited via coupling to the broad mode. Finally, we define the asymmetry factor

$$q_F(\omega) = \frac{\widetilde{\omega}_1^2 - \omega_1^2}{\omega\widetilde{\gamma}_1}, \tag{4.38}$$

allowing us to express $\widetilde{\alpha}(\omega)$ in the form

$$\widetilde{\alpha}(\omega) = \alpha(\omega) \left(\frac{\omega^2 - \widetilde{\omega}_1^2 + \omega\widetilde{\gamma}_1 q_F}{\omega^2 - \widetilde{\omega}_1^2 + i\omega\widetilde{\gamma}_1} \right). \tag{4.39}$$

Substituting this back into Eq. (4.32), we find

$$\langle P_{\text{abs}} \rangle = F(\omega) \langle P_{\text{abs}}^{(0)} \rangle \tag{4.40}$$

where $\langle P_{\text{abs}}^{(0)} \rangle$ is the unperturbed absorbed power (i.e., Eq. (4.32) with $g \to 0$) and $F(\omega)$ is the Fano lineshape,

$$F(\omega) = \left| \frac{\epsilon + q_F}{\epsilon + i} \right|^2 . \tag{4.41}$$

Here, $F(\omega)$ is expressed in terms of the reduced frequency $\epsilon(\omega) = (\omega^2 - \widetilde{\omega}_1^2)/\omega\widetilde{\gamma}_1$. Crucially, q_F is frequency dependent, as are the dressed parameters $\widetilde{\omega}_1$ and $\widetilde{\gamma}_1$. However, none of these parameters appear in $\langle P_{\text{abs}}^{(0)} \rangle$. Separately, analysis of Eq. (4.39) suggests that $\widetilde{\alpha}(\omega)$ rapidly converges to $\alpha(\omega)$ at frequencies away from ω_1 (note that this is only true for $g \ll \gamma_0$). It is therefore appropriate to replace the frequency-dependent parameters q_F, $\widetilde{\omega}_1$, and $\widetilde{\gamma}_1$ by their value at $\omega = \omega_1$,

$$\begin{aligned} \widetilde{\omega}_1^2 &\approx \omega_1^2 + \frac{g^2(\omega_1^2 - \omega_0^2)}{(\omega_1^2 - \omega_0^2)^2 + \omega_1^2\gamma_0^2} \\ \widetilde{\gamma}_1 &\approx \frac{g^2\gamma_0}{(\omega_1^2 - \omega_0^2)^2 + \omega_1^2\gamma_0^2} \\ q_F &\approx \frac{\widetilde{\omega}_1^2 - \omega_1^2}{\omega_1\widetilde{\gamma}_1} = \frac{\omega_1^2 - \omega_0^2}{\omega_1\gamma_0}. \end{aligned} \tag{4.42}$$

It is important to note that the form of Eq. (4.40) is completely general, independent of the relative values of the parameters g and γ_0. However, in the quasi-continuum weak coupling limit $g \ll \gamma_0$, $F(\omega)$ sharply varies around $\omega = \omega_1$ and is close to unity everywhere else. As a result, the absorption spectrum of the composite system $\langle P_{\text{abs}} \rangle$ is nearly identical to that of the bare, uncoupled continuum mode $\langle P_{\text{abs}}^{(0)} \rangle$, aside from a spectrally sharp feature near the discrete mode frequency, show shown in Fig. 4.2b. As illustrated in Fig. 4.2d, the exact shape of this perturbation is dependent upon the value of the asymmetry parameter q_F. Separately, the dressed frequency $\widetilde{\omega}_1$ and linewidth $\widetilde{\gamma}_1$ define the Fano resonance location and width. For systems where the discrete mode has a finite inherent linewidth γ_1, these conclusions remain true, albeit with an additional requirement $\gamma_0/\gamma_1 \gtrsim 10$ that must be satisfied for a Fano-like lineshape to appear. Generalizations to the Fano lineshape for this scenario are presented in Part II.

We conclude our introduction to Fano resonances by appealing to the simple model of Fig. 4.2a for an intuitive explanation of why the asymmetric spectral lineshape emerges.

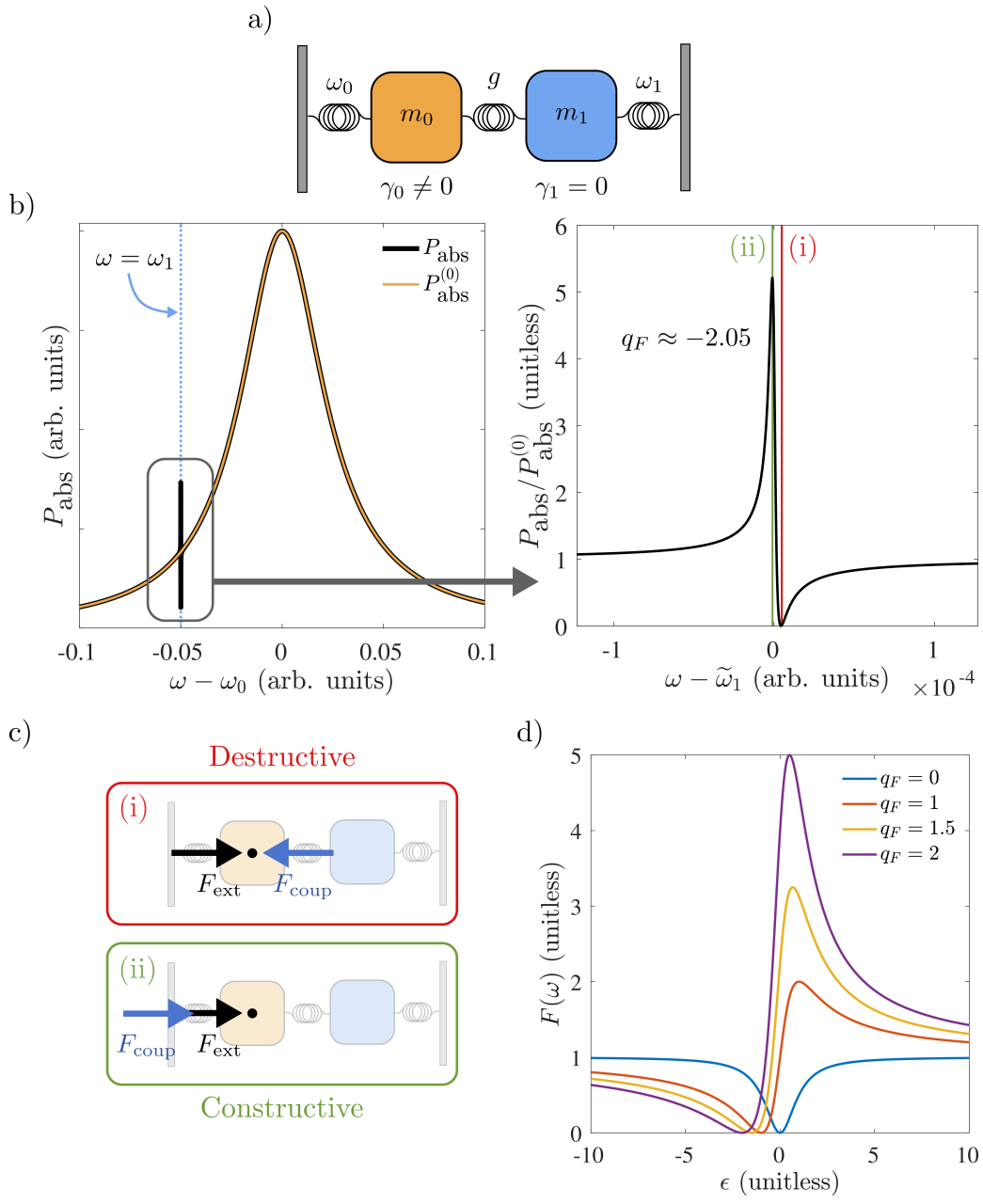

Figure 4.2: *Continued on following page.*

Figure 4.2: (a) Two oscillators, one damped ($\gamma_0 \neq 0$) and one undamped ($\gamma_1 = 0$), coupled with rate g. In the limit where $\gamma_0 \gg g$, a Fano resonance appears in the system absorption spectrum. (b) Left panel: the absorption spectrum of the above coupled oscillator system (black curve), with the bare uncoupled spectrum of the spectrally broad oscillator mode overlaid (orange curve). The spectrum of the coupled system follows that of the bare quasi-continuum mode, aside from a sharp spectral feature at the discrete mode resonant frequency (blue dotted line). Right panel: zoomed-in plot of the region enclosed by the gray box in the left panel, normalized to the bare spectrum of the lossy oscillator. The normalized spectrum reveals a Fano lineshape with asymmetry factor $q_F \approx -2.05$, centered at the dressed frequency $\widetilde{\omega}_1$. (c) Illustration of constructive and destructive forces acting on the broad mode. The red box corresponds to the vertical red line in the right panel of (b), while the green box corresponds to the green line. (d) The Fano lineshape and its dependence on the asymmetry factor q_F. A vanishing value of q_F, corresponding to the case $\omega_0 = \omega_1$, yields a perfectly symmetric dip in absorption. While not shown, q_F can also be negative, resulting in the same lineshapes shown but reflected about $\epsilon = 0$.

From Eq. (4.31), the spectrally broad oscillator is directly driven by an external force, while the discrete mode is (indirectly) driven via the coupling force alone. At steady-state, the phase of a harmonically driven oscillator depends entirely on the driving frequency ω. Taking the broad oscillator as an example, the three limits $\omega \ll \omega_0$, $\omega = \omega_0$ and $\omega \gg \omega_0$ correspond to $\phi_0 = 0$, $\phi_0 = \pi/2$ and $\phi_0 = \pi$, where ϕ is the relative phase between the driving force and the harmonic response of the driven oscillator. While the discrete mode is not driven by an external force, we can still extrapolate on the above limits to determine the phase response of oscillator 1 relative to oscillator 0. Because the response of oscillator 1 is spectrally narrow, varying ω across ω_1 leads to a relative phase $\Delta\phi = \phi_1 - \phi_0$ that rapidly varies from $\Delta\phi = 0$ to $\Delta\phi = \pi$. As a result, the phase of the coupling force $-g\sqrt{m_1 m_2}x_1$ rapidly changes from constructively interfering with $\mathbf{F}_{\text{ext}}$ to destructively interfering as ω is swept across the region near ω_1. For $\gamma_1 = 0$, complete destructive interference is possible, causing a dip in the spectrum where the absorbed power vanishes completely – physically, this special

frequency corresponds to a situation where energy is "trapped" in the discrete mode, unable to dissipate through the broad mode's decay channel due to destructive interference. This phenomenon is also the basis for electromagnetic induced transparency, typically realized for the configuration $\omega_1 = \omega_2$, leading to a symmetric dip with $q_F = 0$ [65].

4.3 Strong coupling: Hybridization

The content of the previous two sections concerns phenomena achievable in the weak coupling regime, where dissipation overwhelms the rate of energy exchange in a coupled system. When the opposite is true – i.e., the rate of energy exchange exceeds the rate of dissipation – the system is said to be in the strong coupling regime. There, dissipation becomes unimportant and the system becomes hybridized, meaning the fundamental excitations of the system are no longer those of the independent coupled modes, but rather concern the normal modes (also sometimes called supermodes) of the system.

Because hybrid light-matter systems comprise both photonic and material components, the hybridized excitations of such a system – termed polaritons – mix light and matter degrees of freedom. The physical properties of the polaritons are highly dependent upon the nature of the underlying material excitations. For realizations of the Jaynes-Cummings Hamiltonian, for example, the polaritonic excitations inherit nonlinearity of the two-level system, allowing for the realization of nonlinear phenomenon such as photon-blockade [99, 100]. As Chapter 10 concerns a more complete discussion of such topics in regards to the Jaynes-Cummings Hamiltonian, here we will specialize to the comparatively simpler scenario described by the linear dipole-cavity Hamiltonian of Eq. (2.69),

$$H = \frac{p_a^2}{2m} + \frac{1}{2}m\omega_a^2 x_a^2 + \frac{V}{2}p_c^2 + \frac{1}{2V}\omega_c^2 q_c^2 + \sqrt{mV}\lambda x_a p_c. \tag{4.43}$$

Here, cavity and atomic parameters are denoted by the subscript c and a where distinction is necessary. Separately, the light-matter coupling strength is defined as

$$\lambda = e\sqrt{\frac{4\pi}{mV}}\mathbf{f}(\mathbf{r}_0)\cdot\hat{\mathbf{x}}_a. \tag{4.44}$$

We will now illustrate how unitary transformations can be used to nonperturbatively reexpress the above Hamiltonian in an alternate basis that highlights the underlying mixed

light-matter excitations. Similar techniques are used consistently throughout Part II and Part III, motivating the brief, high-level treatment here.

There are generally two equivalent approaches to unitary transformation of a Hamiltonian: (i) transform the Hamiltonian itself, and rewrite in terms of "old" operators, or (ii) transform the independent operators and rewrite the "old" Hamiltonian in terms of the "new" operators [101]. Both strategies give equivalent results, and personal taste often dictates which is chosen. Here, and throughout this dissertation, we will favor approach (ii).

All unitary transformation are expressable in the form

$$U = e^{S}, \tag{4.45}$$

where, clearly, unitarity dictates that the generator S is anti-Hermitian, i.e. $S^\dagger = -S$. Each operator $\mathcal{O}$ transforms according the Baker-Campbell-Hausdorff formula [101]

$$\begin{aligned}\widetilde{\mathcal{O}} &= e^{-S}\mathcal{O}e^{S} \\ &= \mathcal{O} + [\mathcal{O}, S] + \frac{1}{2!}[[\mathcal{O}, S], S] + \frac{1}{3!}[[[\mathcal{O}, S], S], S] + \ldots .\end{aligned} \tag{4.46}$$

Because the interaction term in Eq. (4.43) appears as the dipole coordinate x_a coupled to the cavity mode momentum p_c, diagonalization is significantly simpler in the basis of creation and annihilation operators where, following Section 2.3, the Hamiltonian is written as

$$H = \hbar\omega_a a^\dagger a + \hbar\omega_c c^\dagger c + g(c^\dagger a + c a^\dagger). \tag{4.47}$$

As in Section 2.3, we have made the rotating-wave approximation and the light-matter interaction strength g is defined as

$$g = \hbar\sqrt{\frac{\pi e^2 \omega_c}{m\omega_a V_c}}\mathbf{f}(\mathbf{r}_0)\cdot\hat{\mathbf{x}}. \tag{4.48}$$

We wish to apply the transformation generated by

$$S = \theta(a^\dagger c - a c^\dagger). \tag{4.49}$$

Individually transforming the atomic and cavity operators a and c is achieved by computing and resumming the series of commutators in Eq. (4.46) – for two coupled oscillators (as we

have here), this can be carried out exactly. In contrast, the prototypical cavity QED framework of a two-level system coupled to an oscillator is comparatively much more complicated as the relevant commutation relations of the individual operators do not analytically close. For an in-depth analysis of that particular problem, see Chapter 10.

Returning to the problem at hand, direct transformation of the annihilation operators yields the relations

$$\begin{aligned} b_1 \equiv \widetilde{c} &= c\cos\theta + a\sin\theta \\ b_2 \equiv \widetilde{a} &= a\cos\theta - c\sin\theta, \end{aligned} \tag{4.50}$$

where we have defined b_1 and b_2 to denote transformed cavity and dipole annihilation operators, respectively. Inverting these relations and substituting into Eq. (4.47), we find that the choice

$$\theta = \frac{1}{2}\tan^{-1}\left(\frac{2g}{\omega_c - \omega_a}\right) \tag{4.51}$$

reduces the Hamiltonian to its diagonal form,

$$H = \hbar\Omega_1 b_1^\dagger b_1 + \hbar\Omega_2 b_2^\dagger b_2, \tag{4.52}$$

where the normal mode resonant frequencies are

$$\begin{aligned} \Omega_1 &= \omega_c\cos^2\theta + \omega_a\sin^2\theta + 2g\sin\theta\cos\theta \\ \Omega_2 &= \omega_a\cos^2\theta + \omega_c\sin^2\theta - 2g\sin\theta\cos\theta. \end{aligned} \tag{4.53}$$

The parameter θ is known as the mixing angle. Analysis of its analytic form suggests two qualitatively distinct parameter regimes. For $g \gg (\omega_c - \omega_a)$, we see that light and matter degrees of freedom become *hybridized*. In this scenario, θ tends toward $\pi/4$ and the operators b_1 ($b_1^\dagger$) and b_2 ($b_2^\dagger$) describe annihilation (creation) of polaritonic excitations. Separately, when $g \ll (\omega_c - \omega_a)$, $\theta \to 0$. Consequently, b_1 and b_2 revert to the bare cavity and dipole operators c and a. The limit of small mixing $\theta \ll 1$ is often referred to as the dispersive coupling regime – in the context of the Jaynes-Cummings Hamiltonian (which follows quite similarly [102]), dispersive copuling is particularly important for applications such as quantum nondemolition measurement [14, 103].

4.4 A brief introduction to $\mathcal{PT}$-symmetry

In standard quantum theory, a valid Hamiltonian must satisfy two essential properties: it must produce (i) real eigenvalues and (ii) unitary evolution. Conventional wisdom then leads to the conclusion that any valid Hamiltonian must be Hermitian. However, at the close of the 20th century it was discovered that another class of Hamiltonians – obeying $\mathcal{PT}$-symmetry rather than Hermiticity – also satisfy these requirements [104]. Four years later, quantum theory was formally extended to encompass $\mathcal{PT}$-symmetric Hamiltonians [91], and not long after it was discovered that optical systems provided a unique platform for realizing classical analogues of non-Hermitian $\mathcal{PT}$-symmetric Hamiltonians [90].

One of the prototypical examples of a $\mathcal{PT}$-symmetric system is that of two coupled optical resonators with balanced gain and loss, as shown in Fig. 4.3. Upon spatial and temporal reflection, the global system is unchanged, satisfying the basic requirement for $\mathcal{PT}$-symmetry. Importantly, this is not a realization of a true $\mathcal{PT}$-symmetric Hamiltonian, as the inherent non-Hermiticity clearly emerges from tracing out environmental degrees of freedom which account for loss and gain. However, we can approximate the physics of this system by the *effective* Hamiltonian

$$H_{\text{eff}} = \hbar(\omega_0 - i\gamma_1/2)a_1^\dagger a_1 + \hbar(\omega_0 - i\gamma_2/2)a_2^\dagger a_2 + \hbar g(a_1^\dagger a_2 + a_1 a_2^\dagger), \tag{4.54}$$

where we have assumed just a single mode in each resonator with frequency ω_0. We now wish to compute the eigenvalues of H_{eff} through calculation of the normal mode frequencies $\omega_\pm$, a task which may be achieved either using unitary transformations (as in the previous section) or, alternatively, at the level of the Heisenberg equations of motion. Regardless of the path chosen, we find

$$\omega_\pm = \omega_0 - i\frac{(\gamma_1 + \gamma_2)}{4} \pm \frac{1}{2}\sqrt{4g^2 - \frac{(\gamma_1 - \gamma_2)^2}{4}}. \tag{4.55}$$

For a system of two lossy resonators ($\gamma_1 > 0$ and $\gamma_2 > 0$), the normal mode resonant frequencies $\omega_\pm$ (and by extension, the eigenvalues of H_{eff}), are clearly complex. However, if one resonator has gain (achieved, for example, by adding an ionic dopant [90]) that balances loss, $\omega_\pm$ can be completely real for large enough coupling g. To see this, we imagine the

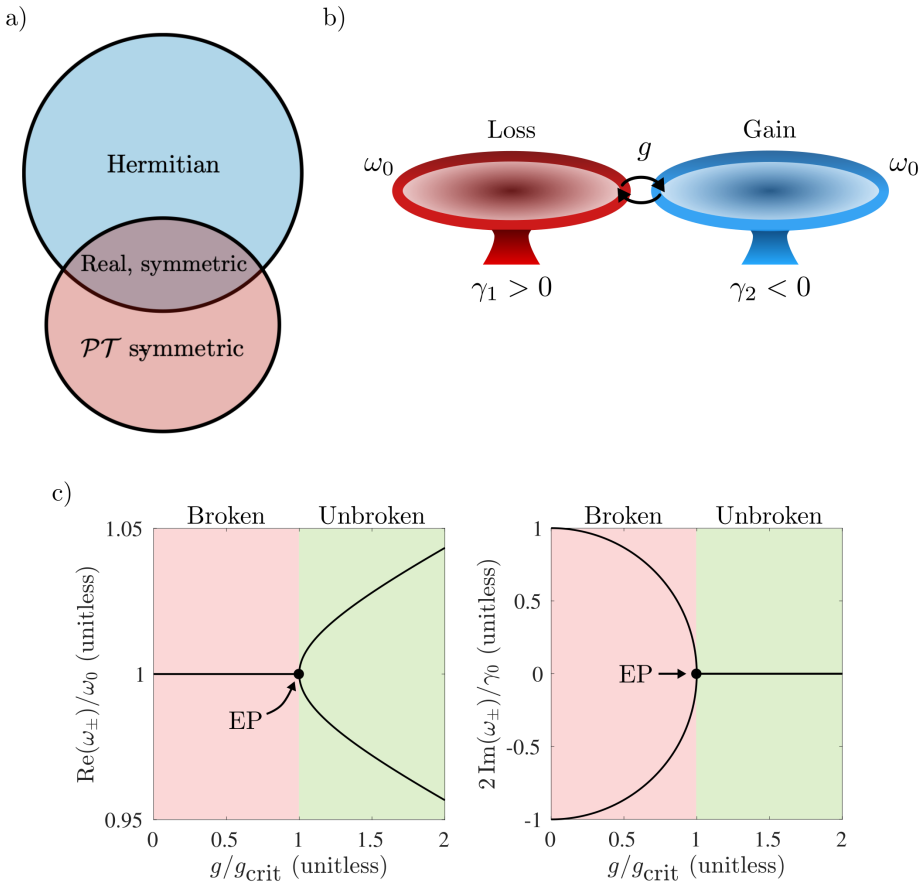

Figure 4.3: (a) For certain parameter regimes, $\mathcal{PT}$-symmetric Hamiltonians have entirely real eigenvalues, and thus offer an alternative to the more conventional scenario of a Hermitian Hamiltonian. Both Hermitian and $\mathcal{PT}$-symmetric Hamiltonians include real, symmetric Hamiltonians as a subset. (b) An experimental realization of a $\mathcal{PT}$-symmetric system (see Ref. [90]) consisting of two coupled resonators, one with loss ($\gamma_1 > 0$) and the other with gain ($\gamma_2 < 0$). (c) Real and imaginary parts of the eigenvalues Eq. (4.55) as a function of g/g_{crit} where $g_{\mathrm{crit}} = |\gamma_1 - \gamma_2|/4$. For $g < g_{\mathrm{crit}}$, $\mathcal{PT}$-symmetry is broken and the normal mode frequencies $\omega_\pm$ are complex. Unbroken $\mathcal{PT}$-symmetry occurs for $g > g_{\mathrm{crit}}$, characterized by completely real eigenvalues. At the interface between broken and unbroken regimes is the exceptional point (EP). There, $g = g_{\mathrm{crit}}$ and both real and imaginary parts of the eigenvalues coalescence.

scenario illustrated in Fig. 4.3b with $\gamma_1 = -\gamma_2 = \gamma_0$. Substituting this choice into Eq. (4.55), we find

$$\omega_\pm = \omega_0 \pm \frac{1}{2}\sqrt{4g^2 - \gamma_0^2}. \tag{4.56}$$

Eq. (4.56) suggests the existence of two distinct parameter regimes exist: for $g > \gamma_0/2$, both ω_+ and ω_- are completely real, while $g < \gamma_0/2$ yields complex eigenfrequencies with equal real contributions. The former is known as the *unbroken* $\mathcal{PT}$-symmetry regime, and the latter the *broken* $\mathcal{PT}$-symmetry regime. At the crossover between the two is the exceptional point, in general defined by

$$g_{\text{crit}} = \frac{|\gamma_1 - \gamma_2|}{4} \tag{4.57}$$

or, with the choice $\gamma_1 = -\gamma_2 = \gamma_0$, $g_{\text{crit}} = \gamma_0/2$. At the exceptional point, both the real and imaginary parts of $\omega_\pm$ coalesce – notably, this leads to a degeneracy with properties distinct from conventional degeneracies and advantageous for sensing applications [25].

4.5 Summary

Throughout this Chapter, we have used simple coupled oscillator models to survey a breadth of physical behavior of interest in quantum optics and nanophotonics. For completeness, Fig. 4.4 illustrates the regions of parameter space where these physical regimes can be realized. Not shown is ultrastrong and deep ultrastrong coupling, both achieved through realization of coupling strengths on the order of or exceeding the average system resonant frequency.

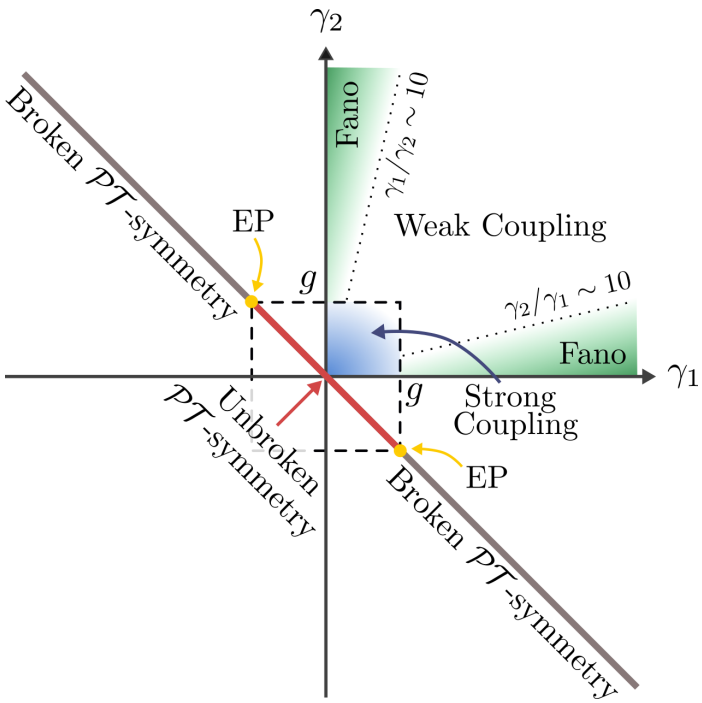

Figure 4.4: A survey of parameter space through the lens of coupled oscillators. This figure was inspired by a similar depiction of parameter space in Ref. [65]

.

Part II

FANO RESONANCES IN HYBRID LIGHT-MATTER AND ALL-PLASMONIC PLATFORMS

Part II of this dissertation includes the following publications verbatim:

- Chapter 5: ⋆Thakkar, N., ⋆Rea, M.T., ⋆**Smith, K. C.**, ⋆Heylman, K.D., Quillin, S.C., Knapper, K.A., Horak, E.H., Masiello, D.J., Goldsmith, R.H. Sculpting Fano resonances to control photonic-plasmonic hybridization. *Nano Letters* 17, 6927-6934. (2017). [105]

- Chapter 6: ⋆Pan, F., ⋆**Smith, K. C.**, Nguyen, H.L., Knapper, K.A., Masiello, D.J., Goldsmith, R.H. Elucidating Energy Pathways through Simultaneous Measurement of Absorption and Transmission in a Coupled Plasmonic–Photonic Cavity. *Nano Letters* 20, 50-58. (2019). [106]

- Chapter 7: **Smith, K. C.**, Olafsson, A., Hu, X., Quillin, S.C., Idrobo, J.C., Collette, R., Rack, P.D., Camden, J.P., Masiello, D.J. Direct Observation of Infrared Plasmonic Fano Antiresonances by a Nanoscale Electron Probe. *Physical Review Letters* 123, 177401. (2019). [107]

⋆ indicates co-first authorship

All three publications concern Fano resonances in experimentally realized nanophotonic platforms. In the first two, Fano resonances serve as a diagnostic tool for studying photonic-plasmonic mixing in a hybrid resonator composed of a gold nanorod deposited on the surface of a toroidal whispering-gallery mode resonator. Such platforms are advantageous for realizing large Purcell enhancements, as the mixed photonic-plasmonic modes of the composite structure can partially inherit both the large Q of the whispering-gallery modes and the nanoscale mode volume of the plasmonic nanoparticle. It must be noted that the second

paper builds upon the first – one consequence of this is that the theoretical modeling is much improved in the second publication and is consistent with the approach taken throughout this dissertation.

The third and final publication included in Part II details the first observation of Fano resonances in electron energy-loss spectroscopy of an all plasmonic system. This work is of broad experimental and theoretical interest, taking advantage of recent advances in monochromated scanning transmission electron microscopy and presenting theoretical generalizations to the Fano lineshape for quasi-discrete and quasi-continuum modes with complex coupling.

Finally, we remark that all three publications enclosed herein were carried out in close collaboration with experimentalists. All publications therefore include both theoretical and experimental contributions, both of which are included here for completeness. Supplementary information/material, while referenced in the text, is not included here and can instead be found with the journal posting online.

Chapter 5

SCULPTING FANO RESONANCES TO CONTROL PHOTONIC-PLASMONIC HYBRIDIZATION

Reprinted with permission from:

Niket Thakkar, Morgan T. Rea, Kevin C. Smith, Kevin D. Heylman, Steven C. Quillin, Kassandra A. Knapper, Erik H. Horak, David J. Masiello, and Randall H. Goldsmith. Sculpting Fano resonances to control photonic–plasmonic hybridization. *Nano Letters*, 17(11):6927–6934, October 2017.

Hybrid photonic-plasmonic systems have tremendous potential as versatile platforms for the study and control of nanoscale light-matter interactions since their respective components have either high quality factors or low mode volumes. Individual metallic nanoparticles deposited on optical microresonators provide an excellent example where ultrahigh-quality optical whispering-gallery modes can be combined with nanoscopic plasmonic mode volumes to maximize the system's photonic performance. Such optimization, however, is difficult in practice because of the inability to easily measure and tune critical system parameters. In this Chapter, we present a general and practical method to determine the coupling strength and tailor the degree of hybridization in composite optical microresonator-plasmonic nanoparticle systems based on experimentally measured absorption spectra. Specifically, we use thermal annealing to control the detuning between a metal nanoparticle's localized surface plasmon resonance and the whispering-gallery modes of an optical microresonator cavity. We demonstrate the ability to sculpt Fano resonance lineshapes in the absorption spectrum and infer system parameters critical to elucidating the underlying photonic-plasmonic hybridization. We show that including decoherence processes is necessary to capture the evolution of the lineshapes. As a result, thermal annealing allows us to directly tune the degree

of hybridization and various hybrid mode quantities such as the quality factor and mode volume and ultimately maximize the Purcell factor to be 10^4.

5.1 Introduction

Hybrid photonic-plasmonic nanosystems, where optical modes of a dielectric cavity couple to collective charge oscillations of a metal nanoparticle, are gaining broad research interest as platforms for maximizing light-matter interactions [108, 109, 110, 111, 112, 113, 114], enabling directional control of emission [115, 116], low-power nonlinear optics [117], versatile optical interconnects [118, 119, 120, 121, 122], and label-free single-molecule detection [123, 124, 125]. In particular, the Purcell factor [126], a measure of an optical cavity mode's ability to enhance the spontaneous decay of a nearby emitter, has been shown to dramatically increase in hybrid systems over uncoupled photonic and plasmonic components [127].

In his original work, Purcell showed that this enhancement is proportional to the mode's quality factor, Q, which describes its temporal decay rate and therefore its ability to localize light in time, and inversely proportional to the mode's volume, V, which describes the volume occupied by the mode's field and therefore its ability to localize light in space [126, 128]. Thus, hybrid photonic-plasmonic structures offer especially high Purcell enhancements due to their ability to combine a microphotonic cavity's unparalleled quality factor (over 10^8) [129, 130] with a plasmonic system's nanoscopic mode volume (down to $10^{-6}\lambda^3$) [131, 132].

This divide-and-conquer strategy, where individual components with high Q and low V are coupled to maximize near-field enhancement, has found considerable success in a variety of implementations [133, 127, 108, 112, 114, 123, 124, 134, 135]. Still, in most cases, there is little control over the resulting enhancement factor and the frequency at which maximum enhancement occurs, limiting the use of these hybrid cavities in applications. Moreover, while Q and V are straightforward to determine in isolated, noninteracting systems [136, 130, 137, 138], their determination in the hybridized case requires accurate estimation of the components' coupling strength, g, and resulting degree of hybridization, θ, both defined explicitly in the text below. Typically, this estimation is done via computationally expensive, multi-material, multi-scale, full-wave electrodynamics simulations [127, 139, 133]. A more versatile method to control and estimate components' coupling strength from experiment,

as well as accounting for the largely unexplored role of decoherence in hybrid systems, is needed before photonic-plasmonic cavities can be used on a wider-scale in nanophotonics applications.

In this Chapter, using a plasmonic, metal nanorod (NR) and a toroidal whispering-gallery mode (WGM) microresonator [129] (SI Section 1), where Fano resonances are diagnostic of photonic-plasmonic hybridization [140, 141], we report a general method for the experimental determination of g and control of θ, as well as downstream quantities such as the hybridized Q and V, from the system's absorption spectrum. Our method entails the sculpting of Fano resonances by controlled thermal annealing of the metal nanorod. We demonstrate that proper inclusion of both photonic and plasmonic loss channels and the consequent role of decoherence in determining the Fano lineshape is critical for accurate determination of the coupling strength. Finally, using an experiment-based approach, we show how the degree of hybridization can be optimized in practice to achieve Purcell enhancements on the order of 10^4, in agreement with purely simulation-based studies of similar systems [127].

5.2 Fano resonances in a hybrid photonic-plasmonic resonator

The hybridized system's absorption spectrum contains the required information needed to determine its photonic properties, and here we demonstrate this by mixing the dipolar localized surface plasmon (LSP) of an individual gold nanorod with the optical modes of a silica toroidal WGM microresonator. Since the plasmonic nanorods examined are non-luminescent, a means of performing single-particle absorption spectroscopy on non-luminescent targets is required to investigate the hybridization [142, 143, 144, 140, 145, 146]. As described previously [140], we use the microresonator as a single-particle, photothermal absorption spectrometer by monitoring via a coupled fiber the shift in a WGM that is detuned from the NR due to local heating from the laser excited NR. As the pump laser frequency is scanned, local heating by the NR varies in proportion to the particle's absorption cross section, resulting in observable shifts in the WGM transmission. Using a double-modulation scheme, this method offers both high sensitivity, allowing us to resolve shifts in the WGM resonance of less than 100 Hz, and high spectral resolution, with fine spectra acquired at a resolution of $\sim$5 μeV [140].

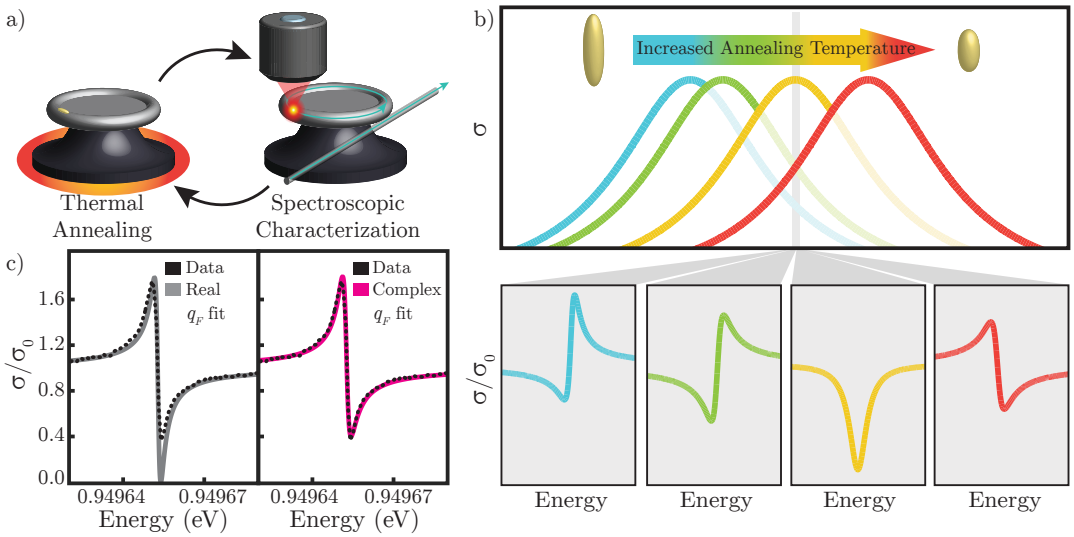

Figure 5.1: Fano resonances in a coupled toroidal WGM microresonator-plasmonic NR system. a) Spectroscopic characterization of the coupled system is alternated with thermal annealing of the NR; at each annealing temperature, a separate absorption spectrum is recorded. b) Increasing the thermal annealing temperature decreases the aspect ratio of the NR, increasing the plasmon resonance energy (top) and reshaping the Fano interference between a fixed WGM of the microresonator and the LSP (bottom). Note that NR aspect ratio changes are exaggerated to highlight the effects of thermal annealing. c) Fits to experimental data (black) using the Fano lineshape with a real q_F (grey dashed) cannot capture the incomplete destructive interference (vanishing absorption signal) while using the complex q_F in Eq. (5.8) (pink dashed) results in an excellent fit.

As shown in Fig. 5.1, characteristic Fano resonances appear in the NR absorption spectrum due to coherent interaction between the spectrally broad LSP and the spectrally narrow WGMs [140]. Each Fano resonance corresponds to a hybrid mode of the NR-microresonator cavity. Asymmetric lineshapes in the electron energy loss study of the auto-ionization of helium [147] were originally described by Fano, and have since been found in a variety of optical [141, 148, 149] and transport [150] experiments where interaction between a discrete state and a broad continuum results in characteristic, asymmetric spectral features. In the original work and since then, Fano resonances take the form

$$\frac{\sigma(\omega)}{\sigma_0(\omega)} = \left| \frac{q_F + \epsilon}{\epsilon + i} \right|^2 , \tag{5.1}$$

where in our case $\sigma(\omega)/\sigma_0(\omega)$ is the absorption spectrum of the composite system normalized to that of the isolated NR, $\sigma_0(\omega)$, and $\epsilon(\omega)$ is a dimensionless reduced frequency. q_F is the so-called Fano asymmetry parameter, which characterizes the degree of asymmetry in the resonance's lineshape as a function of detuning between a discrete state and the continuum [147, 141, 140] and determines the spectral location ($\epsilon(\omega) = -q_F$) where destructive interference between the discrete state and the continuum results in a total loss of absorption.

Because the shape of the Fano resonance is tied to the LSP resonance frequency [140], we can control the lineshape by reducing the initially high aspect ratio (1 : 10) of the gold nanorod to shift the plasmon resonance. To that end, the entire resonator chip is annealed on a hotplate (Fig. 5.1a) at ten distinct temperatures ranging from $140 - 175$ °C. Between annealing steps, the chip is allowed to cool to room temperature before measuring the corresponding absorption spectrum. At these annealing temperatures, NR melting causes a self-limiting, monotonic, and irreversible blueshift in the LSP resonance [151, 152, 153] while changes to the silica microresonator are negligible. Over the thermal range explored, the shifts in LSP resonance frequency suggest a softening in the aspect ratio from approximately (1 : 10) to (1 : 8) [154, 155]. This sculpting method was determined to be more controllable than other methods such as chemical etching [156, 157] and laser heating [158, 159, 160].

Spectroscopic characterization can then be cycled with thermal annealing steps. In Fig. 5.2a, low resolution spectra (where Fano resonances are not visible) taken at room temperature after heating the chip to the indicated temperature display a systematic blue

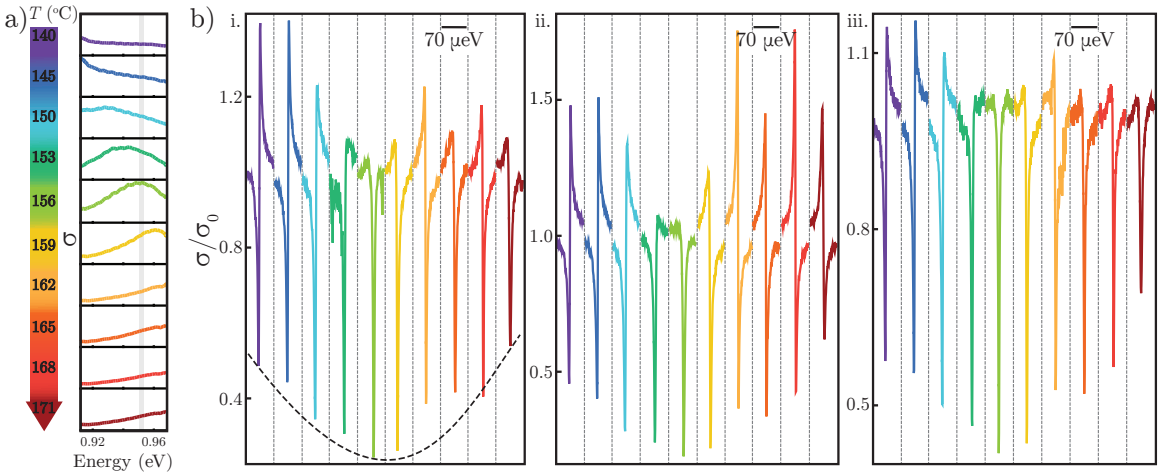

Figure 5.2: Sculpting Fano resonances by thermal annealing. a) Low resolution absorption spectra of a gold NR acquired at room temperature after annealing to the indicated temperature. b) Evolution of three Fano resonances located within the gray region pictured in a), with colors in b) representing the same temperatures as in a). Panels are centered at (i) 0.9496 eV, (ii) 0.9497 eV, and (iii) 0.9498 eV, and each panel is ∼80 μeV wide. Each panel within (i) tracks the same Fano resonance acquired at different annealing temperatures, thus each panel in (i) is of the same spectral region; the same is true for (ii) and (iii). The dashed line in (i) indicates the observed non-monotonic envelope of Fano resonance depths.

shift in the LSP absorption profile as expected; see Fig. 5.1b top. Repeated high resolution spectra of the same coupled WGM-LSP feature in a narrow spectral window (∼80 μeV) show that Fano resonances due to WGM-LSP interaction change shape as the LSP profile passes through the narrow window (Fig. 5.2b) with the expected shift in asymmetry [140], Fig. 5.1b bottom, easily apparent. Surprisingly, no Fano resonances exhibit total destructive interference between the WGM and LSP, behavior repeated across multiple Fano resonances for multiple WGMs and across multiple NRs (SI Section 6). Thus, the lineshape cannot be adequately fit by Eq. (5.1) because the equation predicts that the spectral line will always vanish at some point in the spectrum, Fig. 5.1c, left. Indeed, when repeatedly displaying a normalized resonance in the same spectral window while the LSP energy is shifted via thermal annealing, an envelope is seen defining the depth of the Fano resonance where the depth appears to be a non-monotonic function of the LSP energy. This experimental behavior challenges the canonical Fano interference mechanism and motivates development of a more comprehensive theory.

5.3 Theoretical modeling

Deformation of the Fano resonances as a function of LSP energy can be quantitatively understood by first considering the total electromagnetic field energy of the system [161],

$$H = \sum_{mn} \int \frac{dV}{8\pi} \left[\frac{\partial}{\partial \omega} (\omega \varepsilon(\mathbf{x}, \omega))_{\omega_m} \mathbf{E}_m \cdot \mathbf{E}_n + \mathbf{B}_m \cdot \mathbf{B}_n \right], \tag{5.2}$$

where $\varepsilon(\mathbf{x}, \omega)$ is the piecewise dielectric constant defined to be a free-electron gas in the NR [162], 1.44 for silica in the resonator, and 1 elsewhere, and the total electric and magnetic fields are composed of contributions from the dipolar LSP mode ($m, n = 0$) and the mutually orthogonal resonator modes ($m, n = 1, 2, ...$). Restricting to a single WGM for simplicity and including a driving force on the LSP, the equations of motion associated with H are (SI Section 2)

$$\begin{aligned} \ddot{p}_0 + \gamma_0 \dot{p}_0 + \omega_0^2 p_0 + g^2 \omega_0^2 p_1 &= \omega_0^2 \sqrt{V_0} E_{\text{ext}} e^{-i\omega t} \\ \ddot{p}_1 + \gamma_1 \dot{p}_1 + \omega_1^2 p_1 + g^2 \omega_1^2 p_0 &= 0, \end{aligned} \tag{5.3}$$

where only electric field mediated LSP-WGM interaction is considered. Here, p_0 is the generalized momentum describing the LSP's electric field ($\mathbf{E}_0$), p_1 is the generalized momentum

of the WGM ($\mathbf{E}_1$), and the LSP is driven by a harmonically varying external source, E_{ext}, modeling the frequency ω pump laser polarized along the NR long axis (Fig. 5.1a). Both modes have associated frequencies, ω_0 or ω_1, and mode volumes, V_0 or V_1. Furthermore, via the cross terms in Eq. (5.2), they exchange energy through coupling characterized by g, a dimensionless constant defined by

$$g^2 p_0 p_1 = \int \frac{dV}{8\pi} \Bigg[\frac{\partial}{\partial \omega} \left(\omega \varepsilon(\omega, \mathbf{x})\right)_{\omega_0} \mathbf{E}_0(\mathbf{x}) \cdot \mathbf{E}_1(\mathbf{x}) + \frac{\partial}{\partial \omega} \left(\omega \varepsilon(\omega, \mathbf{x})\right)_{\omega_1} \mathbf{E}_1(\mathbf{x}) \cdot \mathbf{E}_0(\mathbf{x}) \Bigg], \tag{5.4}$$

where $\mathbf{E}_0(\mathbf{x}) \cdot \mathbf{E}_1(\mathbf{x}) = \mathbf{E}_1(\mathbf{x}) \cdot \mathbf{E}_0(\mathbf{x})$ depends on the spatial overlap of the modes' fields and therefore on the NR's location and orientation on the microresonator surface (SI Section 2). As will be shown below, LSP and WGM losses are critical to describe the observed Fano interferences. Thus, we further model LSP and WGM losses with damping rates characterized by γ_0 and γ_1 added to the equations of motion.

It is instructive to first consider the frictionless limit (i.e., $\gamma_0 = \gamma_1 = 0$). In that case, Eq. (5.3) can be solved exactly through a coordinate rotation (SI Section 3), defining a set of noninteracting normal modes, $p_\pm$, related to the original p_0 and p_1 by a rotation angle

$$\theta = \frac{1}{2} \tan^{-1} \left(\frac{2g^2 \omega_0 \omega_1}{\omega_0^2 - \omega_1^2} \right), \tag{5.5}$$

which describes the degree of hybridization between the LSP and WGM modes. As expected, θ depends on both the LSP-WGM coupling g and detuning, $\omega_1 - \omega_0$. In the weak coupling limit ($g^2 \omega_0 \omega_1 / (\omega_0^2 - \omega_1^2) \ll 1$), $\theta = 0$ and no hybridization occurs, while in the strong coupling limit ($g^2 \omega_0 \omega_1 / (\omega_0^2 - \omega_1^2) \gg 1$), $\theta = \pi/4$ and the normal modes are maximally mixed. θ, therefore, can be controlled via thermal annealing which will influence the detuning. In the more general case with losses ($\gamma_0 \neq 0, \gamma_1 \neq 0$), θ is not an exact degree of hybridization but can be used as a qualitative indicator of hybridization (SI Section 4). We find that our annealing process does not significantly modify the overlap of fields, which is proportional to g, but does alter the detuning between modes by shifting ω_0 (SI Section 7). Thus, thermal annealing allows us to optimize and understand the degree of hybridization for a given NR location and orientation on the resonator while keeping g constant.

The absorption cross section can be calculated with losses (friction) using standard methods to solve Eq. (5.3), giving the exact expression (SI Section 5)

$$\frac{\sigma(\omega)}{\sigma_0(\omega)} = \left|\frac{q_F+\epsilon}{\epsilon+i}\right|^2 + \left|\frac{q_F-i}{\epsilon+i}\right|^2 \frac{\mathrm{Im}\, q_F}{1-\mathrm{Im}\, q_F}, \tag{5.6}$$

where $\sigma_0(\omega) = (4\pi\omega\omega_0^2 V_0/c)\mathrm{Im}\, Z_0^{-1}$ is the uncoupled LSP absorption cross section with $Z_0 = \omega_0^2 - \omega^2 - i\omega\gamma_0$ and the second term characterizes a modification to the Fano profile (Eq. (5.1)) which vanishes when the WGM is frictionless as $\mathrm{Im}\, q_F/(1-\mathrm{Im}\, q_F) = \gamma_1/\Gamma$. The spectral location and width of the Fano resonance, here denoted by Ω and Γ, respectively, are defined by

$$\begin{aligned} \Omega^2 &= \omega_1^2 - g_1^4\omega_0^2\omega_1^2 \mathrm{Re}\, Z_0^{-1} \\ \omega\Gamma &= \omega\gamma_1 + g_1^4\omega_0^2\omega_1^2 \mathrm{Im}\, Z_0^{-1}, \end{aligned} \tag{5.7}$$

both in general functions of ω but approximately constant in the weak coupling limit applicable here (SI Section 5). $\epsilon(\omega) = (\omega^2 - \Omega^2)/\omega\Gamma$ is again a dimensionless reduced pump frequency in units of the Fano resonance line width away from resonance location and

$$q_F(\omega) = \frac{\Omega^2 - \omega_1^2}{\omega\Gamma} + i\frac{\gamma_1}{\Gamma}, \tag{5.8}$$

is the now complex-valued Fano asymmetry parameter [141]. Its real part characterizes shift in WGM frequency due to coupling with the LSP and its imaginary part describes the fraction of the total Fano resonance line width attributed to WGM losses. In the limit where $\gamma_1 \to 0$ and the WGM has $Q \to \infty$, $\mathrm{Im}\, q_F \to 0$ and the well-known purely real-valued Fano profile expression, Eq. (5.1), is recovered in Eq. (5.6). In that case, $q_F \approx 2(\omega_1 - \omega_0)/\gamma_0$, qualitatively explaining the observed shape change in Fig. 5.2 as ω_0, and the resulting degree of mixing, θ, are modified by thermal annealing. However, in this limit, the composite system absorption drops to zero when $\epsilon(\omega) = -q_F$ implying $\omega = \omega_1$, on resonance with the WGM, in stark disagreement with experiment. In contrast, use of a complex-valued q_F, arising from the inclusion of loss in both WGM and LSP channels, enables excellent fitting of the Fano features including the incomplete destructive interference as shown in Fig. 5.1c. More generally, since the zero that appears in the original Fano expression is due to complete destructive interference between WGM and LSP, any process that degrades

the phase relationship associated with the WGM and LSP oscillators would then manifest itself as a recovery of the vanishing spectral feature. Complex-valued q_F have also appeared in models of molecular and mesoscopic transport [163, 164, 150] and in strongly coupled plasmonic systems [165, 166, 167, 168]. While this formalism has general applicability to other phenomena, this is the first time that it has been applied in hybrid photonic-plasmonic systems.

In analogy with the Redfield equation governing the spectroscopy of a two-level system coupled to an environment, decoherence can derive from population relaxation (T_1), where energy is transferred from one level to another, or from pure dephasing ($T_2{}^*$), where phase degrades without transition between states due entirely to fluctuations of the environment [169]. Our treatment connects the complex Fano resonance with relaxation in both the photonic and plasmonic channels without the need to include pure dephasing. Much as population relaxation and pure dephasing can both contribute to homogenous linewidths, both processes can also be thought of as mechanisms of breaking time-reversal symmetry, which has previously been associated with complex Fano parameters [141]. Indeed, transport measurements have connected complex q_F to pure dephasing by demonstrating sharp reductions of pure dephasing at low temperatures leading to recoveries of destructive interference [150].

In many past studies [140, 141], including Fano's original work, spectral resolution limitations also contributed to the Fano profile's shape and prevented a total loss of signal when $\epsilon(\omega) = -q_F$. As a result, statistical analysis of spectra could be done with real-valued q_F but required additional scaling and offset parameters to accurately model measurements. Here, however, spectral resolution can not explain the systematic envelope in peak depths, Fig. 5.2b (dotted black line). In fact, we see that the Fano profiles are better modeled by complex q_F shapes even as the spectral resolution is increased (SI Section 6), indicating that the finite WGM Q factor plays a crucial role in determining the Fano lineshape. Thus, as we show in detail below, Eq. (5.6) is an important generalization of Fano's original work that is amenable to statistical analysis without scaling and offset parameters.

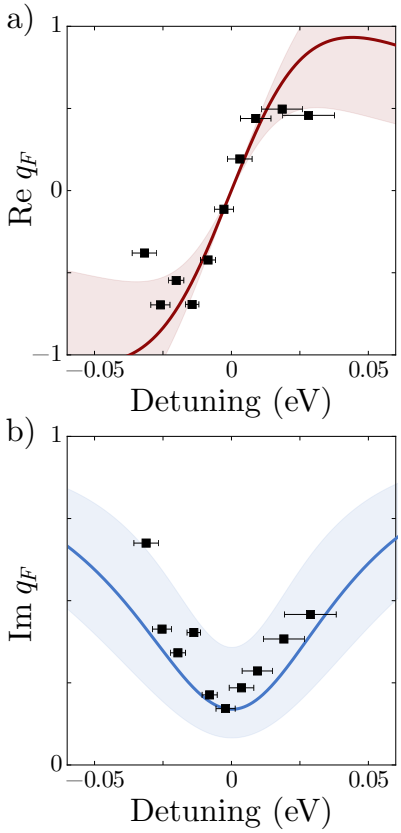

Figure 5.3: The (a) real and (b) imaginary parts of the Fano asymmetry parameter q_F as a function of the detuning, $\omega_1 - \omega_0$, for a single Fano resonance. Using ω_1, γ_0, γ_1 and g as free parameters, experimentally measured Fano resonances are fit to Eq. (5.6) and q_F is computed using Eq. (5.8) (black squares). Theoretical predictions (red and blue lines) are generated using Eq. (5.6) in conjunction with the fit to the Fano lineshape at a single intermediate temperature, here chosen to be 156 °C where the WGM and LSP modes are nearly degenerate ($\omega_1 \approx \omega_0$). Uncertainties in these predictions, which are here shown as one standard deviation intervals (shaded regions), are computed by randomly sampling ω_1, γ_0, γ_1 and g from a normal distribution whose width is determined from uncertainties in the fit parameters. Horizontal error bars are determined from the uncertainty in ω_0 at each temperature (SI Section 7).

5.4 Thermal evolution of the complex asymmetry parameter

We can use our new theory to predict the evolution of the Fano profile throughout the thermal Fano sculpting process. Statistical fitting to the data is done in two steps (SI Section 7). First, low resolution spectra, Fig. 5.2a, are fit to $\sigma_0(\omega)$ to determine ω_0 at each annealing temperature. While these spectra are measured for the composite microresonator-NR system, the resolution is low enough such that only the broad Lorentzian envelope due to the plasmon resonance, and not the spectrally narrow Fano resonances, can be resolved. Next, we fit individual Fano resonances, experimentally measured via high resolution spectra, to Eq. (5.6) with ω_1, γ_0, γ_1 and g as fit parameters, allowing us to use Eq. (5.8) to determine the measured dependence of q_F upon ω_0.

Comparison of the measured (black dots) and predicted (solid curve) evolution of the Fano profile's shape is illustrated for a single Fano resonance in Fig. 5.3. Here, fit results from a single Fano resonance at an intermediate temperature ($T_{\text{anneal}} = 156$ °C) are used to specify the LSP and WGM parameters and their coupling, g. Then, Eq. (5.8) is used to extrapolate and predict the Fano profile's shape for higher and lower LSP energy assuming the annealing process has no effect on the other parameters. Figures 5.3a and b show that the measured evolution (black dots) for the real and imaginary parts of q_F agree well with the model's prediction (red and blue curves). This agreement tells us that the dominant effect of thermal annealing is to shift the LSP energy with little effect on the LSP-WGM field overlap, g. Comparisons to other Fano profile's evolutions yield similar agreement (SI Section 7).

A broader comparison of the model and data is carried out by calculating the distribution of all experimentally observed complex q_F given parameters from the experiment. This test is done for the real and imaginary parts of q_F in Fig. 5.4, which shows the results from fits to 225 Fano resonances across three different NR-microresonator systems (red, blue and green squares). Evolution is plotted as a function of detuning between ω_1 and ω_0, and in both cases the data displays a definitive trend. Theoretical distributions of q_F are calculated by taking $\hbar\gamma_0$ to be the average value from the data, and calculating q_F for randomly sampled WGM parameters and coupling. Resulting distributions are plotted as an average value

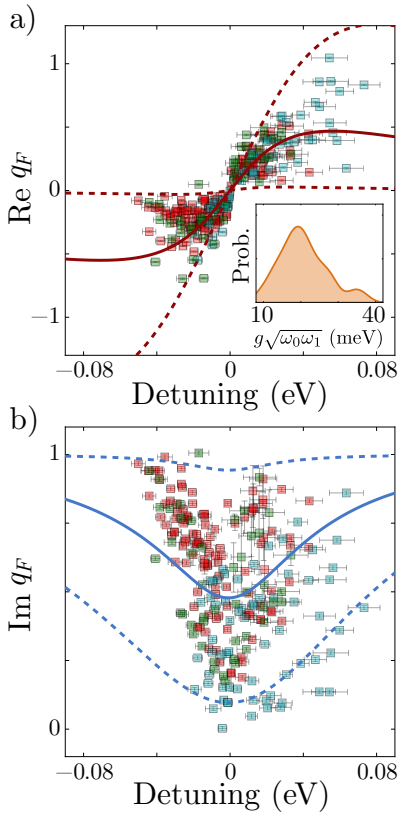

Figure 5.4: The (a) real and (b) imaginary parts of the Fano asymmetry parameter q_F as a function of WGM-LSP detuning, $\omega_1 - \omega_0$, for a collection of 225 Fano lineshapes. Results from statistical fitting to Eq. (5.6) are shown for three separate NR-microresonator systems (red, blue, and green squares). Blue squares correspond to a NR with a smaller relative unannealed LSP resonance frequency and thus represent data at higher detuning relative to red and green squares. Theoretical distributions of both the real and imaginary parts of q_F are determined from Eq. (5.8) using $\hbar\gamma_0 = 56.8$ meV, the average value from the data, along with randomly sampled WGM parameters and couplings. More specifically, ω_1 is sampled from a uniform distribution on the spectral range, γ_1 is sampled randomly from the fit results, and g is sampled from the estimated distribution of the couplings from the fit results (inset). (caption continued on following page)

Figure 5.4: (continued) This sampling process models the random location and orientation of the NR on the toroid surface and allows us to calculate 10^4 randomly generated Fano resonances to determine the theoretical distribution of real and imaginary q_F as a function of detuning. We show both the average (solid line) as well as 95% confidence intervals (dashed lines) of the resulting distributions.

(solid line) and 95% confidence interval (dashed lines) in both panels a and b. We see that for both the real and imaginary parts the model captures the observed behavior under the assumption that all parameters but ω_0 are constant throughout the annealing process.

The excellent agreement between theory and observation in Figs. 5.3 and 5.4 indicates that estimates of the LSP-WGM interaction energy based on our fit procedure are accurate, and indeed, our average coupling energy based on 225 Fano resonances is 22.0 meV, in the same range as other studies of hybridized photonic-plasmonic systems [140, 170, 127]. For a particular Fano resonance, statistical fitting to determine the coupling energy allows us to calculate a variety of important hybrid mode properties. Given the LSP energy and line width, the WGM energy and line width, and g, the parameters on the left-hand-side of Eqs. 5.3 are fully specified. This system can then be rewritten as a set of coupled, first-order differential equations and the corresponding coefficient matrix, $\mathbf{A}$, can be diagonalized to specify the quasi-hybrid modes (QHMs) of the NR-microresonator system (SI Section 4). The QHMs, hybrid modes which incorporate losses and therefore have complex eigenvalues [137, 171, 172], can then be used to calculate the hybrid mode fields, mode volumes, Purcell factors, and other properties.

We calculate the Purcell factor as an example of this procedure. LSP-WGM coupling produces two QHMs, one WGM dominated and the other LSP dominated. In both cases, the QHM electric field is a linear combination of LSP and WGM fields, $\mathbf{E}_{\mathrm{QHM}} = c_0\mathbf{E}_0 + c_1\mathbf{E}_1$, with c_0 and c_1 extracted from the eigenvectors of $\mathbf{A}$. The QHM mode volume [171] is then

$$V_{\mathrm{QHM}} = \frac{\int dV \frac{\partial}{\partial\omega}\left(\omega\varepsilon(\omega,\mathbf{x})\right)_{\omega_{\mathrm{QHM}}} |\mathbf{E}_{\mathrm{QHM}}(\mathbf{x})|^2}{\max\left\{\frac{\partial}{\partial\omega}\left(\omega\varepsilon(\omega,\mathbf{x})\right)_{\omega_{\mathrm{QHM}}} |\mathbf{E}_{\mathrm{QHM}}(\mathbf{x})|^2\right\}}, \tag{5.9}$$

where ω_{QHM} is determined from the eigenvalue associated with the set of c_0 and c_1 for each

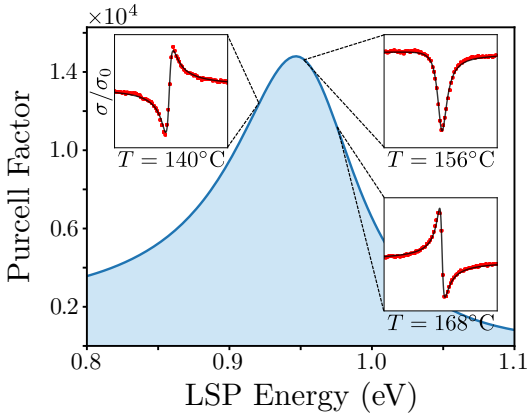

Figure 5.5: The Purcell factor for one photonic-plasmonic QHM is displayed as a function of a microresonator WGM coupled to the LSP of an individual gold NR. Statistical fitting to the Fano resonance in Fig. 5.3 at low annealing temperatures is used to determine the coupling of the nanorod to the WGM and predict the mode volume, quality factor, and Purcell factor of the hybridized system. The mode volume, determined by Eq. (5.9), is minimized when the LSP energy is degenerate with the WGM at $\omega_0 = \omega_1 = 0.9544$ eV. This minimum in the mode volume corresponds to a maximum value exceeding 10^4 for the Purcell factor of the QHM. The insets show the change in the Fano lineshape as the LSP energy moves from below the WGM ($\omega_0 < \omega_1$), to degenerate with the WGM ($\omega_0 = \omega_1$), to above the WGM ($\omega_0 > \omega_1$).

hybridized mode. Expansion of $|\mathbf{E}_{\mathrm{QHM}}|^2$ results in three terms proportional to V_0, V_1, and the overlap of $\mathbf{E}_0 = -p_0\mathbf{f}_0$ and $\mathbf{E}_1 = -p_1\mathbf{f}_1$, where $\mathbf{f}_0$ and $\mathbf{f}_1$ are the mode functions of the nanorod and toroid as dictated by the Helmholtz equation (SI Section 2). Both V_0 and V_1 can be determined through experiment [136, 139] or simple, single-material, single-scale electrodynamics simulations, circumventing the need for computationally intensive multi-scale methods. Meanwhile, the overlap term can be rewritten in terms of the statistically inferred coupling, g, as expressed in Eq. (5.4). Finally, the Purcell factor, F, can be calculated using V_{QHM}:

$$F = \frac{3}{4\pi^2}\left(\frac{\lambda_{\mathrm{QHM}}}{n}\right)^3 \mathrm{Re}\left\{\frac{Q_{\mathrm{QHM}}}{V_{\mathrm{QHM}}}\right\}, \tag{5.10}$$

where λ_{QHM} is the wavelength associated with ω_{QHM}, $n = 1$ is the refractive index at the location of the emitter proximal to the hybridized cavity (assumed to lie in the junction between the WGM resonator and the NR), and $Q_{\mathrm{QHM}} = \omega_{\mathrm{QHM}}/2\gamma_{\mathrm{QHM}}$ is the QHM quality factor, also determined from the eigenvalue associated with c_0 and c_1 (SI Section 8).

We can use this method to estimate the Purcell factor as a function of LSP energy throughout the Fano sculpting process. This process is shown in Fig. 5.5 for the Fano resonance in Fig. 5.3. We see that the Purcell factor is maximized when $\omega_0 = \omega_1$, where the Fano lineshape is symmetric (inset) while asymmetry in the Fano resonance indicates LSP-WGM hybridization is sub-optimal. Due to the high density of WGM resonances supported by the resonator, the frequency at which this maximum occurs can be altered through selection of a different Fano resonance, thus allowing control over the spectral location of the maximum Purcell enhancement. Our maximum Purcell factor for the resonance shown is $\sim 10^4$ with $V_{\mathrm{QHM}} \sim 10^9$ nm^3 and $Q_{\mathrm{QHM}} \sim 10^4$, in agreement with other estimates based on full-wave, multi-scale simulation of this system [127] and estimates of similar systems [171]. Notably, our estimate of the coupling is inferred from an experimental spectrum.

5.5 Conclusion

Using thermal annealing we have experimentally demonstrated how to sculpt the Fano resonances and control the degree of hybridization in a photonic-plasmonic system composed of a coupled WGM microresonator cavity and a plasmonic NR. Guided by analytical modeling,

we find that decoherence from losses from both the WGM and LSP degrees of freedom are needed to capture the lineshape of the Fano resonance, generalizing the Fano asymmetry parameter to be complex-valued. Further statistical treatment enables the prediction of the Fano lineshape as a function of the experimentally controlled detuning between LSP and WGM resonances, in excellent agreement with experimental data. Taken together, our combined experimental, analytic, and statistical approach allows for extraction of critical optical parameters from experimental data, yielding new insights into the fundamental properties of hybridized photonic-plasmonic systems and enabling maximization of the light-matter interaction.

Chapter 6

ELUCIDATING ENERGY PATHWAYS THROUGH SIMULTANEOUS MEASUREMENT OF ABSORPTION AND TRANSMISSION IN A COUPLED PLASMONIC-PHOTONIC CAVITY

Reprinted with permission from:

Feng Pan, Kevin C. Smith, Hoang L. Nguyen, Kassandra A. Knapper, David J. Masiello, and Randall H. Goldsmith. Elucidating energy pathways through simultaneous measurement of absorption and transmission in a coupled plasmonic–photonic cavity. *Nano Letters*, 20(1):50-58, August 2019.

Control of light-matter interactions is central to numerous advances in quantum communication, information, and sensing. The relative ease with which interactions can be tailored in coupled plasmonic-photonic systems makes them ideal candidates for investigation. To exert control over the interaction between photons and plasmons, it is essential to identify the underlying energy pathways which influence the system's dynamics and determine the critical system parameters, such as the coupling strength and dissipation rates. However, in coupled systems which dissipate energy through multiple competing pathways, simultaneously resolving all parameters from a single experiment is challenging as typical observables such as absorption and scattering each probe only a particular path. In this work, we simultaneously measure both photothermal absorption and two-sided optical transmission in a coupled plasmonic-photonic resonator consisting of plasmonic gold nanorods deposited on a toroidal whispering-gallery-mode optical microresonator. We then present an analytical model which predicts and explains the distinct line shapes observed and quantifies the contribution of each system parameter. By combining this model with experiment, we extract all system parameters with a dynamic range spanning 9 orders of magnitude. Our combined approach provides a full description of plasmonic-photonic energy dynamics in a weakly

coupled optical system, a necessary step for future applications that rely on tunability of dissipation and coupling.

6.1 Introduction

In 1946 Purcell theoretically demonstrated that the spontaneous emission rate of an emitter can be enhanced by its dielectric environment [15], prompting the birth of what is now known as cavity quantum electrodynamics (cQED). Following this discovery and its subsequent experimental confirmation [81], cQED has remained an active area of both theoretical and experimental research and has found application in a variety of fields such as quantum communication and information [173, 174, 175, 176, 177, 178, 179], sensing [180, 181, 90, 92], and cavity-controlled chemistry [27, 28, 29, 182, 30, 26, 183, 31]. The development of cQED is intertwined with developments in nanoscience and nanofabrication. In particular, recent years have seen a boom in cQED experiments due to the emergence of sophisticated techniques for fabrication of high-quality-factor, chip-scale optical microcavities [85], and deterministic positioning of "artificial atoms" such as quantum dots and plasmonic nanoparticles on optical microcavities [184, 185, 50, 186, 187].

Whispering-gallery-mode (WGM) microcavities are especially attractive due to the attainable ultrahigh quality factor (up to 10^8) [85, 188] of their optical modes which can allow for Purcell factors as large as 190 [189]. In recent work, it has been predicted that this factor may be improved even further by coupling the cavity modes to the localized surface plasmon (LSP) of a metal nanoparticle, effectively creating a hybrid plasmonic-photonic resonator which inherits the ultrasmall mode volume of the LSP while retaining the large quality factor of the WGMs [105, 190, 191, 192, 193, 194, 195]. In order to both understand and leverage the light-matter interactions in such a system, it is imperative to accurately determine the multiple intrinsic damping rates, the LSP-WGM coupling strength, and additional extrinsic dissipation rates introduced through the measurement. However, these quantities can span many orders of magnitude, particularly in weakly coupled systems, making it difficult for a single experiment to capture all of the information.

Many methods have been used to probe light-matter interactions in cavity-matter systems, including far-field detection of emitted or reflected photons [185, 196, 49, 197, 198,

199, 200, 201, 202], measurement of transmitted/reflected photons in a waveguide coupled to the system [184, 203, 204, 205, 206] and single-particle absorption measurements [105, 207]. Specifically, photoluminescence or scattering measurements collect radiated energy in the far field, transmission/reflection measurements using a waveguide detects energy transferred from the WGM to the tapered fiber, and absorption measurements probe nonradiative dissipation. While these techniques are individually capable of revealing spectral signatures of the underlying light-matter interaction, each serves as a readout for only a particular dissipative pathway and cannot simultaneously resolve all parameters that govern energy flow within the system. For example, nonradiative and radiative damping rates can be inferred from absorption and scattering spectra, respectively, whereas a fiber-based one-sided transmission experiment inherently depends upon the rate of energy exchange between an optically pumped waveguide and the cavity to which it is coupled. Crucially, the line width of any spectral feature contains information about the total dissipation rate of the system but does not distinguish between the various dissipative pathways regardless of the observable. Thus, simultaneous measurement of multiple spectroscopic observ- ables is needed for one to understand how energy is both distributed and dissipated via multiple pathways in a coupled cavity-matter system.

In this work, we demonstrate the ability to simultaneously measure both photothermal absorption and optical transmission in a coupled plasmonic-photonic cavity consisting of plasmonic gold nanorods (AuNRs) deposited on a silica toroidal WGM microresonator [85]. Specifically, the transmission is measured in a two-sided manner [78], where energy is input through a free-space pump laser and output through a fiber to which the LSP-WGM system is coupled. In contrast to previous studies on single AuNRs or quantum dots which have relied on measurements of scattering or photoluminescence, we measure photothermal absorption and two-sided transmission using a single photonic waveguide, where an individual AuNR is optically pumped by a frequency-tunable free-space laser. AuNRs of a high aspect ratio (10:1) are used so that the longitudinal dipolar LSP is efficiently excited by our tunable, narrow-line-width near-infrared free-space pump laser. Taken together, absorption and transmission encode sufficient information about the individual damping rates and mutual coupling strength of the LSP and WGM such that all relevant system parameters (see Fig.

6.1) may be determined. Fig. 6.1 illustrates these system parameters as well as the complete set of observables that both determine and are defined by their specific values.

6.2 Absorption and two-sided transmission

As described previously [105, 207, 208], photothermal absorption spectroscopy is performed with separate pump and probe beams. As shown in the experimental scheme of Fig. 6.2, a narrow-band tunable probe laser coupled to a tapered optical fiber interrogates the microresonator WGMs via evanescent coupling. At the other end of the optical fiber is an avalanche photodiode (APD) to allow monitoring of probe beam transmission. The probe beam is phase-modulated at radio frequencies (RF) and locked to the WGM resonance via the Pound-Drever-Hall locking scheme [207]. Simultaneously, a pump beam is focused to a near diffraction-limited spot and overlapped with individual nanoparticles on the microresonator surface. The pump beam is amplitude-modulated at kilohertz frequencies to maximize the signal-to-noise ratio. This double modulation scheme is capable of resolving resonance shifts down to under one attometer [207]. The amount of resonance shift is then used to compute the power absorbed by the AuNRs with the aid of a FDTD (COMSOL) simulation of the steady-state temperature increase within the microresonator [207]. The pump laser is raster-scanned over the microresonator to search for single AuNRs sparsely deposited on the resonator. Once located, an absorption spectrum is obtained by wavelength-scanning the tunable continuous-wave pump laser polarized along the long axis of the AuNR. High-resolution photothermal absorption spectra show distinctive sharp Fano antiresonance line shapes (shown schematically as σ_{abs} in Fig. 6.1), indicative of mutual interaction between photonic and plasmonic modes [105, 207, 88].

Concurrent with photothermal absorption, we now measure the two-sided transmission (σ_{T} in Fig. 6.1), that is, the power transmitted from the free-space pump laser through the plasmonic-photonic system and into the same tapered fiber used for the above photothermal measurement. In order to implement the simultaneous measurement of photothermal absorption and two-sided transmission, we first relied on the use of an electrical signal diplexer in an electrical separation scheme that can discriminate RF signal from much slower oscillatory signal (kHz to DC, hereafter called DC), as shown in Fig. 6.2. Both signals are

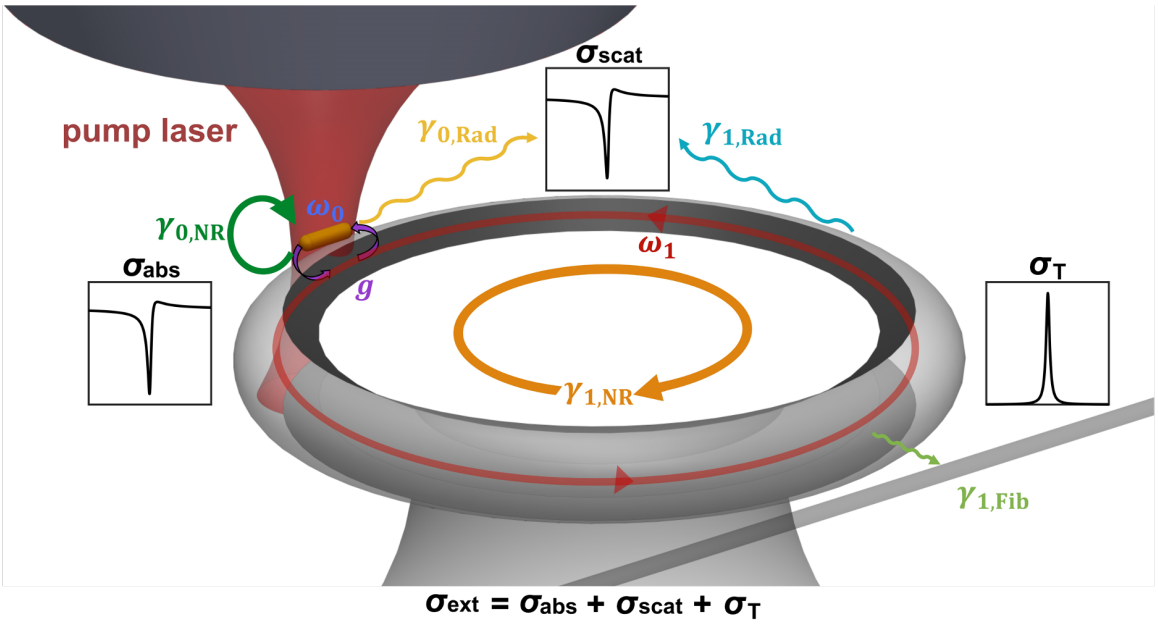

Figure 6.1: Schematic of dissipative coupled AuNR-microresonator system with all parameters (ω_0, $\gamma_{0,\mathrm{NR}}$, $\gamma_{0,\mathrm{Rad}}$, g, ω_1, $\gamma_{1,\mathrm{NR}}$, $\gamma_{1,\mathrm{Rad}}$, $\gamma_{0,\mathrm{Fib}}$) as well as experimental observables (inset spectra). Energy enters the coupled system via pump laser excitation of the dipolar LSP of the AuNR and is dissipated through various pathways. Once excited, the LSP decays through both radiative ($\gamma_{0,\mathrm{Rad}}$) and nonradiative ($\gamma_{0,\mathrm{NR}}$) means, and in addition may exchange energy with the microresonator via LSP-WGM coupling (g). The WGM likewise may exchange energy with the LSP or decay via outcoupling to the waveguide ($\gamma_{1,\mathrm{Fib}}$) in addition to radiative ($\gamma_{1,\mathrm{Rad}}$) and nonradiative ($\gamma_{1,\mathrm{NR}}$) dissipation channels. The conservation of energy through these various pathways in the steady state is reflected by the equality between the extinction cross- section (σ_{ext}), which is a measure of the rate at which energy enters the system, and the sum of the absorption (σ_{abs}), scattering (σ_{scat}), and transmission (σ_{T}) cross sections (inset equation), each of which probes a particular dissipative pathway.

generated by the APD detector. As above, the photothermal absorption signal is decoded from pump-induced phase shifts in the RF signal through both the local oscillator used for phase-modulation of the probe beam and a lock-in amplifier. At the same time, the DC signal is directly connected to a second lock-in amplifier for measurement of the kHz-modulated two-sided transmission. This strategy relies on the fact that while the photothermal and two-sided transmission signals are both modulated via the pump beam's (kHz) modulation, only the photothermal signal is additionally modulated at RF frequencies. However, high-resolution spectra collected over several spectral ranges show that signal measured through the DC channel (Fig. 6.3a, middle) closely follows the asymmetric Fano line shapes measured through the RF channel (Fig. 6.3a, top). In addition, low-resolution spectra measured through the two channels both show broad spectral signatures of the LSP (see Figure S2). The similar spectral line shapes in absorption and transmission (Fig. 6.3a, top and middle) can be understood by examining the resonance shift induced by photothermal response of the microresonator, shown in Fig. 6.3b. The DC channel measures the amplitude difference (labeled with $T_{\text{Electrical}}$) in the vertical direction which is proportional to the WGM resonance shift (labeled with A) in the horizontal direction due to photothermal effect, and therefore, the DC signal provides a scaled replica of the photothermal absorption spectrum. Thus, this scheme cannot discriminate the two-sided transmission from the photothermal signal.

In comparison, the simple optical separation scheme shown in Fig. 6.2 enables the distinction between photons transmitted through the coupled plasmonic-photonic cavity system from the pump beam ($\lambda = 1275-1355$ nm) and those photons originating in the probe beam ($\lambda = 1550 - 1570$ nm) and employed for photothermal spectroscopy. A combination of a wavelength division multiplexer (WDM), short-pass optical filter, and second photodetector (PDA) then allows for a simultaneous direct measurement of photons of different wavelengths traveling through the taper, revealing dramatically distinct spectral features, as shown in the bottom row of Fig. 6.3a. At each WGM energy position lies a resonant line shape that is conspicuously different from the Fano antiresonance seen in the absorption spectra. Measurements on different AuNRs and microresonators show these same phenomena (see Figure S1). Intermediate-resolution spectra over a full spectral range taken through the two chan-

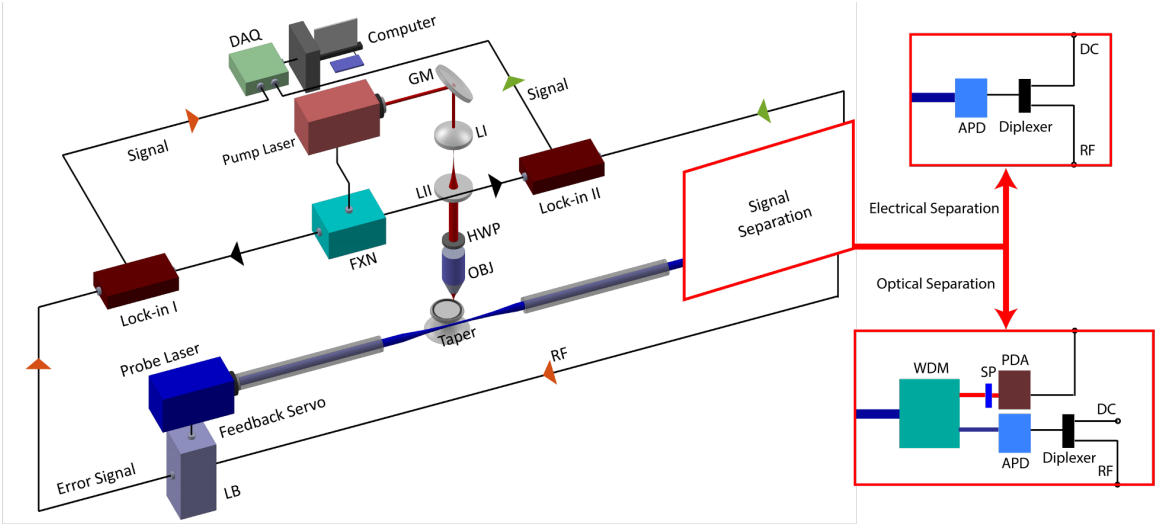

Figure 6.2: Experimental setup for simultaneous measurement of absorption and two-sided transmission. LI, lens I; LII, lens II; GM, galvo mirrors; FXN, function generator; Lock-in, lock-in amplifier; HWP, half-wave plate; OBJ, objective; LB, lock box; WDM, wavelength division multiplexer; SP, short-pass optical filter; PDA, adjustable-gain photodiode detector; APD, avalanche photodiode detector; DAQ, National Instruments LabView data acquisition card; RF, radio frequency electrical signal generated from APD; DC, kHz to DC electrical signal generated from APD. The red box indicates where either an electrical separation (top) or optical separation (bottom) is implemented. Arrows of different colors represent photothermal absorption (orange) and transmission (green) measurements or references (black).

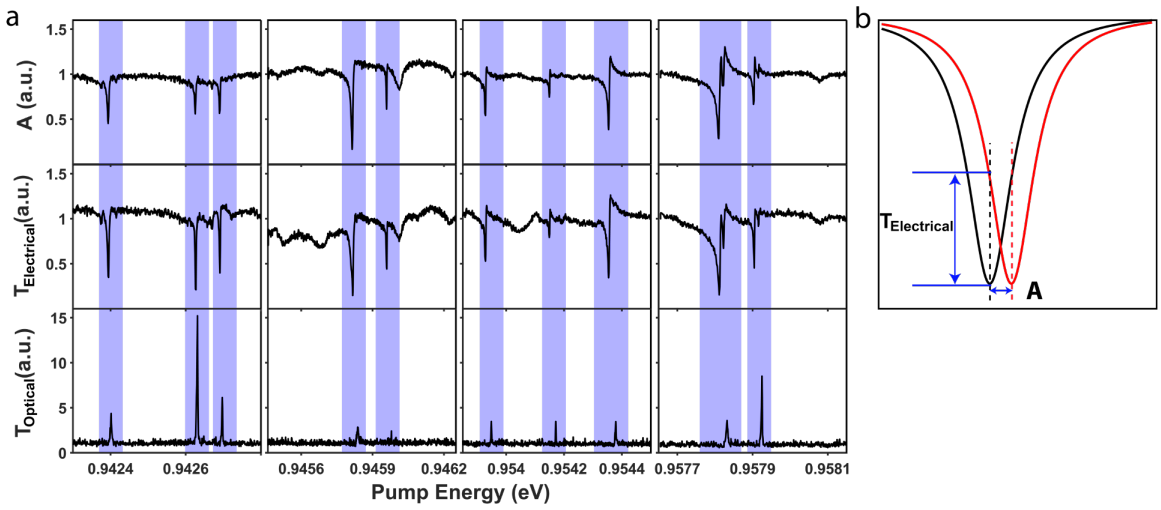

Figure 6.3: Simultaneous spectral measurements. (a) Photothermal absorption (A) measured through the RF channel from APD (top); transmission ($T_{\text{Electrical}}$) measured through DC channel from APD (middle); transmission (T_{Optical}) measured with the WDM included and detected via the PDA (bottom). Note that the resonance "teeth" of transmission (T_{Optical}) are not exactly lined up with other two observables. In this case, $T_{\text{Electrical}}$ and A were measured simultaneously, but T_{Optical} was measured later and the laser scanning actuator experienced minor motion hysteresis. (b) Schematic illustration of how photothermal and transmission measurements are conveyed through RF and DC channels when the pump laser induces a resonance shift.

nels also show distinct spectral features where the spectrally broad LSP resonance measured via photothermal absorption is replaced by a series of resonance "teeth" in the two-sided transmission spectra (see Figure S3). These distinct spectral behaviors are also robust over a range of pump laser modulation frequencies (Figure S4). The two-sided transmission signal is highly dependent on taper position relative to the microresonator with certain positions rendering some WGMs inaccessible while other modes are viable channels for outcoupling photons to the taper (see Figures S8 and S12), as expected [209]. Taken together, adding a WDM-filtered detection channel enables one to realize the simultaneous measurement of absorption and two-sided transmission for a coupled LSP-WGM system using a single optical waveguide.

6.3 Theoretical modeling

The spectral features exposed by simultaneous absorption and transmission measurements can be well-understood through mathematical modeling of the various energy pathways available to the coupled LSP-WGM system. To that effect, we develop a coupled oscillator model which includes physically independent system parameters relevant to each dissipative process and, as will be shown, each spectral observable. Although this model is derived from first-principles (SI), simplifications informed by experimental results are made. For example, the distinct line shapes in transmission spectra indicate that the tapered fiber does not simply play a passive role in the interrogation of the coupled LSP-WGM system. Instead, the propagating modes of the tapered fiber are coupled to the WGMs of the microresonator through the mutual overlap of their evanescent fields. Because this coupling is weak, it manifests itself in the LSP-WGM dynamics as a taper-induced loss mechanism and the dynamics of the fiber modes need not be explicitly considered. In addition, quantum fluctuations, while typically included in input-output theory as a manifestation of the fluctuation-dissipation theorem [78], are ignored here as all excitations are in the many-quanta limit where classical effects dominate. Lastly, only a single WGM need be considered because the modes of the toroid are mutually orthogonal and therefore do not interact directly. Taking all of these considerations into account, the equations of motion for the LSP-WGM system may

be written as

$$\begin{aligned} m\ddot{x} + m\gamma_{0,\mathrm{NR}}\dot{x} + m\omega_0^2 x + g\sqrt{\frac{m}{V}}\dot{q} &= \frac{2e^2}{3c^3}\dddot{x} + eE_{\mathrm{ext}}e^{-i\omega t} \\ \frac{1}{V}\ddot{q} + \frac{1}{V}(\gamma_{1,\mathrm{NR}} + \gamma_{1,\mathrm{Rad}} + \gamma_{1,\mathrm{Fib}})\dot{q} + \frac{1}{V}\omega_1^2 q - g\sqrt{\frac{m}{V}}\dot{x} &= 0, \end{aligned} \tag{6.1}$$

where x and m are the oscillator amplitude and effective mass of the dipolar LSP along the AuNR's long axis, c is the speed of light, $E_{\mathrm{ext}}e^{-i\omega t}$ is the field of the pump laser incident on the AuNR, and the radiation reaction force (proportional to $\dddot{x}$ and e is the elementary charge) acting on the LSP has been included [4]. Where appropriate, the subscripts 0 and 1 are used to signify LSP and WGM parameters, respectively. On the second line, V is the mode volume of the WGM and q is related to its associated electric field by

$$\mathbf{E}(\mathbf{r}, t) = -\frac{\sqrt{4\pi}}{V}\dot{q}(t)\mathbf{f}(\mathbf{r}) \tag{6.2}$$

where the mode function [210, 41] $\mathbf{f}(\mathbf{r})$ is a solution to a generalized form of the vector Helmholtz equation appropriate for an isolated WGM resonator. Finally, appearing in both equations of motion is a term proportional to the coupling strength, g, determined (up to scaling factors) by the projection of the WGM mode function onto the long axis of the AuNR at its center $\mathbf{r}_0$,

$$g = e\sqrt{\frac{4\pi}{mV}}\mathbf{f}(\mathbf{r}_0)\cdot\hat{\mathbf{x}}. \tag{6.3}$$

Whereas the equations of motion (Eq. (6.1)) are similar to those used in our previous work [105, 207] here we explicitly differentiate between the various physical processes which contribute to the decay of both the LSP and WGM excitations. Each distinct damping rate is labeled by γ with a subscript denoting the relevant dissipative pathway. The LSP dissipates energy via nonradiative absorption ($\gamma_{0,\mathrm{NR}}$) and radiation into the far field ($\gamma_{0,\mathrm{NR}} = 2e^2\omega^2/3mc^3$), whereas the WGM can decay through energy transfer to the fiber ($\gamma_{1,\mathrm{Fib}}$) in addition to dissipative processes intrinsic to the WGM, including material absorption, bending loss, and surface inhomogeneity scattering. Additionally, energy may be transferred from the WGM to LSPs of undriven AuNRs on the surface of the toroid which in turn can absorb and radiate. While these taper-independent WGM decay pathways are each the result of physically distinct processes, all terminate in either heating the microresonator or

liberating energy into the far-field via radiation, and therefore can be aggregated into a total nonradiative ($\gamma_{1,\mathrm{NR}}$) and radiative ($\gamma_{1,\mathrm{Rad}}$) damping rate.

Each dissipative pathway is associated with a distinct experimental observable; absorption measurements probe nonradiative dissipation, scattering measurements collect radiated energy in the far field, and the previously described two-sided transmission measurement detects energy transferred from the WGM to the tapered fiber. Accordingly, expressions for various cross sections may be derived by computing the power dissipated in the steady state by the corresponding damping force in Eq. (6.1) and normalizing to the intensity of the pump laser incident on the AuNR (SI). Carrying out this procedure leads to the following expressions for the reduced absorption, scattering, and extinction (i.e., total) cross sections

$$\frac{\sigma_{\mathrm{abs}}}{\sigma^0_{\mathrm{abs}}} = \frac{\widetilde{\gamma}_{0,\mathrm{NR}}}{\gamma_{0,\mathrm{NR}}} F(\omega) \qquad \frac{\sigma_{\mathrm{scat}}}{\sigma^0_{\mathrm{scat}}} = \frac{\widetilde{\gamma}_{0,\mathrm{Rad}}}{\gamma_{0,\mathrm{Rad}}} F(\omega) \qquad \frac{\sigma_{\mathrm{ext}}}{\sigma^0_{\mathrm{ext}}} = \frac{\widetilde{\gamma}_{0,\mathrm{Tot}}}{\gamma_{0,\mathrm{Tot}}} F(\omega) \tag{6.4}$$

where the superscript 0 denotes the cross-section of the isolated LSP and

$$\widetilde{\gamma}_{0,j}(\omega) = \gamma_{0,j} + \frac{\omega^2 g^2}{(\omega^2 - \omega_1^2)^2 + \omega^2 \gamma_{1,\mathrm{Tot}}^2} \gamma_{1,j} \tag{6.5}$$

is the WGM-dressed LSP damping rate where j indicates a particular decay pathway (nonradiative, radiative, or total). Each reduced cross-section scales with the function

$$F(\omega) = \left| \frac{q_F + \epsilon}{\epsilon + i} \right|^2 \tag{6.6}$$

which depends on the scaled and shifted pump frequency $\epsilon(\omega) = (\omega^2 - \Omega^2)/\omega\Gamma$ where explicit forms for $\Omega(\omega)$ and $\Gamma(\omega)$ are given in the SI. In the limit where LSP damping dominates the coupled LSP-WGM dynamics (i.e., $\gamma_{0,\mathrm{Tot}} \gg \gamma_{1,\mathrm{Tot}},\ g$), the complex-values function $q_F(\omega) = (\Omega^2 - \omega_1^2 + i\omega\gamma_{1,\mathrm{Tot}})/\omega\Gamma$ becomes approximately constant over the spectral width of the WGM and can thus be identified as a complex generalization of the Fano asymmetry parameter [105], while $F(\omega)$ becomes the familiar Fano line shape [207, 88, 89] describing an antiresonant effect at pump frequencies near the WGM resonant frequency.

Because the two-sided transmission measurement is unique to the LSP-WGM system and not of the LSP itself, it is not sensible to normalize the transmission cross-section to that of the bare LSP. Instead, it can be shown (SI) that it takes the form

$$\sigma_{\mathrm{T}} = \frac{\gamma_{1,\mathrm{Fib}}}{\gamma_{1,\mathrm{Tot}}} \left(1 - \frac{\gamma_{0,\mathrm{Tot}}}{\widetilde{\gamma}_{0,\mathrm{Tot}}} \right) \sigma_{\mathrm{ext}} \tag{6.7}$$

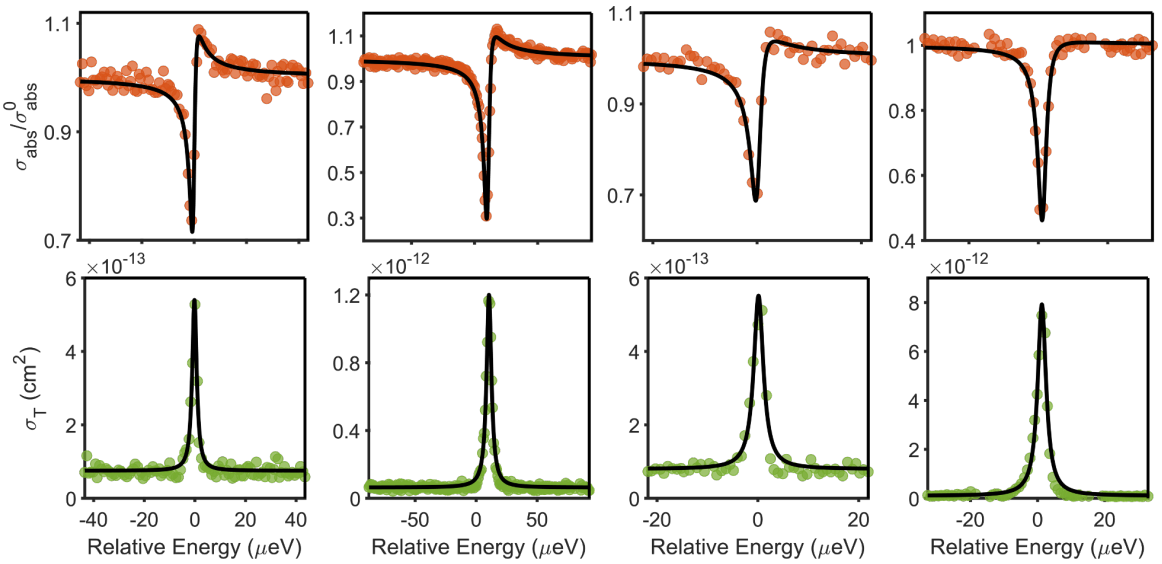

Figure 6.4: Simultaneous fits to reduced absorption cross-section (top) and transmission cross-section (bottom). Though relative energies are plotted here, absolute energies are used for further analysis.

Table 6.1: Mean and standard deviation of the mean for all fit parameters.

	$\hbar\omega_0$ (eV)	$\hbar\omega_1$ (eV)	$\hbar\gamma_{0,\mathrm{NR}}$ (meV)	$\hbar\gamma_{0,\mathrm{Rad}}$ (meV)	$\hbar g$ (meV)	$\hbar\gamma_{1,\mathrm{NR}}$ (μeV)	$\hbar\gamma_{1,\mathrm{Rad}}$ (μeV)	$\hbar\gamma_{1,\mathrm{Fib}}$ (neV)
mean	0.9326	0.9426	62.20249	5.293	0.332	1.74	0.18	26
S.D.	0.0001	0.0002	0.00009	0.002	0.004	0.04	0.02	1

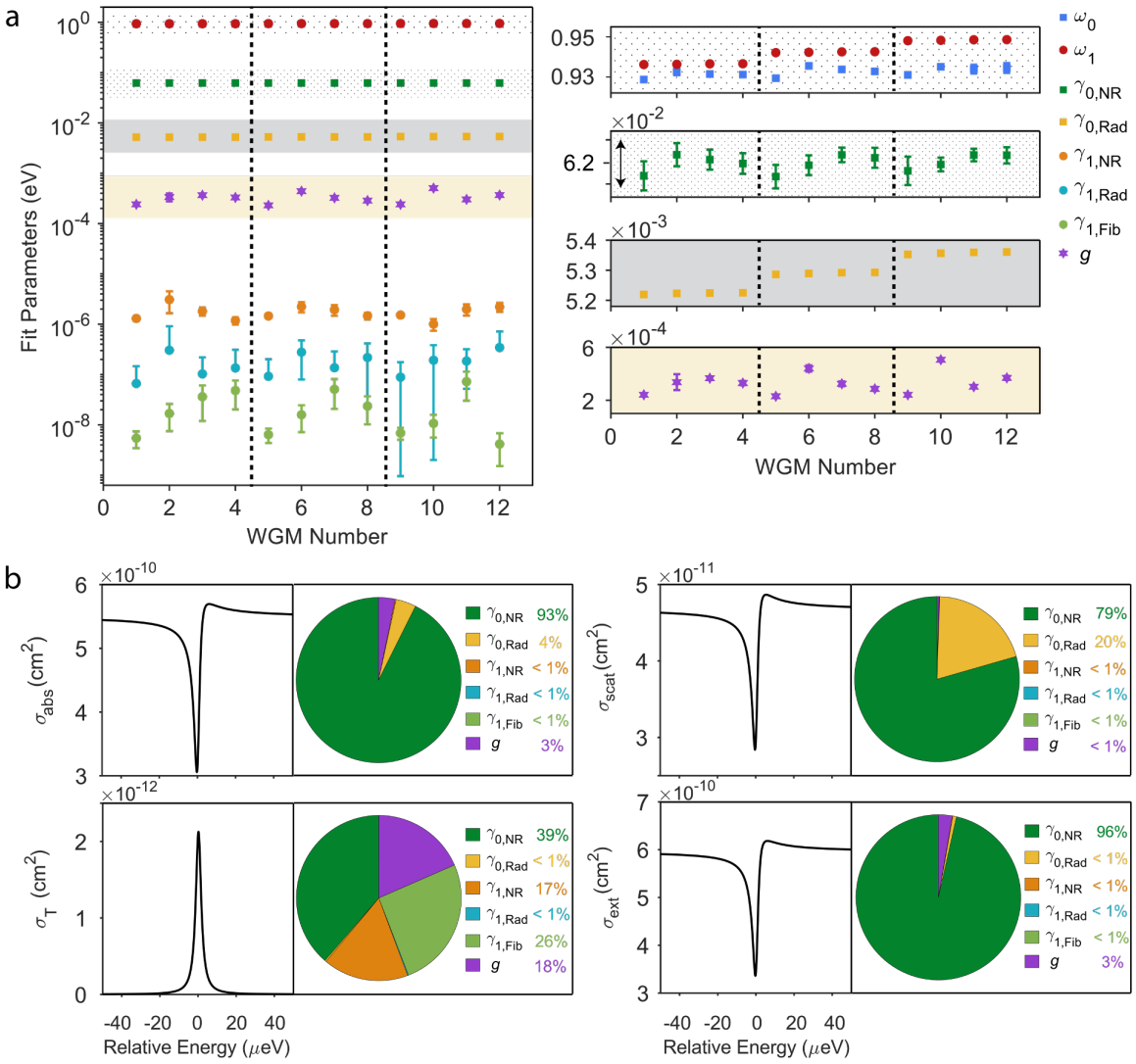

Figure 6.5: (a) All fit parameters in log scale (left side) obtained from simultaneous fits to experimental data in well-separated spectral windows indicated by dark dashed lines. Scaling these parameters between frequency and energy units is accomplished by an implicit factor of $\hbar$. Zoom-in plots in linear scale (right side) for better clarity. The arrow on the second panel indicates a range of 5×10^{-6} eV. (b) Computed spectra (left side) based on the global mean of all fit parameters and pie charts (right side) for the parameters' contributions to the corresponding cross sections.

This expression, although different in form from the other cross sections previously discussed, can be intuitively understood by considering the pathway taken by the transmitted energy prior to its detection in the tapered fiber: the extinction cross-section σ_{ext} characterizes the total fraction of energy imparted into the LSP by the incident pump laser per unit time in the steady state, while the two preceding factors (from right to left) describe the fraction of that energy that is transferred to the WGM and, finally, the fraction that is dissipated into the tapered fiber.

6.4 Extracting system parameters

Although the above model alone yields a qualitative understanding of the physics underlying the coupled LSP-WGM system and the observables which probe its dissipative pathways, quantitative estimates of the parameters relevant to those observables may be obtained through a combination of theory and experimental data through least-squares fitting. Such a quantitative characterization of the system is compelling for a variety of reasons. An order-of-magnitude comparison between various parameters elucidates the breadth of time scales which play a role in the system dynamics, whereas an analysis of the coupling strength in relation to the dominant dissipative rates reveals where the system lies in the range of weak-to-strong coupling (our system is clearly in the weak coupling regime). In addition, an accurate parameter estimation is important for optimizing hybrid cavity design to control light-matter interactions, such as for maximum Purcell enhancement [105].

Because of the multiple order-of-magnitude mismatch between LSP and WGM line widths, both low- and high-resolution absorption spectral measurements are taken into consideration. The low-resolution scan characterizes the spectrally broad Lorentzian "envelope" of the LSP, while the high-resolution scan reveals spectrally narrow Fano line shapes in absorption [105, 207, 88, 89] and sharp resonance "teeth" in transmission, as discussed above. Parameter estimates are obtained through a two-step fitting procedure. First, LSP parameters (ω_0, $\gamma_{0,\text{NR}}$, $\gamma_{0,\text{Rad}}$) are extracted by fitting low-resolution absorption spectra to the bare LSP absorption cross-section

$$\sigma^0_{\text{abs}}(\omega) = \frac{4\pi\omega^2}{c}\frac{\gamma_{0,\text{NR}}}{(\omega^2-\omega_0^2)^2+\omega^2\gamma^2_{0,\text{Tot}}}. \tag{6.8}$$

Subsequently, remaining parameters (ω_1, $\gamma_{1,\mathrm{NR}}$, $\gamma_{1,\mathrm{Rad}}$,$\gamma_{1,\mathrm{Fib}}$, g) are obtained through simultaneous fitting of high-resolution absorption and two-sided transmission spectra to Eqs. (6.4) and (6.7) with LSP parameters bound within 95% confidence intervals. Notably, all fits are carried out on absolute measurements without artificial scaling parameters. Simultaneous fits over several spectral ranges that contain a large number of WGM resonances all show an excellent agreement between experimental measurements and the model, a few of which are shown in Fig. 6.4 and Figure S7.

The plasmon natural frequency (ω_0) and nonradiative damping rate ($\gamma_{0,\mathrm{NR}}$) obtained from fits vary minimally between WGM resonances, as shown in Fig. 6.5a. The stepwise trend of ω_1 results from the fact that individual, well-separated spectral windows are surveyed, each containing multiple WGM resonances. Likewise, a similar stepwise trend is observed for the frequency-dependent LSP radiative damping rate $\gamma_{0,\mathrm{Rad}}(\omega)$ which here is evaluated at $\omega = \omega_1$. Analyzed WGMs consist of those at resonant frequencies both higher and lower than the frequency of the LSP (ω_0). Cavity intrinsic ($\gamma_{0,\mathrm{Rad}}$ and $\gamma_{1,\mathrm{Rad}}$) and taper-induced ($\gamma_{1,\mathrm{Fib}}$) loss rates are less than those contributed by the LSP by over 3 orders of magnitude. We calculate the global mean of individual damping rates obtained from the fitting for each parameter. As shown in Table 6.1, fits to simultaneous absorption and transmission measurements make it possible to extract a high dynamic range of damping rates spread over 6 orders of magnitude. The LSP damping rates are comparable to those reported by Refs [202, 211, 212] reported for single AuNRs, while WGM damping rates are in accordance with typical Q-factors ($\sim$106) of higher-order modes measured in toroidal microresonators with AuNRs deposited on the surface. As expected, the coupled LSP-WGM system is well within the weak coupling regime as the interaction energy g is multiple orders-of-magnitude smaller than the system's total damping rates ($\hbar g \sim 10^{-4}$ eV, $\hbar\gamma_{0,\mathrm{Tot}} \sim 10^{-2}$ eV, $\hbar\gamma_{1,\mathrm{Tot}} \sim 10^{-6}$ eV). $\hbar\gamma_{1,\mathrm{Fib}}$ is the smallest among WGM loss rates, suggesting the taper is undercoupled and can act as a weakly perturbative readout to examine those WGMs that interact with the LSP.

As seen by examining the standard deviation of the mean, the variation among LSP parameters is minimal in comparison to the WGM parameters. This is expected as all measurements were carried out for a single LSP with a well-defined resonance frequency

and line width. In contrast, the mean and standard deviation of the mean for the WGM parameters compiles results across 12 distinct WGM resonances and variation is therefore expected. In particular, the fiber-induced loss rate $\gamma_{1,\mathrm{Fib}}$ and the coupling strength g depend crucially on the field profile of the particular WGM in question and therefore the standard deviation of the mean conveys important information about the range of attainable values for these parameters. Among all parameters, the most uncertain is the WGM radiative loss rate $\gamma_{1,\mathrm{Rad}}$. This is expected as we do not measure scattering and therefore do not directly probe the energy dissipated through radiative means. In other words, the absorption and two-sided transmission measurements provide sufficient information to extract the individual rates $\gamma_{1,\mathrm{NR}}$ and $\gamma_{1,\mathrm{Fib}}$, respectively, whereas the line shape in either observable may be used to determine the total line width $\gamma_{1,\mathrm{Tot}}$. The radiative rate $\gamma_{1,\mathrm{Rad}}$ is inferred through a combination of these independent measurements along with the relation $\gamma_{1,\mathrm{Rad}} = \gamma_{1,\mathrm{Tot}} - \gamma_{1,\mathrm{NR}} - \gamma_{1,\mathrm{Fib}}$. A more direct determination of $\gamma_{1,\mathrm{Rad}}$ would be possible through a scattering measurement simultaneous with the absorption and transmission measurements.

In order to evaluate the sensitivity of each observable on the coupling strength and the various damping rates, we compute all derived observables using the global mean of all fit parameters and examine the effect of the parameters' variation upon that observable (SI), as shown in Fig. 6.5b. The LSP damping rates, particularly $\gamma_{0,\mathrm{NR}}$, dominate the contribution to σ_{abs}, σ_{scat}, and σ_{ext}. However, σ_{T} is more sensitive to the variations of WGM damping rates and coupling strength. Overall, through simultaneous measurement of absorption and transmission, we are able to fully describe this weakly coupled system even though its parameter space spans nearly 9 orders of magnitude in energy. This capability provides a foundation for deterministic control and design of specific dissipative channels for specific purposes.

One example of an application would be to tailor far-field radiation by controlling the influence of the photonic environment on a single nanorod's polarizability. A similar scheme was used in an array of nanorods coupled to a single WGM through backaction [200]. With the addition of a far-field scattering measurement and theoretical modeling, a complete accounting of every photon entering and exiting the system would be possible. As dictated by energy conservation, the sum of the powers scattered, absorbed, and transmitted must

equal the laser power extinguished when averaged over an optical cycle. This conservation is made explicit through the sum rule obeyed by the observables in Eqs. (6.4) and (6.7)

$$\sigma_{\mathrm{ext}}(\omega) = \sigma_{\mathrm{abs}}(\omega) + \sigma_{\mathrm{scat}}(\omega) + \sigma_{\mathrm{T}}(\omega) \tag{6.9}$$

which can be derived by appealing to Newton's equations (SI). Nevertheless, even without a scattering measurement, it is possible to extract parameter values from absorption and transmission measurements and subsequently extrapolate the system's scattering behavior from the model. This method of determining system parameters can be combined with previously reported methods for tuning the plasmonic resonance based on thermal annealing [105] to exert unprecedented control over plasmonic-photonic mode mixing and energy flow.

In general, the emergent properties of cavity-matter systems are determined by the dissipation rates and couplings such as those quantitatively determined in this work. The balance of these parameters must often be precisely controlled in order to achieve certain functionality across a breadth of applications. For example, tunability of LSP and WGM resonance energies in a coupled plasmonic-photonic cavity is crucial for maximizing Purcell enhancement [105]. A perfect balance of gain and loss is imperative for creation of exceptional points in parity-time symmetric systems [90, 104]. To achieve strong cavity-matter coupling, a significant disparity between coupling and total loss is necessary [213, 214]. The ability to dial-in specific coupling strengths and resonance energies is a critical requirement for creation of nonlinear coupled cavities arrays for quantum simulation [215, 216, 35], quantum error correction [217], and optical signal processing [218]. Creation of routing systems in photonic circuits requires precise control of photon transfer rates between component cavities [219]. Realization of all these applications depends upon convenient experimental techniques, such as those presented here, to determine intrinsic system parameters across many time scales.

6.5 Conclusion

In summary, using a single tapered optical fiber, we demonstrate the simultaneous measurement of photothermal absorption and two-sided transmission from individual plasmonic nanorods coupled to an optical microresonator. These observables allow us to track down

the distribution and dissipation of energy through multiple competing pathways. We also present a model of the coupled plasmonic-photonic system that we use to fit the measured data and extract the damping parameters as well as the LSP-WGM coupling strength with a high dynamic range spanning up to 9 orders of magnitude, fully describing the LSP-WGM dynamics in a weakly coupled system. These combined experimental and theoretical techniques may be useful for future spectroscopic investigation of weakly or strongly coupled plasmonic, excitonic, and photonic systems with dissipation and coupling spanning a wide range of time scales. This quantitative understanding is necessary to leverage light-matter interactions through manipulating specific dissipation channels and/or coupling for applications in quantum communication and quantum information science [220, 173, 174, 175, 176, 177, 178], single-molecule detection [221, 222], and cavity-controlled chemistry [27, 28, 29, 182, 30, 26, 183, 31].

Chapter 7

DIRECT OBSERVATION OF INFRARED PLASMONIC FANO ANTIRESONANCES BY A NANOSCALE ELECTRON PROBE

In this Chapter, we exploit recent breakthroughs in monochromated aberration-corrected scanning transmission electron microscopy (STEM) to resolve infrared plasmonic Fano antiresonances in individual nanofabricated disk-rod dimers. Using a combination of electron energy-loss spectroscopy (EELS) and theoretical modeling, we investigate and characterize a subspace of the weak coupling regime between quasi-discrete and quasi-continuum localized surface plasmon resonances where infrared plasmonic Fano antiresonances appear. This work illustrates the capability of STEM instrumentation to experimentally observe nanoscale plasmonic responses that were previously the domain only of higher resolution infrared spectroscopies.

7.1 Introduction

Since the pioneering work of Ruthemann in 1941 [223], inelastic electron scattering experiments using collimated electron beams have made enormous advances in their ability to simultaneously combine and correlate spectroscopic information with spatial imaging at the nanoscale. Today, electron energy-loss spectroscopy (EELS) performed in a monochromated aberration-corrected scanning transmission electron microscope (MAC STEM) can resolve energy losses below 5 meV, with a focused fast electron probe that possesses qualities similar to an ultrafast, near-field, white light source and is only a few atoms in diameter [224]. Paired with modern developments in instrumentation, these properties of the electron probe have made possible the simultaneous spectroscopy and nanometer-scale imaging of optically bright and dark electronic, and even vibrational excitations in nanoparticles [225, 226, 227, 228, 229, 230, 231, 60, 232, 233, 234], plasmonic energy and charge transfer

[235, 236, 228], and magneto-optical metamaterials [237, 238, 239, 240, 241], heralding a new frontier of materials discovery that is inaccessible to far-field optical spectroscopies.

Despite these advances, the asymmetric Fano lineshape [88], first observed in 1959 in the EEL autoionization spectrum of He gas [97, 242], remains elusive in the EELS of plasmonic systems. In his seminal 1961 work [88], Fano interpreted the observed lineshapes in terms of a configuration interaction between Helium's discrete $2s2p$ double electronic excitation and the scattering continuum. In recent years, so-called Fano interferences or antiresonances have been observed in a variety of optical [89, 243, 105, 207, 244, 65, 245], plasmonic [246, 247, 248, 74, 249, 250, 251, 252], and transport [253, 254, 255] experiments that involve weak coupling between spectrally narrow and broad resonances as generalizations of Fano's original discrete and continuum states. Theory has debated the ability of EELS to capture the Fano antiresonance in plasmonic systems [256, 257, 258], providing impetus for a careful experimental investigation.

Motivated by a new generation of STEM monochromators, we construct and measure the spectral response of a plasmonic nanostructure that satisfies two critical requirements for the Fano antiresonance: (1) the individual plasmonic "configurations" are weakly coupled to each other, and (2) there is roughly a factor of ten or greater between the linewidths of each configuration, corresponding to the discrete and continuum channels of Fano's original analysis. These requirements are achieved through the design of a gold disk-rod dimer possessing a series of sharp, experimentally resolvable mid-infrared Fano antiresonances arising from the perturbative influence of the rod's spectrally narrow infrared Fabry-Pérot (FP) surface plasmon polariton (SPP) resonances [259, 260, 261, 262, 263, 57] upon the comparably broad dipole plasmon of the disk. We also present an analytical model that generalizes the Fano lineshape to account for the finite linewidth of both broad (quasi-continuum) and narrow (quasi-discrete) modes, as well as the inherently lossy nature of the interaction between rod and disk modes through the electromagnetic field. Finally, we apply the model to the experimentally measured dimer spectra, showing that it explains the observed features in terms of the incoherent interaction between the rod and disk plasmons in rationally-designed dimers of variable disk diameter and rod length.

7.2 EEL spectra of a plasmonic disk-rod dimer

Fig. 7.1a shows a schematic of the coupled disk-rod system studied, designed such that the dipole plasmon resonance of the disk spans a progression of narrow FP rod modes of alternating parity. Tuning the rod length controls the number of rod modes that overlap with the disk dipole, while both the rod length and disk diameter together determine the degree of spectral overlap between disk and rod modes. Weak coupling is achieved at relatively large disk-rod separations ($\sim$ 50 nm edge-to-edge), with the parameters necessary for Fano antiresonances falling into a subset of this space where, in addition, there is a factor of $\sim$ 10 or greater between the disk dipole plasmon and FP rod resonance linewidths. Extensive preliminary experimental and theoretical studies were performed to optimize the plasmon energies and linewidths of the disk and rod monomers such that the disk-rod dimers meet these criteria while retaining the smallest detuning possible between the disk dipole and lower-order rod modes.

The top panel of Fig. 7.1b shows the point EEL spectrum of a disk-rod dimer composed of an 800 nm diameter disk and a 5 μm rod separated by a 50 nm gap, measured at a beam location 10 nm radially outward from the disk edge along the axis of the rod (green $\times$). For comparison, the bottom panel of Fig. 7.1b displays the EEL spectra for an isolated disk (blue curve) and rod (red curve) of the same size, collected at beam locations indicated by the blue and red $\times$, respectively. The disk monomer spectrum (Fig. 7.1b) reveals a broad resonance around 500 meV attributed to the dipolar disk mode, while the rod monomer spectrum shows a succession of spectrally narrow FP SPP resonances beginning around 200 meV. As anticipated, the spectrum of the coupled system collected on the disk end is not a simple sum of the two monomer spectra, but instead follows the Lorentzian-like "envelope" of the isolated disk dipole peak with narrow asymmetric dips at the spectral location of each rod mode, indicative of weak coupling.

7.3 Theoretical modeling

Analysis and interpretation of measured EEL spectra is facilitated by analytical modeling of the disk-rod dimer. Considering only the interaction between a single FP mode of the rod

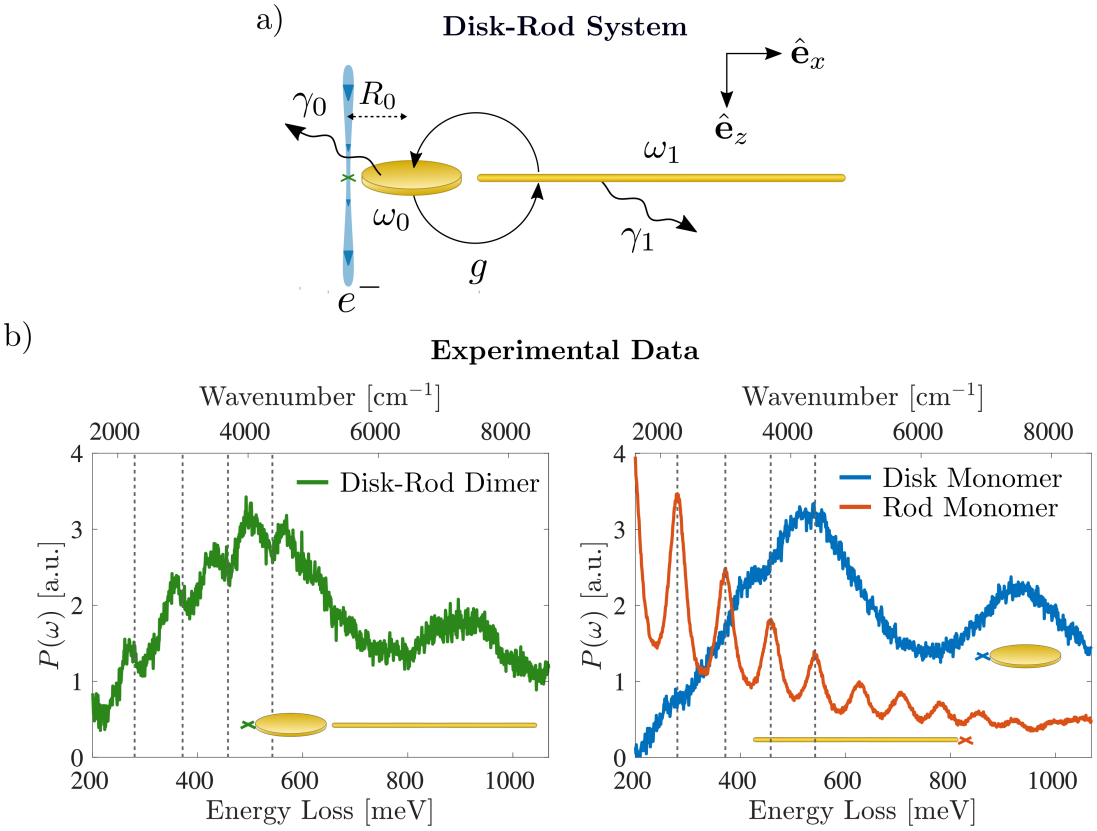

Figure 7.1: (a) Schematic of a gold disk-rod dimer indicating the relevant system parameters and electron-beam location where spectra are acquired (red ×). (b) Experimental EEL spectrum of a dimer consisting of a 800 nm diameter gold disk and a 5 μm long gold rod separated by a 50 nm gap (green curve). Blue and red curves show the monomer spectra for a near-identical disk and rod, respectively. The dimer spectrum is not a simple sum of the two monomer spectra, but instead exhibits a narrow dip at the spectral location of each rod mode (dashed lines). A typical example of the EEL spectrum acquired at the rod end is shown in Fig. 7.5.

with the dipole plasmon of the disk, the surface plasmon resonance solutions of Maxwell's equations can be mapped onto the following set of coupled harmonic oscillators [60, 239],

$$\begin{aligned}\ddot{p}_0 + \gamma_{\rm nr}\dot{p}_0 - \frac{2e^2}{3m_0c^3}\dddot{p}_0 + \omega_0^2 p_0 - \sqrt{\frac{m_1}{m_0}}\int_{-\infty}^{t} dt' g(t-t')p_1(t') &= \frac{e^2}{m_0}E_{\rm el}^x(\mathbf{0},t) \\ \ddot{p}_1 + \gamma_{\rm nr}\dot{p}_1 + \gamma_{\rm rad}\dot{p}_1 + \omega_1^2 p_1 - \sqrt{\frac{m_0}{m_1}}\int_{-\infty}^{t} dt' g(t-t')p_0(t') &= 0.\end{aligned} \tag{7.1}$$

Here p_i labels the x-oriented surface plasmons of the disk ($i = 0$) and rod ($i = 1$) of natural frequency ω_i, nonradiative dissipation rate $\gamma_{\rm nr}$, and effective mass m_i [60, 239]. Radiation-reaction forces have been included to account for radiative losses by the system, which in the frequency domain can be repackaged into the total dissipation rates $\gamma_0(\omega) = \gamma_{\rm nr} + 2e^2\omega^2/3m_0c^3$ for the disk dipole mode [4] and $\gamma_1 = \gamma_{\rm nr} + \gamma_{\rm rad}$ for the rod mode; here $\gamma_{\rm rad}$ has been used in place of the frequency-dependent Larmor rate due to the non-dipolar nature of the rod modes, which are sufficiently spectrally narrow such that $\gamma_{\rm rad}$ is well-approximated as frequency-independent.

The disk dipole plasmon is driven by the electric field $\mathbf{E}_{\rm el}(\mathbf{x},t) = -e(\mathbf{x}-\mathbf{R}_0-\mathbf{v}t)/\gamma_L^2[(z-vt)^2 + (R/\gamma_L)^2]^{3/2}$ of the fast electron moving uniformly with velocity $\mathbf{v} = \hat{\mathbf{e}}_z v$ evaluated at the center of the disk, taken to be the origin. Here $\gamma_L = [1-(v/c)^2]^{-1/2}$ is the Lorentz contraction factor, $\mathbf{R}_0 = -\hat{\mathbf{e}}_x R_0$ the electron beam position (Fig. 7.1a red $\times$), and $R = \sqrt{(x+R_0)^2 + y^2}$ is the lateral distance between electron probe and field observation point in the impact plane ($z = 0$). Due to the relatively large disks studied ($\gtrsim 650$ nm in diameter), the rod modes are not directly driven by the evanescent field of the electron when the electron probe is positioned at the disk end of the dimer. No EEL signal is observable above the background when the disk is removed, illustrating the disk's role as an antenna that transfers energy from the electron probe to the rod.

The coupling strength between the disk and rod plasmon modes depends upon the relative separation and orientation of the disk and rod as well as their respective polarizabilities. In the frequency domain, the coupling is characterized by the complex parameter $g(\omega)$, arising from the interaction energy $U_{\rm int} = -\mathbf{E}_1 \cdot \mathbf{p}_0$, where $\mathbf{E}_1$ is the induced electric field of the rod mode evaluated at the disk dipole center. The real part of $g(\omega)$ defines the rate of energy transfer between the disk and rod plasmon modes, while the imaginary part accounts for the lossy nature of this interaction and is related to the degree of interference between the fields of

the coupled modes (see Chapter 3.2). Because the rod modes are spectrally narrow, the real part of the coupling strength $g(\omega)$ may be treated as approximately frequency-independent. Likewise, the imaginary part is taken to be linear in ω as $g(\omega)$ is purely real for static fields (i.e., $\omega = 0$) and therefore does not have a frequency-independent contribution. Lastly, only the coupled plasmon dynamics oriented parallel to the rod's long axis need be considered due to the high aspect ratio of the rod, justifying the use of the quasi-one dimensional dynamical equations in Eq. (7.1) with all other collective electronic motion occurring at much higher energy.

The EEL probability $P(\omega)$ per unit frequency ω of transferred quanta between electron beam and target is obtained by computing the work done on the electron probe by the field induced in the polarized target [264],

$$P(\omega) = \frac{|\tilde{E}^x_{\rm el}(\mathbf{0},\omega)|^2}{\pi\hbar}{\rm Im}\left[\frac{e^2}{m_0}\left(\omega_0^2 - \omega^2 - i\omega\gamma_0 - \frac{g^2}{\omega_1^2 - \omega^2 - i\omega\gamma_1}\right)^{-1}\right], \tag{7.2}$$

while the EEL probability for the isolated disk $P_0(\omega)$ is obtained from the above expression by taking $g = 0$. The ratio between $P(\omega)$ and $P_0(\omega)$ at the same beam position $\mathbf{R}_0$ can be cast into the reduced form

$$\frac{P(\omega)}{P_0(\omega)} = \left(1 + {\rm Im}\left[\frac{g^2/\omega\gamma_0}{\omega_1^2 - \omega^2 - i\omega\gamma_1}\right]\right)\left|\frac{q+\epsilon}{\epsilon+i}\right|^2 \tag{7.3}$$

which generalizes Fano's original lineshape to account for dissipation in both broad and narrow plasmon resonances as well as complex coupling. Here $q(\omega) = (\Omega^2(\omega) - \omega_1^2 + i\omega\gamma_1(\omega))/\omega\Gamma(\omega)$ and $\epsilon(\omega) = (\omega^2 - \Omega^2(\omega))/\omega\Gamma(\omega)$ are respectively the complex-valued asymmetry function and reduced frequency expressed in terms of the modified frequency $\Omega^2(\omega) = \omega_1^2 - {\rm Re}[g^2(\omega_0^2 - \omega^2 - i\omega\gamma_0)^{-1}]$ and linewidth $\Gamma(\omega) = \gamma_1(\omega) + (1/\omega){\rm Im}[g^2(\omega_0^2 - \omega^2 - i\omega\gamma_0)^{-1}]$ of the spectral feature described by the interaction of disk dipole and rod plasmon modes. For true Fano antiresonances, the function $q(\omega) \approx q(\omega_1)$ is approximately constant and represents the asymmetry parameter originally proposed by Fano to distill the physics of the antiresonance into a single number that depends upon the basic system parameters [88]. Here, since both disk and rod modes are dissipative, the asymmetry parameter generalizes to a complex-valued number, the real part of which characterizes the degree of asymmetry of the antiresonance. It is important to note that without the second term proportional

to γ_1, $q(\omega)$ would be real-valued and the reduced EEL probability spectrum in Eq. (7.3) would vanish at those frequencies where $\epsilon(\omega) = -q(\omega)$ [105]. However, this is not observed experimentally at any coupling strength due to the finite linewidth of the spectrally narrow rod resonances. Lastly, the standard form of the Fano lineshape is scaled by a frequency-dependent prefactor which accounts for the additional non-disk dissipation channels of the dimer.

Since each rod has multiple plasmon modes that spectrally overlap the disk dipole plasmon resonance, the EEL probability is further generalized as

$$P(\omega) = \frac{|\tilde{E}^x_{\mathrm{el}}(\mathbf{0},\omega)|^2}{\pi\hbar}\mathrm{Im}\Big[\Big(\omega_0^2 - \omega^2 - i\omega\gamma_0 - \sum_j \frac{g_j^2}{\omega_j^2 - \omega^2 - i\omega\gamma_j}\Big)^{-1}\Big] \tag{7.4}$$

and the reduced EEL probability may be cast into the approximate form,

$$\frac{P(\omega)}{P_0(\omega)} \approx \mathcal{F}_1\big(q_1(\omega),\epsilon_1(\omega)\big)\mathcal{F}_2\big(q_2(\omega),\epsilon_2(\omega)\big)\cdots\mathcal{F}_N\big(q_N(\omega),\epsilon_N(\omega)\big), \tag{7.5}$$

where $\mathcal{F}_j(q_j(\omega),\epsilon_j(\omega))$ is the Fano lineshape describing the interaction between the jth rod plasmon mode and the disk dipole plasmon mode (labeled by the subscript 0) given by Eq. (7.3). This product factorization of the reduced spectrum, which allows for an estimate of the asymmetry function $q_j(\omega)$ for each individual rod plasmon mode, is approximate as the rod resonances overlap weakly, causing their individual contribution to the dimer spectrum to depend upon neighboring rod modes through their mutual interaction with the disk dipole plasmon. Nonetheless, the exact form of the reduced EEL spectrum inferred from Eq. (7.4) can be used to demonstrate the accuracy of the simple product form in the weak coupling regime when all rod modes are well-separated spectrally (see Appendix). Lastly, while the model parameters (including g_j) could be obtained by approximating the disk and rod by oblate and prolate spheroids and adding the contributions from radiation damping, doing so adds little additional insight into the measurements; thus we obtain these parameters by numerically fitting the experimental spectra.

Measured EEL spectra are collected at $\mathbf{R}_0$ for a set of fabricated gold disk-rod dimers of varying rod length and disk diameter. All system parameters (ω_0, m_0, ω_j, γ_j, and g_j) are obtained for each dimer by least-squares fitting the analytic form for $P(\omega)$ defined by Eq.

(7.4) to the spectra. The nonradiative (Drude) dissipation rate of the disk dipole is set prior to fitting according to the value for gold at optical frequencies ($\hbar\gamma_{\mathrm{Au}} = 69$ meV [265]). Initial guesses for the natural frequency ω_0 and effective mass m_0 of the disk plasmon are estimated for each dimer by fitting the measured EEL spectra collected at $\mathbf{R}_0$ of an isolated disk, while initial guesses for ω_j and γ_j of the N rod plasmons are estimated from the EEL spectra of an isolated rod. As a check of the fitting procedure, the parameters obtained from each dimer spectrum are used to reconstruct the disk monomer spectrum $P_0(\omega)$, rod monomer spectrum $P_{\mathrm{rod}}(\omega) = \sum_j P_j(\omega)$ (where $P_j(\omega)$ is identical in form to $P_0(\omega)$ with indices interchanged where appropriate), and the reduced EEL probability spectrum $P(\omega)/P_0(\omega)$ for each structure. We note that, while any spectrum can be fit by an arbitrary collection of oscillators, the approach here is restricted by the number of oscillators present in the monomer spectra.

7.4 Revealing Fano resonances

Fig. 7.2 shows the result of this analysis for a dimer composed of a 650 nm diameter gold disk and a 5 μm gold rod separated by a 50 nm gap. The dimer point EEL spectrum, collected at a beam position 10 nm radially outward from the disk edge (green $\times$), is shown in the upper panel of Fig. 7.2a (green bullets) with the fit to Eq. (7.4) overlaid (black curve). The bottom panel of Fig. 7.2a compares the experimental EEL spectra obtained from a 650 nm disk monomer (blue bullets) and a 5 μm rod monomer (red bullets) to the theoretical monomer spectra reconstructed from parameters obtained from fitting the dimer spectrum (black curve). Due to small geometrical variations between the isolated monomer rods and disks versus those which compose the dimers, the monomer spectra will not, in general, exactly match those corresponding to the dimer disk and rod. In addition, deviation between the reconstructed and experimental disk monomer spectra is expected on the higher-energy side of the disk dipole peak where the quadrupole plays a non-negligible dynamical role. Despite these limitations, Fig. 7.2a shows excellent agreement between reconstructed and experimental spectra, which further validates our ability to extract the monomer parameters from the dimer spectra. To compare with our theoretical analysis, Fig. 7.2b displays the reduced EEL probability (green bullets) obtained by dividing the experimental spectrum by the theoretically reconstructed isolated disk spectrum $P_0(\omega)$ (top),

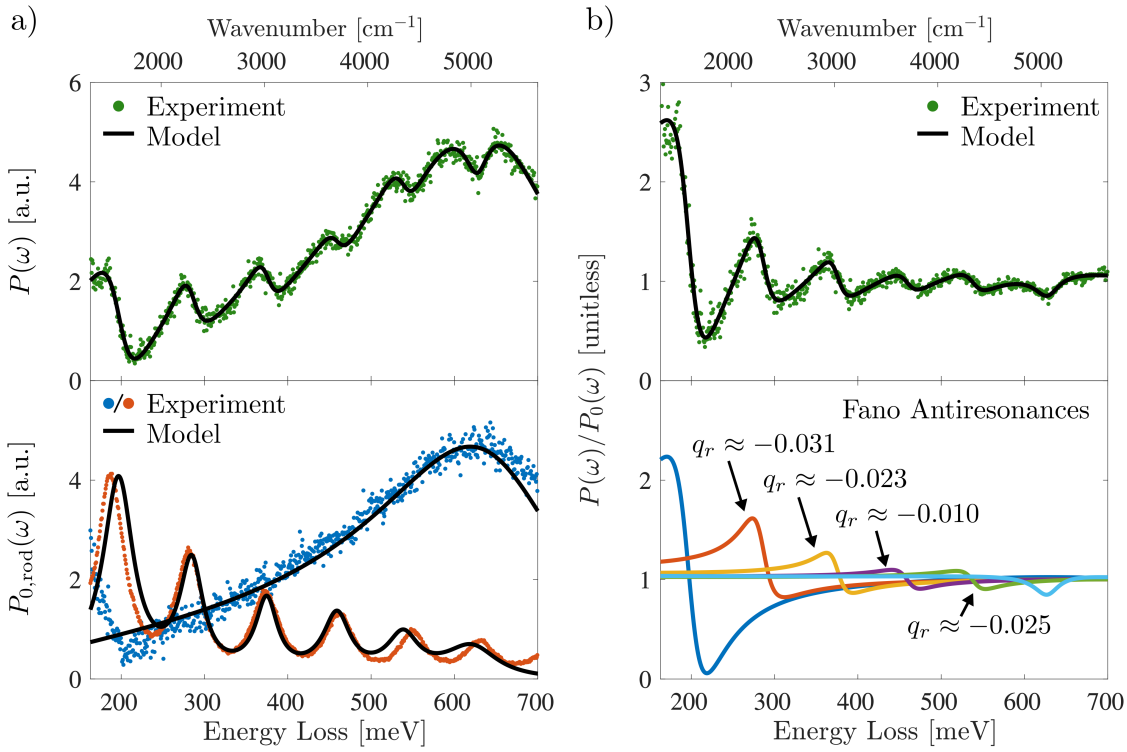

Figure 7.2: EEL point spectrum of a gold disk-rod dimer composed of a 650 nm diameter disk and a 5 μm rod separated by a 50 nm gap. The spectrum exhibits a progression of infrared Fano antiresonances due to the interaction between the broad disk dipole plasmon resonance and the spectrally narrow plasmon modes of the rod. The upper panels display the (a) experimental (green) and fit (black) EEL spectrum and (b) reduced EEL spectrum of the dimer collected at the disk end. The lower panel of (a) shows the experimental monomer spectra of an isolated disk (blue) and rod (red). As an independent check of the fitting procedure, the theoretical monomer spectra are reconstructed from the dimer fit parameters (black curves), showing excellent agreement. The lower panel of (b) displays the decomposition of each antiresonance in the reduced spectrum into a product of Fano lineshapes $\mathcal{F}_j(q_j, \epsilon_j)$ as described in Eq. (7.5) with the corresponding value of the real part of the asymmetry parameter $q_{r,j} = \mathrm{Re}\, q_j(\omega_j)$ indicated above each feature.

along with the decomposition into a progression of individual Fano lineshapes $\mathcal{F}_j(q_j, \epsilon_j)$ (bottom).

This analysis is repeated for a set of four unique disk-rod combinations and summarized in Fig. 7.3 to illustrate the variation in coupling strength and relative linewidth as a function of disk and rod size. Underlying each data point is a particular rod FP mode (labeled j) which interacts with the disk dipole plasmon (labeled 0). Dimers denoted by D1 (D2) consist of a 650 (800) nm disk while those denoted by R1 (R2) contain 2.5 (5) μm long rods. In all cases, the disk and rod are separated by a gap of 50 nm and EEL spectra are collected 10 nm radially outward along the rod long axis from the disk edge (Fig. 7.1a, red $\times$). As each dimer contains multiple overlapping disk and rod modes, these four structures generate 12 modes available for analysis. For all dimers, the lowest and highest energy rod resonances are not included as explicit data points due to uncertainties imposed by subtraction of the zero-loss peak and interactions with the SiO_2 substrate phonon mode at lower energies ($\lesssim$ 200 meV) and the influence of the disk quadrupole at higher energies ($\gtrsim$ 650 meV). The full spectra are displayed in Fig. (7.4).

All disk-rod mode pairs are found to be in the weak coupling regime as each data point satisfies the inequality $\mathrm{Re}\, g_j/\gamma_0(\omega_j)\sqrt{\omega_0\omega_j} < 1$ [64, 63]. Additionally, multiple disk-rod mode pairs are found to obey the linewidth condition $\gamma_j \sim \gamma_0/10$ (Fig. 7.3 red region), including those highlighted in Fig. 7.2, thus satisfying both requirements for the emergence of Fano antiresonances in the coupled spectrum. Additionally, these results indicate that the size of both the rod and disk play a crucial role in determining whether the disparity in linewidths between the disk and rod modes is sufficient to observe a sharp antiresonance. We find that the longer 5 μm rods (R2) in combination with the 650 nm diameter disk (D1) optimally balance the two criteria for sharp Fano antiresonances, while supporting a progression of rod modes which are minimally detuned from the disk dipole such that disk-rod interaction is non-negligible.

7.5 Conclusion

In conclusion, we resolve for the first time Fano antiresonances in the EEL spectrum of a plasmonic nanostructure. This is achieved by rationally designing a gold disk-rod dimer

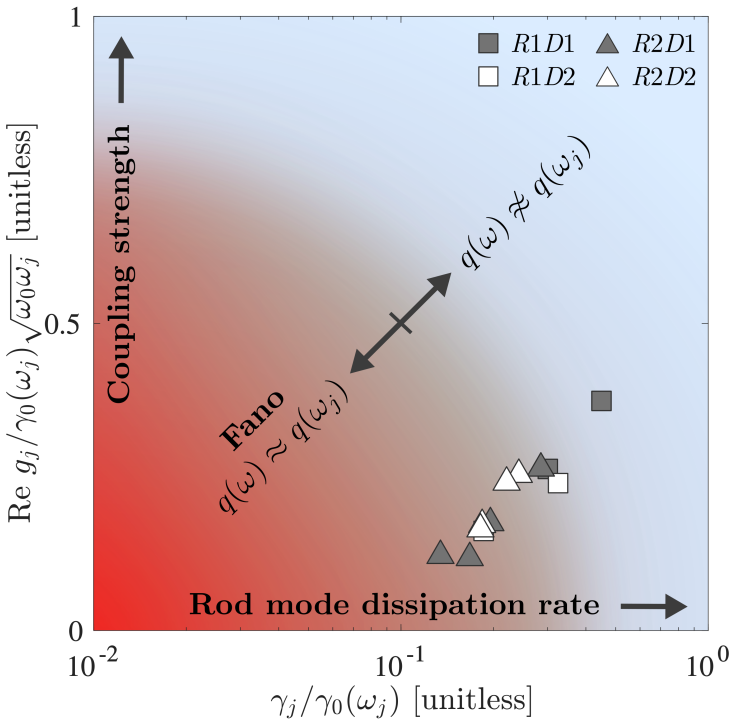

Figure 7.3: Graphical summary of the interaction between individual rod resonances and the disk dipole plasmon in a collection of disk-rod dimers. Each mode pair is represented by a distinct symbol and is characterized by its relative coupling strength $\mathrm{Re}\, g_j/\gamma_0(\omega_j)\sqrt{\omega_0\omega_j}$ and dissipation rate $\gamma_j/\gamma_0(\omega_j)$. Dimers denoted by R1 (R2) consist of 2.5 μm (5 μm) long rods, while those denoted by D1 (D2) consist of 650 (800 nm) diameter disks. In all dimers, the disk and rod are separated by a gap of 50 nm and since $\mathrm{Re}\, g_j/\gamma_0(\omega_j)\sqrt{\omega_0\omega_j} = 1$ denotes the boundary between weak and strong coupling, all dimers are in the weak coupling regime. The gray triangle symbols indicate specific Fano antiresonances shown explicitly in Fig. 7.2.

supporting rod resonances that are spectrally narrow relative to the disk dipole. Observation of the asymmetric lineshapes is facilitated by a new generation of monochromated and aberration-corrected STEMs which open the infrared spectral region to interrogation. We develop a theoretical model which generalizes the original Fano lineshape to account for dissipation in both the quasi-discrete and the quasi-continuum channels in STEM-EELS. This analysis makes explicit the classification of the observed dimer lineshapes in terms of the asymmetry parameter q, as discovered in the autoionization spectrum of He by Fano in 1961 [88]. This combined experimental and theoretical work not only resolves an ongoing discussion in the literature about the existence of Fano lineshapes in the EELS of plasmonic systems [256, 257, 258], but also showcases the ability of the latest generation of monochromated STEMs to observe spectrally narrow plasmonic responses that were previously the domain only of higher resolution optical spectroscopies.

7.6 Appendix

7.6.1 Data preparation

Each EEL spectrum reported in this work was obtained from 100 frames of data, each corresponding to an independent measurement. For each individual frame of data the peak of the ZLP was shifted to 0 eV. The 100 shifted frames were subsequently summed and the resultant spectrum was normalized to unity. Full spectra for each dimer studied in the main text is shown in Fig. 7.4.

7.6.2 Dimer spectrum at rod end

Additional evidence that the disk and rod modes are weakly coupled is revealed through inspection of the dimer spectrum collected at the distal end of the rod, here shown in Fig. 7.5a for a gold disk-rod dimer composed of a 650 nm diameter disk and a 5 μm long rod (black curve). The dimer spectrum is overlaid onto the rod monomer spectrum for comparison (red curve). Indicative of weak coupling, the dimer spectrum is nearly identical to that of the rod monomer excluding a small spectral shift resulting from the perturbative interaction with

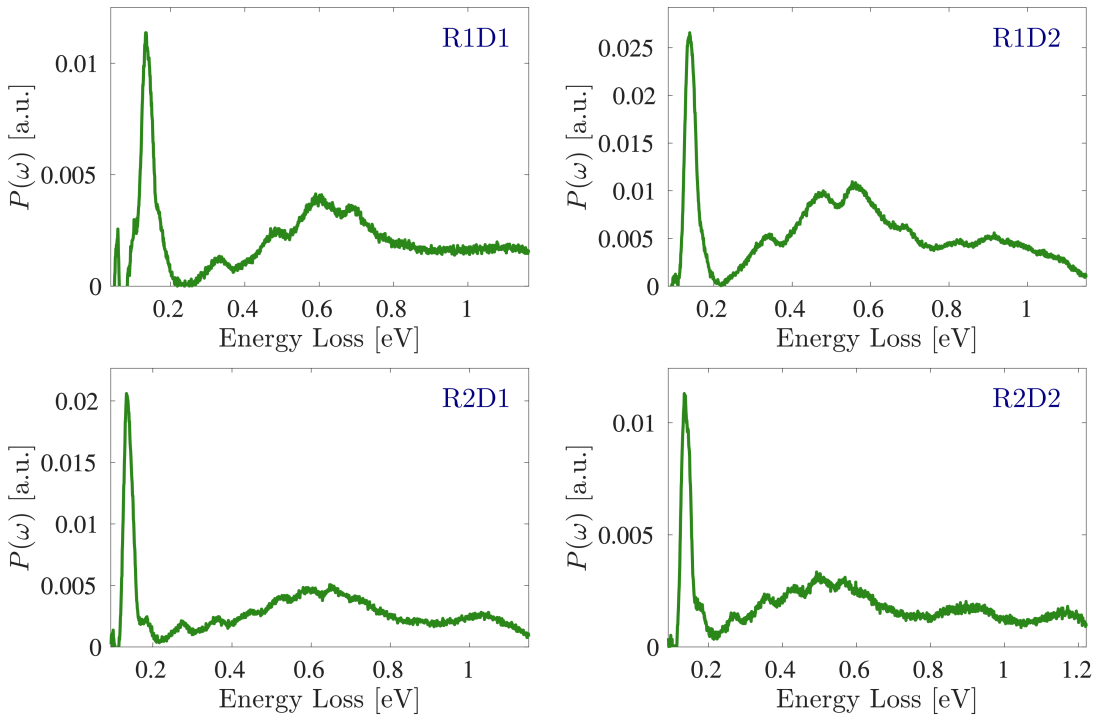

Figure 7.4: Full EEL spectrum for each of the four gold disk-rod dimers studied in the main text collected 10 nm radially outward at the disk end. Due to the influence of the SiO2 substrate phonon below 0.2 eV and the importance of the disk quadrupole above 0.85 eV (0.65 eV) for D1 (D2), we restrict our analysis to the region between these spectral bounds.

the disk dipole. The dissimilarity between the dimer spectrum collected at either end of the dimer (rod end Fig. 7.5a, disk end Fig. 7.5b) may be understood by considering the driven-dissipative dynamics of the weakly coupled modes. When the disk dipole is excited by the field of the electron, it responds according to its polarizability except at energies near a rod resonance, in which case that particular rod mode is driven by the field of the disk dipole. Due to their narrow linewidth, the spectrally-dependent phase response of the rod modes vary much more sharply than that of the comparatively broad disk dipole. This results in sharp asymmetric features at the spectral position of each rod mode. As shown in Fig. 7.5b, these sharp asymmetric spectral features disappear when the gap size is increased from 50 nm to 200 nm, indicating the important role of the rod modes in determining the spectral response of the disk-rod dimer, even when the electron beam is positioned $\gtrsim 700$ nm away from the rod and therefore unable to drive its resonances directly. In contrast, positioning the electron beam at the rod end leads primarily to excitation of the rod modes which may then incoherently transfer energy to the disk dipole. Because the spectrally narrow rod modes "filter" the broadband frequency content of the electron field, the disk dipole merely perturbs the response of the rod, resulting in a nearly imperceptible spectral shift of each resonance peak.

7.6.3 Product Approximation

Fig. 7.6 shows a comparison between the exact expression for $P(\omega)$ and its decomposition into a product of Fano lineshapes (Eq. 5 in the main text) describing the reduced EEL spectrum for the disk-rod dimer for all dimers included in Fig. 3 of the main text. As discussed in the main text, the latter form is not exact due to the interaction between neighboring rod modes mediated by the disk plasmon. In the weak coupling regime, however, this approximation is both accurate and useful as it allows for the extraction of the asymmetry parameter for each individual Fano lineshape.

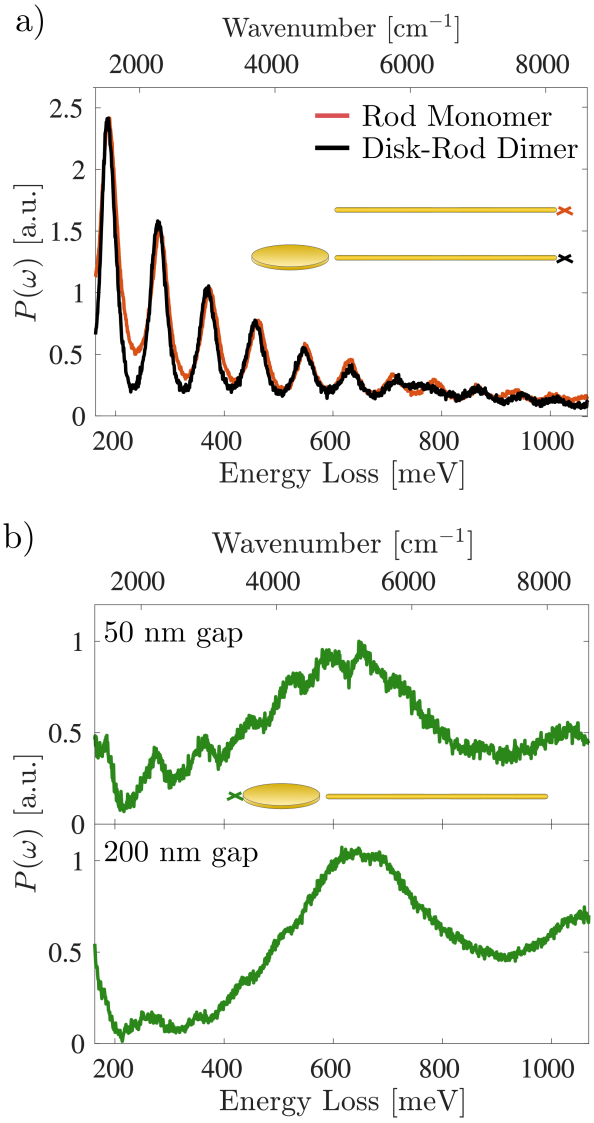

Figure 7.5: (a) Comparison between the point EEL spectra of a 5 μm gold rod monomer and a dimer composed of a 650 nm diameter gold disk and 5 μm gold rod separated by a 50 nm gap. In both cases, spectra are collected at a beam position 10 nm from the rod end (red, black $\times$). The dimer spectrum is nearly identical to the rod monomer spectrum aside from a small spectral shift, indicative of weak coupling. (b) EEL spectra of the same disk-rod dimer collected 10 nm radially outward from the disk edge (green $\times$) for 50 nm (top) and 200 nm (bottom) gap sizes.

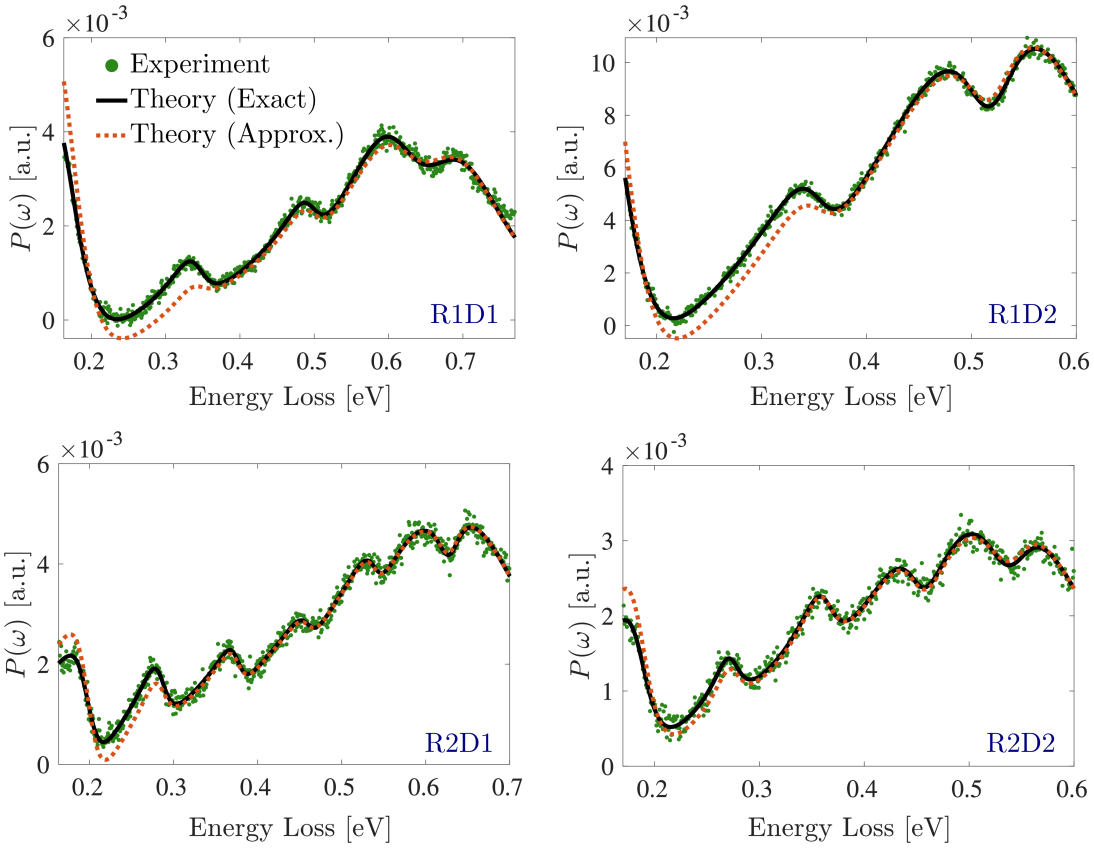

Figure 7.6: Comparison between $P(\omega)$ and its approximate decomposition into a product of Fano lineshapes. In all panels, the experimental EEL spectrum is shown as green circles, while the fit to Eq. 2 of the main text is shown as a black line. For comparison, the red dotted line displays the approximation to $P(\omega)$ on the second line of Eq. 5 of the main text, multiplied by the reconstructed disk monomer spectrum $P_0(\omega)$.

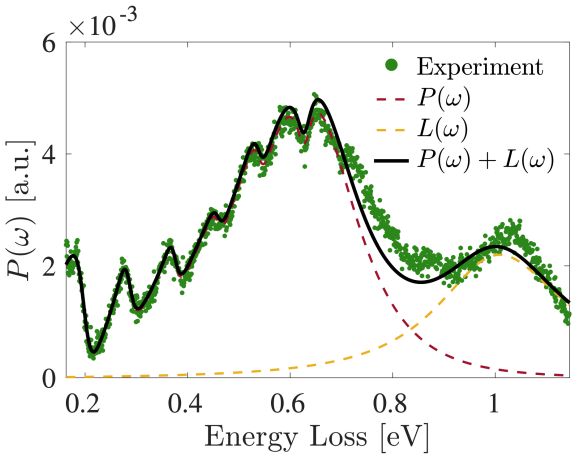

Figure 7.7: Comparison between the fit of $P(\omega)$ and a modified form $P(\omega) + L(\omega)$ to R2D1 (Fig. 7.2 in the main text). $P(\omega) + L(\omega)$ is computed by first fitting $P(\omega)$ in a narrow fit window where the disk quadrupole may be neglected, and subsequently fitting $P(\omega) + L(\omega)$ to the data within an expanded window using only the resonance position (ω_q), width (γ_q) and amplitude (A_q) as free parameters.

7.6.4 Example: Fitting Full R2D1 Spectrum

As explained in the main text, the fit window is chosen such that only the interaction between rod modes and the disk dipole need be considered. At energies $\gtrsim 0.65$ eV, the disk quadrupole becomes important and must be considered in order to accurately fit the full spectrum. As a first approximation, the simplest route is to treat the quadrupole as an independent oscillator uncoupled from the rest of the system by fitting data within an expanded window to the sum $P(\omega) + L(\omega)$, where $P(\omega)$ is the result of the primary fit within the truncated window shown in Fig. 7.2 of the main text and $L(\omega)$ is the independent oscillator response

$$L(\omega) = \frac{A_q}{-\omega^2 + \omega_q^2 - i\omega\gamma_q}. \tag{7.6}$$

While agreement is not perfect, the resulting fit shows that inclusion of the quadrupole only considerably alters the fit at energies higher than those considered in the main text.

Part III

COUPLED CAVITIES AND PHOTON-PHOTON INTERACTIONS

Part III of this dissertation includes two papers verbatim (one published, one under review) as well as a set of notes that form the basis for a third manuscript currently in preparation:

- Chapter 8: **Smith, K. C.**, Masiello, D.J. Coupled dielectric cavities beyond standard coupled mode theory. *In preparation.*

- Chapter 9: ⋆**Smith, K. C.**, ⋆Chen, Y., Majumdar, A. Masiello, D.J. Active tuning of hybridized modes in a heterogeneous photonic molecule. *Physical Review Applied* 13, 044041. (2020). [266]

- Chapter 10: **Smith, K. C.**, Bhattacharya, A., Masiello, D.J. Exact k-body representation of the Jaynes-Cummings interaction in the dressed basis: Insight into many-body phenomena with light. *Under review.* arXiv:2103.07571 [267]

⋆ indicates co-first authorship

Broadly speaking, the entirety of Part III concerns physical behavior in which cavity-confined photons mimic phenomena observed in matter. Chapter 8 introduces a theoretical understanding of hybridization in strongly coupled photonic molecules – i.e., structures composed of two or more coupled dielectric cavities. The presented formalism is an electromagnetic analog of molecular orbital theory, the theoretical tool used to understand the quantum states of a molecule given complete knowledge of the constituent atomic orbitals. Much like their atomic counterparts, photonic molecules support hybridized "super-modes" which can have properties distinct from that of the constituent individual cavities. The primary motivation of developing this theory is to gain an understanding of how super-mode

properties (i) evolve under basic system parameters (such as cavity-cavity separation and mode detuning) without relying on computationally intensive electromagnetic simulations and (ii) can be tuned to achieve controllable light-matter interactions. Chapter 9 extends this work with a simple application to a heterogeneous photonic molecule composed of a ring resonator coupled to a photonic crystal nanobeam cavity.

Chapter 10 concludes with a detailed theoretical analysis of the Jaynes-Cummings Hamiltonian as a building block for realization of an analog quantum simulator, particularly in a cavity QED setting. Photons are relatively easy to control and measure experimentally, but lack a crucial characteristic necessary for emulating complex many-body phenomena – they do not interact with one another. This may be remedied by introducing an intermediary nonlinear element, such as a two-level atom, capable of absorbing at most one photon and causing additional photons to "feel" the influence of the first. Thus, matter can mediate *effective* photon-photon interactions which mimic those of naturally occurring materials, albeit with a mathematical description which shares little resemblance to that of directly interacting particles. To that end, we present a new representation of hybrid light-matter systems which analytically translates effective, atom-mediated interactions into a form that facilitates direct comparison to many-body models in condensed matter physics and quantum chemistry.

Chapter 8

A THEORETICAL FORMALISM FOR COUPLED DIELECTRIC CAVITIES

The ability to confine light to an electromagnetic cavity allows for a degree of control over light-matter interactions that is not possible in free space. Consequently, design and fabrication of better (high Q, small V) cavities has become an increasingly important venture of the years, equally as important as the development of new and improved quantum emitters. At microwave frequencies, superconducting cavities reign supreme, able to store photons for up to a tenth of a second [14]. At optical frequencies, however, sufficiently good conducting materials do not exist and high quality factors must be achieved through alternate means. To that end, high-contrast dielectrics surfaces provide an attractive route for confinement at optical frequencies [268], with optical microcavities – an all encompassing term for dielectric structures that confine optical frequency light using this approach (e.g., whispering gallery mode resonators and photonic crystal cavities) – able to achieve ultrahigh quality factors in excess of 10^8. Separately, several dielectric cavity designs have been proposed to achieve ultrasmall mode volumes orders of magnitude below the diffraction limit (for example, see Refs. [269, 270]).

Among the innumerable applications of dielectric optical microcavities, many have explicitly relied upon interactions between the photonic modes of adjacent cavities. A particularly influential example is the proposal by Yariv et al. to form coupled-resonator optical waveguides (CROWs) in order to achieve slowly propagating light for enhancement of nonlinear phenomena [271]. In the two decades following this formative work, numerous theoretical and experimental investigations have focused on applications which rely on a finite number of coupled dielectric cavities, commonly termed photonic molecules by analogy to their atom based counterparts, such as low-threshold lasing [272, 273], electromagnetic-induced transparency [274, 275, 276], nonclassical light generation [277, 278, 279, 280], quantum

simulation [281, 35, 37], and parity-time symmetry [90, 282].

Since individual cavity modes are often modeled through their isomorphism to harmonic oscillators (see Chapter 2), it stands to reason that systems of electromagnetically interacting dielectric cavities must be well described by coupled oscillator equations. Such is the idea of time-dependent coupled mode theory (CMT) [283, 79], a heuristic workhorse which has been used near-ubiquitously in experimental and theoretical investigations of photonic molecules, including many of those referenced above. While it has proved to be an invaluable tool for facile modeling of coupled cavity systems, CMT is empirical in nature and typically relies on numerical fits to either simulation or experimental data to determine model parameters, with only vague attempts to reconcile those parameters with first principles theory.

The primary goal of this Chapter is to present a first principles generalized coupled-oscillator formalism for modeling coupled dielectric cavities with analytic predictive power and applicability beyond the limits of standard CMT. This is approached through the lens of Lagrangian mechanics and is therefore readily adaptable to modern applications such as photonics-based quantum simulation due to ease of quantization.

8.1 A single dielectric cavity

We begin by considering a single dielectric cavity and show how it may be mapped onto a Lagrangian isomorphic to that of a set of independent harmonic oscillators. It is assumed that the cavity is of high quality factor and therefore dissipation may be neglected except as a correction to be added perturbatively through standard techniques. We note that this assumption is not strictly necessary and much progress has been made in recent years in the understanding of quasinormal modes of leaky cavities [284, 285], but these treatments are beyond the scope of this work.

The electric and magnetic fields of a dielectric cavity obey the macroscopic form of

Maxwell's equations

$$\begin{aligned}
\nabla \cdot \varepsilon(\mathbf{r})\mathbf{E} &= 0 \\
\nabla \cdot \mathbf{B} &= 0 \\
\nabla \times \mathbf{E} &= -\frac{1}{c}\dot{\mathbf{B}} \\
\nabla \times \mathbf{B} &= \frac{4\pi}{c}\varepsilon(\mathbf{r})\dot{\mathbf{E}},
\end{aligned} \tag{8.1}$$

where $\mu = 1$ has been enforced as only non-magnetic materials are of interest in this work, and the spatial and time dependence of $\mathbf{E}$ and $\mathbf{B}$ is implied. The inhomogeneous dielectric function $\varepsilon(\mathbf{r})$, here assumed to be dispersionless, accounts for contributions to the fields due to the polarizable media which support the cavity.

While Maxwell's equations provide sufficient information for solving the modes of a particular cavity, it is convenient to cast them in terms of the potentials defined by the usual relations $\mathbf{E} = -\dot{\mathbf{A}}/c - \nabla\phi$ and $\mathbf{B} = \nabla \times \mathbf{A}$. This reformulation comes at a cost, however, as redundancies arise in the description and must be properly removed. As discussed in Chapter 1, this is typically achieved in nonrelativistic quantum electrodynamics via specialization to the Coulomb gauge ($\nabla \cdot \mathbf{A} = 0$), followed by algebraic elimination of the scalar potential from the electromagnetic Lagrangian [39]. In the present case, however, we are not interested in the free-space electromagnetic degrees of freedom, but rather those supported by an electromagnetic cavity composed of bound matter characterized by the macroscopic dielectric function $\varepsilon(\mathbf{r})$. The analog to the Coulomb gauge in this context is the so-called generalized Coulomb gauge, defined by the condition $\nabla \cdot \varepsilon(\mathbf{r})\mathbf{A} = 0$ [44, 41]. With this choice, the scalar potential becomes entirely dependent upon the *free* matter degrees of the system and may therefore be taken to zero without loss of generality in the present case. Consequently, Maxwell's equations reduce to just a single partial differential equation – the generalized wave equation for the vector potential

$$\nabla \times \nabla \times \mathbf{A} + \frac{\varepsilon(\mathbf{r})}{c^2}\ddot{\mathbf{A}} = 0, \tag{8.2}$$

the solutions of which fully encode the complete set of cavity modes of a cavity in the dielectric environment described by $\varepsilon(\mathbf{r})$.

The vector potential may be written as a sum over these independent solutions as

$$\mathbf{A}(\mathbf{r},t) = \sum_m \frac{c\sqrt{4\pi}}{V_m} q_m(t)\mathbf{f}_m(\mathbf{r}), \tag{8.3}$$

where $q_m(t)$ is a time-dependent amplitude, $\mathbf{f}_m(\mathbf{r})$ is the mode function, and V_m is the mode volume. Crucially, the mode functions are solutions to the generalized Helmholtz equation

$$\nabla \times \nabla \times \mathbf{f}_m(\mathbf{r}) = \varepsilon(\mathbf{r})\frac{\omega_m^2}{c^2}\mathbf{f}_m(\mathbf{r}). \tag{8.4}$$

It is important to note that the label m is really a composite label $\{k,\lambda\}$ where different $k = \omega/c$ correspond to distinct eigenvalues, and λ labels the polarization.

8.1.1 Properties of the mode functions

Following Ref. [44], the properties of the mode functions $\mathbf{f}_m(\mathbf{r})$ (particularly orthogonality and completeness) are most easily proven by introducing their rescaled counterparts $\mathbf{u}_m(\mathbf{r}) = \sqrt{\varepsilon(\mathbf{r})}\mathbf{f}_m(\mathbf{r})$. Substituting this definition into Eq. (8.4), we find that the functions $\mathbf{u}(\mathbf{r})$ solve an eigenvalue equation at every point in space,

$$\mathcal{O}(\mathbf{r})\mathbf{u}_m(\mathbf{r}) = \frac{\omega_m^2}{c^2}\mathbf{u}_m(\mathbf{r}), \tag{8.5}$$

where

$$\mathcal{O}(\mathbf{r}) = \frac{1}{\sqrt{\varepsilon(\mathbf{r})}}\nabla \times \nabla \times \frac{1}{\sqrt{\varepsilon(\mathbf{r})}}. \tag{8.6}$$

Because $\mathcal{O}(\mathbf{r})$ is Hermitian, it follows that the functions $\mathbf{u}_m(\mathbf{r})$ are orthogonal,

$$\int d^3r\, \mathbf{u}_m^*(\mathbf{r}) \cdot \mathbf{u}_n(\mathbf{r}) \propto \delta_{mn}. \tag{8.7}$$

Consequently, the mode functions $\mathbf{f}_m(\mathbf{r})$ obey the generalized orthogonality relation

$$\int d^3r\, \varepsilon(\mathbf{r})\mathbf{f}_m^*(\mathbf{r}) \cdot \mathbf{f}_n(\mathbf{r}) = V_{mn}\delta_{mn}, \tag{8.8}$$

where we have chosen the normalization $\max\{\varepsilon(\mathbf{r})\mathbf{f}^*(\mathbf{r}) \cdot \mathbf{f}(\mathbf{r})\} = 1$, generalizing the normalization condition of Section 2.1 to include the dielectric function $\varepsilon(\mathbf{r})$.

In place of a formal proof of completeness, we rely on the arguments of Ref. [44]: the functions $\mathbf{f}_m(\mathbf{r})$ are evidently complete over the subspace of functions that satisfy that gauge

condition $\nabla \cdot \sqrt{\varepsilon(\mathbf{r})}\mathbf{u}_m(\mathbf{r}) = 0$ and, as a result, the sum $\sum_m \mathbf{u}_m(\mathbf{r}) \cdot \mathbf{u}_m^*(\mathbf{x}')$ forms an identity on this subspace. Returning to the mode functions proper, we may define

$$\delta_{ij}^{\varepsilon}(\mathbf{r}, \mathbf{r}') = \sum_m \frac{1}{V_m} (\mathbf{f}_m(\mathbf{r}) \cdot \hat{r}_i)(\mathbf{f}_m^*(\mathbf{r}') \cdot \hat{r}_j), \tag{8.9}$$

which projects any vector field $\mathbf{V}(\mathbf{r})$ onto the component $\mathbf{V}_{\perp}^{\varepsilon}(\mathbf{r})$ that obeys the gauge condition $\nabla \cdot \varepsilon(\mathbf{r})\mathbf{V}(\mathbf{r}) = 0$ via the integral equation

$$\mathbf{V}_{\perp}^{\varepsilon}(\mathbf{r}) = \int d^3r' \, \varepsilon(\mathbf{r}') \delta_{ij}^{\varepsilon}(\mathbf{r}, \mathbf{r}') \mathbf{V}(\mathbf{r}'). \tag{8.10}$$

Clearly, the distribution $\delta_{ij}^{\varepsilon}(\mathbf{r}, \mathbf{x}')$ is a generalization of the transverse delta function in free-space quantum electrodynamics [39, 40], here generalized for an inhomogeneous dielectric medium described by $\varepsilon(\mathbf{r})$. Similar to the free-space scenario, it follows that the functions $\mathbf{f}_m(\mathbf{r})$ are complete over in the subspace of functions $\{\mathbf{V}(\mathbf{r})\}$ that obey $\nabla \cdot \varepsilon(\mathbf{r})\mathbf{V}(\mathbf{r}) = 0$.

For reference, the properties of the mode functions $\mathbf{f}_m(\mathbf{r})$ can be succinctly listed as follows:

1. *Normalization:* $\mathbf{f}_m(\mathbf{r})$ is normalized such that $\max\{\varepsilon(\mathbf{r}) |\mathbf{f}_m|^2\} = 1$, and therefore the mode volume is naturally defined by

$$V_m = \frac{\int d^3r \, \varepsilon(\mathbf{r}) |\mathbf{E}_m|^2}{\max\{\varepsilon(\mathbf{r}) |\mathbf{E}_m|^2\}} = \int d^3r \, \varepsilon(\mathbf{r}) |\mathbf{f}_m(\mathbf{r})|^2 \tag{8.11a}$$

2. *Orthogonality:* The set of mode functions $\{\mathbf{f}_m(\mathbf{r})\}$ form an orthogonal basis:

$$\int d^3r \, \varepsilon(\mathbf{r}) \mathbf{f}_m^*(\mathbf{r}) \cdot \mathbf{f}_n(\mathbf{r}) = V_m \delta_{mn} \tag{8.11b}$$

3. *Completeness:* This basis is complete over the set of L^2 functions which obey the transversality condition

$$\nabla \cdot \varepsilon(\mathbf{r}) \mathbf{f}_m(\mathbf{r}) = 0 \tag{8.11c}$$

and may be used to construct a generalization of the transverse δ function [44, 39]

$$\delta_{ij}^{\varepsilon\perp}(\mathbf{r}, \mathbf{r}') = \sum_m \frac{1}{V_m} (\mathbf{f}_m(\mathbf{r}) \cdot \hat{\mathbf{e}}_i)(\mathbf{f}_m(\mathbf{r}') \cdot \hat{\mathbf{e}}_j) \tag{8.11d}$$

which projects any vector field $\mathbf{V}(\mathbf{r})$ onto the component $\mathbf{V}^{\varepsilon\perp}(\mathbf{r})$ which obeys the gauge condition $\nabla \cdot \varepsilon(\mathbf{r})\mathbf{V}^{\varepsilon\perp}(\mathbf{r}) = 0$ via the integral equation

$$\mathbf{V}_i^{\varepsilon\perp}(\mathbf{r}) = \int d^3r \, \varepsilon(\mathbf{r}') \delta_{ij}^{\varepsilon\perp}(\mathbf{r}, \mathbf{r}') \mathbf{V}(\mathbf{r}'). \tag{8.11e}$$

8.1.2 System Lagrangian and Hamiltonian

In Chapter 1, we showed that the Lagrangian for the electromagnetic field in the presence of an inhomogeneous dielectric function $\varepsilon(\mathbf{r})$ is given by

$$L = \int \frac{d^3r}{8\pi} \left[\varepsilon(\mathbf{r}) \frac{\dot{\mathbf{A}}(\mathbf{r})^2}{c^2} - (\nabla \times \mathbf{A}(\mathbf{r}))^2 \right]. \tag{8.12}$$

We would now like to write the Lagrangian in terms of the individual eigenmodes of Eq. (8.2). For the present moment, we take $\mathbf{f}_m(\mathbf{r})$ to be a complex function, though this assumption will be relaxed at a later point. This distinction is important as complexity of $\mathbf{f}_m(\mathbf{r})$ introduces several subtleties which we deal with using notation developed in Ref. [44]. In a future manuscript we will present a simpler form of the theory assuming purely real mode functions, but choose to use the present Chapter as an exposition of the more general treatment with complex mode functions.

Hermiticity of the electric field requires $\mathbf{A}^\dagger = \mathbf{A}$, suggesting that the mode functions $\mathbf{f}_m(\mathbf{r})$ and their complex conjugates $\mathbf{f}_m^*(\mathbf{r})$ are not linearly independent. As a result, it must be true that

$$\sum_m \frac{1}{V_m} q_m^* \mathbf{f}_m^*(\mathbf{r}) = \sum_m \frac{1}{V_m} q_m \mathbf{f}_m(\mathbf{r}). \tag{8.13}$$

This relation enforces that the *total* vector potential $\mathbf{A}$ is Hermitian. However, the independent modes need not be individually Hermitian in the most general case. Projecting both sides of this equation onto a particular mode, we have

$$\sum_m \frac{q_m^*}{V_m} \int d^3r\, \varepsilon(\mathbf{r}) \mathbf{f}_m^*(\mathbf{r}) \cdot \mathbf{f}_n(\mathbf{r}) = \sum_m \frac{q_m}{V_m} \int d^3r\, \varepsilon(\mathbf{r}) \mathbf{f}_m(\mathbf{r}) \cdot \mathbf{f}_n(\mathbf{r}) \tag{8.14}$$

Using the orthogonality relation in Eq. (8.11b), we find

$$q_n^* = \sum_m q_m U_{mn}, \tag{8.15}$$

where

$$U_{mn} = \frac{1}{V_m} \int d^3r\, \varepsilon(\mathbf{r}) \mathbf{f}_m(\mathbf{r}) \cdot \mathbf{f}_n(\mathbf{r}). \tag{8.16}$$

Similarly, the reciprocal relationship is given by

$$q_n = \sum_m q_m^* U_{mn}^*. \tag{8.17}$$

Multiplying the two above equations together leads to the conclusion that

$$\sum_m U_{mn} U^*_{mj} = \delta_{nj}. \tag{8.18}$$

One important fact to note is that, unlike the definition of U_{mn} presented in Ref. [44], the form defined here is not symmetric due to the chosen normalization condition. Upon interchange of the two indices, it obeys the relationship

$$U_{mn} = \frac{V_n}{V_m} U_{nm}. \tag{8.19}$$

We now aim to show that U_{mn} and U^*_{mn} are expansion coefficients relating the functions $\mathbf{f}_m(\mathbf{r})$ to their complex conjugates. Substituting Eq. (8.17) into the right-hand side of Eq. (8.13), we find

$$\begin{aligned} \sum_m \frac{q^*_m}{V_m} \mathbf{f}^*_m(\mathbf{r}) &= \sum_m \frac{1}{V_m} \left[\sum_n q^*_n U^*_{nm} \right] \mathbf{f}_m(\mathbf{r}) \\ &= \sum_n \frac{q^*_n}{V_n} \sum_m U^*_{mn} \mathbf{f}_m(\mathbf{r}) \end{aligned} \tag{8.20}$$

Because the set of coefficients q^*_m are independent, it must then be true that

$$\mathbf{f}^*_m(\mathbf{r}) = \sum_n U^*_{nm} \mathbf{f}_n(\mathbf{r}) \tag{8.21}$$

and, by complex conjugation,

$$\mathbf{f}_m(\mathbf{r}) = \sum_n U_{nm} \mathbf{f}^*_n(\mathbf{r}), \tag{8.22}$$

where we have made relabelled dummy indices to avoid confusion. We emphasize that, in the limit where all mode functions $\mathbf{f}_m(\mathbf{r})$ are real, U_{mn} becomes the Dirac delta function δ_{mn}, leading to significant simplifications in the following analysis.

We are now ready to write the Lagrangian in terms of mode expansions via substitution of the mode expansion for $\mathbf{A}$ into Eq. (8.12). Carrying this out, we find

$$L = \frac{1}{2} \sum_{mn} \int d^3r \left[\varepsilon(\mathbf{r}) \frac{\dot{q}_m \dot{q}_n}{V_m V_n} \mathbf{f}_m(\mathbf{r}) \cdot \mathbf{f}_n(\mathbf{r}) - c^2 \frac{q_m q_n}{V_m V_n} (\nabla \times \mathbf{f}_m(\mathbf{r})) \cdot (\nabla \times \mathbf{f}_n(\mathbf{r})) \right] \tag{8.23}$$

Focusing on the first term and using the fact that $\mathbf{f}_m(\mathbf{r}) = \sum_p U_{pm} \mathbf{f}^*_p(\mathbf{r})$, it can be shown

that

$$\begin{aligned}\frac{1}{2}\sum_{mn}\int d^3r\,\varepsilon(\mathbf{r})\frac{\dot{q}_m\dot{q}_n}{V_mV_n}\mathbf{f}_m(\mathbf{r})\cdot\mathbf{f}_n(\mathbf{r}) &= \frac{1}{2}\sum_{mnp}\frac{U_{pm}\dot{q}_m\dot{q}_n}{V_mV_n}\int d^3r\,\varepsilon(\mathbf{r})\mathbf{f}_p^*(\mathbf{r})\cdot\mathbf{f}_n(\mathbf{r}) \\ &= \frac{1}{2}\sum_{mnp}\frac{U_{pm}\dot{q}_m\dot{q}_n}{V_mV_n}V_n\delta_{pn} \\ &= \frac{1}{2}\sum_{mp}\frac{U_{pm}\dot{q}_m\dot{q}_p}{V_m} \\ &= \frac{1}{2}\sum_{m}\frac{\dot{q}_m^*\dot{q}_m}{V_m},\end{aligned} \tag{8.24}$$

where we have used the generalized orthogonality relation Eq. (8.11b) in going from the first line to the second, and used the relation in Eq. (8.15) to arrive at the final form. Simplification of the second term follows similarly, yielding

$$\begin{aligned}\frac{1}{2}\sum_{mn}\int d^3r\,c^2\frac{q_mq_n}{V_mV_n}(\nabla\times\mathbf{f}_m(\mathbf{r}))\cdot(\nabla\times\mathbf{f}_n(\mathbf{r})) &= \frac{1}{2}\sum_{mn}\int d^3r\,c^2\frac{q_mq_n}{V_mV_n}\mathbf{f}_m(\mathbf{r})\cdot(\nabla\times\nabla\times\mathbf{f}_n(\mathbf{r})) \\ &= \frac{1}{2}\sum_{mn}\omega_m^2\frac{q_mq_n}{V_mV_n}\int d^3r\,\varepsilon(\mathbf{r})\mathbf{f}_m(\mathbf{r})\cdot\mathbf{f}_n(\mathbf{r}) \\ &= \frac{1}{2}\sum_{m}\frac{\omega_m^2}{V_m}q_m^*q_m,\end{aligned} \tag{8.25}$$

where integration by parts has been used in tandem with the generalized Helmholtz equation (see Eq. (8.4)), but otherwise following arguments similar to the kinetic energy term.

Combining these simplifications, the system Lagrangian becomes

$$L=\sum_m\left[\frac{1}{2V_m}|\dot{q}_m|^2-\frac{1}{2V_m}\omega_m^2|q_m|^2\right]. \tag{8.26}$$

For completeness, we now compute the system Hamiltonian. Computation of the momenta p_n conjugate to q_n is somewhat messier than usual, but can be simplified using previously

derived relations. Carrying out the relevant partial derivative, we find

$$\begin{aligned} p_n = \frac{\partial L}{\partial \dot{q}_n} &= \frac{\partial}{\partial \dot{q}_n} \sum_m \frac{1}{2V_m} \left[\sum_k \dot{q}_k U_{km} \right] \dot{q}_m \\ &= \sum_{mk} \frac{1}{2V_m} U_{km} \left[\dot{q}_k \delta_{mn} + \dot{q}_m \delta_{kn} \right] \\ &= \frac{1}{2V_n} \left[\sum_k U_{kn} \dot{q}_k + \sum_m \frac{V_n}{V_m} U_{nm} \dot{q}_m \right] \\ &= \frac{1}{2V_n} \left[\sum_k U_{kn} \dot{q}_k + \sum_m U_{mn} \dot{q}_m \right] \end{aligned} \tag{8.27}$$

As k and m are simply dummy indices, this final expression simplifies to yield

$$p_n = \frac{\dot{q}_n^*}{V_n}. \tag{8.28}$$

Legendre transform of the Lagriangian in Eq. (8.26) results in the single cavity Hamiltonian

$$H = \sum_m \left[\frac{V_m}{2} p_m^\dagger p_m + \frac{\omega_m^2}{2V_m} q_m^\dagger q_m \right], \tag{8.29}$$

where we have promoted p_m and q_m to operators. As this Hamiltonian is a complex generalization of a sum of independent harmonic oscillators, reexpression in terms of creation and annihilation operators must be carried out somewhat carefully. Here, our primary goal is to extend this analysis to two coupled cavities, and we therefore defer discussion of such subtleties to Ref. [44].

8.2 Gauge transformation of the cavity mode expansion

We now turn to the problem of two dielectric cavities, each supporting an arbitrary number of modes. This may be approached in two distinct ways. The first involves directly solving the generalized Helmholtz equation in Eq. (8.4), replacing the dielectric function by that of the composite, two-cavity system. While technically correct, this approach is not very flexible – any change in the separation of relative orientation of the two cavities, for example, alters $\varepsilon(\mathbf{r})$ and, by extension, the solutions to Eq. (8.4). Furthermore, it is not a given that Eq. (8.4) can be efficiently solved using standard electromagnetic solvers – this is the case for the heterogeneous photonic molecule in Chapter 9 comprising two dielectric cavities of vastly different characteristic length scales.

A much more flexible strategy involves solving for the modes of each cavity, characterized by dielectric functions $\varepsilon_1(\mathbf{r})$ and $\varepsilon_2(\mathbf{r})$, and subsequently "blending" them together in a way that is consistent with Maxwell's equations to find the super-modes of the composite system. Nuances arise, however, as the modes of each cavity correspond to different gauges – for the ith cavity, we have the generalized Coulomb gauge condition $\nabla \cdot \varepsilon_i(\mathbf{r})\mathbf{f}_{im}(\mathbf{r}) = 0$, yet for a Coulomb-gauge description of the composite system we require individual mode functions that obey $\nabla \cdot \varepsilon(\mathbf{r})\widetilde{\mathbf{f}}_{im}(\mathbf{r}) = 0$ where $\varepsilon(\mathbf{r})$ is the dielectric function of the global system. This issue may be preempted by gauge transforming the isolated cavity mode functions $\mathbf{f}_{im}(\mathbf{r})$ to solve for their modified counterparts $\widetilde{\mathbf{f}}_{im}(\mathbf{r})$. As will be discussed in a future publication, such a transformation corresponds to a repartitioning of matter into "bound" and "free" contributions. Explicit demonstration of this is rather complicated and subtle, however, so here we avoid such a detour for the sake of brevity.

We will now explicitly carry out the appropriate gauge transformation for the ith cavity characterized by the dielectric function $\varepsilon_i(\mathbf{r})$, assuming complete knowledge of its mode function $\mathbf{f}_{im}(\mathbf{r})$. Recalling the mode expansion of the vector potential

$$\mathbf{A}(\mathbf{r},t) = \sum_m \frac{c\sqrt{4\pi}}{V_m} q_{im}(t)\mathbf{f}_{im}(\mathbf{r}), \tag{8.30}$$

obeying $\nabla \cdot \varepsilon_1(\mathbf{r})\mathbf{A} = 0$, we wish to compute its gauge transformed counterpart obeying

$$\nabla \cdot \xi(\mathbf{r})\mathbf{A}' = 0, \tag{8.31}$$

where $\xi(\mathbf{r})$ is an arbitrary function of space. Carrying out a gauge transformation with respect to the arbitrary scalar field $F(\mathbf{r},t)$, we find

$$\begin{aligned} \mathbf{A}'(\mathbf{r},t) &= \mathbf{A}(\mathbf{r},t) + \nabla F(\mathbf{r},t) \\ \phi'(\mathbf{r},t) &= -\dot{F}(\mathbf{r},t)/c \end{aligned} \tag{8.32}$$

To simplify $\mathbf{A}'$ as much as possible, we can make the choice

$$F(\mathbf{r},t) = \sum_m \frac{c\sqrt{4\pi}}{V_{im}} q_{im}(t)\psi_{im}(\mathbf{r}). \tag{8.33}$$

Correspondingly, the gauge transformed vector and scalar potential can be written as

$$\begin{aligned}\mathbf{A}'(\mathbf{r},t) &= \sum_m \frac{c\sqrt{4\pi}}{V_{im}} q_{im}(t)\widetilde{\mathbf{f}}_{im}(\mathbf{r}) \\ \phi'(\mathbf{r},t) &= \sum_m \frac{c\sqrt{4\pi}}{V_{im}} \dot{q}_{im}(t)\psi_{im}(\mathbf{r})\end{aligned} \tag{8.34}$$

where $\widetilde{\mathbf{f}}_{im}(\mathbf{r}) = \mathbf{f}_{im}(\mathbf{r}) + \nabla\psi_{im}(\mathbf{r})$ is the gauge generalized mode function. Enforcing $\mathbf{A}'$ to the gauge condition in Eq. (8.31) yields the constraint

$$\nabla \cdot \xi(\mathbf{r})\nabla\psi_{im}(\mathbf{r}) = \nabla \cdot [\varepsilon_i(\mathbf{r}) - \xi(\mathbf{r})]\mathbf{f}_{im}(\mathbf{r}). \tag{8.35}$$

Eq. (8.35) is essentially a generalized form of the Poisson equation with a fictitious dielectric function $\xi(\mathbf{r})$ and free charge $\rho_{\text{eff}} = -\nabla \cdot \mathbf{P}$ where $\mathbf{P} = [\xi(\mathbf{r}) - \varepsilon_i(\mathbf{r})]\mathbf{f}_{im}(\mathbf{r})/4\pi$. In other words, the true dielectric function $\varepsilon(\mathbf{r})$ has essentially been repartitioned into (i) an effective dielectric environment defined by $\xi(\mathbf{r})$ and (ii) polarizable media that induces an effective free charge in the region where $\varepsilon_i(\mathbf{r}) - \xi(\mathbf{r}) \neq 0$.

At present, the above relations are quite abstract as we are still imagining the scenario of just a single cavity defined by $\varepsilon_i(\mathbf{r})$. However, this is all made much more concrete if we specialize to the case of two cavities with a composite dielectric function $\varepsilon(\mathbf{r})$. Making the replacement $\xi(\mathbf{r}) \to \varepsilon(\mathbf{r})$ in the above description, we find that the contribution to the vector potential from the ith cavity may be written as

$$\mathbf{A}'_i(\mathbf{r},t) = \sum_m \frac{c\sqrt{4\pi}}{V_{im}} q_{im}(t)\widetilde{\mathbf{f}}_{im}(\mathbf{r}), \tag{8.36}$$

where $\widetilde{\mathbf{f}}_{im}(\mathbf{r}) = \mathbf{f}_{im}(\mathbf{r}) + \nabla\psi_{im}(\mathbf{r})$ as before and

$$\nabla \cdot \varepsilon(\mathbf{r})\nabla\psi_{im}(\mathbf{r}) = -\nabla \cdot [\varepsilon(\mathbf{r}) - \varepsilon_i(\mathbf{r})]\mathbf{f}_{im}(\mathbf{r}). \tag{8.37}$$

Here, we can see that $\psi_{im}(\mathbf{r})$ simply accounts for additional longitudinal contributions to $\mathbf{A}_i(\mathbf{r})$ which result from the polarization of "external" media (i.e., belonging to a different cavity) brought into the region of the ith cavity. Through inclusion of such terms, we can build a theory capable of describing strongly coupled photonic molecules composed of cavities whose modes appreciably "spill" into the dielectric makeup of adjacent cavities. Notably, the total scalar potential need not be considered as it necessarily vanishes in the generalized

Coulomb gauge (i.e., $\nabla \cdot \varepsilon(\mathbf{r}) = 0$) where $\varepsilon(\mathbf{r})$ represents the total dielectric function of the multi-cavity system.

While we will not belabor the properties of the longitudinal corrections $\nabla\psi_{im}(\mathbf{r})$, it follows from the properties of the generalized coordinates $q_{im}(t)$ that

$$\begin{aligned} \psi_{im}(\mathbf{r}) &= \sum_n U_{inm}\psi^*_{in}(\mathbf{r}) \\ \psi^*_{im}(\mathbf{r}) &= \sum_n U^*_{inm}\psi_{in}(\mathbf{r}). \end{aligned} \tag{8.38}$$

From this, it follows that the gauge generalized mode functions $\widetilde{\mathbf{f}}_{im}(\mathbf{r})$ obey relations analogous to Eqs. (8.21)–(8.22),

$$\begin{aligned} \widetilde{\mathbf{f}}_{im}(\mathbf{r}) &= \sum_n U_{nm}\widetilde{\mathbf{f}}^*_{im} \\ \widetilde{\mathbf{f}}^*_{im}(\mathbf{r}) &= \sum_n U^*_{nm}\widetilde{\mathbf{f}}_{im}. \end{aligned} \tag{8.39}$$

8.3 Two coupled dielectric cavities

We now turn to the problem of two coupled dielectric cavities. For the most part, our approach follows closely to the single cavity case, albeit with the more complicated mode expansion defined by

$$\mathbf{A}(\mathbf{r},t) = \mathbf{A}_1(\mathbf{r},t) + \mathbf{A}_2(\mathbf{r},t), \tag{8.40}$$

where

$$\begin{aligned} \mathbf{A}_1(\mathbf{r},t) &= \sum_m \frac{c\sqrt{4\pi}}{V_{1m}} q_{1m}(t)[\mathbf{f}_{1m}(\mathbf{r}) + \nabla\psi_{1m}(\mathbf{r})] \\ \mathbf{A}_2(\mathbf{r},t) &= \sum_m \frac{c\sqrt{4\pi}}{V_{2m}} q_{2m}(t)[\mathbf{f}_{2m}(\mathbf{r}) + \nabla\psi_{2m}(\mathbf{r})] \end{aligned} \tag{8.41}$$

and

$$\begin{aligned} \nabla \cdot \varepsilon(\mathbf{r})\nabla\psi_{1m}(\mathbf{r}) &= -\nabla \cdot [\varepsilon(\mathbf{r}) - \varepsilon_1(\mathbf{r})]\mathbf{f}_{1m}(\mathbf{r}) \\ \nabla \cdot \varepsilon(\mathbf{r})\nabla\psi_{2m}(\mathbf{r}) &= -\nabla \cdot [\varepsilon(\mathbf{r}) - \varepsilon_2(\mathbf{r})]\mathbf{f}_{2m}(\mathbf{r}). \end{aligned} \tag{8.42}$$

Recalling the form of the electromagnetic Lagrangian in Eq. (8.12) and using the fact that $\mathbf{A}_1 = \mathbf{A}_1^*$ and $\mathbf{A}_2 = \mathbf{A}_2^*$,

$$\begin{aligned} L &= \int \frac{d^3r}{8\pi}\left[\varepsilon(\mathbf{r})\frac{\dot{\mathbf{A}}(\mathbf{r})^2}{c^2} - (\nabla\times\mathbf{A}(\mathbf{r}))^2\right] \\ &= \sum_{i=1,2}\int \frac{d^3r}{8\pi}\left[\varepsilon(\mathbf{r})\frac{\dot{\mathbf{A}}_i^*(\mathbf{r})\cdot\dot{\mathbf{A}}_i(\mathbf{r})}{c^2} - (\nabla\times\mathbf{A}_i^*(\mathbf{r}))\cdot(\nabla\times\mathbf{A}_i(\mathbf{r}))\right] \\ &+ \int \frac{d^3r}{8\pi}\left[\varepsilon(\mathbf{r})\frac{\dot{\mathbf{A}}_1^*(\mathbf{r})\cdot\dot{\mathbf{A}}_2(\mathbf{r}) + \dot{\mathbf{A}}_2^*(\mathbf{r})\cdot\dot{\mathbf{A}}_1(\mathbf{r})}{c^2}\right] \\ &- \int \frac{d^3r}{8\pi}\left[(\nabla\times\mathbf{A}_1^*(\mathbf{r}))\cdot(\nabla\times\mathbf{A}_2(\mathbf{r})) + (\nabla\times\mathbf{A}_2^*(\mathbf{r}))\cdot(\nabla\times\mathbf{A}_1(\mathbf{r}))\right] \end{aligned} \tag{8.43}$$

It is simplest to deal with the various integrals term-by-term. Focusing first on the diagonal electric field term, we have

$$\begin{aligned} \int \frac{d^3r}{8\pi}\varepsilon\dot{\mathbf{A}}_i^*\dot{\mathbf{A}}_i &= \frac{1}{2}\sum_{mn}\frac{\dot{q}_{im}^*\dot{q}_{in}}{V_{im}V_{in}}\int d^3r\varepsilon(\mathbf{r})\widetilde{\mathbf{f}}_{im}^*(\mathbf{r})\cdot\widetilde{\mathbf{f}}_{in}(\mathbf{r}) \\ &= \frac{1}{2}\sum_{mn}\frac{\dot{q}_{im}^*\dot{q}_{in}}{V_{im}V_{in}}\int d^3r\varepsilon(\mathbf{r})[\mathbf{f}_{im}^*(\mathbf{r}) + \nabla\Lambda_{im}^*(\mathbf{r})]\cdot[\mathbf{f}_{in}(\mathbf{r}) + \nabla\Lambda_{in}(\mathbf{r})] \\ &= \frac{1}{2}\sum_{mn}\frac{\dot{q}_{im}^*\dot{q}_{in}}{V_{im}V_{in}}\left[V_{im}\delta_{mn} + \Sigma_{imn}\sqrt{V_{im}V_{in}}\right], \end{aligned} \tag{8.44}$$

where

$$\Sigma_{imn} = \frac{1}{\sqrt{V_{1m}V_{1n}}}\int d^3r[\varepsilon(\mathbf{r}) - \varepsilon_i(\mathbf{r})]\widetilde{\mathbf{f}}_{im}^*(\mathbf{r})\cdot\mathbf{f}_{in}(\mathbf{r}) \tag{8.45}$$

is the *intracavity* coupling strength. Thus we see this first terms yields two contributions: one which is equivalent to the single cavity case, and another that describes interactions between the modes of a single cavity. Qualitatively, these latter terms emerge because the mode functions are orthogonal over the single-cavity dielectric environment defined by $\varepsilon_i(\mathbf{r})$, but *not* the composite dielectric environment $\varepsilon(\mathbf{r})$, resulting in intracavity interactions. In the limit where the mode function $\mathbf{f}_{im}(\mathbf{r})$ does not appreciably spill into the region where $\varepsilon(\mathbf{r})$ and $\varepsilon_i(\mathbf{r})$ are different, these contributions vanish.

Next, we simplify the diagonal contributions from the magnetic portion of the Lagrangian. Because $\nabla\times\widetilde{\mathbf{f}}_{im}(\mathbf{r}) = \nabla\times\mathbf{f}_{im}(\mathbf{r})$, this proceeds in an identical manner as the single cavity case, yielding

$$\int \frac{d^3r}{8\pi}(\nabla\times\mathbf{A}_i^*)^*(\nabla\times\mathbf{A}_i) = \sum_m \frac{1}{2V_{im}}\omega_{im}^2\cdot q_{im}^*q_{im} \tag{8.46}$$

The only remaining terms are the electric and magnetic cross-terms. Starting with the former, it can be shown that

$$\int \frac{d^3r}{8\pi}\varepsilon(\mathbf{r})\dot{\mathbf{A}}_1^*\cdot\dot{\mathbf{A}}_2+\text{h.c.}=\frac{1}{2}\sum_{mn}\frac{1}{\sqrt{\omega_{1m}\omega_{2n}V_{1m}V_{2n}}}\left(g_{mn}^{(E)}\dot{q}_{1m}^*\dot{q}_{2n}+g_{mn}^{(E)*}\dot{q}_{1m}\dot{q}_{2n}^*\right) \tag{8.47}$$

with

$$g_{mn}^{(E)}=\sqrt{\frac{\omega_{1m}\omega_{2n}}{V_{1m}V_{2n}}}\int d^3r\varepsilon(\mathbf{r})[\mathbf{f}_{1m}^*(\mathbf{r})\cdot\mathbf{f}_{2n}(\mathbf{r})-\nabla\psi_{1m}^*(\mathbf{r})\cdot\nabla\psi_{2n}(\mathbf{r})], \tag{8.48}$$

where $g_{mn}^{(E)}$ has been simplified through generous use of integration by parts, along with properties such as $\nabla\cdot\varepsilon(\mathbf{r})\widetilde{\mathbf{f}}_{im}(\mathbf{r})=0$. Applying similar tricks to the to the magnetic cross-term, we find

$$\int \frac{d^3r}{8\pi}(\nabla\times\mathbf{A}_1^*)\cdot(\nabla\times\mathbf{A}_2)+\text{h.c.}=\frac{1}{2}\sum_{mn}\frac{\sqrt{\omega_{1m}\omega_{2n}}}{\sqrt{V_{1m}V_{2n}}}\left(g_{mn}^{(M)}q_{1m}^*q_{2n}+g_{mn}^{(M)*}q_{1m}q_{2n}^*\right) \tag{8.49}$$

where

$$g_{mn}^{(M)}=\frac{1}{2}\frac{1}{\sqrt{\omega_{1m}\omega_{2n}V_{1m}V_{2n}}}\int d^3r\left[\omega_{1m}^2\varepsilon_1(\mathbf{r})+\omega_{2n}^2\varepsilon_2(\mathbf{r})\right]\mathbf{f}_{1m}^*(\mathbf{r})\cdot\mathbf{f}_{2n}(\mathbf{r}). \tag{8.50}$$

Compiling all of these simplifications, the full Lagrangian can be written as

$$\begin{aligned}L=&\frac{1}{2}\sum_{i=1,2}\sum_{mn}\frac{\dot{q}_{im}^*\dot{q}_{in}}{V_{im}V_{in}}\left[V_{im}\delta_{mn}+\Sigma_{imn}\sqrt{V_{im}V_{in}}\right]-\frac{1}{2}\sum_m\frac{\omega_{im}^2}{V_{im}}|q_{im}|^2\\&+\frac{1}{2}\sum_{mn}\frac{1}{\sqrt{\omega_{1m}\omega_{2n}V_{1m}V_{2n}}}(g_{mn}^{(E)}\dot{q}_{1m}^*\dot{q}_{2n}+g_{mn}^{(E)*}\dot{q}_{1m}\dot{q}_{2n}^*)\\&-\frac{1}{2}\sum_{mn}\sqrt{\frac{\omega_{1m}\omega_{2n}}{V_{1m}V_{2n}}}(g_{mn}^{(M)}q_{1m}^*q_{2n}+g_{mn}^{(M)*}q_{1m}q_{2n}^*)\end{aligned} \tag{8.51}$$

where

$$\begin{aligned}\Sigma_{imn}&=\frac{1}{\sqrt{V_{1m}V_{1n}}}\int d^3r[\varepsilon(\mathbf{r})-\varepsilon_i(\mathbf{r})]\widetilde{\mathbf{f}}_{im}^*(\mathbf{r})\cdot\mathbf{f}_{in}(\mathbf{r})\\g_{mn}^{(E)}&=\sqrt{\frac{\omega_{1m}\omega_{2n}}{V_{1m}V_{2n}}}\int d^3r\varepsilon(\mathbf{r})[\mathbf{f}_{1m}^*(\mathbf{r})\cdot\mathbf{f}_{2n}(\mathbf{r})-\nabla\psi_{1m}^*(\mathbf{r})\cdot\nabla\psi_{2n}(\mathbf{r})]\\g_{mn}^{(M)}&=\frac{1}{2}\frac{1}{\sqrt{\omega_{1m}\omega_{2n}V_{1m}V_{2n}}}\int d^3r\left[\omega_{1m}^2\varepsilon_1(\mathbf{r})+\omega_{2n}^2\varepsilon_2(\mathbf{r})\right]\mathbf{f}_{1m}^*(\mathbf{r})\cdot\mathbf{f}_{2n}(\mathbf{r}).\end{aligned} \tag{8.52}$$

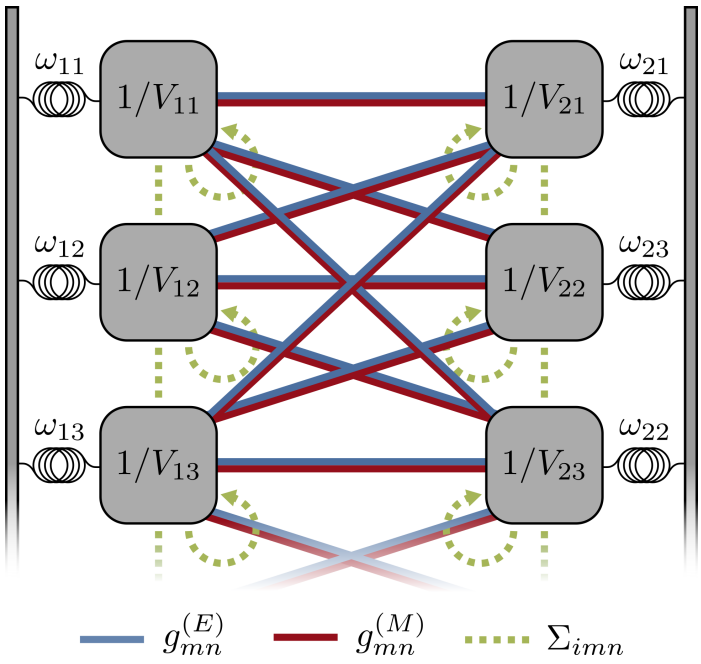

Figure 8.1: The coupled-cavity Lagrangian as coupled oscillators. As discussed in the main text, each independent cavity mode acts as a simple harmonic oscillator with resonant frequency ω_{im} where i and m label the cavity and mode, respectively. Due to the change in the dielectric environment from the one to the two cavity case, orthogonality is broken between the various modes of the ith cavity, inducing an intracavity coupling between modes m and n with strength Σ_{imn}. Separately, two intercavity couplings arise: one stemming from the electric field portion of the Lagrangian ($g^{(E)}_{mn}$) and one from the magnetic field terms ($g^{(M)}_{mn}$). The former results in an effective velocity-velocity coupling, and the latter a more typical coordinate-coordinate coupling, leading to a physical model analogous to "doubly" coupled oscillators with physical properties distinct from the "singly" coupled case.

8.4 Two single-mode cavities

Let us now proceed in the limit where each cavity contains just a single mode. For simplicity, let us assume that both mode functions are completely real. This can be done without loss of generality, as seen through the following argument: first imagine the field of a cavity is described by the single complex mode function $\mathbf{f}(\mathbf{r})$. It is straightforward to show that if $\mathbf{f}(\mathbf{r})$ is a solution to Eq. (8.4), its complex conjugate $\mathbf{f}^*(\mathbf{r})$ must also be a solution with the same eigenvalue. We can then construct the completely real functions through superposition

$$\begin{aligned} \mathbf{a}_{\mathrm{R}}(\mathbf{r}) &= [\mathbf{f}(\mathbf{r}) + \mathbf{f}^*(\mathbf{r})]/2 \\ \mathbf{a}_{\mathrm{I}}(\mathbf{r}) &= [\mathbf{f}(\mathbf{r}) - \mathbf{f}^*(\mathbf{r})]/2i. \end{aligned} \tag{8.53}$$

Because $\mathbf{f}(\mathbf{r})$ and $\mathbf{f}^*(\mathbf{r})$ are both solutions to Eq. (8.4), $\mathbf{a}_{\mathrm{R}}(\mathbf{r})$ and $\mathbf{a}_{\mathrm{I}}(\mathbf{r})$ must also be solutions with the same eigenvalue. Therefore, we can conclude that $\mathbf{a}_{\mathrm{R}}(\mathbf{r})$ and $\mathbf{a}_{\mathrm{I}}(\mathbf{r})$ are scalar multiples of one another, i.e., $\mathbf{a}_{\mathrm{R}}(\mathbf{r}) = c\mathbf{a}_{\mathrm{I}}(\mathbf{r})$ for some real scalar c. Consequently, $\mathbf{f}(\mathbf{r})$ can be made real via the rescaling

$$\mathbf{f}(\mathbf{r}) \to \frac{1 - ic}{1 + |c|^2}\mathbf{f}(\mathbf{r}). \tag{8.54}$$

Because $\mathbf{A} = \mathbf{A}^\dagger$, this also ensures the corresponding dynamical coordinate $q(t)$ is also real.

With just a single mode per cavity, the coupled-cavity Lagrangian simplifies drastically. In particular, we find

$$L = \frac{1}{2}\sum_{i=1,2}\left[\frac{\dot{q}_i^2}{V_i}(1 + \Sigma_i) - \frac{\omega_i^2}{V_i}q_i^2\right] + \frac{g_E}{\omega_1\omega_2 V_1 V_2}\dot{q}_1\dot{q}_2 - g_M\sqrt{\frac{\omega_1\omega_2}{V_1 V_2}}q_1 q_2. \tag{8.55}$$

Similar to the more general Lagrangian in Eq. (8.51), the single mode coupled cavity Lagrangian depends on the three distinct coupling parameters Σ_i, g_E, and g_M. The first of these corresponds to a self-interaction, while the latter two correspond to intercavity electric and magnetic couplings, respectively. Interestingly, we see that the above Lagrangian differs from that of standard coupled oscillators, containing terms that couple both generalized coordinates ($\propto q_1 q_2$) and generalized velocities ($\propto \dot{q}_1\dot{q}_2$). The simultaneous presence of both of these terms is not simply cosmetic, instead having fascinating physical consequences (particularly upon quantization) that will be discussed in greater detail in a future manuscript.

It is advantageous to define the renormalized mode volumes, frequencies and coupling strengths,

$$\begin{aligned}\bar{V}_i &= V_i/(1+\Sigma_i)\\ \bar{\omega}_i &= V_i/\sqrt{1+\Sigma_i}\\ \bar{g}_E &= V_i/[(1+\Sigma_1)(1+\Sigma_2)^{3/4}\\ \bar{g}_M &= V_i/[(1+\Sigma_1)(1+\Sigma_2)^{1/4}.\end{aligned} \tag{8.56}$$

such that the system Lagrangian simplifies to

$$L = \sum_{i=1,2}\frac{1}{2\bar{V}_i}\left[\dot{q}_i^2 - \bar{\omega}_i^2 q_i^2\right] + \frac{\bar{g}_E}{\bar{\omega}_1\bar{\omega}_2\bar{V}_1\bar{V}_2}\dot{q}_1\dot{q}_2 - \bar{g}_M\sqrt{\frac{\bar{\omega}_1\bar{\omega}_2}{\bar{V}_1\bar{V}_2}}q_1 q_2. \tag{8.57}$$

We now are in a position to begin answering the question which first motivated the present theoretical treatment: what are the properties of the super-modes? To that end, we now aim to diagonalize the above Lagrangian. While this can be achieved at the level of the Lagrangian, we will instead turn to the equations of motion,

$$\mathbf{V}^{-1}\ddot{\mathbf{q}} = -\mathbf{C}\mathbf{q}, \tag{8.58}$$

where

$$\begin{aligned}\mathbf{V}^{-1} &= \begin{bmatrix} 1/\bar{V}_1 & \bar{g}_E/\sqrt{\bar{\omega}_1\bar{\omega}_2\bar{V}_1\bar{V}_2} \\ \bar{g}_E/\sqrt{\bar{\omega}_1\bar{\omega}_2\bar{V}_1\bar{V}_2} & 1/\bar{V}_2 \end{bmatrix}\\ \mathbf{C} &= \begin{bmatrix} \bar{\omega}_1^2/\bar{V}_1 & \bar{g}_M\sqrt{\bar{\omega}_1\bar{\omega}_2/\bar{V}_1\bar{V}_2} \\ \bar{g}_M\sqrt{\bar{\omega}_1\bar{\omega}_2/\bar{V}_1\bar{V}_2} & \bar{\omega}_2^2/\bar{V}_2 \end{bmatrix}.\end{aligned} \tag{8.59}$$

and $\mathbf{q} = [q_1 \quad q_2]^T$. Crucially, $\mathbf{V}^{-1}$ and $\mathbf{C}$ do not in general commute, and therefore are not, in general, simultaneously diagonalizable. However, we can force Eq. (8.59) to look like "regular" coupled oscillators (i.e., coupled via coordinates) by multiplying through by $\mathbf{V}$. Carrying this out, we find

$$\frac{\mathrm{d}^2}{\mathrm{d}t^2}\begin{bmatrix} q_1 \\ q_2 \end{bmatrix} = -\begin{bmatrix} \Omega_1^2 & \mathcal{G}_{12} \\ \mathcal{G}_{21} & \Omega_2^2 \end{bmatrix}\begin{bmatrix} q_1 \\ q_2 \end{bmatrix} \tag{8.60}$$

where

$$\Omega_i^2 = \frac{\bar{\omega}_i^2 - \bar{g}_E \bar{g}_M}{1 - \bar{g}_E^2/\bar{\omega}_1\bar{\omega}_2}$$
$$\mathcal{G}_{ij} = \sqrt{\frac{\bar{\omega}_j \bar{V}_i}{\bar{\omega}_i \bar{V}_j}} \left(\frac{\bar{\omega}_i \bar{g}_M - \bar{\omega}_j \bar{g}_E}{1 - \bar{g}_E^2/\bar{\omega}_1\bar{\omega}_2} \right) \tag{8.61}$$

define effective resonant frequencies and couplings. Notably, each of these is much more complicated compared to a typical formulation of coupled oscillators, as the effective resonant frequencies themselves depend on the couplings $\bar{g}_M$ and $\bar{g}_E$. Similarly, the effective couplings $\mathcal{G}_{ij}$ depend upon the renormalized cavity frequencies in a complicated way. As will be shown below, one consequence of the complicated form of Ω_i is the appearance of coupling-induced shifts in the eigenfrequencies of two closely spaced single mode cavities (see Eq. (8.68)). This effect was previously noted in Ref. [286], there explained through introduction of additional parameters to CMT. Here, such an effect is explained via first principles as a consequence of simultaneous velocity-velocity and coordinate-coordinate coupling.

Diagonalization of Eq. (8.60) is achieved through similarity transform with respect to $\mathbf{X} = \mathbf{TRS}$ where

$$\mathbf{T} = \begin{bmatrix} (\mathcal{G}_{12}/\mathcal{G}_{21})^{1/4} & 0 \\ 0 & (\mathcal{G}_{21}/\mathcal{G}_{12})^{1/4} \end{bmatrix} \tag{8.62}$$

is a scaling matrix which forces the couplings to be symmetric,

$$\mathbf{R} = \begin{bmatrix} \cos\theta & -\sin\theta \\ \sin\theta & \cos\theta \end{bmatrix} \tag{8.63}$$

rotates the scaled coordinates into the supermode basis, and

$$\mathbf{S} = \begin{bmatrix} \alpha_+ & 0 \\ 0 & \alpha_- \end{bmatrix} \tag{8.64}$$

encodes a final scaling transformation. While $\mathbf{S}$ plays no role in diagonalizing the system, α_+ and α_- will be chosen at a later point to specify the relative scaling of the super-mode coordinates $q_\pm$ and mode functions $\mathbf{f}_\pm(\mathbf{r})$ to preserve the desired normalization condition in analogy to Eq. (8.11a).

Left multiplying Eq. (8.60) by $\mathbf{X}^{-1}$ and inserting the identity $\mathbf{X}\mathbf{X}^{-1}$ on the right-hand side, we find

$$\frac{\mathrm{d}^2}{\mathrm{d}t^2}\begin{bmatrix} q_+ \\ q_- \end{bmatrix} = -\mathbf{X}^{-1}\begin{bmatrix} \Omega_1^2 & \mathcal{G}_{12} \\ \mathcal{G}_{21} & \Omega_2^2 \end{bmatrix}\mathbf{X}\begin{bmatrix} q_+ \\ q_- \end{bmatrix} \tag{8.65}$$

where $[q_+ \quad q_-]^T = \mathbf{X}^{-1}[q_1 \quad q_2]^T$. Diagonalization of Eq. (8.65) is achieved via the choice

$$\theta = \frac{1}{2}\tan^{-1}\left(\frac{2\sqrt{(\bar{g}_E^2+\bar{g}_M^2)\bar{\omega}_1\bar{\omega}_2 - \bar{g}_E\bar{g}_M(\bar{\omega}_1^2+\bar{\omega}_2^2)}}{\bar{\omega}_1^2-\bar{\omega}_2^2}\right), \tag{8.66}$$

yielding

$$\frac{\mathrm{d}^2}{\mathrm{d}t^2}\begin{bmatrix} q_+ \\ q_- \end{bmatrix} = \begin{bmatrix} \omega_+^2 & 0 \\ 0 & \omega_-^2 \end{bmatrix}\begin{bmatrix} q_+ \\ q_- \end{bmatrix} \tag{8.67}$$

with supermode frequencies defined as

$$\omega_\pm^2 = \frac{\widetilde{\omega}_1^2+\widetilde{\omega}_2^2}{2} - \widetilde{g}_E\widetilde{g}_M \pm \frac{1}{2}\sqrt{(\widetilde{\omega}_1^2-\widetilde{\omega}_2^2)^2 + 4\mathcal{G}_{12}\mathcal{G}_{21}}. \tag{8.68}$$

Here, we have adopted the additional shorthand

$$\begin{aligned} \widetilde{\omega}_i &= \bar{\omega}_i/\sqrt{1-\bar{g}_E^2/\bar{\omega}_1\bar{\omega}_2} \\ \widetilde{g}_E &= \bar{g}_E/\sqrt{1-\bar{g}_E^2/\bar{\omega}_1\bar{\omega}_2} \\ \widetilde{g}_M &= \bar{g}_M/\sqrt{1-\bar{g}_E^2/\bar{\omega}_1\bar{\omega}_2} \end{aligned} \tag{8.69}$$

to indicate further rescaling by $\sqrt{\det(\mathbf{V}^{-1})}$.

8.5 Hybridized mode functions and mode volumes

While much of the above discussion has involved a theoretical framework which depends upon integrating out all spatial information, we will now show that the transformation $\mathbf{X}$ contains sufficient information to solve for the super-mode field profiles $\mathbf{f}_\pm(\mathbf{r})$. To illustrate this, we first write the vector potential in the form

$$\mathbf{A}(\mathbf{r},t) = \sqrt{4\pi}c\begin{bmatrix} \widetilde{\mathbf{f}}_1(\mathbf{r})/V_1 & \widetilde{\mathbf{f}}_2(\mathbf{r})/V_2 \end{bmatrix}\mathbf{X}\mathbf{X}^{-1}\begin{bmatrix} q_1(t) \\ q_2(t) \end{bmatrix}, \tag{8.70}$$

where we have inserted the identity $\mathbf{X}\mathbf{X}^{-1}$. As shown in the previous section, $\mathbf{X}^{-1}$ transforms the dynamical coordinates into the super-mode basis. It then stands to reason that what remains must transform the left-hand vector into the super-mode basis. In other words,

$$\mathbf{A}(\mathbf{r},t) = \sqrt{4\pi}c \begin{bmatrix} \mathbf{f}_+(\mathbf{r})/V_+ & \mathbf{f}_-(\mathbf{r})/V_- \end{bmatrix} \begin{bmatrix} q_+(t) \\ q_-(t) \end{bmatrix}, \tag{8.71}$$

where

$$\begin{bmatrix} \mathbf{f}_+(\mathbf{r})/V_+ & \mathbf{f}_-(\mathbf{r})/V_- \end{bmatrix} = \begin{bmatrix} \widetilde{\mathbf{f}}_1(\mathbf{r})/V_1 & \widetilde{\mathbf{f}}_2(\mathbf{r})/V_2 \end{bmatrix} \mathbf{X}. \tag{8.72}$$

Carrying out the algebra, we find,

$$\begin{aligned} \mathbf{f}_+(\mathbf{r}) &= \frac{V_+}{\alpha_+}\left[\left(\frac{\mathcal{G}_{12}}{\mathcal{G}_{21}}\right)^{1/4}\frac{\widetilde{\mathbf{f}}_1(\mathbf{r})}{V_1}\cos\theta + \left(\frac{\mathcal{G}_{21}}{\mathcal{G}_{12}}\right)^{1/4}\frac{\widetilde{\mathbf{f}}_2(\mathbf{r})}{V_2}\sin\theta\right] \\ \mathbf{f}_-(\mathbf{r}) &= \frac{V_-}{\alpha_-}\left[-\left(\frac{\mathcal{G}_{12}}{\mathcal{G}_{21}}\right)^{1/4}\frac{\widetilde{\mathbf{f}}_1(\mathbf{r})}{V_1}\sin\theta + \left(\frac{\mathcal{G}_{21}}{\mathcal{G}_{12}}\right)^{1/4}\frac{\widetilde{\mathbf{f}}_2(\mathbf{r})}{V_2}\cos\theta\right]. \end{aligned} \tag{8.73}$$

We note that this transformation alone does not uniquely determine either the mode functions or the mode volumes, only their ratio $\mathbf{f}_\pm(\mathbf{r})/V_\pm$. A unique solution therefore requires a particular normalization of $\mathbf{f}_\pm(\mathbf{r})$. Ideally, the super-mode solutions to the two-cavity scenario should be consistent with the treatment of a single-cavity, albeit now defined by some composite dielectric function $\varepsilon(\mathbf{r})$. Naturally, we wish to enforce the properties identified in Section 8.1.1. In particular, we desire solutions which obey the following

1. $\max\{\varepsilon(\mathbf{r})\mathbf{f}_\pm(\mathbf{r})\cdot\mathbf{f}_\pm(\mathbf{r})\} = 1$ (normalization)

2. $\displaystyle\int d^3r\varepsilon(\mathbf{r})\mathbf{f}_\pm(\mathbf{r})\cdot\mathbf{f}_\pm(\mathbf{r}) = V_\pm$ (mode volume)

3. $\displaystyle\int d^3r\varepsilon(\mathbf{r})\mathbf{f}_\pm(\mathbf{r})\cdot\mathbf{f}_\mp(\mathbf{r}) = 0$ (orthogonality)

4. $\nabla\times\nabla\times\mathbf{f}_\pm(\mathbf{r}) = \varepsilon(\mathbf{r})(\omega_\pm^2/c^2)\mathbf{f}_\pm(\mathbf{r})$ (Helmholtz equation)

The desired normalization (Property 1) is enforced through appropriate choice of α_+ and α_-, the elements of the scaling transformation matrix $\mathbf{S}$. Carrying out the algebra, we find

the solutions

$$\begin{aligned}\mathbf{f}_+(\mathbf{r}) &= \frac{1}{A(\theta)}\left[\left(\frac{\mathcal{G}_{12}}{\mathcal{G}_{21}}\right)^{1/4}\sqrt{\frac{V_2}{V_1}}\widetilde{\mathbf{f}}_1(\mathbf{r})\cos\theta + \left(\frac{\mathcal{G}_{21}}{\mathcal{G}_{12}}\right)^{1/4}\sqrt{\frac{V_1}{V_2}}\widetilde{\mathbf{f}}_2(\mathbf{r})\sin\theta\right] \\ \mathbf{f}_-(\mathbf{r}) &= \frac{1}{B(\theta)}\left[\left(\frac{\mathcal{G}_{21}}{\mathcal{G}_{12}}\right)^{1/4}\sqrt{\frac{V_1}{V_2}}\widetilde{\mathbf{f}}_2(\mathbf{r})\cos\theta - \left(\frac{\mathcal{G}_{12}}{\mathcal{G}_{21}}\right)^{1/4}\sqrt{\frac{V_2}{V_1}}\widetilde{\mathbf{f}}_1(\mathbf{r})\sin\theta\right]\end{aligned} \tag{8.74}$$

and their associated mode volumes

$$\begin{aligned}V_+ &= V_1\left[\frac{V_2}{V_1}\left(\frac{\mathcal{G}_{12}}{\mathcal{G}_{21}}\right)^{\frac{1}{2}}\frac{1+\Sigma_1}{A(\theta)^2}\right]\cos^2\theta + V_2\left[\frac{V_1}{V_2}\left(\frac{\mathcal{G}_{21}}{\mathcal{G}_{12}}\right)^{\frac{1}{2}}\frac{1+\Sigma_2}{A(\theta)^2}\right]\sin^2\theta + \sqrt{V_1V_2}\left[\frac{g_E/\sqrt{\omega_1\omega_2}}{A(\theta)^2}\right]\sin 2\theta \\ V_- &= V_1\left[\frac{V_2}{V_1}\left(\frac{\mathcal{G}_{12}}{\mathcal{G}_{21}}\right)^{\frac{1}{2}}\frac{1+\Sigma_1}{B(\theta)^2}\right]\sin^2\theta + V_2\left[\frac{V_1}{V_2}\left(\frac{\mathcal{G}_{21}}{\mathcal{G}_{12}}\right)^{\frac{1}{2}}\frac{1+\Sigma_2}{B(\theta)^2}\right]\cos^2\theta - \sqrt{V_1V_2}\left[\frac{g_E/\sqrt{\omega_1\omega_2}}{B(\theta)^2}\right]\sin 2\theta\end{aligned} \tag{8.75}$$

where

$$\begin{aligned}A(\theta) = \alpha_+\frac{\sqrt{V_1V_2}}{V_+} &= \sqrt{\mathrm{Max}\left\{\varepsilon(\mathbf{r})\left[\left(\frac{\mathcal{G}_{12}}{\mathcal{G}_{21}}\right)^{1/4}\sqrt{\frac{V_2}{V_1}}\widetilde{\mathbf{f}}_1(\mathbf{r})\cos\theta + \left(\frac{\mathcal{G}_{21}}{\mathcal{G}_{12}}\right)^{1/4}\sqrt{\frac{V_1}{V_2}}\widetilde{\mathbf{f}}_2(\mathbf{r})\sin\theta\right]^2\right\}} \\ B(\theta) = \alpha_-\frac{\sqrt{V_1V_2}}{V_-} &= \sqrt{\mathrm{Max}\left\{\varepsilon(\mathbf{r})\left[\left(\frac{\mathcal{G}_{21}}{\mathcal{G}_{12}}\right)^{1/4}\sqrt{\frac{V_1}{V_2}}\widetilde{\mathbf{f}}_2(\mathbf{r})\cos\theta - \left(\frac{\mathcal{G}_{12}}{\mathcal{G}_{21}}\right)^{1/4}\sqrt{\frac{V_2}{V_1}}\widetilde{\mathbf{f}}_1(\mathbf{r})\sin\theta\right]^2\right\}}.\end{aligned} \tag{8.76}$$

Importantly, the above definitions are also consistent with Properties 2 and 3, both of which can be verified through brute force algebraic calculation. Essential to a proof of Property 3 is enforcement of a mixing angle θ consistent with Eq. (8.66), adding validity to the uniqueness of the determined solutions. Finally, proof of Property 4 is fairly straightforward through the following argument. Prior to transformation, the vector potential is expanded as

$$\mathbf{A}(\mathbf{r},t) = \sqrt{4\pi}c\left[\frac{q_1(t)}{V_1}\widetilde{\mathbf{f}}_1(\mathbf{r}) + \frac{q_2(t)}{V_2}\widetilde{\mathbf{f}}_2(\mathbf{r})\right] \tag{8.77}$$

and post-transformation becomes

$$\mathbf{A}(\mathbf{r},t) = \sqrt{4\pi}c\left[\frac{q_+(t)}{V_+}\mathbf{f}_+(\mathbf{r}) + \frac{q_-(t)}{V_-}\mathbf{f}_-(\mathbf{r})\right] \tag{8.78}$$

The vector potential must be a solution to the sourceless wave equation

$$\nabla\times\nabla\times\mathbf{A} + \frac{\varepsilon(\mathbf{r})}{c^2}\ddot{\mathbf{A}} = 0. \tag{8.79}$$

Importantly, $\mathbf{A}$ is completely unchanged upon transformation, so we are free to substitute in either its pre- or post-transformation form. However, because q_1 and q_2 are coupled (see Eq. (8.60)), substitution of the pre-transformation form of $\mathbf{A}$ will yield coupled wave equations. In contrast, substitution of the mode expansion in normal coordinates results in

$$\begin{aligned} 0 &= \frac{q_+}{V_+}\nabla\times\nabla\times\mathbf{f}_+(\mathbf{r}) + \frac{q_-}{V_-}\nabla\times\nabla\times\mathbf{f}_-(\mathbf{r}) + \frac{\varepsilon(\mathbf{r})}{c^2}\frac{\ddot{q}_+}{V_+}\mathbf{f}_+(\mathbf{r}) + \frac{\varepsilon(\mathbf{r})}{c^2}\frac{\ddot{q}_-}{V_-}\mathbf{f}_-(\mathbf{r}) \\ &= \frac{q_+}{V_+}\left\{\nabla\times\nabla\times\mathbf{f}_+(\mathbf{r}) - \varepsilon(\mathbf{r})\frac{\omega_+^2}{c^2}\mathbf{f}_+(\mathbf{r})\right\} + \frac{q_-}{V_-}\left\{\nabla\times\nabla\times\mathbf{f}_-(\mathbf{r}) - \varepsilon(\mathbf{r})\frac{\omega_-^2}{c^2}\mathbf{f}_-(\mathbf{r})\right\}, \end{aligned} \tag{8.80}$$

where we have used the fact that $\ddot{q}_\pm = -\omega_\pm^2 q_\pm$. Noting that (i) the mode functions are orthogonal and (ii) the coordinates q_+ and q_- independent, it must be true that

$$\begin{aligned} \nabla\times\nabla\times\mathbf{f}_+(\mathbf{r}) &= \varepsilon(\mathbf{r})\frac{\omega_+^2}{c^2}\mathbf{f}_+(\mathbf{r}) \\ \nabla\times\nabla\times\mathbf{f}_-(\mathbf{r}) &= \varepsilon(\mathbf{r})\frac{\omega_-^2}{c^2}\mathbf{f}_-(\mathbf{r}). \end{aligned} \tag{8.81}$$

In summary, we have successfully constructed solutions to the Helmholtz equation

$$\nabla\times\nabla\times\mathbf{f}_\pm(\mathbf{r}) = \varepsilon(\mathbf{r})\frac{\omega_\pm}{c^2}\mathbf{f}_\pm(\mathbf{r}) \tag{8.82}$$

given only knowledge of the solutions to

$$\nabla\times\nabla\times\mathbf{f}_i(\mathbf{r}) = \varepsilon_i(\mathbf{r})\frac{\omega_i}{c^2}\mathbf{f}_i(\mathbf{r}). \tag{8.83}$$

Such a framework has grand implications for theoretical analysis of photonic molecules – typically, one would use FDTD electromagnetic solvers to determine the modes of these structures. Depending on the specifics of the photonic molecule, the computational cost of brute force simulation is, at best, extremely expensive and, at worst, completely prohibitive. An example of the latter situation is presented in Chapter 9 where we analyze a heterogeneous photonic molecule composed of individual cavities of vastly different length scales. However, the formalism presented here provides an alternate pathway for analysis where one need only solve for the modes of the independent cavities and "stitch" them together using analytics. The next Section concludes this Chapter with an example of this being carried out for a simple photonic molecule composed of two photonic crystal cavities.

8.6 Example: Two photonic crystal nanobeam cavities

As an example, we apply the above theory to a system consisting of two coupled photonic crystal cavities. Photonic crystals are a broad class of fabricated structures with a spatially periodic dielectric function. Similar to their solid-state namesake, this periodicity can create an electromagnetic bandgap, disallowing propagation of light through the structure across a particular range of frequencies. If the dielectric function is defected (e.g., tapering of the holes in Fig. 8.2a), however, light can become "trapped", confined along (perpendicular to) the direction of periodicity due to Bragg reflection (total internal reflection) [287]. When well-designed, defected photonic crystals (sometimes referred to as nanobeams in the one-dimensional case [288]) serve as high Q realizations of a single-mode cavity, ideal for testing the theoretical formalism presented here. In computing super-mode resonant frequencies (Fig. 8.2b) and mode functions (Fig. 8.3), only two pieces of information were used:

1. The dielectric function of a single nanobeam resonator $\varepsilon_0(\mathbf{r})$

2. The field profile of the nanobeam resonator mode $\mathbf{f}_0(\mathbf{r})$ (solved for using finite-difference time-domain methods, carried out by collaborator Yueyang Chen)

Both super-mode frequencies and mode functions show excellent agreement with simulation. Mode volumes are not shown as they aren't especially interesting in the present case due to the high symmetry – both V_+ and V_- are approximately equal to twice the mode volume of the isolated nanobeam, $2V_0$, with only a slow decrease across the cavity-cavity separations studied resulting from field build-up across the gap (see Fig. 8.3). For a more interesting study of mode volume evolution, see Chapter 9.

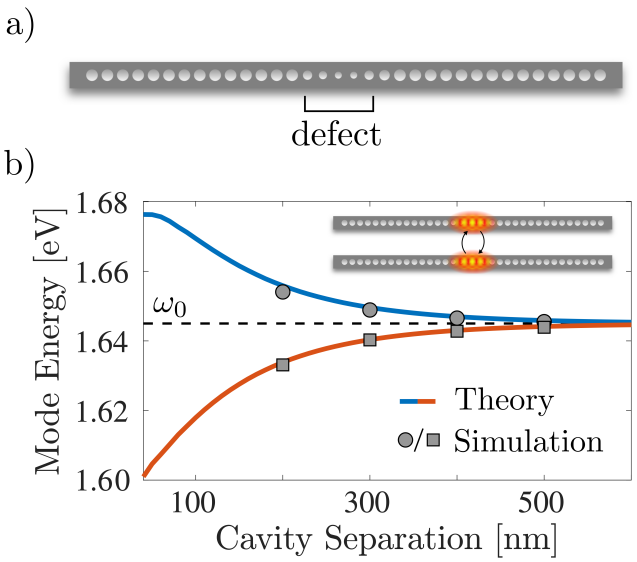

Figure 8.2: (a) An illustration of a photonic crystal nanobeam cavity. (b) Comparison between theoretically predicted and simulated normal mode energies. The dashed line labels the bare resonant frequency ω_0 of an isolated nanobeam cavity. Only cavity separations up to 200 nm were computed due to issues of convergence.

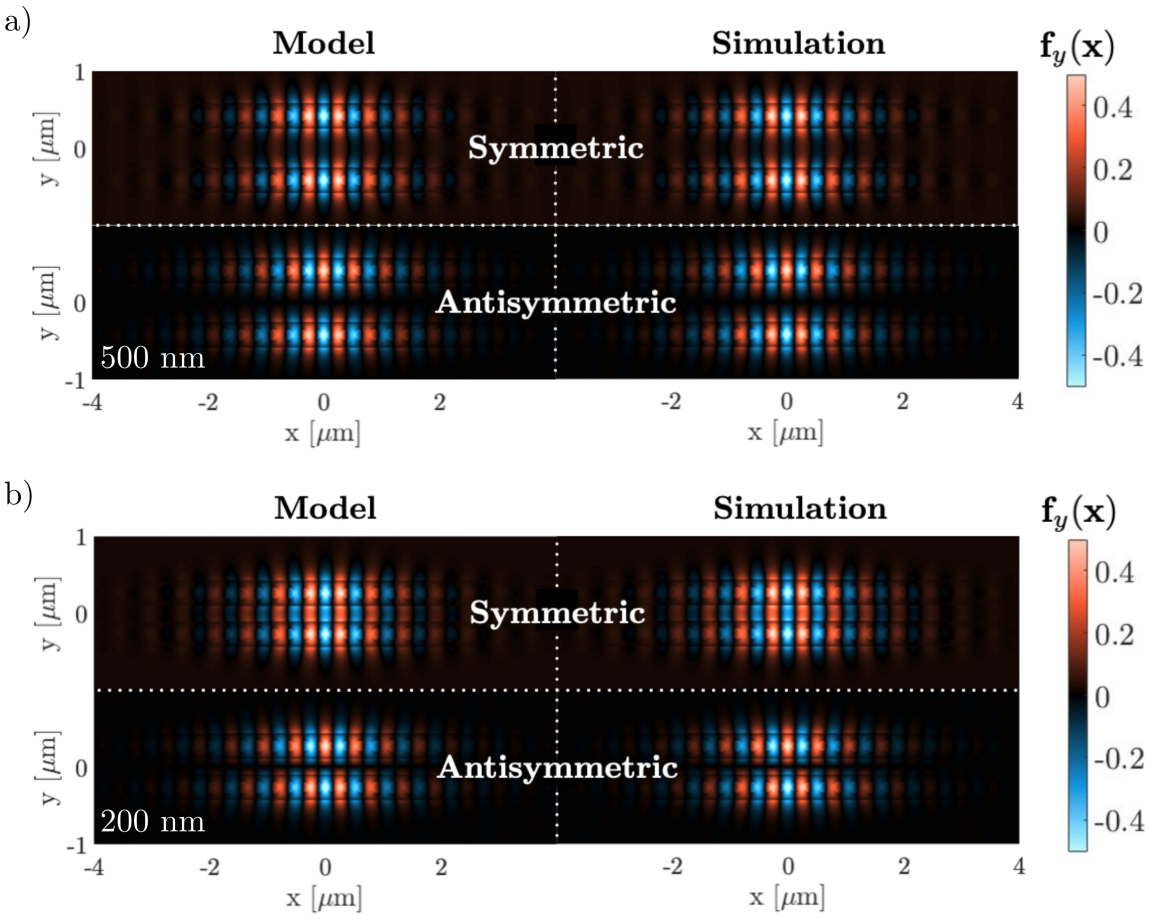

Figure 8.3: Comparison between the y-component of the theoretically predicted and simulated super-mode field profiles for (a) 500 nm and (a) 200 nm, showing excellent agreement.

Chapter 9

ACTIVE TUNING OF HYBRIDIZED MODES IN A HETEROGENEOUS PHOTONIC MOLECULE

From fundamental discovery to practical application, advances in the optical and quantum sciences rely upon precise control of light-matter interactions. Systems of coupled optical cavities are ubiquitous in these efforts, yet design and active modification of the hybridized mode properties remains challenging. Here, we demonstrate the design, fabrication, and analysis of a tunable heterogeneous photonic molecule consisting of a ring resonator strongly coupled to a nanobeam photonic crystal cavity. Leveraging the disparity in mode volume between these two strongly coupled cavities, we combine theory and experiment to establish the ability to actively tune the mode volume of the resulting super-modes over a full order of magnitude. As the mode volume determines the strength of light-matter interactions, this work illustrates the potential for strongly coupled cavities with dissimilar mode volumes in applications requiring designer photonic properties and tunable light-matter coupling, such as photonics-based quantum simulation.

9.1 Introduction

Coupled optical microcavities serve as a basic building block for many integrated photonic systems and technologies. Similar to the way bound electronic states of individual atoms couple to form those of a molecule, confined photonic excitations of two or more optical cavities can electromagnetically interact to form so-called "photonic molecules" [289, 290, 291, 292, 293, 294]. Electronic excitations in molecules are described through hybridization of the orbitals of the constituent atoms and, in analogy, the electromagnetic super-modes of photonic molecules can be constructed by blending the resonances of the individual cavities. While single cavities are instrumental to a diverse set of applications ranging from single

photon generation [295, 296, 297, 99] and strong light-matter coupling [298, 299, 300, 301] to sensing [180, 302, 303, 304, 305, 23, 22, 24, 207] and cavity-controlled chemistry [27, 29, 31, 28, 30, 26], systems of two or more cavities have shown promise in a number of applications, including low-threshold lasing [272, 273, 306], cavity optomechanics [307, 308, 309], nonclassical light generation [277, 278, 310, 311, 279, 280, 312], quantum simulation [36, 281, 35, 313, 37], and biochemical sensing [314, 315].

Critical to the advantages of photonic molecules over individual cavities is the ability to engineer designer super-modes with properties that differ from those of the constituent components. Of particular interest are coupled cavity structures whose optical properties evolve with tunable parameters such as cavity-cavity separation and detuning. In recent years, the active tuning of such photonic molecules has been demonstrated in several experiments [294, 90, 309], but all have focused on coupled structures composed of near-identical individual cavities. While these devices are useful for many applications, homogeneity of the constituent cavities limits the dynamic range of the resulting super-mode properties such as the mode volume, important both for the scaling of light-matter coupling and Purcell enhancement.

In contrast, a heterogeneous photonic molecule composed of two distinctly different cavities allows for a richer set of emergent properties with a wider scope of applications, such as improved single photon indistinguishability of quantum emitters [312, 280]. However, lack of a theoretical framework analogous to molecular orbital theory that is capable of elucidating the dependencies of the composite system upon single cavity parameters makes design and analysis of coupled optical cavities difficult. Absent such a formalism, prediction of super-mode field profiles and other downstream properties such as hybridized resonant frequencies and mode volumes must be left to numerical simulation. The latter can be costly for all but the simplest coupled cavities and impossible for many heterogeneous systems, providing impetus for theoretical advances in understanding cavity mode hybridization.

In this Chapter, we demonstrate thermally tunable hybridization of optical cavity modes in a heterogeneous photonic molecule composed of a ring resonator and a nanobeam photonic crystal (PhC) cavity. This is achieved by embedding the coupled cavity structure in a high thermo-optic coefficient polymer that preferentially blue-shifts the nanobeam reso-

nance relative to the ring due to the "air-mode" design of the PhC cavity [316]. To better understand the resulting super-modes of this heterogeneous optical system, we introduce a theoretical framework which provides rigorous underpinnings to the more familiar coupled mode theory for hybridized cavity systems and, for the first time, derive analytic expressions for the super-mode field profiles and mode volumes expressed in terms of the single cavity field profiles. Using this formalism, we demonstrate the ability to extract crucial system parameters, such as the bare resonant frequencies and couplings, as a function of the temperature-dependent detuning. Lastly, we use this theory to predict the evolution of the resonant frequencies, field profiles, and hybridized mode volumes of the two super-modes, revealing a temperature-dependent progression which spans a full order of magnitude and results in the coalescence of the two mode volumes near zero detuning.

9.2 Experiment: thermal control of mode detuning

Fig. 9.1a. displays a scanning electron microscope (SEM) image of the heterogeneous, coupled cavity system fabricated on a 220 nm thick silicon nitride film, grown on thermal oxide on a silicon substrate. The pattern is defined by e-beam lithography and reactive ion etching [317]. The nanobeam cavity is designed such that a significant portion of the cavity field is concentrated in SU-8 polymer, which both forms a cladding for the entire device and fills the holes of the PhC [316] (see Fig. 9.1b). In contrast, the ring resonator mode is predominantly confined within the silicon nitride. Due to the relatively high thermo-optic coefficient of the polymer ($\sim -10^{-4}/^{\circ}\mathrm{C}$), which is nearly an order of magnitude larger than that of silicon nitride, heating the entire device leads to a blue-shift of the nanobeam cavity mode relative to that of the ring. The detuning between the ring and nanobeam modes can therefore be reversibly controlled by changing the temperature.

To investigate the effect of ring-nanobeam mode detuning, the transmission spectrum is measured through the nanobeam PhC cavity for a range of temperatures spanning $33.5 - 73.5^{\circ}\mathrm{C}$. Spectra are measured using a supercontinuum laser which is coupled to the system via an on-chip grating (see Fig. 1a). The transmitted light is collected through the opposite grating and is sent to the spectrometer. While the gratings already provide a spatial separation to improve the signal to noise ratio, a pinhole is used in the confocal mi-

croscopy setup to collect light only from the output grating. The temperature of the entire chip is controlled using a hot-plate. Fig. 9.1c displays the resulting transmission spectra (gray circles) for a subset of temperatures, with additional measurements included in the Supplemental Material. As the cavity modes of the ring and nanobeam are coupled, it is difficult to distinguish how much of the energy separation between transmission peaks at each temperature is due to detuning versus mode splitting resulting from coupling.

Understanding the impact of these individual contributions and analysis of emergent properties requires a theoretical formalism capable of describing the super-modes of the coupled ring-nanobeam structure. Coupled mode theory provides one such approach, but typically relies on several phenomenological rates which simplify modeling, often at the expense of over-simplifying the underlying physics. Furthermore, coupled mode theory does not provide a means to predict super-mode properties of interest for heterogeneous photonic molecules, such as hybridized mode volumes. To amend these deficiencies we develop a first principles theory that provides analytic understanding of the super-mode resonant frequencies, field profiles, and volumes based only upon knowledge of the individual, uncoupled cavities.

9.2.1 Theoretical model

The resonant modes of an optical cavity are given by the independent harmonic solutions of the wave equation

$$\nabla \times \nabla \times \mathbf{A}(\mathbf{x}, t) + \frac{\varepsilon(\mathbf{x})}{c^2} \ddot{\mathbf{A}}(\mathbf{x}, t) = \mathbf{0}, \tag{9.1}$$

where $\mathbf{A}$ is the vector potential related to the cavity fields by the usual relations $\mathbf{E} = -\dot{\mathbf{A}}/c$ and $\mathbf{B} = \nabla \times \mathbf{A}$, $\varepsilon(\mathbf{x})$ is the dielectric function of the structure of interest, and c is the speed of light. As is typical for cavity quantum electrodynamics calculations, we work entirely in the generalized Coulomb gauge defined by $\nabla \cdot \varepsilon(\mathbf{x})\mathbf{A}(\mathbf{x}) = 0$ which leads to a vanishing scalar potential for systems without free charge [44, 41]. While optical cavities may alternatively be described at the level of the fields themselves, the vector potential accommodates a more natural basis for both a Lagrangian formulation of the cavity dynamics and canonical quantization [39].

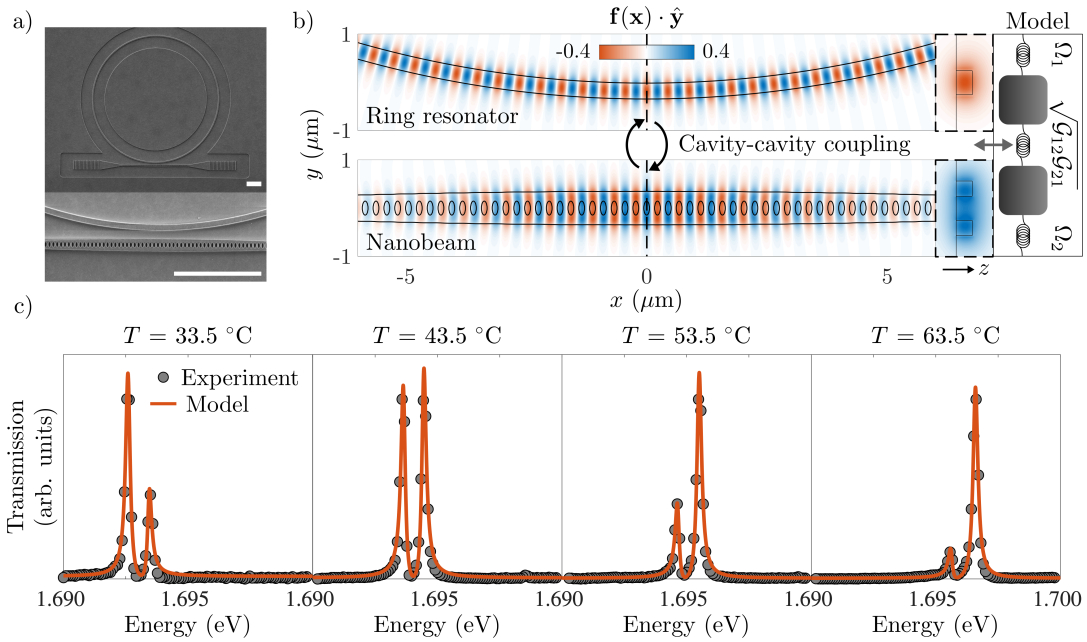

Figure 9.1: (a) SEM image of the SU-8 cladded, coupled ring resonator-nanobeam device with a 500 nm gap between ring and nanobeam at the point of closest separation. Scale bar: 5 μm. (b) y-component of the electric field profiles for the nanobeam cavity mode (bottom) and ring resonator mode (top) studied. The system is modeled as a coupled oscillator, parameterized by an effective coupling strength $\sqrt{\mathcal{G}_{12}\mathcal{G}_{21}}$ and effective frequencies Ω_i distinct from the bare resonant frequencies ω_i. (c) Transmission spectra collected for four equally-spaced temperatures (gray circles) with simultaneous least-squares fits to the model overlaid (red lines).

Given $\varepsilon(\mathbf{x})$, it is in principle straightforward to numerically solve for the modes of the two-cavity structure in Fig. 9.1a. Such an approach, however, offers limited predictivity and insight into the interaction between the individual ring resonator and nanobeam modes. In addition, the vastly different length scales of the ring resonator and nanobeam cavity make electromagnetic simulations of the coupled structures computationally challenging, rendering a purely numerical exploration of parameter space infeasible. A more flexible strategy is to numerically solve for the modes of the individual, uncoupled cavities. With the aid of analytics, these individual modes may then be appropriately mixed to form super-modes dependent on basic system parameters such as the spectral detuning and physical separation between the cavities.

Considering just a single cavity mode of both the ring resonator and nanobeam, the vector potential for the double cavity structure can be expanded as

$$\mathbf{A}(\mathbf{x},t) = \sum_{i=1,2} \frac{\sqrt{4\pi}c}{V_i} q_i(t)\mathbf{f}_i(\mathbf{x}). \tag{9.2}$$

Here, $i = 1, 2$ corresponds to the ring and nanobeam, respectively, while $\mathbf{f}_i(\mathbf{x})$ is a mode function of the ith cavity and $q_i(t)$ a time-dependent amplitude. The former are normalized such that the mode volume [48, 49, 50] is given by

$$V_i = \frac{\int d^3x\, \varepsilon_i(\mathbf{x})\, |\mathbf{E}_i(\mathbf{x})|^2}{\max[\varepsilon_i(\mathbf{x})\, |\mathbf{E}_i(\mathbf{x})|^2]} = \int d^3x\, \varepsilon_i(\mathbf{x})\, |\mathbf{f}_i(\mathbf{x})|^2 \,. \tag{9.3}$$

The mode expansion in Eq. (9.2) is approximate and, in general, requires additional terms to ensure Gauss's law is obeyed [318, 319]. However, these contributions only become physically relevant at small inter-cavity separations where the evanescent field of one cavity "spills" into the dielectric medium composing the other, and therefore may be ignored for the ring-nanobeam resonator studied (see Supplemental Material).

The resonant super-mode frequencies are most easily computed through diagonalization of the equations of motion for the generalized coordinates q_i. Deriving such equations is straightforward using standard techniques of Lagrangian mechanics (see Appendix A), but an equivalent route involves directly integrating Eq. (9.1) [271]. Regardless of the approach, the coupled equations of motion are

$$\frac{d^2}{dt^2}\begin{bmatrix} q_1 \\ q_2 \end{bmatrix} = \begin{bmatrix} \Omega_1^2 & \mathcal{G}_{12} \\ \mathcal{G}_{21} & \Omega_2^2 \end{bmatrix}\begin{bmatrix} q_1 \\ q_2 \end{bmatrix}, \tag{9.4}$$

where $\Omega_i^2 = (\bar{\omega}_i^2 - \bar{g}_E\bar{g}_M)/(1 - \bar{g}_E^2/\bar{\omega}_1\bar{\omega}_2)$ and $\mathcal{G}_{ij} = \sqrt{\bar{\omega}_j\bar{V}_i/\bar{\omega}_i\bar{V}_j}\,(\bar{\omega}_i\bar{g}_M - \bar{\omega}_j\bar{g}_E)\,/(1 - \bar{g}_E^2/\bar{\omega}_1\bar{\omega}_2)$ define effective resonant frequencies and couplings.

These coupled equations of motion differ from those often assumed in application of coupled mode theory to multiple cavity systems [79, 320, 294]. In particular, the diagonal elements of the above coefficient matrix are distinct from the bare resonance frequencies ω_i. This is a consequence of the absence of a weak coupling approximation, resulting in coupling-induced resonance shifts [286] that scale as higher-order products of the three distinct coupling parameters corresponding to the electric (g_E) and magnetic (g_M) inter-cavity couplings, and the polarization-induced intra-cavity self-interaction (Σ_i) defined by

$$\begin{aligned} g_E &= \sqrt{\frac{\omega_1\omega_2}{V_1V_2}}\int d^3x\,\varepsilon(\mathbf{x})\mathbf{f}_1(\mathbf{x})\cdot\mathbf{f}_2(\mathbf{x}) \\ g_M &= \frac{1}{2}\sqrt{\frac{1}{\omega_1\omega_2V_1V_2}}\int d^3x\,\left[\omega_1^2\varepsilon_1(\mathbf{x}) + \omega_2^2\varepsilon_2(\mathbf{x})\right]\mathbf{f}_1(\mathbf{x})\cdot\mathbf{f}_2(\mathbf{x}) \\ \Sigma_i &= \sqrt{\frac{1}{V_1V_2}}\int d^3x\,\left[\varepsilon(\mathbf{x}) - \varepsilon_i(\mathbf{x})\right]|\mathbf{f}_i(\mathbf{x})|^2\,. \end{aligned} \tag{9.5}$$

The intra-cavity self-interaction Σ_i does not explicitly appear in Eq. (9.4) as all inter-cavity couplings, resonant frequencies (ω_i), and mode volumes (V_i) have been replaced by renormalized counterparts (indicated by a bar), defined explicitly in Appendix A.

While coupled mode theory often reduces cavity-mode interactions to a single coupling parameter independent of the detuning, we note that this is not completely accurate, and more rigorous first-principles treatments relying on tight-binding methods [271, 321] have revealed three distinct coupling parameters in agreement with those defined above. However, as shown in Eq. (9.4), these three parameters may be combined, along with the resonant frequencies, to form effective coupled oscillator equations which account for these subtleties. Notably, all parameters may be computed given only the dielectric function composing the individual cavities along with associated field mode profiles.

9.3 *Extracting system parameters*

Aided by the effective oscillator equations in Eq. (9.4), the transmission spectrum is derived through standard input-output methods [79, 77], yielding

$$\mathcal{T}(\omega) = \left| \frac{\kappa}{\omega - \Omega_1 + i\kappa + \frac{\mathcal{G}_{12}\mathcal{G}_{21}/4\Omega_1\Omega_2}{\omega - \Omega_2}} \right|^2 . \tag{9.6}$$

Simultaneous least-squares fits are performed to transmission spectra at the eight experimentally probed temperatures shown in Fig. 9.1c and the Supplemental Material. To minimize the number of free parameters, Σ_1, Σ_2, V_1 and V_2 are calculated using the theory, supplemented by numerically calculated single cavity field profiles. Similarly, g_E and g_M are constrained to within $\pm 1\%$ of their theoretical values, while the waveguide-induced dissipation rate κ is estimated from electromagnetic simulation of the nanobeam.

The remaining free parameters, displayed in the top row of Table 9.1, are extracted through a simultaneous least-squares fit to all measured transmission spectra. Among them is the resonant frequency of both the ring resonator and nanobeam at room temperature T_0 and associated intrinsic dissipation rates, the latter of which may be introduced via input-output theory in the standard way by generalizing Ω_1 and Ω_2 to be complex-valued [79]. We find that the temperature dependence of the resonant wavelength of each cavity is well-approximated as linear. All other parameters are assumed to depend negligibly upon temperature and are treated as constant. Even with these simplifying approximations, agreement between experiment (circles) and theory (solid lines) is excellent, as evident in Fig. 9.1c.

Fig. 9.2a displays the full set of transmission measurements (circles) and fits (curves) for all eight probed temperatures, while Fig. 9.2b shows the super-mode resonant frequencies ($\omega_\pm$) as a function of energy detuning $\hbar\omega_2 - \hbar\omega_1$. For each temperature measured, resonant frequencies are estimated from the peaks in transmission spectra and are shown as black circles. Theory curves (red and blue) are computed through diagonalization of the effective oscillator model in Eq. (9.4) which we parameterize according to Table 9.1. Because both ring and nanobeam modes blue-shift with increasing temperature, plotted curves and points are shifted with respect to the average resonant energy $\omega_{\text{avg}} = (\omega_+ + \omega_-)/2$ for both panels.

Table 9.1: Parameter Estimates

$\hbar\omega_1(T_0)$	$\hbar\omega_2(T_0)$	$d\lambda_1/dT$	$d\lambda_2/dT$	$\hbar\gamma_1$	$\hbar\gamma_2$	
1.6922 eV	1.6918 eV	-39 pm/°nC	-50 pm/°nC	0.16 meV	0.23 meV	
V_1	V_2	κ	$\hbar g_E$	$\hbar g_M$	Σ_1	Σ_2
5.0 μm^3	0.49 μm^3	9.7 μeV	-16.4 meV	-15.6 meV	1.1×10^{-5}	8.5×10^{-5}

The resonant frequencies undergo an anticrossing as the system nears zero detuning around $T = 40$ °C, with upper and lower cavity polariton energies differing by ~ 0.8 meV. Because the coupled oscillator model is parameterized by the effective frequencies Ω_1 and Ω_2, and not the bare cavity resonances ω_1 and ω_2, the anticrossing occurs where the former, and not the latter, are co-resonant. Thus, the anticrossing in Fig. 9.2 is slightly shifted from zero detuning. In addition, the super-mode resonances $\omega_\pm$ tend towards the effective frequencies (dotted lines) at large positive and negative values of the detuning. Strong coupling is confirmed quantitatively through comparison of the computed effective coupling strength with the dissipation rates reported in Table 9.1 [64, 63]. In particular, we find that $\left|\hbar\sqrt{\mathcal{G}_{12}\mathcal{G}_{21}/4\Omega_1\Omega_2}\right| \approx 0.40$ meV, nearly double the dominant intrinsic dissipation rate $\hbar\gamma_1 = 0.23$ meV.

9.4 Analysis of super-mode properties

Hybridization is further investigated through inspection of the super-mode profiles

$$\begin{aligned}
\mathbf{f}_\mp(\mathbf{x}) &= \frac{1}{A(\theta)}\left[\left(\frac{\mathcal{G}_{12}}{\mathcal{G}_{21}}\right)^{1/4}\sqrt{\frac{V_2}{V_1}}\mathbf{f}_1(\mathbf{x})\cos\theta - \left(\frac{\mathcal{G}_{21}}{\mathcal{G}_{12}}\right)^{1/4}\sqrt{\frac{V_1}{V_2}}\mathbf{f}_2(\mathbf{x})\sin\theta\right] \\
\mathbf{f}_\pm(\mathbf{x}) &= \frac{1}{B(\theta)}\left[\left(\frac{\mathcal{G}_{21}}{\mathcal{G}_{12}}\right)^{1/4}\sqrt{\frac{V_1}{V_2}}\mathbf{f}_2(\mathbf{x})\cos\theta + \left(\frac{\mathcal{G}_{12}}{\mathcal{G}_{21}}\right)^{1/4}\sqrt{\frac{V_2}{V_1}}\mathbf{f}_1(\mathbf{x})\sin\theta\right]
\end{aligned} \tag{9.7}$$

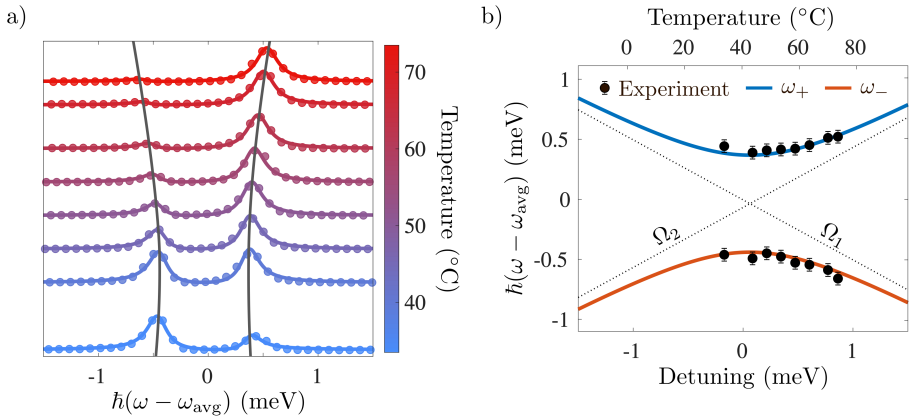

Figure 9.2: (a) Anticrossing resulting from strong coupling between the ring resonator and nanobeam cavity modes. Experimental data are shown as circles, while colored solid lines display the resulting least-squares fit to Eq. (9.6). Gray lines overlay the theoretical values of $\omega_{\pm}$, extrapolated via parameter values obtained from the fits. (b) Evolution of the super-mode resonant frequencies as a function of detuning. Black points correspond to experimentally measured peak transmission energies, while error bars indicate uncertainty in the peak energy due to the finite density of transmission energies measured. Solid curves display theoretical super-mode energies computed from Eq. (9.4), parameterized through simultaneous fits to transmission measurements.

and their associated mode volumes

$$V_{\mp} = V_1 \left[\frac{V_2}{V_1}\sqrt{\frac{\mathcal{G}_{12}}{\mathcal{G}_{21}}}\frac{1+\Sigma_1}{A(\theta)^2}\right]\cos^2\theta + V_2\left[\frac{V_1}{V_2}\sqrt{\frac{\mathcal{G}_{21}}{\mathcal{G}_{12}}}\frac{1+\Sigma_2}{A(\theta)^2}\right]\sin^2\theta - \sqrt{V_1V_2}\left[\frac{g_E/\sqrt{\omega_1\omega_2}}{A(\theta)^2}\right]\sin 2\theta$$
$$V_{\pm} = V_2 \left[\frac{V_1}{V_2}\sqrt{\frac{\mathcal{G}_{21}}{\mathcal{G}_{12}}}\frac{1+\Sigma_2}{B(\theta)^2}\right]\cos^2\theta + V_1\left[\frac{V_2}{V_1}\sqrt{\frac{\mathcal{G}_{12}}{\mathcal{G}_{21}}}\frac{1+\Sigma_1}{B(\theta)^2}\right]\sin^2\theta + \sqrt{V_1V_2}\left[\frac{g_E/\sqrt{\omega_1\omega_2}}{B(\theta)^2}\right]\sin 2\theta, \tag{9.8}$$

where $A(\theta)$ and $B(\theta)$ are normalization factors defined by

$$\begin{aligned} A(\theta)^2 &= \mathrm{Max}\left\{\varepsilon(\mathbf{x})\left[\left(\frac{\mathcal{G}_{12}}{\mathcal{G}_{21}}\right)^{1/4}\sqrt{\frac{V_2}{V_1}}\,\mathbf{f}_1(\mathbf{x})\cos\theta + \left(\frac{\mathcal{G}_{21}}{\mathcal{G}_{12}}\right)^{1/4}\sqrt{\frac{V_1}{V_2}}\,\mathbf{f}_2(\mathbf{x})\sin\theta\right]^2\right\} \\ B(\theta)^2 &= \mathrm{Max}\left\{\varepsilon(\mathbf{x})\left[\left(\frac{\mathcal{G}_{21}}{\mathcal{G}_{12}}\right)^{1/4}\sqrt{\frac{V_1}{V_2}}\,\mathbf{f}_2(\mathbf{x})\cos\theta - \left(\frac{\mathcal{G}_{12}}{\mathcal{G}_{21}}\right)^{1/4}\sqrt{\frac{V_2}{V_1}}\,\mathbf{f}_1(\mathbf{x})\sin\theta\right]^2\right\}, \end{aligned} \tag{9.9}$$

$\theta = (1/2)\tan^{-1}(2\sqrt{\mathcal{G}_{12}\mathcal{G}_{21}}/[\Omega_2^2 - \Omega_1^2])$ is the mixing angle, and the upper (lower) subscript corresponds to the case $\theta > 0$ ($\theta < 0$). The mixing angle has two distinct regimes; when the detuning is much larger than the effective coupling strength ($\theta \to 0$), the above mode functions reduce to those of the bare ring resonator and nanobeam cavity. In contrast, for small detuning relative to the coupling ($\theta \to \pm\pi/4$) the mode functions become a superposition of $\mathbf{f}_1(\mathbf{x})$ and $\mathbf{f}_2(\mathbf{x})$.

Fig. 9.3a shows the evolution of the y-component of the upper (top) and lower (bottom) cavity polariton field profiles across the experimentally measured temperature range. Because the limits of this range constrain the mixing angle to $-\pi/8 \lesssim \theta \lesssim \pi/6$, neither $\mathbf{f}_+(\mathbf{x})$ nor $\mathbf{f}_-(\mathbf{x})$ entirely localize to one of the constituent cavities at any probed temperature. For all mode profiles shown, a significant portion of the field is contributed by the mode function of the nanobeam $\mathbf{f}_2(\mathbf{x})$. We note, however, that there is no fundamental reason that the device could not be heated past the maximum temperature studied here (73 °C), or cooled below room temperature.

Notably, the super-mode profiles are not equal superpositions of $\mathbf{f}_1(\mathbf{x})$ and $\mathbf{f}_2(\mathbf{x})$ near zero detuning ($T = 40$ °C). This may be understood by considering the large mismatch in mode volume between the ring resonator and nanobeam modes ($V_1/V_2 \sim 10$). According to Eq. (9.7), the nanobeam contribution to both $\mathbf{f}_+(\mathbf{x})$ and $\mathbf{f}_-(\mathbf{x})$ scales like $(V_1/V_2)^{1/4}$,

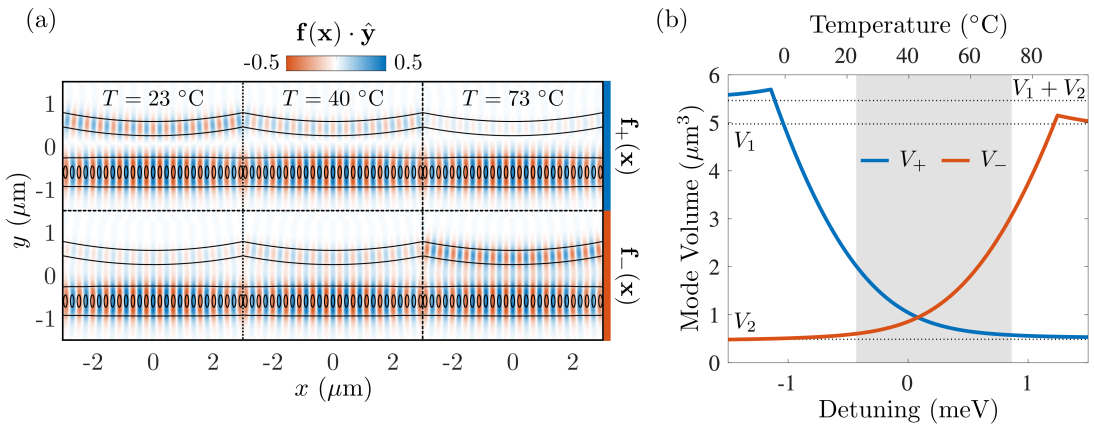

Figure 9.3: (a) Field profile for the upper (top) and lower (bottom) cavity polaritons at various temperatures. Both super-modes are dominated by the nanobeam field at all observed temperatures due to the weighting of $\mathbf{f}_1(\mathbf{x})$ and $\mathbf{f}_2(\mathbf{x})$ in Eq. (9.7). (b) Hybridized mode volumes V_+ (blue curve) and V_- (red curve) of the upper and lower cavity polaritons. The gray region indicates the range of experimentally measured temperatures, while dotted lines specify V_1, V_2, and $V_1 + V_2$. Due to the predominant localization of both modes in the nanobeam cavity, both V_+ and V_- coalesce at a value less than 5 times the mode volume of the isolated ring resonator mode.

while that of the ring resonator scales like $(V_2/V_1)^{1/4}$. As a result, both super-modes are predominantly localized to the nanobeam.

Fig. 9.3b shows theoretical predictions for the hybridized mode volumes as a function of temperature-controlled detuning, calculated using Eq. (9.8) paired with the experimentally-informed parameter values in Table 9.1. As before, blue and red curves correspond to the upper and lower cavity polaritons in Fig. 9.2a. The gray region indicates the range of experimentally probed temperatures. Both hybridized mode volumes tend towards those of the individual cavities at large positive and negative detuning and coalesce at a value of $V_\pm \approx 0.95\ \mu\text{m}^3$, more than a factor of 5 less than the mode volume of the isolated ring resonator.

While the nanobeam mode volume V_2 clearly serves as a lower bound for $V_\pm$, analysis of Eq. (9.8) indicates a maximum near $V_1 + V_2$. V_+ slightly exceeds this value due to constructive interference between the two modes, while V_- peaks at a value below $V_1 + V_2$ due to destructive interference. Both mode volumes display a "turning point" at values of the mixing angle θ such that $\mathbf{f}_1(\mathbf{x})$ and $\mathbf{f}_2(\mathbf{x})$ are equally-weighted in either $\mathbf{f}_+(\mathbf{x})$ or $\mathbf{f}_-(\mathbf{x})$. Due to the large mismatch between V_1 and V_2, between these two points is a full order-of-magnitude of attainable values for both hybridized mode volumes, illustrating the potential of this heterogeneous device for actively-tunable photonic properties.

9.5 Conclusion

In conclusion, for the first time we have demonstrated actively tunable hybridization in a heterogeneous photonic molecule consisting of a ring resonator coupled to a photonic crystal cavity. Critically, we establish an ability to exert control over the coupled cavity's mode volumes, spanning over a full order of magnitude. Aided by a theoretical formalism developed to study hybridized cavity states, we rigorously extract system parameters from experiment and derive analytic expressions for the super-mode resonant frequencies, field profiles, and mode volumes, elucidating their evolution with temperature. As the mode volume is a critical parameter dictating the degree of Purcell enhancement and scaling of light-matter interaction, these results bear impact upon diverse efforts in the emerging fields of quantum simulation and quantum information processing.

9.6 Appendix

9.6.1 Dynamics for two single mode cavities

As mentioned in the main text, the equations of motions for coupled cavity modes may be computed either through integration of the wave equation [271], or via an Euler-Lagrange approach. Here, we follow the latter strategy and use the standard electromagnetic Lagrangian

$$L = \int \frac{d^3x}{8\pi} \left[\varepsilon(\mathbf{x}) \frac{\dot{\mathbf{A}}^2}{c^2} - (\nabla \times \mathbf{A})^2 \right] \tag{9.10}$$

in the modified Coulomb gauge (and in the absence of free charge). Plugging in the expansion Eq. (9.2) for the vector potential leads to

$$L = \frac{1}{2} \sum_i \frac{\dot{q}_i}{V_i} \left[1 + \Sigma_i\right] - \frac{1}{2} \sum_i \frac{\omega_i^2}{V_i} q_i^2 + \frac{g_E}{\sqrt{\omega_1 \omega_2 V_1 V_2}} \dot{q}_1 \dot{q}_2 - g_M \sqrt{\frac{\omega_1 \omega_2}{V_1 V_2}} q_1 q_2, \tag{9.11}$$

where the analytic forms of g_E, g_M, and Σ_i are given in the main text. Application of the Euler-Lagrange equations then gives

$$\begin{aligned} \frac{\ddot{q}_1}{\bar{V}_1} + \bar{\omega}_1^2 \frac{q_1}{\bar{V}_1} + \frac{\bar{g}_E}{\sqrt{\bar{\omega}_1 \bar{\omega}_2 \bar{V}_1 \bar{V}_2}} \ddot{q}_2 + \bar{g}_M \sqrt{\frac{\bar{\omega}_1 \bar{\omega}_2}{\bar{V}_1 \bar{V}_2}} q_2 = 0 \\ \frac{\ddot{q}_2}{\bar{V}_2} + \bar{\omega}_2^2 \frac{q_2}{\bar{V}_2} + \frac{\bar{g}_E}{\sqrt{\bar{\omega}_1 \bar{\omega}_2 \bar{V}_1 \bar{V}_2}} \ddot{q}_1 + \bar{g}_M \sqrt{\frac{\bar{\omega}_1 \bar{\omega}_2}{\bar{V}_1 \bar{V}_2}} q_1 = 0 \end{aligned} \tag{9.12}$$

where renormalized mode volumes, frequencies and coupling strengths are defined as

$$\begin{aligned} \bar{V}_1 = V_1/(1+\Sigma_1) \quad \bar{V}_2 = V_2/(1+\Sigma_2) \\ \bar{\omega}_1 = \omega_1/\sqrt{1+\Sigma_1} \quad \bar{\omega}_2 = \omega_2/\sqrt{1+\Sigma_2} \\ \bar{g}_E = g_E/[(1+\Sigma_1)(1+\Sigma_2)]^{3/4} \\ \bar{g}_M = g_M/[(1+\Sigma_1)(1+\Sigma_2)]^{1/4}. \end{aligned} \tag{9.13}$$

Further algebra yields the equations of motion defined in the main text,

$$\frac{d^2}{dt^2} \begin{bmatrix} q_1 \\ q_2 \end{bmatrix} = \begin{bmatrix} \Omega_1^2 & \mathcal{G}_{12} \\ \mathcal{G}_{21} & \Omega_2^2 \end{bmatrix} \begin{bmatrix} q_1 \\ q_2 \end{bmatrix} \tag{9.14}$$

where $\Omega_i^2 = (\bar{\omega}_i^2 - \bar{g}_E \bar{g}_M)/(1 - \bar{g}_E^2/\bar{\omega}_1\bar{\omega}_2)$ and $\mathcal{G}_{ij} = \sqrt{\bar{\omega}_j \bar{V}_i / \bar{\omega}_i \bar{V}_j} \left(\bar{\omega}_i \bar{g}_M - \bar{\omega}_j \bar{g}_E\right) / (1 - \bar{g}_E^2/\bar{\omega}_1\bar{\omega}_2)$.

9.6.2 *Physical importance of the mode volume*

The mode volume is a critical figure-of-merit for dielectric cavities which determines the strength of light matter interactions [270, 50, 49]. Here, we show that this remains true in the basis of super-modes of a photonic molecule, lending physical meaning to $V_{\pm}$. The interaction energy between a dipole emitter and the two-cavity field is given by

$$H_{\text{int}} = -\mathbf{d} \cdot \mathbf{E}(\mathbf{r}_0). \tag{9.15}$$

where $\mathbf{d}$ is the dipole moment of the emitter and $\mathbf{r}_0$ its position. Upon transformation to the super-mode basis, the field of the cavity may be written as

$$\mathbf{E} = -\frac{\dot{\mathbf{A}}}{c} = -\frac{\sqrt{4\pi}}{V_+}\dot{q}_+(t)\mathbf{f}_+(\mathbf{x}) - \frac{\sqrt{4\pi}}{V_-}\dot{q}_-(t)\mathbf{f}_-(\mathbf{x}) \tag{9.16}$$

Plugging this into the interaction Hamiltonian and writing the dipole moment in terms a generalized coordinate $\mathbf{d} = e\mathbf{x}$,

$$H_{\text{int}} = -\frac{e\sqrt{4\pi}}{V_+}[\mathbf{f}_+(\mathbf{r}_0) \cdot \hat{\mathbf{x}}]x\dot{q}_+ - \frac{e\sqrt{4\pi}}{V_-}[\mathbf{f}_-(\mathbf{r}_0) \cdot \hat{\mathbf{x}}]x\dot{q}_-, \tag{9.17}$$

which clearly reveals the dependence of the coupling strength on the mode volume $V_{\pm}$. Importantly, the mode functions are normalized such that $\max[\varepsilon(\mathbf{x})\mathbf{f}_{\pm}(\mathbf{x}) \cdot \mathbf{f}_{\pm}(\mathbf{x})] = 1$, and therefore the limit $\mathbf{f}_{\pm}(\mathbf{r}_0) \cdot \hat{\mathbf{x}} \to 1$ corresponds to the case of maximal coupling when $\varepsilon(\mathbf{x})$ is real and dispersionless.

9.6.3 *Effective Hamiltonian approach for calculation of transmission spectra*

Computation of the power transmitted through the coupled ring-nanobeam system is most easily achieved in the basis of creation and annihilation operators. Standard canonical quantization techniques rely on computation of the Hamiltonian associated with the Lagrangian in Eq. (9.11). Due to the coupling between $\dot{q}_1$ and $\dot{q}_2$, however, this leads to conjugate momenta which themselves are coupled in the Hamiltonian. The result of this is that the rotating-wave approximation is no longer valid, and standard techniques of input-output theory for coupled systems become ineffective.

The most straightforward path to quantization is via the effective Lagrangian

$$L = \frac{1}{2}\sum_i \left[\frac{\dot{q}_i^2}{\mathcal{V}_i} - \Omega_i^2 \frac{q_i^2}{\mathcal{V}_i}\right] - \sqrt{\frac{\mathcal{G}_{12}\mathcal{G}_{21}}{\mathcal{V}_1\mathcal{V}_2}} q_1 q_2 \tag{9.18}$$

where $1/\mathcal{V}_1 = (\mathcal{G}_{21}/\bar{\omega}_1\bar{\omega}_2)/\sqrt{\bar{V}_1\bar{V}_2}$ and $1/\mathcal{V}_2 = (\mathcal{G}_{12}/\bar{\omega}_1\bar{\omega}_2)/\sqrt{\bar{V}_1\bar{V}_2}$. While different in form from the standard Lagrangian in Eq. (A1), application of the Euler-Lagrange equations yields the exact same equations of motion. Notably, there is no direct coupling between $\dot{q}_1$ and $\dot{q}_2$, significantly simplifying quantization.

Legendre transform of the above Lagrangian yields the effective Hamiltonian

$$\begin{aligned} H &= \sum_i \left[\frac{\mathcal{V}_i}{2} p_i^2 + \frac{\Omega_i^2}{2\mathcal{V}_i} q_i^2\right] + \sqrt{\frac{\mathcal{G}_{12}\mathcal{G}_{21}}{\mathcal{V}_1\mathcal{V}_2}} q_1 q_2 \\ &= \sum_i \hbar\Omega_i a_i^\dagger a_i + \hbar\sqrt{\frac{\mathcal{G}_{12}\mathcal{G}_{21}}{4\Omega_1\Omega_2}}(a_1^\dagger a_2 + a_1 a_2^\dagger) \end{aligned} \tag{9.19}$$

where $a_i = \sqrt{\Omega_i/2\hbar\mathcal{V}_i}[q_i + i(\mathcal{V}_i/\Omega_i)p_i]$ and counter-rotating terms have been discarded in accordance with the rotating wave approximation. This procedure also allows us to identify $\sqrt{\mathcal{G}_{12}\mathcal{G}_{21}/4\Omega_1\Omega_2}$ as the "effective coupling strength" to be compared with the dissipation rates in quantitatively testing for strong coupling. The transmission spectrum may then be computed through standard input-output methods [79, 77], yielding

$$\mathcal{T}(\omega) = \left|\frac{\kappa}{\omega - \Omega_1 + i\kappa + \frac{\mathcal{G}_{12}\mathcal{G}_{21}/4\Omega_1\Omega_2}{\omega - \Omega_2}}\right|^2. \tag{9.20}$$

Chapter 10

EXACT K-BODY REPRESENTATION OF THE JAYNES-CUMMINGS INTERACTION IN THE DRESSED BASIS: INSIGHT INTO MANY-BODY PHENOMENA WITH LIGHT

Analog quantum simulation – the technique of using one experimentally well-controlled physical system to mimic the behavior of another – has quickly emerged as one of the most promising near term strategies for studying strongly correlated quantum many-body systems. In particular, systems of interacting photons, realizable in solid-state cavity and circuit QED frameworks, for example, hold tremendous promise for the study of nonequilibrium many-body phenomena in part due to the capability to locally create and destroy photons. These systems are typically modeled using a Jaynes-Cummings-Hubbard (JCH) Hamiltonian, named due to similarities with the Bose-Hubbard model. While comparisons between the two are often made in the literature, the JCH Hamiltonian comprises both bosonic and psuedo-spin operators, leading to physical deviations from the Bose-Hubbard model for particular parameter regimes. Here, we present a non-perturbative procedure for transforming the Jaynes-Cummings Hamiltonian into a dressed operator representation that, in its most general form, admits an infinite sum of bosonic k-body terms where k is bound only by the number of excitations in the system. We closely examine this result in both the dispersive and resonant coupling regimes, finding rapid convergence in the former and contributions from $k \gg 1$ in the latter. Through extension to the simple case of a two-site JCH system, we demonstrate that this approach facilitates close inspection of the analogy between the JCH and Bose-Hubbard models and its breakdown for resonant light-matter coupling. Finally, we use this framework to survey the many-body character of a two-site JCH for general system parameters, identifying four unique quantum phases and the parameter regimes in which they are realized, thus highlighting phenomena realizable with finite JCH-based quantum simulators beyond the Bose-Hubbard model. More broadly, this work is intended to serve as a clear mathematical exposition of bosonic many-body interac-

tions underlying Jaynes-Cummings-type systems, often postulated either through analogy to Kerr-like nonlinear susceptibilities or by matching coefficients to obtain the appropriate eigenvalue spectrum.

10.1 Introduction

Efficient simulation of strongly correlated many-body systems remains one of the most important unsolved problems in the physical sciences today, promising advances in a diverse set of fields ranging from high-energy physics and cosmology to quantum chemistry and condensed matter physics [322, 323]. It is also one of the most challenging, as such systems involve dynamics within a Hilbert space whose size increases exponentially with added degrees of freedom, rendering brute force study of many-body systems impractical with even the most powerful classical computers. Feynman famously recognized this problem nearly four decades ago and proposed what is now termed a quantum simulator – a programmable machine whose underlying degrees of freedom are quantum mechanical, circumventing the exponential scaling problem and thus enabling efficient simulation of quantum systems [324, 325, 326, 327]. These devices generally fall into two classes: digital and analog quantum simulators. The former are an application of universal quantum computers which, despite rapid advancement in recent years, are likely decades away from a practical, fault-tolerant realization [328, 329, 330, 322, 331]. In contrast, the latter are specialized, comparatively less ambitious devices comprising a well-controlled quantum system which mimics a particular quantum system of interest with some degree of tunability [323, 332]. Analog quantum simulators thus offer a viable near-term solution for study of quantum many-body phenomena, and consequently a wide array of physical systems have been experimentally and theoretically studied as platforms for analog quantum simulation in recent years [333, 334, 335, 336, 337, 338, 339, 340, 341, 329, 323, 342, 343, 344, 345, 346].

One of the most unique classes of proposed platforms entails emulation of quantum many-body physics with light. As photons do not naturally interact, replicating an interacting many-body system relies on experimental realization of single-photon nonlinearities, a difficult task particularly in the optical domain. In cavity and circuit QED settings, one strategy for achieving nonlinearity involves realization of the Jaynes-Cummings model,

which describes a single quantized cavity mode interacting with a two-level system (TLS). If the rate of dissipation to the environment is exceeded by the rate of coherent energy exchange between the cavity mode and TLS, the system is said to be in the strong coupling regime and a phenomenon known as photon blockade can occur whereby absorption of a single photon of a particular frequency prevents further absorption at that same frequency, thus enabling single photon nonlinearity and, consequently, Kerr-type photon-photon interactions [347, 348, 349, 350, 351, 352]. A suitable platform for quantum simulation is then realized by an array of TLS-enabled nonlinear cavities, where the pure photonic modes of adjacent cavities are coupled through the mutual overlap of their evanescent fields. Such a system shares similarities with the Bose-Hubbard model and is commonly referred to as the Jaynes-Cummings-Hubbard (JCH) model [353, 354, 36, 355, 356], combining Hubbard-like on-site interactions (mediated by the TLS) with bosonic hopping between adjacent sites.

Unlike other notable quantum simulation platforms, such as those composed of ultracold atoms in optical lattices [357, 358, 359], an array of TLS-enabled nonlinear cavities does not provide an exact analog of the Bose-Hubbard model. For one, the JCH Hamiltonian is composed of both bosonic and psuedospin operators, while the Bose-Hubbard Hamiltonian contains only the former. In addition, whereas the insulator-to-superfluid phase transition of the Bose-Hubbard model is understood through analysis of the competition between on-site repulsion U and hopping strength J, the various phases of the JCH model are determined by three competing energy scales: on-site repulsion U, hopping strength J, and TLS-cavity detuning Δ. Despite these differences, it has been shown that the JCH model admits an insulator-to-superfluid phase transition much like that of the Bose-Hubbard model [353, 354, 360, 355, 36, 361, 362, 363, 364] and, consequently, the two have been closely compared in a number of publications [353, 354, 365, 360, 366, 355, 367, 36, 368, 369, 362, 363, 364, 370, 371, 372, 373, 374, 375].

Here, we present a thorough analysis of the many-body character underlying the Jaynes-Cummings Hamiltonian and ultimately revisit the analogy between the JCH and Bose-Hubbard models for the simplest possible implementation: a two-site system. We begin by considering just a single Jaynes-Cummings system and introduce a parameter-independent strategy for exposing an infinite hierarchy of bosonic many-body interactions at the level of

dressed operators. In contrast to similar methods prominent in the literature [376, 377, 16], our approach is non-perturbative and is therefore valid for general system parameters, facilitating analysis of both dispersive and resonant light-matter coupling regimes and providing explicit mathematical relations between the parameters and operators appearing in the Jaynes-Cummings Hamiltonian and its many-body representation. We apply this methodology toward analysis of a two-site JCH model in both photonic and polaritonic regimes, and show that the dispersive coupling limit provides an approximate analog to the Bose-Hubbard model, albeit with weak nonlinearities. In the resonant regime, we illustrate the disconnect between these two models, and make explicit the polaritonic-to-photonic transition which accompanies the two-site analog to the familiar insulator-to-superfluid transition of the Bose-Hubbard model. To that end, we show that the resonant coupling case admits of a third, intermediary phase consistent with a polaritonic superfluid, highlighting the distinct possibilities afforded by the JCH model over the Bose-Hubbard case. Taken together, the goal of this paper is to present a unique, parameter-independent approach for studying the effective many-body interactions realizable in Jaynes-Cummings-type systems and, via extension to a two-site system, fully explore the various parameter regimes of a simple, finite Jaynes-Cummings-Hubbard system with an eye towards experimental study of many-body phenomena using photonics-based platforms.

The subsequent sections are organized as follows. In Section 10.2 we derive a many-body representation for the Jaynes-Cummings Hamiltonian in terms of dressed operators and discuss its limiting cases for various parameter regimes. This is carried out in three parts: Section 10.2.1 contains a derivation of the dressed operator representation of the Jaynes-Cummings Hamiltonian, followed by a discussion of the behavior of the dressed operators in 10.2.2 and, in Section 10.2.3, a derivation and analysis of our main result – an exact, many-body representation of the Jaynes-Cummings Hamiltonian. Section 10.3 extends our methods to the two-site JCH model, beginning with a brief comparison between the Bose-Hubbard and JCH models in Section 10.3.1. This is followed by a more thorough analysis of the two-site JCH in the dispersive and two excitation limits in Sections 10.3.2 and 10.3.3. We then examine the various quantum phases of the two-site JCH in Section 10.3.4 before concluding with a summary of our findings in Section 10.4.

10.2 Non-perturbative many-body representation of the Jaynes-Cummings Hamiltonian

We begin by examining the hidden bosonic many-body nature of the Jaynes-Cummings Hamiltonian, one of the simplest and most versatile models in quantum optics describing the coherent interaction between a single cavity mode and a TLS, as shown in Fig. 10.1. Defining $a^\dagger$ and a as creation and annihilation operators for the bosonic cavity mode and $\sigma^+ = |e\rangle\langle g|$ and $\sigma^- = |g\rangle\langle e|$ as psuedo-spin raising and lowering operators describing transitions between the ground $|g\rangle$ and excited $|e\rangle$ states of the TLS, the Jaynes-Cummings Hamiltonian is given by

$$H = \hbar\omega_c a^\dagger a + \frac{1}{2}\hbar\omega_a \sigma^z + \hbar g(a^\dagger\sigma^- + a\sigma^+). \tag{10.1}$$

Here, ω_c is the resonant frequency of the cavity mode and ω_a that of the TLS or "atom" - terminology which will be used interchangeably for the remainder of this work. We emphasize that the physical implementation of the TLS need not be an atom, and may instead describe the energy levels of a so-called *artificial* atom such as a superconducting qubit [378, 379, 17, 16] or quantum dot [380, 381, 382, 383]. The rate of energy exchange between the cavity and TLS is defined by the coupling strength g, here assumed to be fast enough such that the atom and cavity are strongly coupled and dissipation may be neglected at first approximation [384, 383], yet not so fast that the counter-rotating terms of the Rabi model be considered (i.e., $g \ll \{\omega_c, \omega_a\}$) [38, 385]. Finally, σ^z is the Pauli operator $\sigma^z = [\sigma^+, \sigma^-] = |e\rangle\langle e| - |g\rangle\langle g|$.

The eigenvectors and eigenvalues of Eq. (10.1) are most easily found by recognizing that the Hamiltonian conserves the total number of quanta

$$N = a^\dagger a + \sigma^+\sigma^-. \tag{10.2}$$

Consequently, only states within the same excitation number manifold couple and Eq. (10.1) may be rewritten as a block-diagonal matrix with each 2×2 block independently diagonalizable. Following Ref. [376], we define

$$\lambda = g/\Delta \tag{10.3}$$

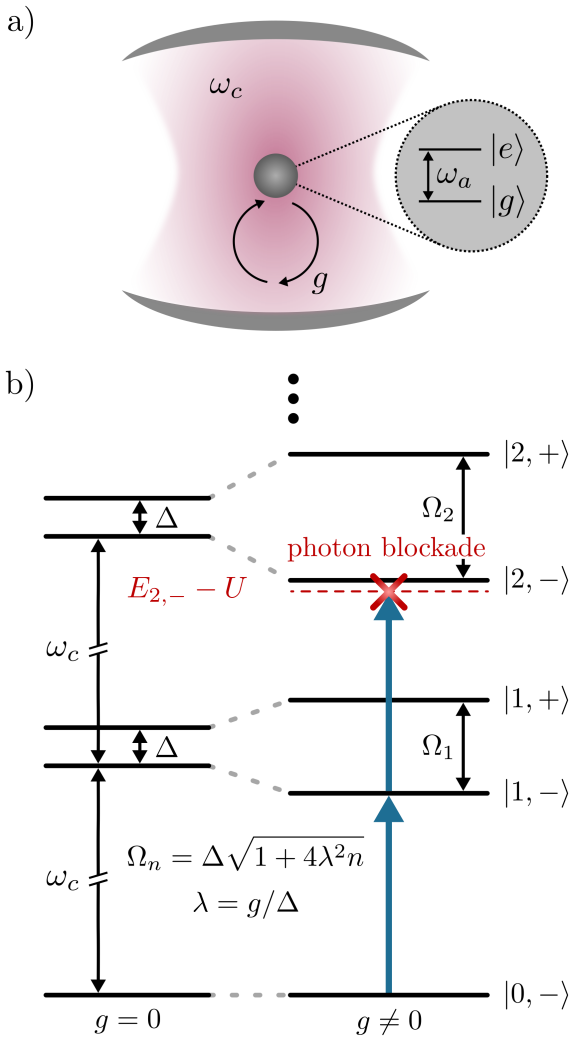

Figure 10.1: (a) A realization of the Jaynes-Cummings model consisting of a single cavity mode and a two-level system (TLS) of resonant frequency ω_c and ω_a, respectively. The two interact, exchanging quanta at a rate determined by the coupling strength g. (b) The eigenspectrum of the Jaynes-Cummings Hamiltonian for $\Delta > 0$. The left set of horizontal black lines indicates the eigenenergies of the bare cavity mode and TLS, while the right portrays the impact of light-matter coupling. Pairs of states with the same total number of excitations n hybridize, yielding pairs of dressed eigenstates $|n, \pm\rangle$ which are split by the frequency Ω_n. (caption continued on following page)

Figure 10.1: (continued) If the system begins in the ground state $|0,-\rangle$, absorption of one photon of frequency $(E_{1,-} - E_{0,-})$ prohibits absorption of a second of the same frequency due to the additional energy cost U. This phenomenon is known as photon blockade, and may be used to realize effective photon-photon interactions.

where $\Delta = \omega_a - \omega_c$ is the atom-cavity detuning. Then the eigenvalues may be written as

$$E_{n,\pm} = \left(n - \frac{1}{2}\right)\hbar\omega_c \pm \frac{\hbar}{2}\Delta\sqrt{1 + 4\lambda^2 n} \tag{10.4}$$

with associated eigenvectors

$$\begin{aligned} |n,-\rangle &= \cos\theta\,|n,g\rangle - \sin\theta\,|n-1,e\rangle \\ |n,+\rangle &= \sin\theta\,|n,g\rangle + \cos\theta\,|n-1,e\rangle\,, \end{aligned} \tag{10.5}$$

where n are eigenvalues of the total number operator N which label the excitation manifold and the mixing angle $\theta = \tan^{-1}(2\lambda\sqrt{n})/2$ describes the degree of hybridization between photonic and atomic degrees of freedom, taking values in the range $-\pi/4 \leq \theta \leq \pi/4$ with upper and lower bounds corresponding to maximal mixing and $\theta = 0$ indicating an uncoupled system.

The eigenspectrum of Eq. (10.1) is often referred to as the Jaynes-Cummings ladder [386, 387, 388, 389], shown in Fig. 10.1b. Crucially, this spectrum is nonlinear in n, leading to a phenomenon known as *photon blockade* [347, 349], whereby absorption of a photon at a particular frequency inhibits further absorption of photons at that same frequency (see Fig. 10.1c). In this way, the Jaynes-Cummings Hamiltonian facilitates *effective* photon-photon interactions in the few photon limit. Caution must be exercised, however, in attempting to write down an effective Hamiltonian which accounts for these effects. In particular, it is clear from Fig. 10.1b that transition to the state $|2,-\rangle$ through absorption of successive photons of frequency $\omega = (E_{1,-} - E_{0,-})/\hbar$ requires an additional energy of $U > 0$, leading to an effective repulsion of the second photon. This effect is similar to a Kerr-type nonlinearity of the form

$$H_{\text{Kerr}} = U_{\text{eff}}\, N(N-1) \tag{10.6}$$

and therefore parallels the on-site interactions of the Bose-Hubbard model [390, 353, 367]. However, this comparison must be approached with caution due to two key subtleties. First, applicability for an arbitrary number of excitations requires that U_{eff} itself depends on the number operator N, as in the large excitation limit the Jaynes-Cummings ladder approaches a linear spectrum [391, 392]. This idea – defining an explicit, excitation number dependent U_{eff} – has been explored in several publications to date [353, 355, 370] but, as noted in Ref. [355], leads to inaccuracies in the dispersive coupling regime. Second, the operators appearing in Eq. (10.6) correspond not to the number of photons in the cavity, but the number of *dressed* photons. As a result, the very nature of the underlying excitations themselves depend upon the parameter regime, changing from photonic in the dispersive regime to polaritonic for resonant coupling, behavior which is not apparent from Eq. (10.6). A useful effective bosonic many-body representation of Eq. (10.1) therefore requires a more careful consideration of these subtleties.

In the following subsections, we present a transformed representation of Eq. (10.1) which makes explicit the bosonic many-body interactions generated through photon-blockade for general system parameters. In contrast with similar methods in the literature relying on Schrieffer-Wolff perturbation theory [376, 377, 16], our approach is applicable for both resonant ($\Delta \ll g$) and dispersive ($\Delta \gg g$) light-matter coupling. Through techniques of unitary transformation, we systematically develop an exact many-body description of the Jaynes-Cummings Hamiltonian and expose a hierarchy of normally ordered, effective k-body interactions and their parameter-dependent scaling. The end result is an exact generalization of Eq. (10.6) which is absent of excitation number dependent coefficients. Particular attention is given in identifying the physically appropriate basis for the many-body interactions as it has been shown that insulator-to-superfluid quantum phase transitions of the JCH model are accompanied by a polaritonic-to-photonic transition in the nature of the excitations [353, 354, 361].

10.2.1 Unitary diagonalization of the Jaynes-Cummings Hamiltonian

While it is straightforward to find the eigenvalues and eigenvectors of the Jaynes-Cummings Hamiltonian by considering each excitation number manifold individually, an alternate route toward diagonalizing Eq. (10.1) involves unitary transformation of the canonical operators. This approach was first reported in Ref. [393] and has since been adopted in a number of more recent works [377, 376, 16]. At first glance, this strategy appears to be a more complicated pathway toward computing the well-known eigenvalues and eigenvectors of Eqs. (10.4−10.5). However, it provides additional physical insight into the diagonal form of the Hamiltonian through an analytic understanding of the dressed canonical operators and will allow us to more clearly compare between Hamiltonians endowed with Jaynes-Cummings interactions and those having two-body bosonic interactions of the form of Eq. (10.6).

We begin by writing the Jaynes-Cummings Hamiltonian as

$$H = H_0 + \hbar g I_+, \tag{10.7}$$

where we have adopted the shorthand notation [376]

$$\begin{aligned} H_0 &= \hbar\omega_c a^\dagger a + \frac{1}{2}\hbar\omega_a \sigma^z \\ I_\pm &= a^\dagger \sigma^- \pm a\sigma^+. \end{aligned} \tag{10.8}$$

Defining the unitary transformation operator

$$\mathcal{U} = e^{-\Lambda I_-}, \tag{10.9}$$

we aim to find the appropriate choice of Λ for which the Hamiltonian is diagonal once cast in terms of the transformed operators $\widetilde{a} = \mathcal{U}^\dagger a \mathcal{U}$ and $\widetilde{\sigma}^- = \mathcal{U}^\dagger \sigma^- \mathcal{U}$. Due to the unitarity of $\mathcal{U}$, all commutation relations are invariant under transformation.

Here we employ the method of *explicit* transformation, whereby the Hamiltonian H is rewritten in terms of transformed operators. This strategy typically entails finding closed analytic relationships between each canonical operator $\mathcal{O}$ and its transformed pair $\widetilde{\mathcal{O}}$ using the Baker-Campbell-Hausdorff formula [394],

$$\begin{aligned} \widetilde{\mathcal{O}} &= \mathcal{U}^\dagger \mathcal{O} \mathcal{U} \\ &= \mathcal{O} + [\mathcal{O}, S] + \frac{1}{2!}[[\mathcal{O}, S], S] + \frac{1}{3!}[[[\mathcal{O}, S], S], S] + \ldots, \end{aligned} \tag{10.10}$$

where $\mathcal{U} = e^S$. In the case of the Jaynes-Cummings Hamiltonian, however, direct application of Eq. (10.10) to the canonical operators a and σ^- leads to an infinite series of commutation relations which do not close, and a "nonunitarian short circuit" must be employed to obtain closed form expressions through this approach [394]. Instead, it is advantageous to transform H_0 and I_+ in their entirety. Using the commutation relations

$$\begin{aligned} [H_0, I_-] &= -\hbar\Delta I_+ \\ [I_+, I_-] &= 2N\sigma^z \end{aligned} \tag{10.11}$$

along with the inverted form of Eq. (10.10), it can be shown that

$$\begin{aligned} H_0 &= \widetilde{H}_0 + \Lambda[\widetilde{H}_0, I_-] + \frac{\Lambda^2}{2!}[[\widetilde{H}_0, I_-], I_-] + \ldots \\ &= \widetilde{H}_0 - \hbar\Delta \sum_{n=1} \frac{\Lambda^n}{n!} \widetilde{F}_{n-1} \\ I_+ &= \widetilde{I}_+ + \Lambda[\widetilde{I}_+, I_-] + \frac{\Lambda^2}{2!}[[\widetilde{I}_+, I_-], I_-] + \ldots \\ &= \sum_{n=0} \frac{\Lambda^n}{n!} \widetilde{F}_n \end{aligned} \tag{10.12}$$

where $\widetilde{F}_n$ is the nth order commutator of $\widetilde{I}_+$ and I_- given by

$$\widetilde{F}_n = \begin{cases} (-1)^{\frac{n-1}{2}} (2\sqrt{N})^{n+1}\, \widetilde{\sigma}^z/2 & n \text{ odd} \\ (-1)^{\frac{n}{2}} (2\sqrt{N})^n\, \widetilde{I}_+ & n \text{ even} \end{cases} \tag{10.13}$$

and transformed operators are indicated by tildes. Note that both N and I_- commute with $\mathcal{U}$ and, consequently, tildes on these operators are neglected for simplicity.

Using the relations in Eq. (10.13), the commutator expansions of H_0 and I_+ may be formally summed and substituted into Eq. (10.7), yielding

$$\begin{aligned} H = {} & \hbar\omega_c \left(N - \frac{1}{2} \right) \\ & - \frac{\hbar}{2\sqrt{N}} \left[\Delta \sin\left(2\Lambda\sqrt{N}\right) - 2g\sqrt{N} \cos\left(2\Lambda\sqrt{N}\right) \right] \widetilde{I}_+ \\ & + \frac{\hbar}{2} \left[\Delta \cos\left(2\Lambda\sqrt{N}\right) + 2g\sqrt{N} \sin\left(2\Lambda\sqrt{N}\right) \right] \widetilde{\sigma}^z. \end{aligned} \tag{10.14}$$

Diagonalization is achieved through elimination of the second term proportional $\widetilde{I}_+$, leading to the constraint

$$\Lambda(N) \equiv \frac{\theta(N)}{\sqrt{N}} = \frac{1}{2\sqrt{N}} \tan^{-1}\left(2\lambda\sqrt{N}\right), \tag{10.15}$$

defined here in terms of the mixing angle θ, previously introduced in Eq. (10.5) but now appearing as a function of the number operator N rather than its eigenvalue n. Critically, Λ is also a function of the operator N. This is allowed only because N commutes with H_0 and $I_\pm$ and therefore may be effectively treated as a scalar in writing the commutation series of Eq. (10.12). We emphasize, however, that caution must be exercised in endowing Λ with arbitrary operator dependence.

With the above choice of Λ, simplification of Eq. (10.14) yields

$$H = \hbar\omega_c \left(N - \frac{1}{2}\right) + \frac{\hbar}{2}\Delta\sqrt{1 + 4\lambda^2 N}\,\widetilde{\sigma}^z. \tag{10.16}$$

The above Hamiltonian is now entirely diagonal written in terms of the dressed bosonic and TLS operators, the former appearing via the total number operator $N = \widetilde{a}^\dagger\widetilde{a} + \widetilde{\sigma}^+\widetilde{\sigma}^-$. While it is evidently clear that this Hamiltonian returns the same eigenvalues previously reported in Eq. (10.4), this procedure allows for an exact operator representation of Jaynes-Cummings Hamiltonian in terms of the dressed *operators* rather than a description of the dressed *states* provided by the manifold-by-manifold approach. As will be shown in later sections, the dressed operator form of the Jaynes-Cummings Hamiltonian provides a deeper understanding of the underlying bosonic many-body interactions mediated by the TLS. More immediately, it is imperative to first understand how the dressed operators act on the composite Hilbert space of the dressed states of the Jaynes-Cummings Hamiltonian.

10.2.2 Behavior of the dressed operators

As previously discussed, direct transformation of the bosonic and TLS operators a and σ^- does not yield easily interpretable closed-form expressions for the dressed operators $\widetilde{a}$ and $\widetilde{\sigma}^-$. Despite this, one may still determine the action of the dressed operators on the eigenstates of Eq. (10.5) by transforming both the states and operators to the original basis where the action of the bare operators is known. Given the unitary transformation Eq. (10.9), the state $|\Psi\rangle$ transforms according to

$$|\Psi\rangle_S = e^{-S}\,|\Psi\rangle \tag{10.17}$$

where the subscript identifies a state transformed with respect to the generating function $S = -\Lambda I_-$. In order to work out transformations of the states explicitly, it is helpful to first cast the unitary operator $\mathcal{U} = e^S$ in an alternate form via Taylor expansion and subsequent resummation. In particular, it may be shown that

$$e^{\pm S} = \cos(\theta) \mp \frac{1}{\sqrt{N}} \sin(\theta) I_-, \tag{10.18}$$

where θ is the mixing angle defined in Eq. (10.15). Then the basis states $\{|n, g\rangle, |n, e\rangle\}$ transform as

$$\begin{aligned} |n, g\rangle_S = |n, -\rangle &= \cos(\theta) |n, g\rangle - \sin(\theta) |n-1, e\rangle \\ |n-1, e\rangle_S = |n, +\rangle &= \sin(\theta) |n, g\rangle + \cos(\theta) |n-1, e\rangle , \end{aligned} \tag{10.19}$$

where we have made explicit the equivalence between the transformed states and the well-known eigenstates of the Jaynes-Cummings Hamiltonian introduced in Eq. (10.5). As expected, then, the unitary operator $\mathcal{U}^\dagger$ maps the bare basis states onto the set of eigenstates $\{|n, g\rangle_S, |n, e\rangle_S\}$. It is important to note that the ground state is included within the set $\{|n, -\rangle\}$ which corresponds to the "lower branch" of the Jaynes-Cummings ladder for $\Delta \geq 0^+$ ($\theta > 0$) and to the "upper branch" for $\Delta \leq 0^-$ ($\theta < 0$), where superscripts indicate the direction of approach for the case $\Delta = 0$. We note, however, that the choice of which branch includes the ground state is arbitrary, and the roles of $|n, -\rangle$ and $|n, +\rangle$ may be reversed by adding an overall minus sign to S or, equivalently, swapping $\mathcal{U}$ and $\mathcal{U}^\dagger$ in the convention adopted for the similarity transform Eq. (10.10). Nonetheless, a choice has been made in identifying $|0, -\rangle$ with the ground state and, because the $n = 0$ manifold consists of only one state, $|0, +\rangle$ does not represent a physical state of the system.

Turning now to the action of the dressed operators, one may show that for a general operator $\mathcal{O}$,

$$\widetilde{\mathcal{O}} |n, m\rangle_S = e^{-S} \mathcal{O} |n, m\rangle = (\mathcal{O} |n, m\rangle)_S \tag{10.20}$$

where $m = \{g, e\}$. Accordingly, the action of the operator $\widetilde{\mathcal{O}}$ in the basis of transformed states $|n, m\rangle_S$ is exactly analogous the action of $\mathcal{O}$ in the original basis spanned by the Fock states $|n, m\rangle$. The action of the dressed operators on the conventionally labeled states $|n, \pm\rangle$, however, is more subtle as here n indicates the excitation manifold or, equivalently, the total

number of combined bosonic and TLS excitations rather than the number of dressed bosonic excitations alone as in the labeling $|n,m\rangle_S$. We emphasize that these subtleties are solely a consequence of notation and are of little physical importance, and as a result it is often simpler to work with the more physically apparent notation $|n,m\rangle_S$ labeling Fock states in the dressed boson/TLS basis. Still the action of the dressed operators on the states $|n,\pm\rangle$ may be easily worked out through combination of Eqs. (10.19−10.20), with results summarized for reference in Table 10.1 and Fig. 10.2.

Although the description of the dressed operators thus far has been exact for general system parameters, it is instructive to contrast two important parameter regimes of the Jaynes-Cummings model: resonant coupling ($\lambda \gg 1$) and dispersive coupling ($\lambda \ll 1$). In the former case, the mixing angle θ approaches $\pm\pi/4$ and the eigenvectors of Eq. (10.19) are maximally mixed superpositions of bosonic cavity and atomic excitations. Consequently, the dressed bosonic and TLS operators induce transitions between the hybridized light-matter eigenstates of the system and the fundamental excitations of the system are polaritonic. In contrast, the dispersive regime is most easily analyzed by first recognizing that Taylor expansion of the rightmost side of Eq. (10.15) yields $\Lambda \approx \lambda$ and therefore the unitary transformation operator may be approximated as $\mathcal{U} = e^{-\Lambda I_-} \approx e^{-\lambda I_-}$. Approximate forms of the transformed operators are then obtained through Schrieffer-Wolff perturbation theory for $\lambda \ll 1$ [376, 16], leading to

$$\begin{aligned} \widetilde{a} &\approx a - \lambda\sigma^- \\ \widetilde{\sigma}^- &\approx \sigma^- - \lambda a\sigma^z, \end{aligned} \tag{10.21}$$

where only first order corrections in λ have been kept. Here, the bosonic operators $\widetilde{a}^\dagger$ and $\widetilde{a}$ create and destroy photons weakly perturbed by the presence of the TLS. Likewise, the perturbed operators $\widetilde{\sigma}^+$ and $\widetilde{\sigma}^-$ include the expected action of raising or lowering the bare TLS and additionally inherit a small photonic contribution conditioned on the state of the bare TLS via σ^z.

It is important to note that the transformed operators $\widetilde{a}$ and $\widetilde{\sigma}^-$ form an appropriate operator basis regardless of the parameter regime, and their action on the transformed states is independent of whether the system is resonantly or dispersively coupled. However,

	$\lvert n,-\rangle = \lvert n,g\rangle_S$	$\lvert n,+\rangle = \lvert n-1,e\rangle_S$
$\widetilde{a}$	$\sqrt{n}\,\lvert n-1,-\rangle$	$\sqrt{n-1}\,\lvert n-1,+\rangle$
$\widetilde{a}^\dagger$	$\sqrt{n+1}\,\lvert n+1,-\rangle$	$\sqrt{n}\,\lvert n+1,+\rangle$
$\widetilde{a}^\dagger\widetilde{a}$	$n\,\lvert n,-\rangle$	$(n-1)\,\lvert n,+\rangle$
$\widetilde{\sigma}^-$	0	$\lvert n-1,-\rangle$
$\widetilde{\sigma}^+$	$\lvert n+1,+\rangle$	0
$\widetilde{\sigma}^z$	$-\lvert n,-\rangle$	$\lvert n,+\rangle$
$\widetilde{\sigma}^+\widetilde{\sigma}^-$	0	$\lvert n,+\rangle$
$\widetilde{\sigma}^-\widetilde{\sigma}^+$	$\lvert n,-\rangle$	0
N	$n\,\lvert n,-\rangle$	$n\,\lvert n,+\rangle$

Table 10.1: Behavior of the dressed operators acting on the Jaynes-Cummings ladder states $\lvert n,\pm\rangle$.

the underlying character of the transformed operators and states changes as a function of system parameters, most easily seen by relating the transformed operators and states back to those describing the uncoupled system as shown above. For example, it is clear that the bosonic operators $\widetilde{a}$ and $\widetilde{a}^\dagger$ describe either creation and annihilation of polaritons or photons depending on the value of the mixing angle θ (or equivalently, λ). As a result, the dressed operator description of the Jaynes-Cummings Hamiltonian is appropriate independent of the parameter regime under consideration. Still, it is crucially important to maintain an understanding of the parameter-dependent underlying physical character of the excitations described by the transformed operators and states. This will hold especially true in Section 10.3 where it will be shown that the physical interpretation of the distinct quantum phases of a two-site JCH model requires knowledge of the underlying nature of the transformed states across parameter space.

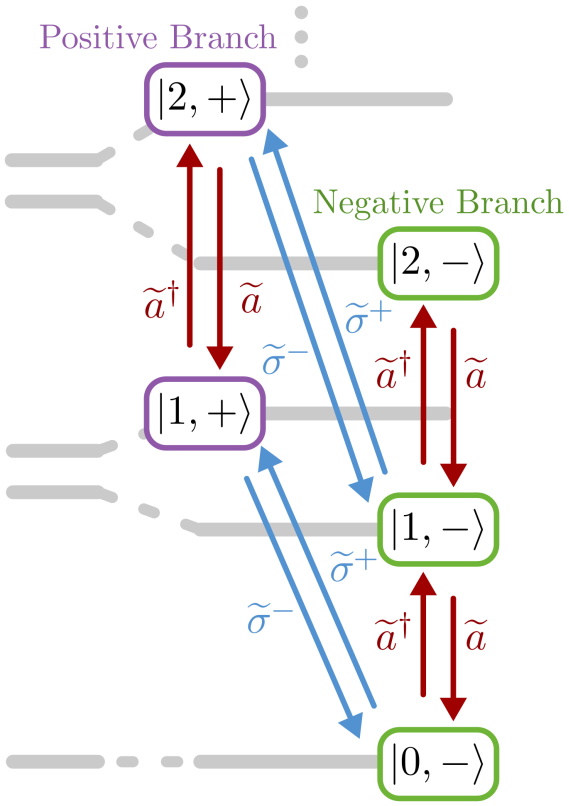

Figure 10.2: Action of the dressed operators on the Jaynes-Cummings ladder. Upon diagonalization, the Jaynes-Cummings Hamiltonian may be repackaged into a positive and negative branch, the former comprising the states $|n,-\rangle$ and the latter $|n,+\rangle$. The dressed bosonic operators $\widetilde{a}^\dagger$ and $\widetilde{a}$ induce transitions between states of the same branch, raising and lowering the total number of excitations by one, respectively. In contrast, the dressed psuedospin operators $\widetilde{\sigma}^+$ and $\widetilde{\sigma}^-$ facilitate transitions between the two branches. Similar to the bare pseudospin operators σ^+ and σ^- acting on the states $|e\rangle$ and $|g\rangle$, respectively, applying $\widetilde{\sigma}^\pm$ to a state denoted by the same sign returns zero.

10.2.3 Revealing the hidden many-body nature of the Jaynes-Cummings Hamiltonian

Paired with the results of the previous section, the Hamiltonian of Eq. (10.16) provides a complete description of the Jaynes-Cummings Hamiltonian in the dressed operator basis. In its present form, the second term clearly endows the system with a nonlinear dependence on the total number of excitations, reminiscent of the Kerr-like, two-body bosonic interactions of the Bose-Hubbard model in Eq. (10.6). The goal of this section is to make this analogy more apparent by casting Eq. (10.16) in a form which accentuates the underlying many-body bosonic interactions. One route for achieving this involves Taylor expansion of Eq. (10.16) about small values of λ and truncating at finite order [376]. Alternatively, identical results are attained by direct Schrieffer-Wolff transformation of the Jaynes-Cummings Hamiltonian in its original representation, whereby the unitary operator $\mathcal{U} = e^{-\Lambda I_-}$ is replaced by its approximate form $\mathcal{U} = e^{-\lambda I_-}$ [376, 16] and all transformations are carried out to finite order. However, the two described strategies are only applicable in the dispersive limit where $\lambda \ll 1$, and it is therefore the purpose of this section to leverage the exact solution of Eq. (10.16) toward a non-perturbative method equally applicable in both the dispersive and resonant coupling regimes.

Focusing on the nonlinear portion of Eq. (10.16) alone, it is useful to define the function

$$f(x) = \sqrt{1 + 4\lambda^2 x} \tag{10.22}$$

such that the dressed operator representation of the Jaynes-Cummings may be written as

$$H = \hbar\omega_c \left(N - \frac{1}{2}\right) + \frac{\hbar}{2}\Delta f(N)\widetilde{\sigma}^z. \tag{10.23}$$

Using the identity $\widetilde{\sigma}^z = \widetilde{\sigma}^+\widetilde{\sigma}^- - \widetilde{\sigma}^-\widetilde{\sigma}^+$ and defining the projection operator $\mathcal{P}_n^{\pm} = |n, \pm\rangle \langle n, \pm|$, the product $f(N)\widetilde{\sigma}^z$ may be further reexpressed as

$$f(N)\widetilde{\sigma}^z = -\mathcal{P}_0 + \sum_{n=1} f(n)(\mathcal{P}_n^+ - \mathcal{P}_n^-). \tag{10.24}$$

As shown in Appendix 10.5, one may Taylor expand $f(n)$ about $n = n_0$ and recast in terms

of dressed operators to find

$$\begin{aligned} f(N)\widetilde{\sigma}^z = &\sum_{r=0}^{\infty}\sum_{m=0}^{r}\binom{1/2}{r}\binom{r}{m}(2\lambda)^{2r}f(n_0)^{1-2r}(-n_0)^{r-m} \\ &\times\sum_{k=0}^{m}(\widetilde{a}^\dagger)^k(\widetilde{a})^k\left[\left\{{m+1\atop k+1}\right\}\widetilde{\sigma}^+\widetilde{\sigma}^- - \left\{{m\atop k}\right\}\widetilde{\sigma}^-\widetilde{\sigma}^+\right], \end{aligned} \tag{10.25}$$

where $\left\{{n\atop k}\right\}$ are Stirling numbers of the second kind. Taking care to adjust upper and lower bounds as needed, the three sums appearing in Eq. (10.25) may be reordered such that the total Hamiltonian becomes

$$H = \hbar\omega_c\left(N-\frac{1}{2}\right) + \sum_{k=0}^{\infty}\frac{1}{k!}\left[C_k^+\widetilde{\sigma}^+\widetilde{\sigma}^- + C_k^-\widetilde{\sigma}^-\widetilde{\sigma}^+\right](\widetilde{a}^\dagger)^k(\widetilde{a})^k, \tag{10.26}$$

where the coefficients of the k-body terms include the remaining sums over m and r in Eq. (10.25). After partial resummation and further manipulation (see Appendix 10.5), it may be shown that these k-body interaction coefficients are given by

$$\begin{aligned} C_k^-/\hbar &= -\frac{\Delta}{2}\sum_{p=0}^{k}\binom{k}{p}(-1)^{k+p}\sqrt{1+4\lambda^2 p} \\ C_k^+/\hbar &= \frac{\Delta}{2}\sum_{p=0}^{k}\binom{k}{p}(-1)^{k+p}\sqrt{1+4\lambda^2(p+1)}. \end{aligned} \tag{10.27}$$

Together, Eqs. (10.26 – 10.27) form an exact bosonic many-body representation of the Jaynes-Cummings Hamiltonian and constitute one of the primary results of this manuscript. Critically, this final form of the Hamiltonian is independent of the expansion point n_0. We note that

$$\begin{aligned} \frac{1}{k!}(\widetilde{a}^\dagger)^k(\widetilde{a})^k\,|n,-\rangle &= \binom{n}{k}\,|n,-\rangle \\ \frac{1}{k!}(\widetilde{a}^\dagger)^k(\widetilde{a})^k\,|n,+\rangle &= \binom{n-1}{k}\,|n,+\rangle \end{aligned} \tag{10.28}$$

and thus each k-body term scales as $C_k^\pm$ multiplied by a combinatorial factor. When applied to the eigenstates $|n,\pm\rangle$, the infinite sum of k-body interactions may be evaluated, resulting in the closed form

$$\sum_{k=0}^{\infty}\frac{1}{k!}C_k^\pm(\widetilde{a}^\dagger)^k(\widetilde{a})^k\,|n,\pm\rangle = \pm\frac{\hbar}{2}\Delta\sqrt{1+4\lambda^2 n}\,|n,\pm\rangle\,, \tag{10.29}$$

thus verifying that the dressed operator many-body form of the Jaynes-Cummings Hamiltonian in Eq. (10.26) returns the well known eigenvalues in Eq. (10.4).

Critical to the usefulness of Eq. (10.26) is a clear partitioning of the Hilbert space into two branches, each spanned by either set of states $|n-1,e\rangle_S = |n,+\rangle$ or $|n,g\rangle_S = |n,-\rangle$. Because the two branches are uncoupled, one may consider each subspace independently. As previously discussed, it is the latter set which includes the global ground state $|0,g\rangle_S = |0,-\rangle$, and we thus focus our analysis on the "negative" branch, noting that much of the discussion follows similarly for the "positive" branch with the caveat that, there, the state $|0,e\rangle_S = |1,+\rangle$ effectively serves as the ground state within the subspace spanned by $|n,+\rangle$. We reemphasize, however, that the states $|n,-\rangle$ are the lower energy eigenstates of each excitation number manifold for $\Delta \geq 0^+$ ($\theta > 0$) only, and the eigenstates $|n,-\rangle$ exceed $|n,+\rangle$ in energy for $\Delta \leq 0^-$ ($\theta < 0$). As a result, one may access the entirety of the Jaynes-Cummings ladder for the resonant coupling case simply by choosing to approach $\Delta = 0$ either from the positive or negative direction, yielding $\theta = \pi/4$ or $\theta = -\pi/4$, respectfully. We will find that this freedom allows for a mathematical description of either repulsive or attractive many-body interactions within the subspace of states $|n,-\rangle$ depending on the sign of θ. Separately, in the dispersive regime, the negative branch comprises perturbed photonic excitations with the weakly dressed TLS in its unexcited state.

Before proceeding with a closer analysis of the coefficients $C_k^{\pm}$, it is important to note that the effects of environmental coupling have, up to this point, not been considered. As a result, the many-body terms of Eq. (10.26) seemingly play an important role for all $C_k^{\pm} \neq 0$ and, as illustrated in Fig. (10.1b), perfect photon blockade is achieved as long as $g \neq 0$. In an experimental setting, however, coupling to the environment broadens the levels of the Jaynes-Cummings ladder such that photon blockade is impaired when the dominant rate of dissipation $\Gamma = \max\{\kappa,\gamma\}$ exceeds the light-matter coupling strength g, where κ and γ denote the cavity and atomic linewidth, respectively. As a consequence, strong effective many-body interactions are realizable only in the strong coupling regime (i.e., $g > \Gamma$), as the impact of each k-body term depends not on $C_k^{\pm}$ alone, but rather on the ratio $C_k^{\pm}/\hbar\Gamma$. Although the effects of environmental coupling will not be explicitly considered in the present work, given the discussion above it is convenient to consider all parameters

in units of Γ as it determines the appropriate time scale for a specific realization of the Jaynes-Cummings Hamiltonian, allowing for a general discussion agnostic of the particulars of each experimental platform.

While Eqs. (10.26–10.27) provide an exact bosonic many-body representation of the Jaynes-Cummings Hamiltonian for general system parameters, the infinite sum over competing k-body terms obscures simple interpretation. It is therefore advantageous to closely analyze several limiting cases to gain insight into the contributions of the hierarchy of many-body terms appearing in Eq. (10.26). In the following, we restrict analysis to the few excitation limit and investigate both the dispersive and resonant coupling regimes independently. We then conclude the current section with a brief discussion of the more general n excitation case.

The few excitation limit: $n \leq 2$

We begin by examining the Hamiltonian in Eq. (10.26) in the limit where the total number of excitations is fixed to two or fewer. In this scenario, the normally ordered terms $(\widetilde{a}^\dagger)^k(\widetilde{a}^\dagger)^k$ do not contribute for $k > 3$ for the negative branch and $k > 2$ for the positive branch. Consequently, the $n \leq 2$ limit allows for analysis of the Hamiltonian in the scenario where the highest order contributing many-body interactions correspond to two-body terms, leading to the effective Hamiltonian

$$\begin{aligned} H^{\text{eff}}_{n\leq 2} =& \widetilde{\sigma}^+\widetilde{\sigma}^- \left[(\hbar\omega_c + C_1^+)\widetilde{a}^\dagger\widetilde{a} + \frac{1}{2}\hbar\omega_c + C_0^+\right] \\ &+ \widetilde{\sigma}^-\widetilde{\sigma}^+ \left[(\hbar\omega_c + C_1^-)\widetilde{a}^\dagger\widetilde{a} + \frac{C_2^-}{2}\widetilde{a}^\dagger\widetilde{a}^\dagger\widetilde{a}\widetilde{a} - \frac{1}{2}\hbar\omega_c + C_0^-\right], \end{aligned} \tag{10.30}$$

where the first and second lines correspond to the effective Hamiltonian projected onto the positive and negative branches, respectively, and

$$\begin{aligned} C_0^-/\hbar &= -\frac{\Delta}{2} \\ C_1^-/\hbar &= -\frac{\Delta}{2}(-1+\sqrt{1+4\lambda^2}) \\ C_2^-/\hbar &= +\frac{\Delta}{2}(-1+2\sqrt{1+4\lambda^2}-\sqrt{1+8\lambda^2}) \\ C_0^+/\hbar &= -\frac{\Delta}{2}(\sqrt{1+4\lambda^2}) \\ C_1^+/\hbar &= -\frac{\Delta}{2}(-\sqrt{1+4\lambda^2}+\sqrt{1+8\lambda^2}) \end{aligned} \tag{10.31}$$

are the explicit forms of the interaction coefficients. In all cases, the above coefficients are written in such a way that the factor in parenthesis is positive for all values of λ and therefore the overall sign of the coefficient is indicated explicitly in the prefactor. Notably, the overall sign of the coefficients $C_i^{\pm}$ depends upon the sign of the detuning Δ. Two-body bosonic interaction terms appear only for the negative branch as the positive branch consists of states with the dressed TLS in its excited state, and limiting the total number of excitations to two or fewer therefore ensures at most one dressed photonic excitation.

Focusing only on the negative branch, the Hamiltonian may be written within this subspace as

$$H_{n\leq 2}^{\mathrm{eff}(-)} = (\hbar\omega_c + C_1^-)N + \frac{C_2^-}{2}N(N-1) - \frac{1}{2}\hbar\omega_c + C_0^-. \tag{10.32}$$

where we have used the fact that N and $\widetilde{a}^\dagger\widetilde{a}$ are identical for the negative branch. This effective Hamiltonian is, up to an overall energy shift, identical in form to the on-site terms of the Bose-Hubbard model [353],

$$H_{\mathrm{BH,on\text{-}site}} = -\mu N + \frac{U}{2}N(N-1), \tag{10.33}$$

where the on-site interaction strength U is determined by C_2^- and N describes the number of *dressed* bosonic excitations. Despite the fact that the linear energy $\hbar\omega_c + C_1^-$ is strictly positive for realistic parameters and thus naturally describes a system with $\mu < 0$, we note that one may transform to a rotating frame via the unitary operator $e^{-i\omega_c\widetilde{a}^\dagger\widetilde{a}t}$ such that C_1^-, which is negative for $\Delta \geq 0^+$, becomes analogous to the chemical potential. As discussed in Section 10.2.2, the dressed operators $\widetilde{a}^\dagger$ and $\widetilde{a}$ describe creation and annihilation of bosonic

excitations whose character varies from polaritonic ($\lambda \gg 1$) to photonic ($\lambda \ll 1$) depending on the choice of g and Δ. Furthermore, as the overall sign of C_2^- is determined by the sign of Δ, the interaction energy U can be either positive or negative. The former case results in an effective polariton-polariton (or photon-photon) repulsion, whereas the latter corresponds to polariton-polariton (or photon-photon) attraction.

Fig. 10.3a shows the absolute value of C_2^- as a function of system parameters g and Δ, all relative to a fictitious dissipation rate Γ which sets the relevant energy scale pertaining to a particular experimental platform, as discussed previously. As expected, the scaling of the two-body interaction is largest for resonant coupling where the bosonic modes and TLS maximally mix. Evaluating C_2^- for the perfectly resonant case leads to

$$C_2^-/\hbar = \pm(2-\sqrt{2})g, \qquad \text{(resonant)} \tag{10.34}$$

where the sign of C_2^- is determined by the direction in which $\Delta = 0$ is approached and it is assumed that $g \geq 0$. Then for resonant coupling, C_2^- scales linearly with g and strong two-body interactions ($C_2^- \gtrsim \hbar\Gamma$) are achieved for

$$g/\Gamma \gtrsim 1/(2-\sqrt{2}), \tag{10.35}$$

a slightly higher threshold than strong coupling.

In the dispersive regime, C_k^- depends nonlinearly on λ and, as a result, spans many orders of magnitude for constant Δ depending upon the value of g. Expanding C_2^- about small values of λ leads to the result

$$C_2^-/\hbar \approx 2\lambda^3 g, \qquad \text{(dispersive)} \tag{10.36}$$

indicating that the fall off of two-body interactions for decreasing g is dependent on how far into the dispersive regime the system is tuned. To realize strong two-body interactions (i.e., $C_2^- \gtrsim \hbar\Gamma$) in the dispersive coupling regime, exceptionally large values of g/Γ must be attained such that the condition

$$g/\Gamma \gtrsim 1/2\lambda^3 \tag{10.37}$$

is satisfied, a limit which has been approached in circuit QED platforms (for $\lambda \sim 0.1$), reaching values of g/Γ in the several hundreds [379]. Eq. (10.37) may be thought of as a

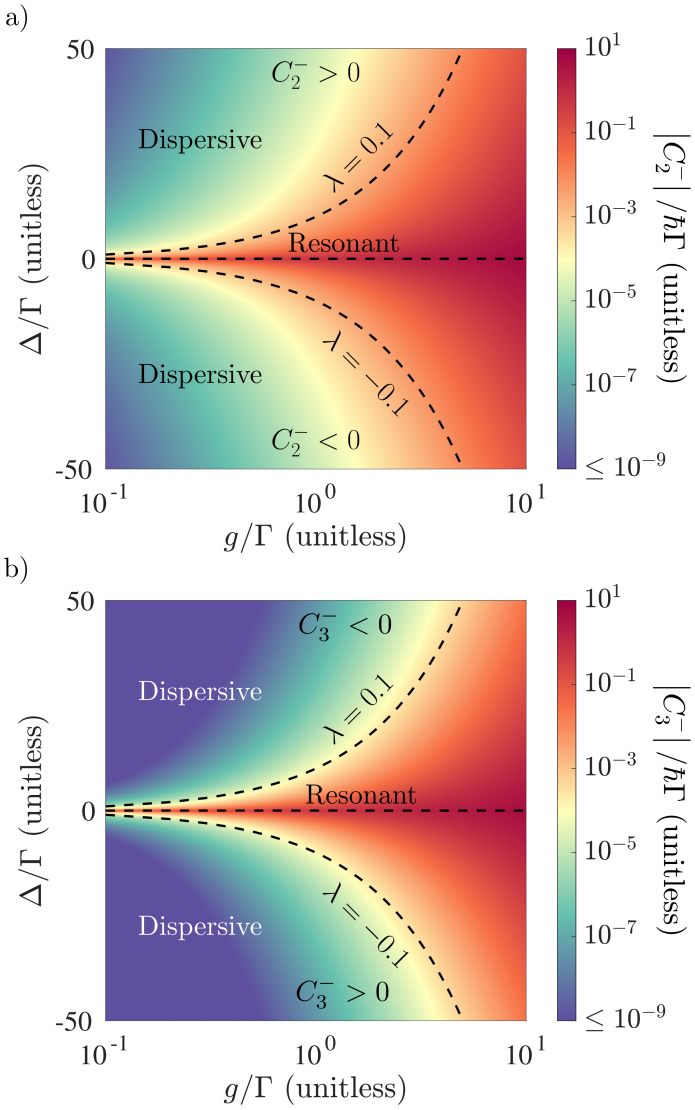

Figure 10.3: (a) Sign and magnitude of the two-body coefficient C_2^- as a function of Δ and g. For practical purposes, all parameters are normalized to Γ which sets the relevant frequency scale for the particular experimental platform in consideration. Regardless of the parameter regime, C_2^- always takes the same sign as Δ. As discussed in the main text, C_2^- is discontinuous at $\Delta = 0$ and may take on a positive or negative values depending on the direction of approach. For all g, C_2^- is maximized for resonant coupling ($\lambda \gg 1$), and is comparably smaller for dispersive coupling ($\lambda \ll 1$), requiring $g/\Gamma \gtrsim 1/2\lambda^3$ to achieve strong photon-photon interactions ($C_2^-/\Gamma \gtrsim 1$). (caption continued on following page)

Figure 10.3: (continued) The dashed line indicates $\lambda = 0.1$, typically considered the onset of the dispersive regime. (b) Sign and magnitude of the three-body coefficient C_3^- as a function of Δ and g, all normalized to Γ. C_3^- displays a qualitatively similar trend to C_2^-, taking on a maximal magnitude at $\Delta = 0$ and falling off rapidly for decreasing λ. For all parameters, $|C_3^-| < |C_2^-|$ and, in contrast to C_2^-, the sign of C_3^- is opposite to that of Δ.

higher order generalization of the strong-dispersive regime [395, 396], defined by the condition $g/\Gamma \gtrsim 1/\lambda$ (for $\lambda \lesssim 0.1$) which characterizes the portion of parameter space in which the first order frequency shift $C_1^{\pm}$ exceeds $\hbar\Gamma$.

While boson-boson interactions are most easily attained in the case of resonant coupling, it is in the dispersive parameter regime in which the bosonic many-body interactions take on a photonic nature. As we shall see in Sec. 10.3 where the present analysis is extended to a two-site Jaynes-Cummings-Hubbard system, it is *photonic* two-body interactions in the dispersive regime, rather than *polaritonic* two-body interactions on resonance, which will mostly clearly provide a route for analog quantum simulation of Bose-Hubbard physics.

The few excitation limit: $n \leq 3$

The Hamiltonian in Eq. (10.30) is exact for $n \leq 2$. Consideration of states with $n = 3$ requires inclusion of three-body terms, leading to the effective Hamiltonian

$$H_{n\leq 3}^{\text{eff}} = H_{n\leq 2}^{\text{eff}} + \widetilde{\sigma}^{+}\widetilde{\sigma}^{-}\left[\frac{C_2^+}{2}\widetilde{a}^{\dagger}\widetilde{a}^{\dagger}\widetilde{a}\widetilde{a}\right] + \widetilde{\sigma}^{-}\widetilde{\sigma}^{+}\left[\frac{C_3^-}{2}\widetilde{a}^{\dagger}\widetilde{a}^{\dagger}\widetilde{a}^{\dagger}\widetilde{a}\widetilde{a}\widetilde{a}\right], \tag{10.38}$$

where

$$\begin{aligned} C_3^-/\hbar &= -\frac{\Delta}{2}(-1 + 3\sqrt{1+4\lambda^2} - 3\sqrt{1+8\lambda^2} + \sqrt{1+12\lambda^2}) \\ C_2^+/\hbar &= +\frac{\Delta}{2}(-\sqrt{1+4\lambda^2} + 2\sqrt{1+8\lambda^2} - \sqrt{1+12\lambda^2}) \end{aligned} \tag{10.39}$$

describe the strength of three-body (two-body) interactions within the negative (positive) branch of the Jaynes-Cummings ladder. Similar to the the $n \leq 2$ case, three-body terms do not appear for the positive branch as the states considered allow for up to two bosonic excitations. We note that the trends followed by the positive branch for $n \leq 3$ are similar

to those of the negative branch for $n \leq 2$ (with signs reversed), and therefore will not be explicitly discussed.

Fig. 10.3b shows the magnitude of C_3^- as a function of Δ and g, again relative to the maximal dissipative rate $\Gamma = \max\{\kappa, \gamma\}$. Notably, C_2^- and C_3^- differ by an overall sign with the latter of smaller magnitude for all parameters. Otherwise the two follow a similar trend, albeit with C_3^- declining much more rapidly with decreasing g.

Following the analysis of the two-body interaction strength C_2^-, it is helpful to derive expressions for C_3^- for the cases of resonant and dispersive coupling. For the former, evaluating C_3^- for $\Delta = 0$ leads to

$$C_3^- = \mp(3 - 3\sqrt{2} + \sqrt{3})g \qquad \text{(resonant)}, \tag{10.40}$$

where, similar to Eq. (10.34), the sign of C_3^- is dependent on the direction in which $\Delta = 0$ is approached and the overall expression is proportional to g, here with a smaller prefactor such that $|C_2^-| > |C_3^-|$.

In contrast, evaluating C_3^- for small values of λ via Taylor expansion yields

$$C_3^- \approx -12\lambda^5 g \qquad \text{(dispersive)}, \tag{10.41}$$

similar to the result Eq. (10.36) yet scaling at fifth order in λ rather than third. Consequently, C_3^- falls off much more rapidly than C_2^- in the dispersive regime, indicating that the strength of three-body interactions are small relative to their two-body counterparts and may therefore be discarded for small enough λ. For all g and Δ, C_2^- and C_3^- are of opposite sign and therefore counteract one another in systems with at least three excitations, with positively and negative valued interactions describing repulsion and attraction, respectively.

Nature of the many-body coefficients for arbitrary n

Following the preceding analysis of the parameter dependent strength of two- and three-body interactions in the few excitation limit, extension to the general n excitation limit is straightforward. Focusing again on the negative branch, it is convenient to independently analyze the form of the k-body coefficient C_k^- for the cases of resonant and dispersive coupling. It is worth emphasizing again that for any finite n, each k-body term will only contribute if

$k \leq n$, and the sum in Eq. (10.26) therefore always terminates. However, the $n \to \infty$ limit of the Jaynes-Cummings Hamiltonian is important to analyze as the eigenspectrum becomes approximately linear, inhibiting photon blockade for large values of n [391, 392]. Evaluating the general form of C_k^- for $\Delta = 0$ (see Eq. (10.27)), we find

$$C_k^- = \pm(-1)^k \left[\sum_{p=1}^{k} \binom{k}{p} (-1)^{p+1} \sqrt{p} \right] g \qquad \text{(resonant)}, \tag{10.42}$$

where the upper and lower signs corresponds to the limit $\Delta \to 0^{\pm}$ and $\theta = \pm\pi/4$. Therefore the linear relationship with g previously found for C_2^- and C_3^- is general for all k. Furthermore, the factor in parentheses is positive and convergent for all k. The overall sign of the coefficients C_k^- therefore alternate in k, a trend which can be shown more generally from Eq. (10.27) without specializing to the case of resonant coupling. In the limit of very large k, the above sum asymptotically trends toward the closed expression [397] $C_k^- = (-1)^k g/\sqrt{\pi \ln(k)}$ and thus vanishes in the limit $k \to \infty$.

For the case of dispersive coupling ($\lambda \ll 1$), C_k^- may be written as

$$C_k^-/\hbar \approx -k! \binom{1/2}{k} (2\lambda)^{2k-1} g \qquad \text{(dispersive)}, \tag{10.43}$$

where only the lowest order term in λ has been retained. In deriving this expression, $\sqrt{1+4\lambda^2 p}$ was evaluated using a binomial expansion which, strictly speaking, is convergent only for $p \leq k < 1/4\lambda^2$, setting an upper bound of $\lambda < \sqrt{1/4k}$ for which Eq. (10.43) is valid.

Panels (a) and (b) of Fig. 10.4 contrast the behavior of C_k^- for resonant (Eq. (10.42)) and dispersive (Eq. (10.43)) coupling. As stated previously, the sign of the C_k^- alternates in k independent of parameter regime, indicated by the color of the markers. In particular, blue (red) markers represent coefficients which are positive (negative) for $\Delta \geq 0^+$, with signs inverted for $\Delta \leq 0^-$. For dispersive coupling, the relative strength of $|C_k^-/\hbar\Gamma|$ falls off rapidly due to the λ^{2k-1} dependence in Eq. (10.43) and, as a result, the sum in Eq. (10.26) may be truncated at some cutoff order $k_{\max}$ dependent upon the coupling strength g, dispersive parameter λ, and the desired accuracy. For $k_{\max} = 2$, Eq. (10.26) becomes an approximate analog to the on-site portion of the Bose-Hubbard Hamiltonian in Eq. (10.33).

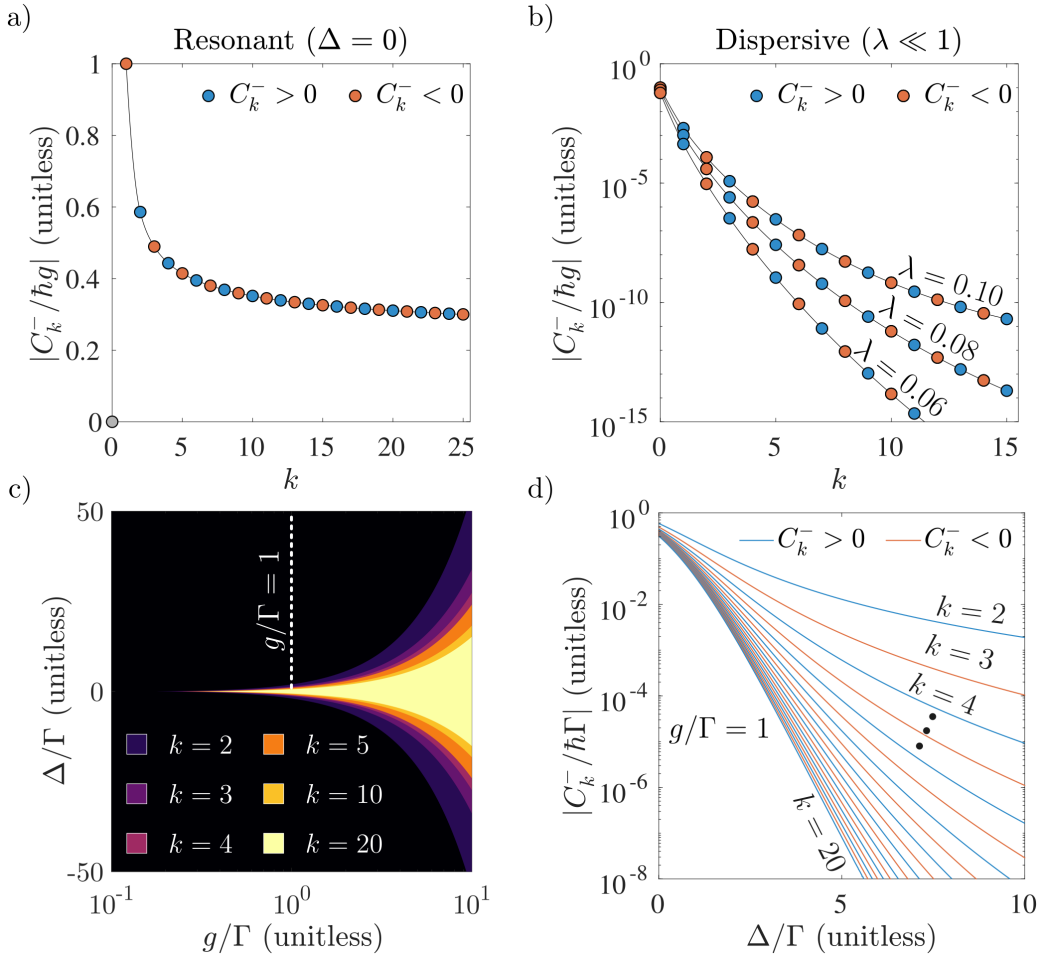

Figure 10.4: Top panels: sign and magnitude of the k-body coefficient C_k^- normalized to $\hbar g$ for (a) resonant and (b) dispersive coupling, plotted for discrete values of k. Red circles correspond to a negative value, blue a positive value, and gray a value of zero, with black interpolating lines shown as a guide. (a) Resonant coupling is characterized by a relatively slow fall off in magnitude of C_k^- for increasing k, asymptotically approaching the value $g/\sqrt{\pi \ln(k)}$ for very large k and vanishing for $k \to \infty$. (b) In contrast, $|C_2^-|$ falls off very rapidly for dispersive coupling, allowing for truncation of the sum over k-body interactions at a small, finite value of k according to the accuracy desired. The three lines show this trend for distinct values of λ, with smaller λ displaying a faster fall off. (caption continued on following page)

Figure 10.4: (continued) (c) The region of parameter space for which $|C_k^-/\hbar\Gamma| > 0.1$, with each colored region corresponding to a particular value of k. As seen explicitly for C_2^- and C_3^- in Fig. 10.3, each coefficient follows a similar trend, with areas of highest (lowest) magntitude coinciding with $\lambda \gg 1$ ($\lambda \ll 1$). For increasing k, the subset of parameter space in which the threshold $|C_k^-/\hbar\Gamma| > 0.1$ is met tightens, with each region corresponding to order k encompassing the smaller region corresponding to $k+1$. The maximal value $k = 20$ was chosen for simplicity, with higher values of k continuing the same trend. (d) The evolution of $|C_k^-/\hbar\Gamma|$ from resonant to dispersive coupling, shown as a function of Δ/Γ for constant coupling strength tuned to the onset of strong coupling $g/\Gamma = 1$ (white dashed line in panel (c)). Red and blue lines display the alternating sign of C_k^-. All large k coefficients experience a similar, rapid fall-off as Δ is increased from the resonant case. In comparison, smaller k coefficients decrease in magnitude more slowly. A "fan out" effect is observed as the detuning trends toward $\Delta = 10g$, corresponding to the onset of dispersive coupling (i.e., $\lambda = 0.1$). In contrast, all coefficients take on values comparable in magnitude for $\Delta = 0$.

In contrast, perfectly resonant coupling is characterized by many-body coefficients C_k^- which fall off slowly in k and, consequently, the sum in Eq. (10.26) cannot be truncated unless only a finite number of excitations n are considered.

For all k, the trend followed by the coefficients C_k^- as a function of g and Δ resembles that of C_2^- and C_3^- shown in Fig. 10.3, differing only in the rapidity with which the magnitude of C_k^- falls off as Δ trends away from zero. Fig. 10.4c illustrates the relative magnitude of various coefficients C_k^- across all parameter space, with colored sections corresponding to regions where $|C_k^-/\hbar\Gamma| \geq 0.1$. Note that this threshold is somewhat arbitrary and therefore should not be taken as an exact measure of the importance of each term, as this is dependent upon the particular system and context under study. Still, the relative importance of higher order k-body interactions is clearly evident both for perfect resonant coupling ($\Delta = 0$) and for near-resonant coupling ($\lambda \gg 1$). This is further illustrated by Fig. 10.4 showing the magnitude of the many-body coefficients C_k^- (relative to $\hbar\Gamma$) at the onset of strong coupling, $g/\Gamma = 1$, indicated by a white dotted line in Fig. 10.4c. Similar to panels (a) and (b),

blue (red) lines indicate a positive (negative) value of C_k^- for $\Delta \geq 0^+$, with signs reverse for $\Delta \leq 0^-$.

Finally, we note that the presented many-body form of the Jaynes-Cummings Hamiltonian must become approximately linear in the limit $n \to \infty$, inhibiting photon blockade entirely. This behavior of the Jaynes-Cummings Hamiltonian is well-known [391, 392, 353] and can most easily be seen by analyzing the difference $E_{n+1,\pm} - E_{n,\pm}$ (see Eq. (10.4)) in the large n limit. In the form Eq. (10.26), however, this limiting behavior is not at all obvious, particularly for resonant coupling, as the contributions of the individual, normally ordered k-body products $(\widetilde{a}^\dagger)^k(\widetilde{a}^\dagger)^k/k!$ return the binomial coefficient $\binom{n}{k}$ when acted on a dressed Fock state and therefore diverge for $n \to \infty$. Despite this, Eq. (10.29) shows that the k-body interactions sum together to produce the correct eigenvalues and, as a result,

$$\lim_{n\to\infty} \sum_{k=0}^{\infty} \frac{1}{k!} C_k^{\pm} (\widetilde{a}^\dagger)^k (\widetilde{a})^k (|n+1,\pm\rangle - |n,\pm\rangle) = 0. \tag{10.44}$$

More qualitatively, this behavior is understood as a consequence of the alternating sign of the many-body coefficients $C_k^{\pm}$, causing all odd k-body interactions to counteract those with even k. As a result, the individual nonlinear interactions together conspire to give a purely linear spectrum, in alignment with the known behavior of the Jaynes-Cummings ladder in the large n limit.

10.3 Extension to a two site Jaynes-Cummings-Hubbard system and analysis of its quantum phases

The results of the previous section hint at a similarity between the on-site portion of the Bose-Hubbard and Jaynes-Cummings Hamiltonians – the former containing bosonic two-body interactions, and the latter k-body interactions up to some order $k_{\max}$ dependent upon the ratio $\lambda = g/\Delta$ and maximum number of excitations considered. Because only a single site was under study, the most interesting aspects of the Bose-Hubbard model, e.g., the superfluid to insulating quantum phase transition, were not discussed. The purpose of the present section is to revisit this comparison for the simplest extension possible: a two-site system. We note that qualitative and quantitative analogies between the Bose-Hubbard and Jaynes-Cummings Hubbard (JCH) models are numerous in the literature [353, 354, 365, 360,

366, 355, 367, 36, 368, 369, 362, 363, 364, 370, 371, 372, 373, 374, 375] and, as such, we refer to these other works for a mathematically rigorous analysis of the quantum phase transition admitted by the JCH model for both a finite [36, 364] and infinite [353, 355, 367, 398] number of sites. Here, our aim is to illustrate the unique and complementary perspective afforded by the many-body form of the Jaynes-Cummings Hamiltonian presented in Eq. (10.26). Furthermore, we hope that the analysis and discussion contained herein can provide guidance for analog quantum simulators which aim to simulate many-body bosonic Hamiltonians using Jaynes-Cummings nonlinearities.

10.3.1 Comparison between the Jaynes-Cummings-Hubbard and Bose-Hubbard models

The two-site Bose-Hubbard model is given by

$$\begin{aligned} H_{\text{BH}} &= \sum_{i=1,2} H^{(i)}_{\text{BH,on-site}} + H_{\text{BH,hop}} \\ H^{(i)}_{\text{BH,on-site}} &= -\mu b_i^\dagger b_i + \frac{U}{2} b_i^\dagger b_i^\dagger b_i b_i \\ H_{\text{BH,hop}} &= J(b_1^\dagger b_2 + b_1 b_2^\dagger). \end{aligned} \tag{10.45}$$

Here, b and $b^\dagger$ are bosonic annihilation and creation operators, J the hopping rate between the two sites labeled $i = 1, 2$, and U and μ are the on-site interaction strength and chemical potential, here assumed to be identical for both sites for simplicity. It is well known that this Hamiltonian admits a quantum phase transition facilitated by tuning the ratio J/U at zero temperature [399, 357]. For $J \gg U$, the system is said to be in a superfluid phase, characterized by a large variance in single site particle number and a delocalized many-body ground state of the form

$$|\Psi_{\text{SF}}\rangle \propto \left(\sum_{i=1,2} (\mp)^i b_i^\dagger \right)^n |0\rangle \,, \tag{10.46}$$

where n is the total number of particles in the ground state (fixed through choice of μ) and the upper (lower) sign corresponds to $J > 0$ ($J < 0$). For simplicity, the convention $J > 0$ will be assumed for the remainder of this manuscript. In the opposite limit $J \ll U$, the repulsive interaction dominates site-to-site tunneling and single site particle number fluctuations are suppressed as a result. Consequently, the ground state becomes the localized Mott-insulating

state,

$$|\Psi_{\mathrm{MI}}\rangle \propto \prod_{i=1,2} \left(b_i^\dagger\right)^{n/2} |0\rangle \,. \tag{10.47}$$

Similar to Eq. (10.45), the two-site JCH model may be written as

$$\begin{aligned} H_{\mathrm{JCH}} &= \sum_{i=1,2} H_{\mathrm{JC}}^{(i)} + H_{\mathrm{hop}} \\ H_{\mathrm{JC}}^{(i)} &= \hbar\omega_c a_i^\dagger a_i + \frac{1}{2}\hbar\omega_a \sigma_i^z + \hbar g_i (a_i^\dagger \sigma_i^- + a_i \sigma_i^-) \\ H_{\mathrm{hop}} &= J(a_1^\dagger a_2 + a_1 a_2^\dagger), \end{aligned} \tag{10.48}$$

where on-site parameters ω_c, ω_a, and g have been taken to be identical for both sites for simplicity. The parallel structure of Eq. (10.45) and Eq. (10.48) underscores an obvious connection between the Bose-Hubbard and JCH models: both contain identical bosonic tunneling terms and similar on-site interactions, with the only distinguishing features appearing as the source of nonlinearity in $H^i_{\mathrm{BH,on\text{-}site}}$ and H^i_{JC}, the former naturally including bosonic two-body terms, and the latter comprising an additional degree of freedom in the form of a TLS which ultimately mediates effective photon-photon interactions. Still, qualitative comparison between the two is merited and previous works have shown the JCH model to admit a superfluid-to-insulator quantum phase transition similar to that of the Bose-Hubbard model [353, 354, 360, 355, 36, 361, 362, 363, 364], albeit with some key differences. For one, while the quantum phases of the Bose-Hubbard model are realized at opposing limits of the ratio J/U, the JCH model involves three distinct tunable parameters (J, Δ, g) and, consequently, multiple pathways exist for tuning across a phase transition [353, 36, 355, 367]. In addition, the very nature of the interacting bosonic excitations are themselves dependent upon the parameter regime, leading to a photonic-to-polaritonic transition which accompanies the superfluid-to-insulator transition in the JCH model [361, 36], behavior which is absent in the Bose-Hubbard case. Finally, as noted previously, the JCH Hamiltonian becomes approximately linear in the limit of large n, while the Bose-Hubbard model maintains nonlinearity for all n. These distinguishing features have received qualitative recognition in the literature, yet have not been formally analyzed in the context of dressed operators where bosonic many-body interactions are brought to the forefront, as in Eq. (10.26). The findings of the previous section therefore compel a closer reexamination of the differences between the

JCH and Bose-Hubbard models, and consequences thereof, using the techniques of unitary transformation.

Following the procedure of Section 10.2.1, we begin analysis by transforming Eq. (10.48) into the dressed polariton basis. Here, we apply the transformation operator $\mathcal{U} = e^{S_1+S_2}$ where the generator S_i is defined as

$$S_i = -\Lambda(N_i) I_-^{(i)} \tag{10.49}$$

where $I_-^{(i)}$ and $\Lambda(N_i) = \theta(N_i)/\sqrt{N_i}$ are defined exactly as before (see Eqs. (10.8) and (10.15)) with the subscript i inserted where appropriate to label quantities which differ between sites. For example, here N_i represents the total number operator at site i alone, and the total number of excitations in the system is therefore given by $N = N_1 + N_2$. It is important to emphasize that the generators S_1 and S_2 commute and the operator $\mathcal{U}$ may therefore be rewritten as a product of unitary operators $\mathcal{U} = \mathcal{U}_1\mathcal{U}_2$ where $\mathcal{U}_1 = e^{S_1}$ and $\mathcal{U}_2 = e^{S_2}$. Critically, $\mathcal{U}_i$ commutes with all operators associated solely with the opposite site and, as a result, transformation of the on-site contributions to the JCH proceeds exactly as in Section 10.2.1. The two-site JCH Hamiltonian may therefore be written as

$$H_{\text{JCH}} = H_{\text{hop}} + \sum_{i=1,2} \hbar\omega_c \left(N_i - \frac{1}{2}\right) + \sum_{i=1,2}\sum_{k=0}^{\infty} \frac{1}{k!} \left[C_k^+ \widetilde{\sigma}_i^+ \widetilde{\sigma}_i^- + C_k^- \widetilde{\sigma}_i^- \widetilde{\sigma}_i^+\right] (\widetilde{a}_i^\dagger)^k (\widetilde{a}_i)^k, \tag{10.50}$$

where notation has been maintained from the previous section such that the coefficients $C_k^\pm$ are defined by Eq. (10.27) and

$$\begin{aligned} \widetilde{a}_i &= \mathcal{U}^\dagger a_i \mathcal{U} \\ \widetilde{\sigma}_i^- &= \mathcal{U}^\dagger \sigma_i^- \mathcal{U} \end{aligned} \tag{10.51}$$

are the transformed operators describing annihilation of the dressed excitations at site i. We remark that Eq. (10.50) is similar in form to the effective Hamiltonian presented in Ref. [361] [1]. There, on-site contributions to the JCH model are written for the case $\Delta = 0$ in terms of branch-dependent polaritonic operators obeying neither bosonic nor psuedo-spin

[1] In particular, see Eq. (5) of the referenced paper by Noh and Angelakis

commutation relations. The form presented here is therefore unique in that the dressed operators describe the true quasiparticle excitations at each site, maintaining the appropriate commutation relations, and all many-body interactions are described without use of excitation number dependent coefficients for general g and Δ.

Because H_{hop} describes an exchange of purely photonic quanta, writing this explicitly in terms of dressed operators for general system parameters yields an infinite set of terms which are not obviously expressible in a closed form. Up to first order in Λ alone, transformation of H_{hop} yields terms corresponding to polariton hopping $J(\widetilde{a}_1^\dagger \widetilde{a}_2 + \widetilde{a}_1 \widetilde{a}_2^\dagger)$, linear cross-site interactions $J\Lambda(N_1)(\widetilde{a}_2^\dagger \widetilde{\sigma}_1^- + \widetilde{a}_2 \widetilde{\sigma}_1^+) + J\Lambda(N_2)(\widetilde{a}_1^\dagger \widetilde{\sigma}_2^- + \widetilde{a}_1 \widetilde{\sigma}_2^+)$, and, in addition – because the hopping term preserves the total number of excitations $N_1 + N_2$ but not the number of excitations at each site N_i – a number of nonlinear terms which vanish in the dispersive regime (where $\Lambda(N_i) \approx \lambda$) but become important near resonant coupling. Matters are further complicated at second order in Λ, primarily due to a cascade of additional two-site terms which do not commute with N_i. As a result, there is little to be gained by attempting to write H_{hop} in terms of dressed operators for general system parameters as the physics of the site to site hopping is most apparent in the bare photonic basis, and it is advantageous to instead consider several limiting cases independently.

10.3.2 Dispersive coupling: $\lambda \ll 1$

As previously discussed in Section 10.2.3, when projected onto the negative branch the on-site terms of the JCH model directly mirror those of Bose-Hubbard model for dispersive coupling due to a sharp drop off in the coefficients C_k^- for increasing k. Neglecting terms second order and higher in λ, the full two-site JCH Hamiltonian may be expressed as

$$
\begin{aligned}
H_{\mathrm{JCH}} \approx\ & \mathcal{P}_1^- \mathcal{P}_2^- \left[\sum_{i=1,2} \left(\hbar\Omega_0^- \widetilde{a}_i^\dagger \widetilde{a}_i + \frac{U_{\mathrm{eff}}^-}{2} \widetilde{a}_i^\dagger \widetilde{a}_i^\dagger \widetilde{a}_i \widetilde{a}_i \right) + J(\widetilde{a}_1^\dagger \widetilde{a}_2 + \widetilde{a}_1 \widetilde{a}_2^\dagger) + 2E_0^- \right] \\
& + \mathcal{P}_1^+ \mathcal{P}_2^+ \left[\sum_{i=1,2} \left(\hbar\Omega_0^+ \widetilde{a}_i^\dagger \widetilde{a}_i + \frac{U_{\mathrm{eff}}^+}{2} \widetilde{a}_i^\dagger \widetilde{a}_i^\dagger \widetilde{a}_i \widetilde{a}_i \right) + J(\widetilde{a}_1^\dagger \widetilde{a}_2 + \widetilde{a}_1 \widetilde{a}_2^\dagger) + 2E_0^+ \right] \\
& + \mathcal{P}_1^+ \mathcal{P}_2^- \left[\hbar\Omega_0^+ \widetilde{a}_1^\dagger \widetilde{a}_1 + \frac{U_{\mathrm{eff}}^+}{2} \widetilde{a}_1^\dagger \widetilde{a}_1^\dagger \widetilde{a}_1 \widetilde{a}_1 + \hbar\Omega_0^- \widetilde{a}_2^\dagger \widetilde{a}_2 + \frac{U_{\mathrm{eff}}^-}{2} \widetilde{a}_2^\dagger \widetilde{a}_2^\dagger \widetilde{a}_2 \widetilde{a}_2 + J(\widetilde{a}_1^\dagger \widetilde{a}_2 + \widetilde{a}_1 \widetilde{a}_2^\dagger) + E_0^+ + E_0^- \right] \\
& + \mathcal{P}_1^- \mathcal{P}_2^+ \left[\hbar\Omega_0^- \widetilde{a}_1^\dagger \widetilde{a}_1 + \frac{U_{\mathrm{eff}}^-}{2} \widetilde{a}_1^\dagger \widetilde{a}_1^\dagger \widetilde{a}_1 \widetilde{a}_1 + \hbar\Omega_0^+ \widetilde{a}_2^\dagger \widetilde{a}_2 + \frac{U_{\mathrm{eff}}^+}{2} \widetilde{a}_2^\dagger \widetilde{a}_2^\dagger \widetilde{a}_2 \widetilde{a}_2 + J(\widetilde{a}_1^\dagger \widetilde{a}_2 + \widetilde{a}_1 \widetilde{a}_2^\dagger) + E_0^+ + E_0^- \right] \\
& + J\lambda(\widetilde{a}_1^\dagger \widetilde{\sigma}_2^- + \widetilde{a}_1 \widetilde{\sigma}_2^+) + J\lambda(\widetilde{a}_2^\dagger \widetilde{\sigma}_1^- + \widetilde{a}_2 \widetilde{\sigma}_1^+)
\end{aligned}
\tag{10.52}
$$

where $\Omega_0^\pm = \omega_c + C_1^\pm/\hbar$ denotes an effective resonant energy, $U_{\mathrm{eff}}^\pm = C_2^\pm$ an effective interaction strength, $E_0^\pm = C_0^\pm \pm \hbar\omega_c/2$ a constant energy shift, and $\mathcal{P}_i^\pm = \widetilde{\sigma}_i^\pm \widetilde{\sigma}_i^\mp$ the projector onto the positive (upper sign) or negative (lower sign) branch of the ith site.

In writing Eq. (10.52), the on-site terms were cast into the dressed basis using the techniques of Section 10.2.3, while the hopping Hamiltonian H_{hop} was reexpressed in terms of dressed operators using the transformed form of the relations Eq. (10.21). Thus, using the techniques presented here, we have made the analogy between the two-site JCH and Bose-Hubbard models for $\lambda \ll 1$ as explicit as possible – Eq. (10.52) illustrates that, in the dispersive limit, the two-site JCH describes physical behavior which mirrors the Bose-Hubbard model independently within each of its four branches. Interestingly, these four branches allow for realization of either a symmetric ($\propto \mathcal{P}^\pm\mathcal{P}^\pm$) or an asymmetric ($\propto \mathcal{P}^\pm\mathcal{P}^\mp$) Bose-Hubbard type system. Unlike the single Jaynes-Cummings Hamiltonian, however, transitions between the various branches are allowed due to the cross-site boson-TLS couplings induced by transformation of H_{hop}. This effect was previously noted and analyzed in Refs. [36] and [355], there described in the context of polariton operators as an interconversion between + and − polariton types. Due to their scaling with $\lambda \ll 1$, these terms only weakly contribute in comparison to the dressed bosonic hopping term $J(\widetilde{a}_1^\dagger \widetilde{a}_2 + \widetilde{a}_1 \widetilde{a}_2^\dagger)$ for arbitrary J. This fact is not unsurprising as, in the dispersive regime, the dressed bosonic operators are photon-like. As a result, the purely photonic hopping term H_{hop} is well-approximated by

a photon-like dressed bosonic hopping and, consequently, the influence of the last two terms of Eq. (10.52) may be approximated using second-order perturbation theory or, depending on the value of λ and the accuracy desired, entirely neglected.

It is clear from a qualitative argument alone that the Hamiltonian in Eq. (10.52) admits an insulator-to-superfluid transition analogous to that of the Bose-Hubbard model largely unaltered by the final two inter-branch terms: focusing on the branch corresponding to the projector $\mathcal{P}_1^-\mathcal{P}_2^-$ and recalling that $C_2^-/\hbar \approx 2\lambda^3 g$ in the dispersive regime, the limit $J/U_{\text{eff}} \ll 1$ (equivalent to $J/\hbar g \ll 2\lambda^3$ in terms of basic system parameters) yields a localized, insulator-like n particle ground state identical to Eq. (10.47). In the opposite limit $J/U_{\text{eff}}^- \gg 1$ (or identically, $J/\hbar g \gg 2\lambda^3$), the influence of the inter-branch terms is felt only at second order perturbation theory in λ. For $\lambda \ll 1$, the n particle ground state becomes identical to the delocalized, superfluid-like, state Eq. (10.46).

10.3.3 The $n \leq 2$ limit

As evidenced in Section 10.2.3, another useful strategy for theoretical analysis involves truncating the composite Hilbert space by restricting the total number of excitations to a finite, maximal value. This approach is particularly relevant for comparison with the Bose-Hubbard model, where the chemical potential μ naturally determines the total number of particles in the many-body ground state [400]. Fixing to a particular excitation number in the JCH Hamiltonian therefore facilitates a straightforward comparison. Furthermore, truncating the Hilbert space allows for closer inspection of the resonant coupling regime which, as previously discussed, is challenging to analyze for general n due to the difficulty of casting H_{hop} in terms of dressed operators for general system parameters. For simplicity, we specialize to the case of $n \leq 2$. As shown in Section 10.2.3, this limit results in an exact analogy between the on-site terms of the Bose-Hubbard model and the negative branch of the many-body representation of the Jaynes-Cummings model for both resonant and dispersive coupling.

It is convenient to first reexpress the two-site JCH Hamiltonian in terms of projectors onto the positive and negative branch at each site:

$$H_{\text{JCH}} = \sum_{s_1,s_2,s_1',s_2'} \left|s_1', s_2'\right\rangle \left\langle s_1', s_2'\right| H \left|s_1, s_2\right\rangle \left\langle s_1, s_2\right|. \tag{10.53}$$

Here, each s_i is summed over the values + and −, the first and second entry of each bra/ket indicate the state of the TLS at the first and second sites, and the subscript "JCH" has been dropped from the various matrix elements for simplicity. For convenience, we define the notation $\mathcal{H}_{s_1 s_2}$ to represent to subspace spanned by the states $\{|m_1, m_2, s_1, s_2\rangle\}$, where the four indices denote, in order, the eigenvalues of $\widetilde{a}_1^\dagger \widetilde{a}_1$, $\widetilde{a}_2^\dagger \widetilde{a}_2$, $\widetilde{\sigma}_1^z$, and $\widetilde{\sigma}_2^z$. Note that here we are adopting notation for the states which is slightly modified from Section 10.2, as the first index no longer corresponds to the total number of excitations at the ith site but rather the number of quanta in the dressed bosonic mode alone. This simplification is made both to avoid confusion with the prefactors returned by dressed operators (see Table 10.1), but also because N_1 and N_2 are no longer independently conserved quantities and therefore their notational utility is diminished.

Drawing upon the discussion of the Jaynes-Cummings Hamiltonian in Section 10.2.3, it is the subspace $\mathcal{H}_{--}$ which includes the vacuum state. Consequently, our analysis will focus on the many-body physics within this subspace. As previously shown for the case of dispersive coupling, the two site JCH Hamiltonian differs from the single site Jaynes-Cummings Hamiltonian in that inter-branch transitions can occur due to nonzero off-diagonal elements of Eq. (10.53) contributed by the purely photonic hopping term. In order to simplify discussion of these matrix elements in the present formalism, we introduce the notation

$$\bar{H} \equiv \langle -, - | \, H \, | -, - \rangle \tag{10.54}$$

to denote the block of H_{JCH} which contributes to dynamics confined within the target subspace $\mathcal{H}_{--}$. Similarly, let

$$V_{s_1 s_2} \equiv \langle s_1, s_2 | \, H \, | -, - \rangle \tag{10.55}$$

denote the set of matrix elements describing allowed transitions from $\mathcal{H}_{--}$ to its complement $\mathcal{H}_{+-} \cup \mathcal{H}_{-+} \cup \mathcal{H}_{++}$. Because H_{JCH} is Hermitian, for every allowed transition from $\mathcal{H}_{--}$ to $\mathcal{H}_{s_1 s_2}$, there exists a transition of equal probability describing the inverse process described by the matrix elements of $V_{s_1 s_2}^\dagger$.

Constraining the full Hilbert space to two or fewer excitations, the projection of H onto

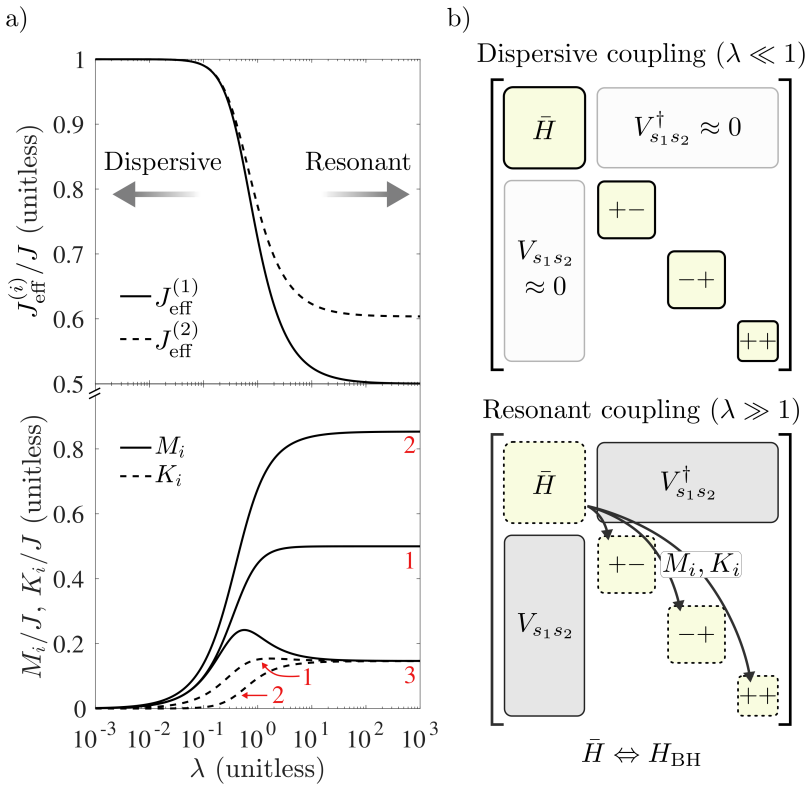

Figure 10.5: (a) The top panel shows the one and two excitation effective hopping strengths $J_{\text{eff}}^{(1)}$ and $J_{\text{eff}}^{(2)}$ while the bottom panel displays the value of the three unique linear (M_1, M_2, M_3) and nonlinear (K_1, K_2) transition amplitudes M_1, M_2, M_3, K_1 and K_2. All are plotted as a function of λ and normalized to the bare photonic hopping rate J. Notably, the first set of parameters $J_{\text{eff}}^{(i)}$ describe the amplitude of *intra*-branch transitions within the subspace $\mathcal{H}_{--}$, while the second set describes the amplitudes of *inter*-branch transitions between the subspace $\mathcal{H}_{--}$ and its complement $\mathcal{H}_{+-} \cup \mathcal{H}_{-+} \cup \mathcal{H}_{++}$ via cross-site light-matter interactions in the dressed representation. In the dispersive limit, all inter-branch transition amplitudes become small and the effective hopping strengths tend toward J. In the opposite regime, $J_{\text{eff}}^{(1)}$ and $J_{\text{eff}}^{(2)}$ differ by scalar prefactors and the coefficients M_i and K_i become comparable to J, leading to appreciable dissimilarity with the two-site Bose-Hubbard model. (b) Illustration of the two-site JCH Hamiltonian H_{JCH} in the dispersive (top panel) and resonant (bottom panel) coupling regimes. (caption continued on following page)

Figure 10.5: (continued) For the truncated space of two or fewer total excitations, each panel represents a 13×13 matrix comprising the four branches shown along each diagonal and denoted by the state of each dressed TLS. Note that in place of "$--$" is the 6×6 matrix $\bar{H}$, defined via the projection of the two-site JCH onto the target subspace $\mathcal{H}_{--}$. In general, the ten nonvanishing matrix elements of $V_{s_1 s_2}$ yield five unique values given by the coefficients M_i and K_i defined in Eq. (10.60). In the dispersive regime, H_{JCH} becomes approximately block diagonal in the dressed basis as $M_i/J \ll 1$ and $K_i/J \ll 1$ and inter-branch transitions become negligible. As a result, $\bar{H}$ becomes an appropriate effective Hamiltonian and analogy to the Bose-Hubbard model is realized. In the resonant regime, inter-branch transitions become important and, consequently, direct correspondence with the Bose-Hubbard model collapses.

the subspace $\mathcal{H}_{--}$ may be expressed in the block-diagonal form

$$\bar{H} = \begin{bmatrix} \bar{H}_{n=0} & 0 & 0 \\ 0 & \bar{H}_{n=1} & 0 \\ 0 & 0 & \bar{H}_{n=2} \end{bmatrix} \tag{10.56}$$

where $\bar{H}_n$ is a square matrix of dimension 2^n corresponding to the subspace of n excitations, containing diagonal and off-diagonal entries given by the on-site and hopping terms of Eq. (10.50), respectively. Because the JCH conserves the total number of excitations, transitions between states of different total particle number n are not allowed, hence the block-diagonal form of Eq. (10.56). Discarding the vacuum energy $\bar{H}_{n=0} = 2C_0^- - \hbar\omega_c$, the single and double excitation blocks of $\bar{H}$ may be written in the form

$$\begin{aligned} \bar{H}_{n=1} &= \begin{bmatrix} \hbar\Omega_0 & J_{\text{eff}}^{(1)} \\ J_{\text{eff}}^{(1)} & \hbar\Omega_0 \end{bmatrix} \\ \bar{H}_{n=2} &= \begin{bmatrix} 2\hbar\Omega_0 + U_{\text{eff}} & 0 & \sqrt{2}J_{\text{eff}}^{(2)} \\ 0 & 2\hbar\Omega_0 + U_{\text{eff}} & \sqrt{2}J_{\text{eff}}^{(2)} \\ \sqrt{2}J_{\text{eff}}^{(2)} & \sqrt{2}J_{\text{eff}}^{(2)} & 2\hbar\Omega_0 \end{bmatrix}. \end{aligned} \tag{10.57}$$

Here, the effective on-site resonant energy and interaction strength are $\Omega_0 = \omega_c + C_1^-/\hbar$ and

$U_{\text{eff}} = C_2^-$, where negative sign superscripts have been removed from Ω_0 and U_{eff} relative to Eq. (10.52) for simplicity. In addition, the effective hopping strengths are defined by

$$\begin{aligned} J_{\text{eff}}^{(1)} &= J\cos^2\theta(1) \\ J_{\text{eff}}^{(2)} &= J\cos\theta(1)\big[\cos\theta(1)\cos\theta(2) + \sin\theta(1)\sin\theta(2)/\sqrt{2}\big], \end{aligned} \tag{10.58}$$

where $\theta(N)$ is the mixing angle previously defined in Eq. (10.15) and the vector space is ordered as $\{|10\rangle, |01\rangle\}$ for $n = 1$ and $\{|20\rangle, |02\rangle, |11\rangle\}$ for $n = 2$. We emphasize again that Eq. (10.57) does not fully describe the dynamics of the two-site JCH, even for the limit $n \leq 2$, due to possible transitions to and from the target subspace $\mathcal{H}_{--}$ described by $V_{s_1 s_2}$. Still, it is useful to first examine the similarities between Eq. (10.57) and the Bose-Hubbard model in isolation. Making as explicit a comparison as possible, projecting the Bose-Hubbard Hamiltonian onto the subspace $n \leq 2$ leads to

$$\begin{aligned} H_{\text{BH},n=1} &= \begin{bmatrix} -\mu & J \\ J & -\mu \end{bmatrix} \\ H_{\text{BH},n=2} &= \begin{bmatrix} -2\mu + U & 0 & \sqrt{2}J \\ 0 & -2\mu + U & \sqrt{2}J \\ \sqrt{2}J & \sqrt{2}J & -2\mu \end{bmatrix}. \end{aligned} \tag{10.59}$$

Though nearly identical in form to Eq. (10.57), a few key differences must be highlighted. First, the one and two excitation manifolds of the two-site JCH are characterized by different tunneling strengths $J_{\text{eff}}^{(1)}$ and $J_{\text{eff}}^{(2)}$ which identically approach J in the dispersive limit, but plateau to different values for the resonant case (see Fig. 10.5a, top panel). Second, as already emphasized, underlying the two-site JCH is a larger range of independently tunable parameters (ω_c, Δ, g, J) compared to the two-site Bose-Hubbard model which is characterized by μ, U and J alone. At the level of the effective parameters in Eq. (10.57), however, it is important to be mindful – particularly for the purpose of quantum simulation of Bose-Hubbard models with JCH systems – that tuning U_{eff} while holding J_{eff} constant, for example, requires the explicit understanding of how these effective parameters depend upon those in the fundamental parameters (e.g., Δ, g) as demonstrated here. Likewise, changing g while holding Δ constant can impact not only the effective repulsion strength

U_{eff}, as expected, but also the effective two excitation tunneling strength $J^{(2)}_{\text{eff}}$. Thus, the analytic forms for these parameters is not of just theoretical, but also experimental interest.

To better illustrate the nontrivial relationship between the effective parameters (U_{eff} and $J^{(2)}_{\text{eff}}$) and their base parameter counterparts (g and J), Fig. 10.6a displays the ratio $J^{(2)}_{\text{eff}}/U_{\text{eff}}$ as a function of λ and $J/\hbar g$. In computing these values, the cavity resonant frequency and light-matter coupling strength were fixed at $\omega_c/\Gamma = 10^3$ and $g/\Gamma = 1$ while Δ and J were allowed to vary. Notably, the limits $J^{(2)}_{\text{eff}}/U_{\text{eff}} \ll 1$ and $J^{(2)}_{\text{eff}}/U_{\text{eff}} \gg 1$, relevant for realization of Mott-insulating-like and superfluid-like phases, are reached not just through choice of $J/\hbar g$ but also λ. Fig. 10.5b therefore serves to illustrate the complexity in navigating the comparably larger parameter space of the JCH model for realization of behavior analogous to the Bose-Hubbard model, while also serving as a useful guide for achieving a particular effective parameter regime of interest.

In isolation, Eqs. (10.57) and (10.59) define Hamiltonians closely mirroring one another and thus describe analogous physical behavior. However, a more honest comparison must take into account the matrix elements of $V_{s_1 s_2}$. In total, there are ten unique transitions (twenty including the reverse processes described by $V^\dagger_{s_1 s_2}$), all of which may be divided into two categories: linear cross-site bosonic-TLS couplings and more complicated nonlinear interactions involving both on-site and cross-site exchange of quanta. Symmetry of the two sites dictates that each transition is accompanied by a parity reversed pair. All twenty allowed transitions may therefore be summarized by the outcoupling coefficients

$$\begin{aligned}
M_1 &\equiv \langle 0,0|\, V_{+-}\, |0,1\rangle = \langle 0,0|\, V_{-+}\, |1,0\rangle \\
M_2 &\equiv \langle 0,1|\, V_{+-}\, |0,2\rangle = \langle 1,0|\, V_{-+}\, |2,0\rangle \\
M_3 &\equiv \langle 1,0|\, V_{+-}\, |1,1\rangle = \langle 0,1|\, V_{-+}\, |1,1\rangle \\
K_1 &\equiv \langle 0,1|\, V_{+-}\, |2,0\rangle = \langle 1,0|\, V_{-+}\, |0,2\rangle \\
K_2 &\equiv \langle 0,0|\, V_{++}\, |2,0\rangle = \langle 0,0|\, V_{++}\, |0,2\rangle
\end{aligned} \tag{10.60}$$

and their Hermitian conjugates, where M_i denotes a linear cross-site interaction (i.e., exchange of a single quantum) and K_i labels a nonlinear process (i.e., exchange of multiple quanta). All are similar in form to the effective hopping strength $J^{(i)}_{\text{eff}}$ – proportional to J but otherwise dependent only on the mixing angle θ or, equivalently, $\lambda = g/\Delta$, via products

of trigonometric functions. For explicit analytic forms of each coefficient, see Sec. 10.6.

As shown in the bottom panel of Fig. 10.5a, the magnitude of the coefficients M_i and K_i depend drastically on λ and, as a result, the transition rate out of the subspace $\mathcal{H}_{--}$ differs between the dispersive and resonant coupling regimes. In the former case, the various outcouplings may be approximated to lowest order as

$$\begin{aligned} M_1 &\approx M_3 \approx \lambda J \\ M_2 &\approx \sqrt{2}\lambda J, \end{aligned} \tag{10.61}$$

where the nonlinear transition amplitudes $K_1 \approx \mathcal{O}(\lambda^3)$ and $K_2 \approx \mathcal{O}(\lambda^4)$ are comparatively small and may therefore be neglected. This result is in agreement with the more general Hamiltonian of Eq. (10.52). As previously established, tunneling within the subspace $\mathcal{H}_{--}$ clearly dominates outcoupling for $\lambda \ll 1$ and, to first approximation, Eq. (10.56) serves as an appropriate effective Hamiltonian without consideration of outcouplings. It is interesting to note, however, that the outcouplings which contribute most meaningfully – namely, M_1, M_2 and M_3 – all resemble single excitation losses from the perspective of the dressed bosons. This suggests the possibility for a non-perturbative treatment via projective methods, ultimately leading to a repackaging at the level of effective dissipation rates and energy shifts which renormalize the matrix elements of Eq. (10.56) [384]. This approach would not qualitatively alter the parallel structure with the Bose-Hubbard model, however, so we leave the described strategy as a possible future avenue for analyses where quantitative agreement is desired.

In contrast with the dispersive case, resonant coupling is characterized by nonvanishing linear and nonlinear transition amplitudes which plateau to values of order J. In the limit $U_{\text{eff}} \gg J$, these contributions are unimportant as $M_i, K_i < J$ for all λ and the system is therefore dominated by on-site interactions, leading to a Mott-insulating, two particle ground state comprising polaritonic excitations. In the opposite limit $U_{\text{eff}} \ll J$, however, Eq. (10.57) fails to capture the entirety of the dynamics due to the importance of inter-branch transitions, as illustrated in Fig. 10.5c.

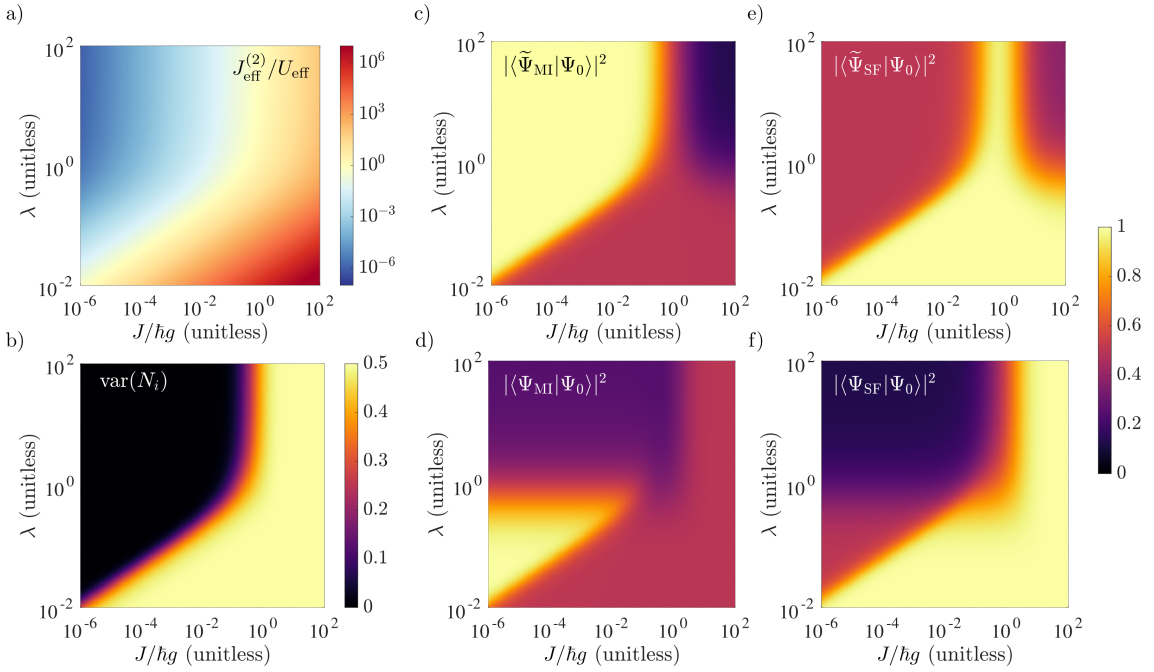

Figure 10.6: (a) Ratio of the analytically derived effective two excitation hopping rate $J^{(2)}_{\text{eff}}$ and dressed boson-boson interaction strength U_{eff} as a function of λ and $J/\hbar g$. (b) Variance of the total number of excitations at site i as a function of λ and $J/\hbar g$. Due to symmetry there is no distinction in the variance at site one or two. This quantity serves as a useful order parameter for finite lattice systems, with var(N_i) vanishing for a Mott-insulating state but taking a finite value for a superfluid, reaching var$(N_i) = 0.5$ for an ideal $n = 2$ superfluid state. Clearly, panel (b) suggests the possibility for both an insulating and superfluid phase in either the dispersive or resonant regimes independently. Comparing to panel (a), regions of $J^{(2)}_{\text{eff}}/U_{\text{eff}} \ll 1$ and $J^{(2)}_{\text{eff}}/U_{\text{eff}} \gg 1$ correlate near perfectly with regions of vanishing and nonvanishing variance, respectively, with $J^{(2)}_{\text{eff}}/U_{\text{eff}} \sim 1$ demarcating the boundary. (c–f) Overlap of the two-particle ground state $|\Psi_0\rangle$ with the idealized (c) dressed Mott-insulating, (d) photonic Mott-insulating, (e) dressed superfluid and (f) photonic superfluid states, defined in Eq. (10.62), as a function of λ and $J/\hbar g$. Depending on the value of λ, the dressed states take on a either a photonic ($\lambda \ll 1$) or ($\lambda \gg 1$) polaritonic character, where this former limit is responsible for the noticeable agreement between top and bottom panels for $\lambda \ll 1$. (caption continued on following page)

Figure 10.6: (continued) In the dispersive regime, tuning from small to large values of $J/\hbar g$ facilitates a transition from a photonic Mott-insulating phase to a photonic superfluid phase. In the resonant coupling regime, tuning $J/\hbar g$ results in three distinct phases, with a polaritonic Mott-insulating state occuring for $J_{\text{eff}} \ll 1$, a polaritonic superfluid for $J_{\text{eff}} \sim 1$, and a photonic superfluid $J_{\text{eff}} \gg 1$.

10.3.4 The $n = 2$ ground state: quantum phases in the dispersive and resonant coupling regimes

To better understand the turn on of these inter-branch transitions and their impact on the quantum phase transition admitted by the two-site JCH, we numerically compute the two-particle ground state as a function of $J/\hbar g$ and λ taking into account both intra- and inter-branch dynamics of Eq. (10.50). In general, this ground state is a superposition of the eight possible two excitation states $\{|2,0,-,-\rangle,\ |0,2,-,-\rangle,\ |1,1,-,-\rangle,\ |1,0,+,-\rangle,\ |0,1,+,-\rangle,\ |1,0,-,+\rangle,\ |0,1,-,+\rangle,\ |0,0,+,+\rangle\}$, gaining contributions not only from the target subspace $\mathcal{H}_{--}$ but also its complement. Similar to Fig. 10.5b, all calculations were carried out for the fixed values $\omega_c/\Gamma = 10^3$ and $g/\Gamma = 1$, allowing Δ and J to independently vary. Following Ref. [36], we use the variance in particle number at the ith site, $\text{var}(N_i)$, as an order parameter. The computed variance for the two particle ground state is shown in Fig. 10.6b as a function of $J/\hbar g$ and λ.

Comparing Figs. 10.6a and 10.6b, it is clear that the variance tracks the value of $J^{(2)}_{\text{eff}}/U_{\text{eff}}$, as would be expected in the Bose-Hubbard model, with regions of vanishing variance (i.e., a Mott-insulator) corresponding to $J^{(2)}_{\text{eff}}/U_{\text{eff}} \ll 1$ and regions which plateau to $\text{var}(N_i) = 0.5$ (i.e., a superfluid) where $J^{(2)}_{\text{eff}}/U_{\text{eff}} \gg 1$. In the dispersive regime, the onset of the superfluid-like phase occurs at increasingly smaller values of $J/\hbar g$ as λ is decreased. This phenomenon is easily understood through appeal to the analytic correspondence $U_{\text{eff}} = C_2^-$ and reference to previously derived results. In particular, in Section 10.2.3 it was shown that $C_2^-/\hbar \approx 2\lambda^3 g$ in the dispersive regime. Then simultaneously maintaining a constant photon-photon interaction strength (C_2^-) while increasing Δ (i.e., decreasing λ) requires a relative increase

in g, pushing the regime where photon-photon interactions dominate over photonic hopping toward smaller values of $J/\hbar g$ as as the system moves further into dispersive coupling. Oppositely, on resonance, it was found that $C_2^-/\hbar = (2-\sqrt{2})g$. Then U_{eff} is equivalent to g up to some scalar prefactor and the phase transition will occur at roughly the same value of $J/\hbar g$ for all $\lambda \gg 1$.

It is important to reemphasize that N_i commutes with the unitary transformation operator $\mathcal{U} = e^{S_1+S_2}$, and thus Fig. 10.6b may equally well be interpreted as the variance in the total number of bare or dressed photonic and atomic excitations. Given this, it is notable that the "phase boundary" is qualitatively demarcated by the $J_{\text{eff}}^{(2)}/U_{\text{eff}} = 1$ line, entirely dependent on effective parameters appearing in the dressed basis. This agreement therefore indicates not only that the effective parameters $J_{\text{eff}}^{(2)}$ and U_{eff} analytically derived here are the appropriate JCH model counterparts of the Bose-Hubbard parameters J and U, but also that the dressed operator basis provides the most approrpriate representation for understanding the many-body phenomena of the JCH.

Because the order parameter $\text{var}(N_i)$ does not distinguish between excitations which are photonic in nature and those which are polaritonic, Fig. 10.6b provides little insight into the physical makeup of the excitations composing the two-particle ground state. For instance, the black, $\text{var}(N_i) = 0$ region of Fig. 10.6b clearly suggests that the system is in an insulating state, characterized by a constant number of quanta at each site. It does not, however, provide any information about whether these excitations are fundamentally photonic or polaritonic. In order to gain a deeper understanding of the ground state, we compute its squared overlap with the four distinct states

$$\left|\widetilde{\Psi}_{\text{MI}}\right\rangle = \widetilde{a}_1^\dagger \widetilde{a}_2^\dagger \left|0\right\rangle \tag{10.62a}$$

$$\left|\Psi_{\text{MI}}\right\rangle = a_1^\dagger a_2^\dagger \left|0\right\rangle \tag{10.62b}$$

$$\left|\widetilde{\Psi}_{\text{SF}}\right\rangle = \frac{1}{2\sqrt{2}}(\widetilde{a}_1^\dagger - \widetilde{a}_2^\dagger)^2 \left|0\right\rangle \tag{10.62c}$$

$$\left|\Psi_{\text{SF}}\right\rangle = \frac{1}{2\sqrt{2}}(a_1^\dagger - a_2^\dagger)^2 \left|0\right\rangle \tag{10.62d}$$

which denote Mott-insulating (a,b) and superfluid-like (c,d) states in both the bare and dressed dressed excitation bases via action of the appropriate creation operators on the

vacuum state $|0\rangle = |0,0,g,g\rangle = |0,0,-,-\rangle$.

Figs. 10.6c and 10.6e show the squared projection of the computed ground state onto the dressed Mott-insulating and superfluid states, while Figs. 10.6d and 10.6f show the corresponding projections onto their bare photonic counterparts. Focusing first on the dispersive regime (i.e., roughly the bottom third of each plot), comparison of the upper and lower panels agrees with theoretical intuition – for $\lambda \ll 1$, the dressed basis is a merely perturbed version of the bare basis due to the weak light-matter mode mixing and, as a result, there is little distinction between the bare and dressed photons. Using Fig. 10.6a as a visual guide, regions where $J_{\text{eff}}/U_{\text{eff}} \ll 1$ correspond to near unity overlap with the photonic Mott-insulating state $|\Psi_{\text{MI}}\rangle$ while regions of $J_{\text{eff}}/U_{\text{eff}} \gg 1$ perfectly conform to the photonic superfluid state $|\Psi_{\text{SF}}\rangle$. The phase boundary occurs roughly at $J_{\text{eff}}/U_{\text{eff}} \approx 1$, further establishing the utility of the analytic mapping between basic system parameters and the effective Bose-Hubbard like parameters presented here. Thus, the quantum phase transition as $J/\hbar g$ is tuned for constant $\lambda \ll 1$ behaves exactly as predicted in Sec. 10.3.3.

In the resonant coupling regime (roughly the top third of each plot), the physical character of bare and dressed excitations fundamentally differ as $\theta \approx \pi/4$ and the operators $\widetilde{a}_i^\dagger$ and $\widetilde{a}_i$ therefore describe creation and annihilation of polaritons. This divergence in physical character between dressed and bare excitations is evident in Figs. 10.6c–10.6f as top and bottom panels bear little resemblance for $\lambda \gg 1$. Interestingly, the ground state overlap with the dressed Mott-insulator, dressed superfluid and photonic superfluid all display regions of near-unity as $J/\hbar g$ is tuned, indicating a much more complicated phase transition in comparison to the dispersive case. Referring again to Fig. 10.6a, regions where the polariton-polariton repulsion strength U_{eff} dominates the effective tunneling strength $J_{\text{eff}}^{(2)}$ coincide with a polaritonic Mott-insulating ground state $\left|\widetilde{\Psi}_{\text{MI}}\right\rangle$, as expected. In the far-opposite regime, where the effective tunneling dominates, it is evident that the dressed Mott-insulating and superfluid states fail to accurately capture the character of the ground state. Instead, it is the photonic superfluid state $|\Psi_{\text{SF}}\rangle$ which characterizes the ground state in the regime $J/\hbar g \gg 1$, $\lambda \gg 1$. To understand this phenomenon, it is helpful to consider the original, untransformed form of the JCH Hamiltonian in Eq. (10.48) where the cross-site tunneling appears in terms of purely photonic operators. For $J \gg \hbar g$, the on-site light-matter

interactions contribute only perturbatively and may be neglected at first approximation. In this limit, then, the dressed operators no longer describe the fundamental excitations of the system and purely photonic character underlies the resulting superfluid-like ground state.

Remarkably, Fig. 10.6e indicates that a third phase, consistent with a polaritonic superfluid, appears between the regions coinciding with a polaritonic Mott-insulator and photonic superfluid for $\lambda \gg 1$. The existence of such a phase in the JCH model has been both theoretically [363] and experimentally [371] examined in the literature, and may be explained as follows: as the ratio between the photonic hopping strength and light-matter coupling rate is tuned from its far limit $J/\hbar g \ll 1$ (leading to localized polaritonic excitations) to its counterpart $J/\hbar g \gg 1$ (resulting in delocalized photonic excitations), the system passes through an intermediate region $J/\hbar g \sim 1$ where J is large enough such that the cross-site cavity-TLS couplings M_2 and M_3 become appreciable, yet not so large that the photonic hopping completely dominates light-matter interactions and the atomic degrees of freedom are eliminated. The result is a two particle ground state which assumes a near-unity overlap with the polaritonic superfluid state, reaching $|\left\langle \widetilde{\Psi}_{\mathrm{SF}}|\Psi_0\right|\widetilde{\Psi}_{\mathrm{SF}}|\Psi_0\rangle|^2 \approx 0.95$ at its peak. It is interesting to note that in this parameter regime, the dynamics are not entirely restrained to the subspace $\mathcal{H}_{--}$ as was the case for dispersive coupling. Yet, the ground state is well-characterized by $\left|\widetilde{\Psi}_{\mathrm{SF}}\right\rangle$ which is composed of the three individual states $|2,0,-,-\rangle$, $|0,2,-,-\rangle$, and $|1,1,-,-\rangle$, which collectively span the two excitation manifold of $\mathcal{H}_{--}$. Inspection of the excited states illustrates that this is not the case in general, indicating that quantum interference between the inter-branch transitions likely plays an important role in the system dynamics near the ground state energy.

We conclude our analysis by making a few remarks on additional phenomena of the JCH model not explored here. The preceding calculations are restricted to the case $\Delta > 0$ which, as discussed in Section 10.2.3, corresponds to repulsive on-site boson-boson interactions. Not included in the present analysis is the $\Delta < 0$ limit of the two-site JCH, where attractive on-site boson-boson interactions are realized and, consequently, multiple photon (or polariton) bound states may be formed. We defer discussion of these effects to existing literature on this subject (see, for example, Refs. [401] and [402] for theoretical analyses pertaining to JCH systems and Refs. [403] and [404] for related studies in atomic Rydberg platforms),

and leave an in-depth analysis through the lens of the bosonic many-body form of the JCH model presented here as an interesting potential future avenue. Separately, dispersive coupling offers additional possibilities not explicitly discussed here, such as the realization of XY spin models by either (i) mapping polariton operators onto psuedo spin operators in the Mott regime [36, 355] or, alternatively, (ii) explicit separation of photonic and atomic degrees of freedom and realization of photon mediated spin-spin like interactions between the weakly dressed atoms [405, 406]. Here, the former approach is equivalent to consideration of Eq. (10.52) in the hardcore limit $U_{\text{eff}}^{\pm} \to \infty$, while the latter involves inclusion of terms proportional to $\widetilde{\sigma}_1^+\widetilde{\sigma}_2^- + \widetilde{\sigma}_1^-\widetilde{\sigma}_2^+$ which appear at second order in λ in Eq. (10.52) and play a particularly important role in the low energy dynamics of the atomic dispersive limit ($|\lambda| \ll 1$ with $\Delta < 0$). Thus the results presented here not only provide a direct route for comparison between the two-site JCH and Bose-Hubbard models, but also demonstrate a more general utility as a potential aid for theoretical discovery and experimental realization of other quantum Hamiltonians of interest for analog quantum simulation using cavity and circuit QED platforms.

10.4 Conclusion

Systems of interacting photons are among the most promising experimental platforms for studying quantum many-body phenomena. As photons do not naturally interact with each other, however, a nonlinear element, such as a quantum emitter or superconducting qubit, is required to mediate effective photon-photon interactions. Here, we have presented a comprehensive theoretical study of the effective many-body interactions underlying the Jaynes-Cummings model, the prototypical description of light-matter coupling in cavity and circuit QED systems. This was achieved through techniques of unitary transformation, ultimately resulting in a reexpression of the Jaynes-Cummings Hamiltonian in terms of dressed bosonic and psuedo-spin operators. Upon non-perturbative expansion of its diagonal form, we have shown that the resulting dressed operator representation of the Jaynes-Cummings Hamiltonian includes an infinite sum of bosonic k-body interactions partitioned into two distinct branches. We have demonstrated that this many-body representation facilitates a close inspection of the parameter-dependent analogy between the Jaynes-Cummings Hamiltonian

and the on-site portion of the Bose-Hubbard model. While prior studies have qualitatively compared the two – even going so far as to define an effective Hubbard-like interaction strength U_{eff} for the Jaynes-Cummings Hamiltonian [370, 355, 361] – our approach is unique in that the resulting many-body form is exact for both resonant and dispersive regimes for an arbitrary number of excitations. Furthermore, our results provide a novel interpretation of the breakdown in this analogy for resonant coupling, occurring due to the emergent role of higher effective k-body interactions which suppress the influence of the two-body terms. These findings thus not only serve as a unique lens for comparison with the onsite interactions of the Bose-Hubbard model, but also provide a theoretical avenue for explicit study of large effective k-body interactions facilitated by the Jaynes-Cummings interaction for potential realization of exotic quantum behavior not realizable in conventional quantum systems [407, 408].

In addition, we have extended our analysis to the two-site Jaynes-Cummings-Hubbard (JCH) model and have demonstrated that, in the dispersive coupling regime, unitary transformation to the dressed operator representation allows for a near exact realization of the two-site Bose-Hubbard model, complete with explicit, analytic forms for all effective parameters. To better understand the resonant coupling case, we then restricted to a total of two excitations or fewer, derived an explicit form for the dressed state representation of the two-site JCH, and identified the block of matrix elements which map to Bose-Hubbard-like dynamics, deriving effective two excitation hopping ($J^{(2)}_{\text{eff}}$) and effective two-body interaction (U_{eff}) strengths in the process. Drawing upon this theoretical foundation, we have illustrated that, for resonant coupling, the turn on of inter-branch transitions induced by cross-site dressed light-matter couplings is ultimately the downfall of analogy with the two-site Bose-Hubbard model. We then concluded with an analysis of the quantum phases of the two-site JCH model for $n = 2$ excitations, illustrating the possibility for either a photonic (dispersive coupling) or polaritonic (resonant coupling) Mott-insulating state for $J^{(2)}_{\text{eff}}/U_{\text{eff}} \ll 1$, while $J^{(2)}_{\text{eff}}/U_{\text{eff}} \gg 1$ uniformly leads to a photonic superfluid state. Finally, we identified the possibility for a third quantum phase near $J^{(2)}_{\text{eff}}/U_{\text{eff}} \sim 1$ for resonant coupling, corresponding to a polaritonic superfluid-like state. While these four unique quantum phases have been identified in the literature previously [353, 354, 363, 361], the dressed operator

picture developed here provides an explicit analytic mapping between the parameters of the JCH model and those of the effective many-body representation through which its quantum phases are easily understood, resulting in a clear, all-encompassing exposition of the various parameter regimes and their association with the quantum phases of the JCH model. The present work thus demonstrates the general utility of the dressed many-body description of the Jaynes-Cummings model and its extensions to a lattice, opening avenues for further exploration of quantum many-body phenomena realizable in coupled light-matter systems.

10.5 Appendix A: Derivation of the many-body coefficients $C_k^{\pm}$

The purpose of this appendix is to expand upon the steps taken in arriving at Eqs. (10.26–10.27). As mentioned in the main text, a crucial step involves Taylor expanding $f(n)$ not about small λ as is typical for studies in the dispersive regime [376, 16], but about $n = n_0$ where n_0 is an undetermined constant chosen to be sufficiently large such that the convergence condition $n_0 > (n - 1/4\lambda^2)/2$ is satisfied. Carrying out this expansion leads to

$$\begin{aligned} f(n) &= \sum_{r=0}^{\infty} \binom{\frac{1}{2}}{r} (2\lambda)^{2r} f(n_0)^{1-2r} (n-n_0)^r \\ &= \sum_{r=0}^{\infty} \sum_{m=0}^{r} \binom{\frac{1}{2}}{r} \binom{r}{m} (2\lambda)^{2r} f(n_0)^{1-2r} (-n_0)^{r-m} n^m, \end{aligned} \tag{10.63}$$

where the binomial theorem was used in going from the first to second line. Reexpressing in terms of operators using Eq. (10.24),

$$\begin{aligned} f(N)\widetilde{\sigma}^z = \sum_{r=0}^{\infty} \sum_{m=0}^{r} &\binom{\frac{1}{2}}{r} \binom{r}{m} (2\lambda)^{2r} f(n_0)^{1-2r} (-n_0)^{r-m} \\ &\times \left[(\widetilde{a}\,\widetilde{a}^\dagger)^k \widetilde{\sigma}_+ \widetilde{\sigma}_- + (\widetilde{a}^\dagger \widetilde{a})^m \widetilde{\sigma}_- \widetilde{\sigma}_+ \right], \end{aligned} \tag{10.64}$$

where the commutator $[\widetilde{a}, \widetilde{a}^\dagger] = 1$ has been used in rewriting the projected number operator $N\sigma_+\sigma_- = \widetilde{a}^\dagger \widetilde{a} + 1$ as $\widetilde{a}\,\widetilde{a}^\dagger$. The above relation can be further rewritten using the identity [409]

$$(\widetilde{a}^\dagger \widetilde{a})^m = \sum_{k=0}^{m} \left\{ {m \atop k} \right\} (\widetilde{a}^\dagger)^k (\widetilde{a})^k, \tag{10.65}$$

where the coefficients $\left\{ {m \atop k} \right\}$ are Stirling numbers of the second kind, related to the binomial coefficients via

$$\left\{ {m \atop k} \right\} = \frac{1}{k!} \sum_{p=0}^{k} \binom{k}{p} (-1)^{p-k} p^m \tag{10.66}$$

Similarly, through combination of Eq. (10.65) and the binomial theorem, the following identity may be derived:

$$(\widetilde{a}\,\widetilde{a}^\dagger)^m = \sum_{k=0}^{m} \left\{ {m+1 \atop k+1} \right\} (\widetilde{a}^\dagger)^k (\widetilde{a})^k. \tag{10.67}$$

Then Eq. (10.64), using the above identities, may be written in the form given by Eq. (10.25), restated here for clarity:

$$\begin{aligned} f(N)\widetilde{\sigma}^z = & \sum_{r=0}^{r} \sum_{m=0} \binom{\frac{1}{2}}{r} \binom{r}{m} (2\lambda)^{2r} f(n_0)^{1-2r} (-n_0)^{r-m} \\ & \times \sum_{k=0}^{m} (\widetilde{a}^\dagger)^k (\widetilde{a})^k \left[\left\{ {m+1 \atop k+1} \right\} \widetilde{\sigma}^+ \widetilde{\sigma}^- - \left\{ {m \atop k} \right\} \widetilde{\sigma}^- \widetilde{\sigma}^+ \right]. \end{aligned} \tag{10.68}$$

As currently written, the above expression is nearly in the desired form, containing terms proportional to the normally-ordered product $(\widetilde{a}^\dagger)^k (\widetilde{a})^k$ describing effective k-body bosonic interactions. In order to write a Hamiltonian as a sum over these interactions, the three nested sums of Eq. (10.68) must be reordered such that all k-body terms can be factored. Noting that the indices obey $0 \leq k \leq m \leq r \leq \infty$, the ordering of the nested sums may be reversed by rewriting the upper and lower bounds, leading to Eq. (10.26) of the main text:

$$H = \hbar\omega_c \left(N - \frac{1}{2} \right) + \sum_{k=0}^{\infty} \frac{1}{k!} \left[C_k^+ \widetilde{\sigma}_+ \widetilde{\sigma}_- + C_k^- \widetilde{\sigma}_- \widetilde{\sigma}_+ \right] (\widetilde{a}^\dagger)^k (\widetilde{a})^k, \tag{10.69}$$

where

$$\begin{aligned} \frac{C_k^-}{k!} &= -\frac{\hbar}{2} \Delta \sum_{m=k}^{\infty} \left\{ {m \atop k} \right\} (-n_0)^{-m} f(n_0) \sum_{r=m}^{\infty} \binom{\frac{1}{2}}{r} \binom{r}{m} \beta^r \\ \frac{C_k^+}{k!} &= \frac{\hbar}{2} \Delta \sum_{m=k}^{\infty} \left\{ {m+1 \atop k+1} \right\} (-n_0)^{-m} f(n_0) \sum_{r=m}^{\infty} \binom{\frac{1}{2}}{r} \binom{r}{m} \beta^r, \end{aligned} \tag{10.70}$$

and $\beta = -4\lambda^2 n_0 / f(n_0)^2$. The above expressions may be simplified through explicit evaluation of the sum over m using properties of the generalized binomial coefficients. In particular,

it can be shown that

$$\begin{aligned}\sum_{r=m}^{\infty}\binom{\frac{1}{2}}{r}\binom{r}{m}\beta^r &= \binom{\frac{1}{2}}{r}\beta^m(1+\beta)^{\frac{1}{2}-m} \\ &= \binom{\frac{1}{2}}{r}(4\lambda^2)^m(-n_0)^m/f(n_0).\end{aligned} \tag{10.71}$$

Focusing on C_k^-, evaluating the sum over m gives

$$\begin{aligned}\frac{C_k^-}{k!} &= -\frac{\hbar}{2}\Delta\sum_{m=k}^{\infty}\left\{{m \atop k}\right\}\binom{\frac{1}{2}}{m}(4\lambda^2)^m \\ &= -\frac{\hbar}{2k!}\Delta\sum_{p=0}^{k}\binom{k}{p}(-1)^{p-k}\sum_{m=0}^{\infty}\binom{\frac{1}{2}}{m}(4\lambda^2 p)^m\end{aligned} \tag{10.72}$$

where the identity in Eq. (10.66) has been applied and the two sums reordered. Evaluating the rightmost sum (and ignoring issues of convergence as the double sum, taken together, must be convergent) yields the desired result

$$C_k^- = -\frac{\hbar}{2}\Delta\sum_{p=0}^{k}\binom{k}{p}(-1)^{p+k}\sqrt{1+4\lambda^2 p}, \tag{10.73}$$

which is identical to the form of C_k^- Eq. (10.27). The derivation of C_k^+ follows in an analogous fashion and is therefore not made explicit here.

Finally, we verify the form of C_k^- through explicit action of the sum over all k-body terms on the a generic basis state $|n,-\rangle$. The methods here may again be trivially extended to verify C_k^+ through action on the positive branch $|n,+\rangle$. Using the properties of bosonic creation and annihilation operators,

$$\begin{aligned}H_{\mathrm{MB}}|n,-\rangle &= \sum_{k=0}^{\infty}\frac{1}{k!}C_k^-(\widetilde{a}^\dagger)^k(\widetilde{a})^k|n,-\rangle \\ &= \sum_{k=0}^{n}\binom{n}{k}C_k^-|n,-\rangle.\end{aligned} \tag{10.74}$$

Substituting the definition for C_k^- and reordering the two resulting sums, again taking care to change the bounds as needed, yields,

$$H_{\mathrm{MB}}|n,-\rangle = -\frac{\hbar}{2}\Delta\sum_{p=0}^{n}(-1)^p\sqrt{1+4\lambda^2 p}\sum_{k=p}^{n}\binom{n}{k}\binom{k}{p}(-1)^k|n,-\rangle. \tag{10.75}$$

Applying the identity

$$\sum_{k=p}^{n} \binom{n}{k}\binom{k}{p}(-1)^k = (-1)^n \delta_{np}, \tag{10.76}$$

the above relation becomes

$$H_{\mathrm{MB}}|n,-\rangle = -\frac{\hbar}{2}\Delta\sqrt{1+4\lambda^2 n}|n,-\rangle, \tag{10.77}$$

thus verifying that the form of the Jaynes-Cummings Hamiltonian given in Eq. (10.26) returns the known eigenvalues for the negative branch states $|n,-\rangle$.

10.6 Appendix B: Explicit forms for M_i and K_i

The following lists the explicit analytic forms for the coefficients M_i and K_i, each of which describes the amplitude of an allowed transition from the Hilbert space $\mathcal{H}_{--}$ to its complement as well as its inverse process:

$$\begin{aligned}
M_1 &= J\cos\theta(1)\sin\theta(1) \\
M_2 &= J\sin\theta(1)\left[\sqrt{2}\cos\theta(1)\cos\theta(2)+\sin\theta(1)\sin\theta(2)\right] \\
M_3 &= J\cos\theta(1)\left[\sqrt{2}\cos\theta(1)\sin\theta(2)-\sin\theta(1)\cos\theta(2)\right] \\
K_1 &= J\cos\theta(1)\left[\sqrt{2}\sin\theta(1)\cos\theta(2)-\cos\theta(1)\sin\theta(2)\right] \\
K_2 &= J\sin\theta(1)\left[\sqrt{2}\sin\theta(1)\cos\theta(2)-\cos\theta(1)\sin\theta(2)\right]
\end{aligned} \tag{10.78}$$

BIBLIOGRAPHY

[1] Olivier Darrigol. *A History of Optics from Greek Antiquity to the Nineteenth Century*. Oxford University Press, March 2012.

[2] Max Herzberger. Optics from Euclid to Huygens. *Applied Optics*, 5(9):1383, September 1966.

[3] Jim Al-Khalili. In retrospect: Book of optics. *Nature*, 518(7538):164–165, February 2015.

[4] John David Jackson. *Classical Electrodynamics*. Wiley, August 1998.

[5] Heinrich Hertz. *Electric waves being researches on the propagation of electric action with finite velocity through space*. Macmillan, 1893.

[6] Martin J Klein. Max Planck and the beginnings of the quantum theory. *Archive for History of Exact Sciences*, 1(5):459–479, 1961.

[7] A. Pais. Einstein and the quantum theory. *Reviews of Modern Physics*, 51(4):863–914, October 1979.

[8] P. A. M. Dirac. *The Principles of Quantum Mechanics*. Oxford University Press, January 1981.

[9] S. S. Schweber. *QED and the men who made it: Dyson, Feynman, Schwinger, and Tomonaga*. Princeton University Press, Princeton, N.J, 1994.

[10] D. Hanneke, S. Fogwell, and G. Gabrielse. New measurement of the electron magnetic moment and the fine structure constant. *Physical Review Letters*, 100(12), March 2008.

[11] Richard H. Parker, Chenghui Yu, Weicheng Zhong, Brian Estey, and Holger Müller. Measurement of the fine-structure constant as a test of the standard model. *Science*, 360(6385):191–195, April 2018.

[12] S. R. Lundeen and F. M. Pipkin. Measurement of the Lamb shift in hydrogen, n=2. *Physical Review Letters*, 46(4):232–235, January 1981.

[13] M. Weitz, F. Schmidt-Kaler, and T. W. Hänsch. Precise optical Lamb shift measurements in atomic hydrogen. *Physical Review Letters*, 68(8):1120–1123, February 1992.

[14] Serge Haroche and Jean-Michel Raimond. *Exploring the Quantum: Atoms, Cavities, and Photons*. Oxford University Press, October 2006.

[15] E. M. Purcell, H. C. Torrey, and R. V. Pound. Resonance absorption by nuclear magnetic moments in a solid. *Physical Review*, 69(1-2):37–38, January 1946.

[16] Alexandre Blais, Arne L. Grimsmo, S. M. Girvin, and Andreas Wallraff. Circuit quantum electrodynamics, 2020.

[17] S. Haroche, M. Brune, and J. M. Raimond. From cavity to circuit quantum electrodynamics. *Nature Physics*, 16(3):243–246, March 2020.

[18] A. F. Koenderink, A. Alu, and A. Polman. Nanophotonics: Shrinking light-based technology. *Science*, 348(6234):516–521, April 2015.

[19] Matthew Pelton. Modified spontaneous emission in nanophotonic structures. *Nature Photonics*, 9(7):427–435, June 2015.

[20] P Törmä and W L Barnes. Strong coupling between surface plasmon polaritons and emitters: a review. *Reports on Progress in Physics*, 78(1):013901, December 2014.

[21] D. E. Chang, A. S. Sørensen, P. R. Hemmer, and M. D. Lukin. Strong coupling of single emitters to surface plasmons. *Physical Review B*, 76(3), July 2007.

[22] F. Vollmer, S. Arnold, and D. Keng. Single virus detection from the reactive shift of a whispering-gallery mode. *Proceedings of the National Academy of Sciences*, 105(52):20701–20704, December 2008.

[23] Jiangang Zhu, Şahin Kaya Özdemir, Yun-Feng Xiao, Lin Li, Lina He, Da-Ren Chen, and Lan Yang. On-chip single nanoparticle detection and sizing by mode splitting in an ultrahigh-Q microresonator. *Nature Photonics*, 4(1):46–49, December 2010.

[24] Lina He, Şahin Kaya Özdemir, Jiangang Zhu, Woosung Kim, and Lan Yang. Detecting single viruses and nanoparticles using whispering gallery microlasers. *Nature Nanotechnology*, 6(7):428–432, June 2011.

[25] Weijian Chen, Şahin Kaya Özdemir, Guangming Zhao, Jan Wiersig, and Lan Yang. Exceptional points enhance sensing in an optical microcavity. *Nature*, 548(7666):192–196, August 2017.

[26] Jyoti Lather, Pooja Bhatt, Anoop Thomas, Thomas W. Ebbesen, and Jino George. Cavity catalysis by cooperative vibrational strong coupling of reactant and solvent molecules. *Angewandte Chemie International Edition*, 58(31):10635–10638, July 2019.

[27] Felipe Herrera and Frank C. Spano. Cavity-controlled chemistry in molecular ensembles. *Physical Review Letters*, 116(23):238301, June 2016.

[28] Christian Schäfer, Michael Ruggenthaler, Heiko Appel, and Angel Rubio. Modification of excitation and charge transfer in cavity quantum-electrodynamical chemistry. *Proceedings of the National Academy of Sciences*, 116(11):4883–4892, February 2019.

[29] A. D. Dunkelberger, B. T. Spann, K. P. Fears, B. S. Simpkins, and J. C. Owrutsky. Modified relaxation dynamics and coherent energy exchange in coupled vibration-cavity polaritons. *Nature Communications*, 7(1):13504, November 2016.

[30] Matthew Du, Raphael F. Ribeiro, and Joel Yuen-Zhou. Remote control of chemistry in optical cavities. *Chem*, 5(5):1167–1181, May 2019.

[31] A. Thomas, L. Lethuillier-Karl, K. Nagarajan, R. M. A. Vergauwe, J. George, T. Chervy, A. Shalabney, E. Devaux, C. Genet, J. Moran, and T. W. Ebbesen. Tilting a ground-state reactivity landscape by vibrational strong coupling. *Science*, 363(6427):615–619, February 2019.

[32] Alexandre Blais, Ren-Shou Huang, Andreas Wallraff, S. M. Girvin, and R. J. Schoelkopf. Cavity quantum electrodynamics for superconducting electrical circuits: An architecture for quantum computation. *Physical Review A*, 69(6), June 2004.

[33] Alexandre Blais, Steven M. Girvin, and William D. Oliver. Quantum information processing and quantum optics with circuit quantum electrodynamics. *Nature Physics*, 16(3):247–256, March 2020.

[34] G Romero, D Ballester, YM Wang, V Scarani, and E Solano. Ultrafast quantum gates in circuit qed. *Physical Review Letters*, 108(12):120501, 2012.

[35] Arka Majumdar, Armand Rundquist, Michal Bajcsy, Vaishno D. Dasika, Seth R. Bank, and Jelena Vučković. Design and analysis of photonic crystal coupled cavity arrays for quantum simulation. *Physical Review B*, 86(19):195312, November 2012.

[36] Dimitris G. Angelakis, Marcelo Franca Santos, and Sougato Bose. Photon-blockade-induced Mott transitions and XY spin models in coupled cavity arrays. *Physical Review A*, 76(3):031805, September 2007.

[37] Michael J. Hartmann. Quantum simulation with interacting photons. *Journal of Optics*, 18(10):104005, September 2016.

[38] Anton Frisk Kockum, Adam Miranowicz, Simone De Liberato, Salvatore Savasta, and Franco Nori. Ultrastrong coupling between light and matter. *Nature Reviews Physics*, 1(1):19–40, January 2019.

[39] Claude Cohen-Tannoudji, Jacques Dupont-Roc, and Gilbert Grynberg. *Photons and atoms: Introduction to quantum electrodynamics*. Wiley, Weinheim, Germany, 1997.

[40] D. P. Craig, D. D. Paige, and T. Thirunamachandran. *Molecular Quantum Electrodynamics*. Dover, 1998.

[41] B. J. Dalton, E. S. Guerra, and P. L. Knight. Field quantization in dielectric media and the generalized multipolar Hamiltonian. *Physical Review A*, 54(3):2292–2313, September 1996.

[42] Mark Hillery and Leonard D. Mlodinow. Quantization of electrodynamics in nonlinear dielectric media. *Physical Review A*, 30(4):1860–1865, October 1984.

[43] Lev Davidovich Landau and Evgenii Mikhailovich Lifshitz. *Mechanics: Volume 1*. Butterworth-Heinemann, 1976.

[44] Roy J. Glauber and M. Lewenstein. Quantum optics of dielectric media. *Physical Review A*, 43(1):467–491, January 1991.

[45] M. Babiker and R. Loudon. Derivation of the Power-Zienau-Woolley Hamiltonian in quantum electrodynamics by gauge transformation. *Proceedings of the Royal Society of London. A. Mathematical and Physical Sciences*, 385(1789):439–460, February 1983.

[46] E. A. Power and T. Thirunamachandran. Quantum electrodynamics in a cavity. *Physical Review A*, 25(5):2473–2484, May 1982.

[47] David L. Andrews, Garth A. Jones, A. Salam, and R. Guy Woolley. Perspective: Quantum Hamiltonians for optical interactions. *The Journal of Chemical Physics*, 148(4):040901, January 2018.

[48] O. Painter. Two-dimensional photonic band-gap defect mode laser. *Science*, 284(5421):1819–1821, June 1999.

[49] Dirk Englund, David Fattal, Edo Waks, Glenn Solomon, Bingyang Zhang, Toshihiro Nakaoka, Yasuhiko Arakawa, Yoshihisa Yamamoto, and Jelena Vučković. Controlling the spontaneous emission rate of single quantum dots in a two-dimensional photonic crystal. *Physical Review Letters*, 95(1), July 2005.

[50] Peter Lodahl, Sahand Mahmoodian, and Søren Stobbe. Interfacing single photons and single quantum dots with photonic nanostructures. *Reviews of Modern Physics*, 87(2):347–400, May 2015.

[51] S. M. Dutra. *Cavity quantum electrodynamics: the strange theory of light in a box*. Wiley, New York, 2005.

[52] J. J. Sakurai and Jim Napolitano. *Modern Quantum Mechanics*. Cambridge University Press, September 2020.

[53] Stefan Alexander Maier. *Plasmonics: Fundamentals and Applications*. Springer, May 2007.

[54] Craig Bohren. *Absorption and scattering of light by small particles*. Wiley, New York, 1998.

[55] Xiaofeng Fan, Weitao Zheng, and David J Singh. Light scattering and surface plasmons on small spherical particles. *Light: Science & Applications*, 3(6):e179–e179, June 2014.

[56] Neil W Ashcroft and Mermin. *Solid state physics*. Holt, Rinehart and Winston, New York, 1976.

[57] Yueying Wu, Zhongwei Hu, Xiang-Tian Kong, Juan Carlos Idrobo, Austin G. Nixon, Philip D. Rack, David J. Masiello, and Jon P. Camden. Infrared plasmonics: STEM-EELS characterization of Fabry-Pérot resonance damping in gold nanowires. *Physical Review B*, 101(8):085409, February 2020.

[58] Rashad Baiyasi, Harrison J. Goldwyn, Lauren A. McCarthy, Claire A. West, Seyyed Ali Hosseini Jebeli, David J. Masiello, Stephan Link, and Christy F. Landes. Coupled-dipole modeling and experimental characterization of geometry-dependent trochoidal dichroism in nanorod trimers. *ACS Photonics*, March 2021.

[59] Grace Pakeltis, Enzo Rotunno, Siamak Khorassani, David A. Garfinkel, Robyn Collette, Claire A. West, Scott T. Retterer, Juan Carlos Idrobo, David J. Masiello, and Philip D. Rack. High spatial and energy resolution electron energy loss spectroscopy of the magnetic and electric excitations in plasmonic nanorod oligomers. *Optics Express*, 29(3):4661, January 2021.

[60] Charles Cherqui, Niket Thakkar, Guoliang Li, Jon P. Camden, and David J. Masiello. Characterizing localized surface plasmons using electron energy-loss spectroscopy. *Annual Review of Physical Chemistry*, 67(1):331–357, May 2016.

[61] Charles Cherqui, Guoliang Li, Jacob A. Busche, Steven C. Quillin, Jon P. Camden, and David J. Masiello. Multipolar nanocube plasmon mode-mixing in finite substrates. *The Journal of Physical Chemistry Letters*, 9(3):504–512, January 2018.

[62] Klaus Hepp and Elliott H Lieb. On the superradiant phase transition for molecules in a quantized radiation field: the Dicke maser model. *Annals of Physics*, 76(2):360–404, April 1973.

[63] Lukas Novotny. Strong coupling, energy splitting, and level crossings: A classical perspective. *American Journal of Physics*, 78(11):1199–1202, November 2010.

[64] Said Rahimzadeh-Kalaleh Rodriguez. Classical and quantum distinctions between weak and strong coupling. *European Journal of Physics*, 37(2):025802, January 2016.

[65] Mikhail F. Limonov, Mikhail V. Rybin, Alexander N. Poddubny, and Yuri S. Kivshar. Fano resonances in photonics. *Nature Photonics*, 11(9):543–554, September 2017.

[66] Xiaohua Wu, Stephen K. Gray, and Matthew Pelton. Quantum-dot-induced transparency in a nanoscale plasmonic resonator. *Optics Express*, 18(23):23633, October 2010.

[67] Barry M. Garraway. The Dicke model in quantum optics: Dicke model revisited. *Philosophical Transactions of the Royal Society A: Mathematical, Physical and Engineering Sciences*, 369(1939):1137–1155, March 2011.

[68] Kotni Santhosh, Ora Bitton, Lev Chuntonov, and Gilad Haran. Vacuum Rabi splitting in a plasmonic cavity at the single quantum emitter limit. *Nature Communications*, 7(1), June 2016.

[69] C. K. Law. Interaction between a moving mirror and radiation pressure: A Hamiltonian formulation. *Physical Review A*, 51(3):2537–2541, March 1995.

[70] T. J. Kippenberg and K. J. Vahala. Cavity optomechanics: Back-action at the mesoscale. *Science*, 321(5893):1172–1176, August 2008.

[71] A. Nunnenkamp, K. Børkje, and S. M. Girvin. Single-photon optomechanics. *Physical Review Letters*, 107(6), August 2011.

[72] Markus Aspelmeyer, Tobias J. Kippenberg, and Florian Marquardt. Cavity optomechanics. *Reviews of Modern Physics*, 86(4):1391–1452, December 2014.

[73] Harrison J. Goldwyn, Kevin C. Smith, Jacob A. Busche, and David J. Masiello. Mislocalization in plasmon-enhanced single-molecule fluorescence microscopy as a dynamical Young's interferometer. *ACS Photonics*, 5(8):3141–3151, May 2018.

[74] Andrea Lovera, Benjamin Gallinet, Peter Nordlander, and Olivier J.F. Martin. Mechanisms of fano resonances in coupled plasmonic systems. *ACS Nano*, 7(5):4527–4536, April 2013.

[75] M. Gross and S. Haroche. Superradiance: An essay on the theory of collective spontaneous emission. *Physics Reports*, 93(5):301–396, December 1982.

[76] Nicholas E. Rehler and Joseph H. Eberly. Superradiance. *Physical Review A*, 3(5):1735–1751, May 1971.

[77] M. J. Collett and C. W. Gardiner. Squeezing of intracavity and traveling-wave light fields produced in parametric amplification. *Physical Review A*, 30(3):1386–1391, September 1984.

[78] C. W. Gardiner and M. J. Collett. Input and output in damped quantum systems: Quantum stochastic differential equations and the master equation. *Physical Review A*, 31(6):3761–3774, June 1985.

[79] Hermann A. Haus. *Waves and fields in optoelectronics*. Prentice-Hall, Englewood Cliffs, NJ, 1984.

[80] Marlan O. Scully, M. Suhail Zubairy, and Ian A. Walmsley. Quantum optics. *American Journal of Physics*, 67(7):648–648, July 1999.

[81] P. Goy, J. M. Raimond, M. Gross, and S. Haroche. Observation of cavity-enhanced single-atom spontaneous emission. *Physical Review Letters*, 50(24):1903–1906, June 1983.

[82] Randall G. Hulet, Eric S. Hilfer, and Daniel Kleppner. Inhibited spontaneous emission by a Rydberg atom. *Physical Review Letters*, 55(20):2137–2140, November 1985.

[83] Daniel Kleppner. Inhibited spontaneous emission. *Physical Review Letters*, 47(4):233–236, July 1981.

[84] D. Meschede, H. Walther, and G. Müller. One-atom maser. *Physical Review Letters*, 54(6):551–554, February 1985.

[85] Kerry J. Vahala. Optical microcavities. *Nature*, 424(6950):839–846, August 2003.

[86] Y. Kaluzny, P. Goy, M. Gross, J. M. Raimond, and S. Haroche. Observation of self-induced Rabi oscillations in two-level atoms excited inside a resonant cavity: The ringing regime of superradiance. *Physical Review Letters*, 51(13):1175–1178, September 1983.

[87] M. G. Raizen, R. J. Thompson, R. J. Brecha, H. J. Kimble, and H. J. Carmichael. Normal-mode splitting and linewidth averaging for two-state atoms in an optical cavity. *Physical Review Letters*, 63(3):240–243, July 1989.

[88] U. Fano. Effects of configuration interaction on intensities and phase shifts. *Physical Review*, 124(6):1866–1878, December 1961.

[89] Andrey E. Miroshnichenko, Sergej Flach, and Yuri S. Kivshar. Fano resonances in nanoscale structures. *Reviews of Modern Physics*, 82(3):2257–2298, August 2010.

[90] Bo Peng, Şahin Kaya Özdemir, Fuchuan Lei, Faraz Monifi, Mariagiovanna Gianfreda, Gui Lu Long, Shanhui Fan, Franco Nori, Carl M. Bender, and Lan Yang. Parity-time-symmetric whispering-gallery microcavities. *Nature Physics*, 10(5):394–398, April 2014.

[91] Carl M. Bender, Dorje C. Brody, and Hugh F. Jones. Complex extension of quantum mechanics. *Physical Review Letters*, 89(27), December 2002.

[92] Ş. K. Özdemir, S. Rotter, F. Nori, and L. Yang. Parity–time symmetry and exceptional points in photonics. *Nature Materials*, 18(8):783–798, April 2019.

[93] Linbo Shao, Wenbo Mao, Smarak Maity, Neil Sinclair, Yaowen Hu, Lan Yang, and Marko Lončar. Non-reciprocal transmission of microwave acoustic waves in nonlinear parity–time symmetric resonators. *Nature Electronics*, 3(5):267–272, May 2020.

[94] Lukas Novotny. *Principles of nano-optics*. Cambridge University Press, Cambridge, 2006.

[95] Guoping Lin, Aurélien Coillet, and Yanne K. Chembo. Nonlinear photonics with high-Q whispering-gallery-mode resonators. *Advances in Optics and Photonics*, 9(4):828, November 2017.

[96] A. F. Koenderink. On the use of Purcell factors for plasmon antennas. *Optics Letters*, 35(24):4208, December 2010.

[97] Edwin N. Lassettre. Collision cross-section studies on molecular gases and the dissociation of oxygen and water. *Radiation Research Supplement*, 1:530, 1959.

[98] Boris Luk'yanchuk, Nikolay I. Zheludev, Stefan A. Maier, Naomi J. Halas, Peter Nordlander, Harald Giessen, and Chong Tow Chong. The Fano resonance in plasmonic nanostructures and metamaterials. *Nature Materials*, 9(9):707–715, August 2010.

[99] K. M. Birnbaum, A. Boca, R. Miller, A. D. Boozer, T. E. Northup, and H. J. Kimble. Photon blockade in an optical cavity with one trapped atom. *Nature*, 436(7047):87–90, July 2005.

[100] A. Imamoğlu, H. Schmidt, G. Woods, and M. Deutsch. Strongly interacting photons in a nonlinear cavity. *Physical Review Letters*, 79(8):1467–1470, August 1997.

[101] M Wagner. *Unitary transformations in solid state physics*. Elsevier, New York, 1986.

[102] J. Dalibard and C. Cohen-Tannoudji. Dressed-atom approach to atomic motion in laser light: the dipole force revisited. *Journal of the Optical Society of America B*, 2(11):1707, November 1985.

[103] Maxime Boissonneault, J. M. Gambetta, and Alexandre Blais. Dispersive regime of circuit QED: Photon-dependent qubit dephasing and relaxation rates. *Physical Review A*, 79(1), January 2009.

[104] Carl M. Bender and Stefan Boettcher. Real spectra in non-Hermitian Hamiltonians having pt symmetry. *Physical Review Letters*, 80(24):5243–5246, June 1998.

[105] Niket Thakkar, Morgan T. Rea, Kevin C. Smith, Kevin D. Heylman, Steven C. Quillin, Kassandra A. Knapper, Erik H. Horak, David J. Masiello, and Randall H. Goldsmith. Sculpting Fano resonances to control photonic–plasmonic hybridization. *Nano Letters*, 17(11):6927–6934, October 2017.

[106] Feng Pan, Kevin C. Smith, Hoang L. Nguyen, Kassandra A. Knapper, David J. Masiello, and Randall H. Goldsmith. Elucidating energy pathways through simultaneous measurement of absorption and transmission in a coupled plasmonic–photonic cavity. *Nano Letters*, 20(1):50–58, August 2019.

[107] Kevin C. Smith, Agust Olafsson, Xuan Hu, Steven C. Quillin, Juan Carlos Idrobo, Robyn Collette, Philip D. Rack, Jon P. Camden, and David J. Masiello. Direct observation of infrared plasmonic Fano antiresonances by a nanoscale electron probe. *Physical Review Letters*, 123(17):177401, October 2019.

[108] Michael Barth, Stefan Schietinger, Sabine Fischer, Jan Becker, Nils Nusse, Thomas Aichele, Bernd Löchel, Carsten Sönnichsen, and Oliver Benson. Nanoassembled plasmonic-photonic hybrid cavity for tailored light-matter coupling. *Nano Letters*, 10(3):891–895, 2010.

[109] Xiaodong Yang, Atsushi Ishikawa, Xiaobo Yin, and Xiang Zhang. Hybrid photonic-plasmonic crystal nanocavities. *ACS Nano*, 5(4):2831–2838, 2011.

[110] Ye Luo, Maysamreza Chamanzar, Aniello Apuzzo, Rafael Salas-Montiel, Kim Ngoc Nguyen, Sylvain Blaize, and Ali Adibi. On-chip hybrid photonic–plasmonic light concentrator for nanofocusing in an integrated silicon photonics platform. *Nano Letters*, 15(2):849–856, 2015.

[111] Shanying Cui, Xingyu Zhang, Tsung-li Liu, Jonathan Lee, David Bracher, Kenichi Ohno, David Awschalom, and Evelyn L Hu. Hybrid plasmonic photonic crystal cavity for enhancing emission from near-surface nitrogen vacancy centers in diamond. *ACS Photonics*, 2(4):465–469, 2015.

[112] Yun-Feng Xiao, Yong-Chun Liu, Bei-Bei Li, You-Ling Chen, Yan Li, and Qihuang Gong. Strongly enhanced light-matter interaction in a hybrid photonic-plasmonic resonator. *Physical Review A*, 85(3):031805, 2012.

[113] Oliver Benson. Assembly of hybrid photonic architectures from nanophotonic constituents. *Nature*, 480(7376):193–199, 2011.

[114] Ralf Ameling and Harald Giessen. Microcavity plasmonics: strong coupling of photonic cavities and plasmons. *Laser & Photonics Review*, 7(2):141–169, 2013.

[115] Martín López-García, Juan F Galisteo-López, Alvaro Blanco, Jorge Sánchez-Marcos, Cefe López, and Antonio García-Martín. Enhancement and directionality of spontaneous emission in hybrid self-assembled photonic–plasmonic crystals. *Small*, 6(16):1757–1761, 2010.

[116] Boyang Ding, Calin Hrelescu, Nikita Arnold, Goran Isic, and Thomas A Klar. Spectral and directional reshaping of fluorescence in large area self-assembled plasmonic–photonic crystals. *Nano Letters*, 13(2):378–386, 2013.

[117] Alexander M Stolyarov, Lei Wei, Ofer Shapira, Fabien Sorin, Song L Chua, John D Joannopoulos, and Yoel Fink. Microfluidic directional emission control of an azimuthally polarized radial fibre laser. *Nature Photonics*, 6(4):229–233, 2012.

[118] Xin Guo, Min Qiu, Jiming Bao, Benjamin J Wiley, Qing Yang, Xining Zhang, Yaoguang Ma, Huakang Yu, and Limin Tong. Direct coupling of plasmonic and photonic nanowires for hybrid nanophotonic components and circuits. *Nano Letters*, 9(12):4515–4519, 2009.

[119] Ivan S Maksymov. Optical switching and logic gates with hybrid plasmonic–photonic crystal nanobeam cavities. *Physics Letters A*, 375(5):918–921, 2011.

[120] Shuai Sun, Abdel-Hameed A Badawy, V Narayana, Tarek El-Ghazawi, and Volker J Sorger. The case for hybrid photonic plasmonic interconnects (hyppis): Low-latency energy-and-area-efficient on-chip interconnects. *IEEE Photonics Journal*, 7(6):1–14, 2015.

[121] Maysamreza Chamanzar and Ali Adibi. Hybrid nanoplasmonic-photonic resonators for efficient coupling of light to single plasmonic nanoresonators. *Optics Express*, 19(22):22292–22304, 2011.

[122] Xiaoli Wang, Roberta Morea, Jose Gonzalo, and Bruno Palpant. Coupling localized plasmonic and photonic modes tailors and boosts ultrafast light modulation by gold nanoparticles. *Nano Letters*, 15(4):2633–2639, 2015.

[123] Venkata R Dantham, Stephen Holler, Curtis Barbre, David Keng, Vasily Kolchenko, and Stephen Arnold. Label-free detection of single protein using a nanoplasmonic-photonic hybrid microcavity. *Nano Letters*, 13(7):3347–3351, 2013.

[124] Martin D Baaske, Matthew R Foreman, and Frank Vollmer. Single-molecule nucleic acid interactions monitored on a label-free microcavity biosensor platform. *Nature Nanotechnology*, 9(11):933–939, 2014.

[125] Francesco De Angelis, Maddalena Patrini, Gobind Das, Ivan Maksymov, Matteo Galli, Luca Businaro, Lucio Claudio Andreani, and Enzo Di Fabrizio. A hybrid plasmonic-photonic nanodevice for label-free detection of a few molecules. *Nano Letters*, 8(8):2321–2327, 2008.

[126] Edward M Purcell. Proceedings of the American Physical Society. *Physical Review*, 69:681, 1946.

[127] Hugo M Doeleman, Ewold Verhagen, and A Femius Koenderink. Antenna–cavity hybrids: matching polar opposites for Purcell enhancements at any linewidth. *ACS Photonics*, 3(10):1943–1951, 2016.

[128] Mario Agio and Diego Martin Cano. Nano-optics: The Purcell factor of nanoresonators. *Nature Photonics*, 7(9):674–675, 2013.

[129] DK Armani, TJ Kippenberg, SM Spillane, and KJ Vahala. Ultra-high-Q toroid microcavity on a chip. *Nature*, 421(6926):925–928, 2003.

[130] Kerry J Vahala. Optical microcavities. *Nature*, 424(6950):839–846, 2003.

[131] Rohit Chikkaraddy, Bart de Nijs, Felix Benz, Steven J Barrow, Oren A Scherman, Edina Rosta, Angela Demetriadou, Peter Fox, Ortwin Hess, and Jeremy J Baumberg. Single-molecule strong coupling at room temperature in plasmonic nanocavities. *Nature*, 535(7610):127–130, 2016.

[132] Jon A Schuller, Edward S Barnard, Wenshan Cai, Young Chul Jun, Justin S White, and Mark L Brongersma. Plasmonics for extreme light concentration and manipulation. *Nature Materials*, 9(3):193–204, 2010.

[133] Bumki Min, Eric Ostby, Volker Sorger, Erick Ulin-Avila, Lan Yang, Xiang Zhang, and Kerry Vahala. high-Q surface-plasmon-polariton whispering-gallery microcavity. *Nature*, 457(7228):455–458, 2009.

[134] Matthew R Foreman and Frank Vollmer. Level repulsion in hybrid photonic-plasmonic microresonators for enhanced biodetection. *Physical Review A*, 88(2):023831, 2013.

[135] Matthew R Foreman and Frank Vollmer. Theory of resonance shifts of whispering gallery modes by arbitrary plasmonic nanoparticles. *New Journal of Physics*, 15(8):083006, 2013.

[136] Shuang Zhang, Yong-Shik Park, Yongmin Liu, Thomas Zentgraf, and Xiang Zhang. Far-field measurement of ultra-small plasmonic mode volume. *Optics Express*, 18(6):6048–6055, 2010.

[137] Philip Trøst Kristensen and Stephen Hughes. Modes and mode volumes of leaky optical cavities and plasmonic nanoresonators. *ACS Photonics*, 1(1):2–10, 2013.

[138] Stefan A Maier. Effective mode volume of nanoscale plasmon cavities. *Optical and Quantum Electronics*, 38(1-3):257–267, 2006.

[139] TJ Kippenberg, SM Spillane, and KJ Vahala. Demonstration of ultra-high-Q small mode volume toroid microcavities on a chip. *Applied Physics Letters*, 85(25):6113–6115, 2004.

[140] Kevin D Heylman, Niket Thakkar, Erik H Horak, Steven C Quillin, Charles Cherqui, Kassandra A Knapper, David J Masiello, and Randall H Goldsmith. Optical microresonators as single-particle absorption spectrometers. *Nature Photonics*, 10(12):788–795, 2016.

[141] Andrey E Miroshnichenko, Sergej Flach, and Yuri S Kivshar. Fano resonances in nanoscale structures. *Review of Modern Physics*, 82(3):2257, 2010.

[142] Jean-Christophe Blancon, Matthieu Paillet, Huy Nam Tran, Xuan Tinh Than, Samuel Aberra Guebrou, Anthony Ayari, Alfonso San Miguel, Ngoc-Minh Phan, Ahmed-Azmi Zahab, Jean-Louis Sauvajol, et al. Direct measurement of the absolute absorption spectrum of individual semiconducting single-wall carbon nanotubes. *Nature Communications*, 4:2542, 2013.

[143] Mustafa Yorulmaz, Sara Nizzero, Anneli Hoggard, Lin-Yung Wang, Yi-Yu Cai, Man-Nung Su, Wei-Shun Chang, and Stephan Link. Single-particle absorption spectroscopy by photothermal contrast. *Nano Letters*, 15(5):3041–3047, 2015.

[144] Matthias Mader, Jakob Reichel, Theodor W Hänsch, and David Hunger. A scanning cavity microscope. *Nature Communications*, 6:7249, 2015.

[145] P Kukura, M Celebrano, A Renn, and V Sandoghdar. Imaging a single quantum dot when it is dark. *Nano Letters*, 9(3):926–929, 2008.

[146] Stéphane Berciaud, Laurent Cognet, Philippe Poulin, R Bruce Weisman, and Brahim Lounis. Absorption spectroscopy of individual single-walled carbon nanotubes. *Nano Letters*, 7(5):1203–1207, 2007.

[147] Ugo Fano. Effects of configuration interaction on intensities and phase shifts. *Physical Review*, 124(6):1866, 1961.

[148] Yong-Chun Liu, Bei-Bei Li, and Yun-Feng Xiao. Electromagnetically induced transparency in optical microcavities. *Nanophotonics*, 6(5):789–811, 2017.

[149] Joonhee Lee, Shawn M Perdue, Alejandro Rodriguez Perez, and Vartkess Ara Apkarian. Vibronic motion with joint angstrom–femtosecond resolution observed through Fano progressions recorded within one molecule. *ACS Nano*, 8(1):54–63, 2014.

[150] Andreas Bärnthaler, Stefan Rotter, Florian Libisch, Joachim Burgdörfer, Stefan Gehler, Ulrich Kuhl, and Hans-Jürgen Stöckmann. Probing decoherence through Fano resonances. *Physical Review Letters*, 105:056801, July 2010.

[151] Yu Liu, Eric N Mills, and Russell J Composto. Tuning optical properties of gold nanorods in polymer films through thermal reshaping. *Journal of Materials Chemistry*, 19(18):2704–2709, 2009.

[152] W Joshua Kennedy, Keith A Slinker, Brent L Volk, Hilmar Koerner, Trenton J Godar, Gregory J Ehlert, and Jeffery W Baur. High-resolution mapping of thermal history in polymer nanocomposites: gold nanorods as microscale temperature sensors. *ACS Applied Materials & Interfaces*, 7(50):27624–27631, 2015.

[153] Hristina Petrova, Jorge Perez Juste, Isabel Pastoriza-Santos, Gregory V Hartland, Luis M Liz-Marzán, and Paul Mulvaney. On the temperature stability of gold nanorods: comparison between thermal and ultrafast laser-induced heating. *Physical Chemistry Chemical Physics*, 8(7):814–821, 2006.

[154] Stephan Link, MB Mohamed, and MA El-Sayed. Simulation of the optical absorption spectra of gold nanorods as a function of their aspect ratio and the effect of the medium dielectric constant. *The Journal of Physical Chemistry B*, 103(16):3073–3077, 1999.

[155] Gregory V Hartland. Coherent vibrational motion in metal particles: Determination of the vibrational amplitude and excitation mechanism. *The Journal of chemical physics*, 116(18):8048–8055, 2002.

[156] Chia-Kuang Tsung, Xiaoshan Kou, Qihui Shi, Jinping Zhang, Man Hau Yeung, Jianfang Wang, and Galen D Stucky. Selective shortening of single-crystalline gold nanorods by mild oxidation. *Journal of the American Chemical Society*, 128(16):5352–5353, 2006.

[157] Renxian Zou, Xia Guo, Jian Yang, Dandan Li, Feng Peng, Lei Zhang, Hongjuan Wang, and Hao Yu. Selective etching of gold nanorods by ferric chloride at room temperature. *CrystEngComm*, 11(12):2797–2803, 2009.

[158] Stephan Link, Clemens Burda, B Nikoobakht, and Mostafa A El-Sayed. Laser-induced shape changes of colloidal gold nanorods using femtosecond and nanosecond laser pulses. *The Journal of Physical Chemistry B*, 104(26):6152–6163, 2000.

[159] Christopher J DeSantis, Da Huang, Hui Zhang, Nathaniel J Hogan, Hangqi Zhao, Yifei Zhang, Alejandro Manjavacas, Yue Zhang, Wei-Shun Chang, Peter Nordlander, et al. Laser-induced spectral hole-burning through a broadband distribution of au nanorods. *The Journal of Physical Chemistry B*, 120(37):20518–20524, 2015.

[160] Adam B Taylor, Arif M Siddiquee, and James WM Chon. Below melting point photothermal reshaping of single gold nanorods driven by surface diffusion. *ACS Nano*, 8(12):12071–12079, 2014.

[161] Julian Schwinger, Lester L DeRaad Jr, Kimball A Milton, and Wu-yang Tsai. *Classical Electrodynamics*. Westview Press, 1998.

[162] Neil W. Ashcroft and N. David Mermin. *Solid State Physics*. Cengage Learning, 2011.

[163] Kensuke Kobayashi, Hisashi Aikawa, Shingo Katsumoto, and Yasuhiro Iye. Tuning of the Fano effect through a quantum dot in an Aharonov-Bohm interferometer. *Physical Review Letters*, 88(25):256806, 2002.

[164] AA Clerk, X Waintal, and PW Brouwer. Fano resonances as a probe of phase coherence in quantum dots. *Physical Review Letters*, 86(20):4636, 2001.

[165] Sassan N Sheikholeslami, Aitzol García-Etxarri, and Jennifer A Dionne. Controlling the interplay of electric and magnetic modes via Fano-like plasmon resonances. *Nano Letters*, 11(9):3927–3934, 2011.

[166] Jianji Yang, Mathias Perrin, and Philippe Lalanne. Analytical formalism for the interaction of two-level quantum systems with metal nanoresonators. *Physical Review X*, 5(2):021008, 2015.

[167] Wei Zhang and Alexander O Govorov. Quantum theory of the nonlinear Fano effect in hybrid metal-semiconductor nanostructures: the case of strong nonlinearity. *Physical Review B*, 84(8):081405, 2011.

[168] Yong He and Ka-Di Zhu. Fano correlation effect of optical response due to plasmon–exciton–plasmon interaction in an artificial hybrid molecule system. *Journal of the Optical Society of America B*, 30(4):868–873, 2013.

[169] Abraham Nitzan. *Chemical Dynamics in Condensed Phases: Relaxation, Transfer and Reactions in Condensed Molecular Systems*. Oxford University Press, 2006.

[170] D Langbein. Non-retarded dispersion energy between macroscopic spheres. *Journal of Physics and Chemistry of Solids*, 32(7):1657–1667, 1971.

[171] C. Sauvan, J. P. Hugonin, I. S. Maksymov, and P. Lalanne. Theory of the spontaneous optical emission of nanosize photonic and plasmon resonators. *Physical Review Letters*, 110(23):237401, 2013.

[172] P. T. Leung, S. Y. Liu, and K. Young. Completeness and orthogonality of quasinormal modes in leaky optical cavities. *Physical Review A*, 49(4):3057–3067, 1994.

[173] Kristiaan De Greve, Leo Yu, Peter L. McMahon, Jason S. Pelc, Chandra M. Natarajan, Na Young Kim, Eisuke Abe, Sebastian Maier, Christian Schneider, Martin Kamp, Sven Höfling, Robert H. Hadfield, Alfred Forchel, M. M. Fejer, and Yoshihisa Yamamoto. Quantum-dot spin–photon entanglement via frequency downconversion to telecom wavelength. *Nature*, 491(7424):421–425, November 2012.

[174] A. Imamoğlu, D. D. Awschalom, G. Burkard, D. P. DiVincenzo, D. Loss, M. Sherwin, and A. Small. Quantum information processing using quantum dot spins and cavity QED. *Physical Review Letters*, 83(20):4204–4207, November 1999.

[175] T. Pellizzari, S. A. Gardiner, J. I. Cirac, and P. Zoller. Decoherence, continuous observation, and quantum computing: A cavity QED model. *Physical Review Letters*, 75(21):3788–3791, November 1995.

[176] Shi-Biao Zheng and Guang-Can Guo. Efficient scheme for two-atom entanglement and quantum information processing in cavity QED. *Physical Review Letters*, 85(11):2392–2395, September 2000.

[177] H. J. Kimble. The quantum internet. *Nature*, 453(7198):1023–1030, June 2008.

[178] Mika A. Sillanpää, Jae I. Park, and Raymond W. Simmonds. Coherent quantum state storage and transfer between two phase qubits via a resonant cavity. *Nature*, 449(7161):438–442, September 2007.

[179] Daqing Wang, Hrishikesh Kelkar, Diego Martin-Cano, Dominik Rattenbacher, Alexey Shkarin, Tobias Utikal, Stephan Götzinger, and Vahid Sandoghdar. Turning a molecule into a coherent two-level quantum system. *Nature Physics*, 15(5):483–489, February 2019.

[180] J. McKeever, J. R. Buck, A. D. Boozer, and H. J. Kimble. Determination of the number of atoms trapped in an optical cavity. *Physical Review Letters*, 93(14):143601, September 2004.

[181] P. Münstermann, T. Fischer, P. Maunz, P. W. H. Pinkse, and G. Rempe. Dynamics of single-atom motion observed in a high-finesse cavity. *Physical Review Letters*, 82(19):3791–3794, May 1999.

[182] Xiaolan Zhong, Thibault Chervy, Lei Zhang, Anoop Thomas, Jino George, Cyriaque Genet, James A. Hutchison, and Thomas W. Ebbesen. Energy transfer between spatially separated entangled molecules. *Angewandte Chemie International Edition*, 56(31):9034–9038, June 2017.

[183] Anoop Thomas, Jino George, Atef Shalabney, Marian Dryzhakov, Sreejith J. Varma, Joseph Moran, Thibault Chervy, Xiaolan Zhong, Eloïse Devaux, Cyriaque Genet, James A. Hutchison, and Thomas W. Ebbesen. Ground-state chemical reactivity under vibrational coupling to the vacuum electromagnetic field. *Angewandte Chemie International Edition*, 55(38):11462–11466, August 2016.

[184] Kartik Srinivasan and Oskar Painter. Linear and nonlinear optical spectroscopy of a strongly coupled microdisk–quantum dot system. *Nature*, 450(7171):862–865, December 2007.

[185] Ryuichi Ohta, Yasutomo Ota, Masahiro Nomura, Naoto Kumagai, Satomi Ishida, Satoshi Iwamoto, and Yasuhiko Arakawa. Strong coupling between a photonic crystal nanobeam cavity and a single quantum dot. *Applied Physics Letters*, 98(17):173104, April 2011.

[186] K. Hennessy, A. Badolato, M. Winger, D. Gerace, M. Atatüre, S. Gulde, S. Fält, E. L. Hu, and A. Imamoğlu. Quantum nature of a strongly coupled single quantum dot-cavity system. *Nature*, 445(7130):896–899, January 2007.

[187] Yueyang Chen, Albert Ryou, Max R. Friedfeld, Taylor Fryett, James Whitehead, Brandi M. Cossairt, and Arka Majumdar. Deterministic positioning of colloidal quantum dots on silicon nitride nanobeam cavities. *Nano Letters*, 18(10):6404–6410, September 2018.

[188] D. K. Armani, T. J. Kippenberg, S. M. Spillane, and K. J. Vahala. Ultra-high-Q toroid microcavity on a chip. *Nature*, 421(6926):925–928, February 2003.

[189] B. Gayral, J. M. Gérard, A. Lemaître, C. Dupuis, L. Manin, and J. L. Pelouard. High-Q wet-etched GaAs microdisks containing InAs quantum boxes. *Applied Physics Letters*, 75(13):1908–1910, September 1999.

[190] Hugo M. Doeleman, Ewold Verhagen, and A. Femius Koenderink. Antenna–cavity hybrids: Matching polar opposites for Purcell enhancements at any linewidth. *ACS Photonics*, 3(10):1943–1951, September 2016.

[191] S. I. Shopova, R. Rajmangal, S. Holler, and S. Arnold. Plasmonic enhancement of a whispering-gallery-mode biosensor for single nanoparticle detection. *Applied Physics Letters*, 98(24):243104, June 2011.

[192] Miguel A. Santiago-Cordoba, Svetlana V. Boriskina, Frank Vollmer, and Melik C. Demirel. Nanoparticle-based protein detection by optical shift of a resonant microcavity. *Applied Physics Letters*, 99(7):073701, August 2011.

[193] S. V. Boriskina and B. M. Reinhard. Spectrally and spatially configurable superlenses for optoplasmonic nanocircuits. *Proceedings of the National Academy of Sciences*, 108(8):3147–3151, February 2011.

[194] S. I. Shopova, C. W. Blackledge, and A. T. Rosenberger. Enhanced evanescent coupling to whispering-gallery modes due to gold nanorods grown on the microresonator surface. *Applied Physics B*, 93(1):183–187, August 2008.

[195] Wonmi Ahn, Svetlana V. Boriskina, Yan Hong, and Björn M. Reinhard. Photonic–plasmonic mode coupling in on-chip integrated optoplasmonic molecules. *ACS Nano*, 6(1):951–960, December 2011.

[196] A. Badolato. Deterministic coupling of single quantum dots to single nanocavity modes. *Science*, 308(5725):1158–1161, May 2005.

[197] Dirk Englund, Andrei Faraon, Ilya Fushman, Nick Stoltz, Pierre Petroff, and Jelena Vučković. Controlling cavity reflectivity with a single quantum dot. *Nature*, 450(7171):857–861, December 2007.

[198] Jui-Nung Liu, Qinglan Huang, Keng-Ku Liu, Srikanth Singamaneni, and Brian T. Cunningham. Nanoantenna–microcavity hybrids with highly cooperative plasmonic–photonic coupling. *Nano Letters*, 17(12):7569–7577, November 2017.

[199] G. S. Solomon, M. Pelton, and Y. Yamamoto. Single-mode spontaneous emission from a single quantum dot in a three-dimensional microcavity. *Physical Review Letters*, 86(17):3903–3906, April 2001.

[200] Freek Ruesink, Hugo M. Doeleman, Ewold Verhagen, and A. Femius Koenderink. Controlling nanoantenna polarizability through backaction via a single cavity mode. *Physical Review Letters*, 120(20):206101, May 2018.

[201] Pan Wang, Yipei Wang, Zongyin Yang, Xin Guo, Xing Lin, Xiao-Chong Yu, Yun-Feng Xiao, Wei Fang, Lei Zhang, Guowei Lu, Qihuang Gong, and Limin Tong. Single-band 2-nm-line-width plasmon resonance in a strongly coupled au nanorod. *Nano Letters*, 15(11):7581–7586, October 2015.

[202] C. Sönnichsen, T. Franzl, T. Wilk, G. von Plessen, J. Feldmann, O. Wilson, and P. Mulvaney. Drastic reduction of plasmon damping in gold nanorods. *Physical Review Letters*, 88(7):077402, January 2002.

[203] Freek Ruesink, Hugo M. Doeleman, Ruud Hendrikx, A. Femius Koenderink, and Ewold Verhagen. Perturbing open cavities: Anomalous resonance frequency shifts in a hybrid cavity-nanoantenna system. *Physical Review Letters*, 115(20):203904, November 2015.

[204] Pai Peng, Yong-Chun Liu, Da Xu, Qi-Tao Cao, Guowei Lu, Qihuang Gong, and Yun-Feng Xiao. Enhancing coherent light-matter interactions through microcavity-engineered plasmonic resonances. *Physical Review Letters*, 119(23):233901, December 2017.

[205] Kartik Srinivasan, Oskar Painter, Andreas Stintz, and Sanjay Krishna. Single quantum dot spectroscopy using a fiber taper waveguide near-field optic. *Applied Physics Letters*, 91(9):091102, August 2007.

[206] Yun-Feng Xiao, Yong-Chun Liu, Bei-Bei Li, You-Ling Chen, Yan Li, and Qihuang Gong. Strongly enhanced light-matter interaction in a hybrid photonic-plasmonic resonator. *Physical Review A*, 85(3):031805, March 2012.

[207] Kevin D. Heylman, Niket Thakkar, Erik H. Horak, Steven C. Quillin, Charles Cherqui, Kassandra A. Knapper, David J. Masiello, and Randall H. Goldsmith. Optical microresonators as single-particle absorption spectrometers. *Nature Photonics*, 10(12):788–795, November 2016.

[208] Erik H. Horak, Morgan T. Rea, Kevin D. Heylman, David Gelbwaser-Klimovsky, Semion K. Saikin, Blaise J. Thompson, Daniel D. Kohler, Kassandra A. Knapper, Wei Wei, Feng Pan, Padma Gopalan, John C. Wright, Alán Aspuru-Guzik, and Randall H. Goldsmith. Exploring electronic structure and order in polymers via single-particle microresonator spectroscopy. *Nano Letters*, 18(3):1600–1607, January 2018.

[209] G. Lin, B. Qian, F. Oručević, Y. Candela, J.-B. Jager, Z. Cai, V. Lefèvre-Seguin, and J. Hare. Excitation mapping of whispering gallery modes in silica microcavities. *Optics Letters*, 35(4):583, February 2010.

[210] D. W. Vernooy, A. Furusawa, N. Ph. Georgiades, V. S. Ilchenko, and H. J. Kimble. Cavity QED with high-Q whispering gallery modes. *Physical Review A*, 57(4):R2293–R2296, April 1998.

[211] Vincent Juvé, M. Fernanda Cardinal, Anna Lombardi, Aurélien Crut, Paolo Maioli, Jorge Pérez-Juste, Luis M. Liz-Marzán, Natalia Del Fatti, and Fabrice Vallée. Size-dependent surface plasmon resonance broadening in nonspherical nanoparticles: Single gold nanorods. *Nano Letters*, 13(5):2234–2240, April 2013.

[212] Zhongming Li, Weizhi Mao, Mary Sajini Devadas, and Gregory V. Hartland. Absorption spectroscopy of single optically trapped gold nanorods. *Nano Letters*, 15(11):7731–7735, October 2015.

[213] Daniele Sanvitto and Stéphane Kéna-Cohen. The road towards polaritonic devices. *Nature Materials*, 15(10):1061–1073, July 2016.

[214] Matthew Du, Luis A. Martínez-Martínez, Raphael F. Ribeiro, Zixuan Hu, Vinod M. Menon, and Joel Yuen-Zhou. Theory for polariton-assisted remote energy transfer. *Chemical Science*, 9(32):6659–6669, 2018.

[215] Andrew D. Greentree, Charles Tahan, Jared H. Cole, and Lloyd C. L. Hollenberg. Quantum phase transitions of light. *Nature Physics*, 2(12):856–861, November 2006.

[216] Iacopo Carusotto and Cristiano Ciuti. Quantum fluids of light. *Reviews of Modern Physics*, 85(1):299–366, February 2013.

[217] Joseph Kerckhoff, Hendra I. Nurdin, Dmitri S. Pavlichin, and Hideo Mabuchi. Designing quantum memories with embedded control: Photonic circuits for autonomous quantum error correction. *Physical Review Letters*, 105(4):040502, July 2010.

[218] Hideo Mabuchi. Nonlinear interferometry approach to photonic sequential logic. *Applied Physics Letters*, 99(15):153103, October 2011.

[219] Vilson R. Almeida, Carlos A. Barrios, Roberto R. Panepucci, and Michal Lipson. All-optical control of light on a silicon chip. *Nature*, 431(7012):1081–1084, October 2004.

[220] Yin-Hai Li, Zhi-Yuan Zhou, Zhao-Huai Xu, Li-Xin Xu, Bao-Sen Shi, and Guang-Can Guo. Multiplexed entangled photon-pair sources for all-fiber quantum networks. *Physical Review A*, 94(4):043810, October 2016.

[221] Martin D. Baaske, Matthew R. Foreman, and Frank Vollmer. Single-molecule nucleic acid interactions monitored on a label-free microcavity biosensor platform. *Nature Nanotechnology*, 9(11):933–939, August 2014.

[222] Venkata R. Dantham, Stephen Holler, Curtis Barbre, David Keng, Vasily Kolchenko, and Stephen Arnold. Label-free detection of single protein using a nanoplasmonic-photonic hybrid microcavity. *Nano Letters*, 13(7):3347–3351, June 2013.

[223] G. Ruthemann. Diskrete energieverluste schneller elektronen in festkörpern. *Die Naturwissenschaften*, 29(42-43):648–648, October 1941.

[224] Ondrej L. Krivanek, Tracy C. Lovejoy, Niklas Dellby, and R.W. Carpenter. Monochromated STEM with a 30 meV-wide, atom-sized electron probe. *Microscopy*, 62(1):3–21, January 2013.

[225] F. J. García de Abajo. Optical excitations in electron microscopy. *Reviews of Modern Physics*, 82(1):209–275, February 2010.

[226] Ai Leen Koh, Antonio I. Fernández-Domínguez, David W. McComb, Stefan A. Maier, and Joel K. W. Yang. High-resolution mapping of electron-beam-excited plasmon modes in lithographically defined gold nanostructures. *Nano Letters*, 11(3):1323–1330, March 2011.

[227] Huigao Duan, Antonio I. Fernández-Domínguez, Michel Bosman, Stefan A. Maier, and Joel K. W. Yang. Nanoplasmonics: Classical down to the nanometer scale. *Nano Letters*, 12(3):1683–1689, February 2012.

[228] Nicholas W. Bigelow, Alex Vaschillo, Vighter Iberi, Jon P. Camden, and David J. Masiello. Characterization of the electron- and photon-driven plasmonic excitations of metal nanorods. *ACS Nano*, 6(8):7497–7504, August 2012.

[229] Jonathan A. Scholl, Aitzol García-Etxarri, Ai Leen Koh, and Jennifer A. Dionne. Observation of quantum tunneling between two plasmonic nanoparticles. *Nano Letters*, 13(2):564–569, January 2013.

[230] Ondrej L. Krivanek, Tracy C. Lovejoy, Niklas Dellby, Toshihiro Aoki, R. W. Carpenter, Peter Rez, Emmanuel Soignard, Jiangtao Zhu, Philip E. Batson, Maureen J. Lagos, Ray F. Egerton, and Peter A. Crozier. Vibrational spectroscopy in the electron microscope. *Nature*, 514(7521):209–212, October 2014.

[231] Mathieu Kociak and Odile Stéphan. Mapping plasmons at the nanometer scale in an electron microscope. *Chemical Society Reviews*, 43(11):3865, 2014.

[232] Maureen J. Lagos, Andreas Trügler, Ulrich Hohenester, and Philip E. Batson. Mapping vibrational surface and bulk modes in a single nanocube. *Nature*, 543(7646):529–532, March 2017.

[233] Hugo Lourenço-Martins and Mathieu Kociak. Vibrational surface electron-energy-loss spectroscopy probes confined surface-phonon modes. *Physical Review X*, 7(4):041059, December 2017.

[234] Yueying Wu, Guoliang Li, and Jon P. Camden. Probing nanoparticle plasmons with electron energy loss spectroscopy. *Chemical Reviews*, 118(6):2994–3031, December 2017.

[235] Shaunak Mukherjee, Florian Libisch, Nicolas Large, Oara Neumann, Lisa V. Brown, Jin Cheng, J. Britt Lassiter, Emily A. Carter, Peter Nordlander, and Naomi J. Halas. Hot electrons do the impossible: Plasmon-induced dissociation of H2 on Au. *Nano Letters*, 13(1):240–247, December 2012.

[236] Sarah Griffin, Nicholas P. Montoni, Guoliang Li, Patrick J. Straney, Jill E. Millstone, David J. Masiello, and Jon P. Camden. Imaging energy transfer in pt-decorated au nanoprisms via electron energy-loss spectroscopy. *The Journal of Physical Chemistry Letters*, 7(19):3825–3832, September 2016.

[237] J. A. Fan, C. Wu, K. Bao, J. Bao, R. Bardhan, N. J. Halas, V. N. Manoharan, P. Nordlander, G. Shvets, and F. Capasso. Self-assembled plasmonic nanoparticle clusters. *Science*, 328(5982):1135–1138, May 2010.

[238] Burcu Ögüt, Nahid Talebi, Ralf Vogelgesang, Wilfried Sigle, and Peter A. van Aken. Toroidal plasmonic eigenmodes in oligomer nanocavities for the visible. *Nano Letters*, 12(10):5239–5244, September 2012.

[239] Charles Cherqui, Nicholas W. Bigelow, Alex Vaschillo, Harrison Goldwyn, and David J. Masiello. Combined tight-binding and numerical electrodynamics understanding of the STEM/EELS magneto-optical responses of aromatic plasmon-supporting metal oligomers. *ACS Photonics*, 1(10):1013–1024, October 2014.

[240] Charles Cherqui, Yueying Wu, Guoliang Li, Steven C. Quillin, Jacob A. Busche, Niket Thakkar, Claire A. West, Nicholas P. Montoni, Philip D. Rack, Jon P. Camden, and David J. Masiello. STEM/EELS imaging of magnetic hybridization in symmetric and symmetry-broken plasmon oligomer dimers and all-magnetic Fano interference. *Nano Letters*, 16(10):6668–6676, September 2016.

[241] Nicholas P. Montoni, Steven C. Quillin, Charles Cherqui, and David J. Masiello. Tunable spectral ordering of magnetic plasmon resonances in noble metal nanoclusters. *ACS Photonics*, 5(8):3272–3281, May 2018.

[242] E. N. Lassettre, M. E. Krasnow, and S. Silverman. Inelastic scattering of electrons by helium. *The Journal of Chemical Physics*, 40(5):1242–1248, March 1964.

[243] Yong-Chun Liu, Bei-Bei Li, and Yun-Feng Xiao. Electromagnetically induced transparency in optical microcavities. *Nanophotonics*, 6(5):789–811, March 2017.

[244] Mikhail V. Rybin, Dmitry S. Filonov, Pavel A. Belov, Yuri S. Kivshar, and Mikhail F. Limonov. Switching from visibility to invisibility via Fano resonances: Theory and experiment. *Scientific Reports*, 5(1), March 2015.

[245] Hua Lu, Xueming Liu, Dong Mao, and Guoxi Wang. Plasmonic nanosensor based on Fano resonance in waveguide-coupled resonators. *Optics Letters*, 37(18):3780, September 2012.

[246] Sabrina Simoncelli, Yi Li, Emiliano Cortés, and Stefan A. Maier. Imaging plasmon hybridization of Fano resonances via hot-electron-mediated absorption mapping. *Nano Letters*, 18(6):3400–3406, May 2018.

[247] Pablo Alonso-Gonzalez, Martin Schnell, Paulo Sarriugarte, Heidar Sobhani, Chihhui Wu, Nihal Arju, Alexander Khanikaev, Federico Golmar, Pablo Albella, Libe Arzubiaga, Felix Casanova, Luis E. Hueso, Peter Nordlander, Gennady Shvets, and Rainer Hillenbrand. Real-space mapping of Fano interference in plasmonic metamolecules. *Nano Letters*, 11(9):3922–3926, September 2011.

[248] Mingsong Wang, Alex Krasnok, Tianyi Zhang, Leonardo Scarabelli, He Liu, Zilong Wu, Luis M. Liz-Marzán, Mauricio Terrones, Andrea Alù, and Yuebing Zheng. Tunable Fano resonance and plasmon-exciton coupling in single au nanotriangles on monolayer WS2 at room temperature. *Advanced Materials*, 30(22):1705779, April 2018.

[249] Farbod Shafiei, Francesco Monticone, Khai Q. Le, Xing-Xiang Liu, Thomas Hartsfield, Andrea Alù, and Xiaoqin Li. A subwavelength plasmonic metamolecule exhibiting magnetic-based optical Fano resonance. *Nature Nanotechnology*, 8(2):95–99, January 2013.

[250] F López-Tejeira, R Paniagua-Domínguez, R Rodríguez-Oliveros, and J A Sánchez-Gil. Fano-like interference of plasmon resonances at a single rod-shaped nanoantenna. *New Journal of Physics*, 14(2):023035, February 2012.

[251] Niels Verellen, Fernando López-Tejeira, Ramón Paniagua-Domínguez, Dries Vercruysse, Denitza Denkova, Liesbet Lagae, Pol Van Dorpe, Victor V. Moshchalkov, and José A. Sánchez-Gil. Mode parity-controlled Fano- and Lorentz-like line shapes arising in plasmonic nanorods. *Nano Letters*, 14(5):2322–2329, April 2014.

[252] Feng Hao, Yannick Sonnefraud, Pol Van Dorpe, Stefan A. Maier, Naomi J. Halas, and Peter Nordlander. Symmetry breaking in plasmonic nanocavities: Subradiant LSPR sensing and a tunable Fano resonance. *Nano Letters*, 8(11):3983–3988, October 2008.

[253] J. Göres, D. Goldhaber-Gordon, S. Heemeyer, M. A. Kastner, Hadas Shtrikman, D. Mahalu, and U. Meirav. Fano resonances in electronic transport through a single-electron transistor. *Physical Review B*, 62(3):2188–2194, July 2000.

[254] Andreas Bärnthaler, Stefan Rotter, Florian Libisch, Joachim Burgdörfer, Stefan Gehler, Ulrich Kuhl, and Hans-Jürgen Stöckmann. Probing decoherence through Fano resonances. *Physical Review Letters*, 105(5):056801, July 2010.

[255] S. Rotter, F. Libisch, J. Burgdörfer, U. Kuhl, and H.-J. Stöckmann. Tunable Fano resonances in transport through microwave billiards. *Physical Review E*, 69(4):046208, April 2004.

[256] Nicholas W. Bigelow, Alex Vaschillo, Jon P. Camden, and David J. Masiello. Signatures of Fano interferences in the electron energy loss spectroscopy and cathodoluminescence of symmetry-broken nanorod dimers. *ACS Nano*, 7(5):4511–4519, April 2013.

[257] Sean M. Collins, Olivia Nicoletti, David Rossouw, Tomas Ostasevicius, and Paul A. Midgley. Excitation dependent Fano-like interference effects in plasmonic silver nanorods. *Physical Review B*, 90(15), October 2014.

[258] Arthur Losquin and Mathieu Kociak. Link between cathodoluminescence and electron energy loss spectroscopy and the radiative and full electromagnetic local density of states. *ACS Photonics*, 2(11):1619–1627, October 2015.

[259] D. Rossouw, M. Couillard, J. Vickery, E. Kumacheva, and G. A. Botton. Multipolar plasmonic resonances in silver nanowire antennas imaged with a subnanometer electron probe. *Nano Letters*, 11(4):1499–1504, April 2011.

[260] Olivia Nicoletti, Martijn Wubs, N. Asger Mortensen, Wilfried Sigle, Peter A. van Aken, and Paul A. Midgley. Surface plasmon modes of a single silver nanorod: an electron energy loss study. *Optics Express*, 19(16):15371, July 2011.

[261] David Rossouw and Gianluigi A. Botton. Plasmonic response of bent silver nanowires for nanophotonic subwavelength waveguiding. *Physical Review Letters*, 110(6):066801, February 2013.

[262] Moussa N'Gom, Jan Ringnalda, John F. Mansfield, Ashish Agarwal, Nicholas Kotov, Nestor J. Zaluzec, and Theodore B. Norris. Single particle plasmon spectroscopy of silver nanowires and gold nanorods. *Nano Letters*, 8(10):3200–3204, September 2008.

[263] Jérôme Martin, Mathieu Kociak, Zackaria Mahfoud, Julien Proust, Davy Gérard, and Jérôme Plain. High-resolution imaging and spectroscopy of multipolar plasmonic resonances in aluminum nanoantennas. *Nano Letters*, 14(10):5517–5523, September 2014.

[264] R. H. Ritchie. Plasma losses by fast electrons in thin films. *Physical Review*, 106(5):874–881, June 1957.

[265] C Sönnichsen. *Plasmons in metal nanostructures, Ludwig-Maximilians-University Munich Ph. D.* PhD thesis, thesis, 2001.

[266] Kevin C. Smith, Yueyang Chen, Arka Majumdar, and David J. Masiello. Active tuning of hybridized modes in a heterogeneous photonic molecule. *Physical Review Applied*, 13(4), April 2020.

[267] Kevin C. Smith, Aniruddha Bhattacharya, and David J. Masiello. Exact k-body representation of the Jaynes-Cummings interaction in the dressed basis: Insight into many-body phenomena with light. March 2021.

[268] Kerry Vahala. *Optical Microcavities*, volume 5. World Scientific, 2004.

[269] Jacob T. Robinson, Christina Manolatou, Long Chen, and Michal Lipson. Ultrasmall mode volumes in dielectric optical microcavities. *Physical Review Letters*, 95(14):143901, September 2005.

[270] Hyeongrak Choi, Mikkel Heuck, and Dirk Englund. Self-similar nanocavity design with ultrasmall mode volume for single-photon nonlinearities. *Physical Review Letters*, 118(22):223605, May 2017.

[271] Amnon Yariv, Yong Xu, Reginald K. Lee, and Axel Scherer. Coupled-resonator optical waveguide: A proposal and analysis. *Optics Letters*, 24(11):711, June 1999.

[272] Atsuo Nakagawa, Satoru Ishii, and Toshihiko Baba. Photonic molecule laser composed of GaInAsP microdisks. *Applied Physics Letters*, 86(4):041112, January 2005.

[273] Svetlana V. Boriskina. Theoretical prediction of a dramatic Q-factor enhancement and degeneracy removal of whispering gallery modes in symmetrical photonic molecules. *Optics Letters*, 31(3):338, 2006.

[274] Qianfan Xu, Sunil Sandhu, Michelle L. Povinelli, Jagat Shakya, Shanhui Fan, and Michal Lipson. Experimental realization of an on-chip all-optical analogue to electromagnetically induced transparency. *Physical Review Letters*, 96(12):123901, March 2006.

[275] David D. Smith, Hongrok Chang, Kirk A. Fuller, A. T. Rosenberger, and Robert W. Boyd. Coupled-resonator-induced transparency. *Physical Review A*, 69(6):063804, June 2004.

[276] Xiaodong Yang, Mingbin Yu, Dim-Lee Kwong, and Chee Wei Wong. All-optical analog to electromagnetically induced transparency in multiple coupled photonic crystal cavities. *Physical Review Letters*, 102(17):173902, April 2009.

[277] T. C. H. Liew and V. Savona. Single photons from coupled quantum modes. *Physical Review Letters*, 104(18):183601, May 2010.

[278] Motoaki Bamba, Atac Imamoğlu, Iacopo Carusotto, and Cristiano Ciuti. Origin of strong photon antibunching in weakly nonlinear photonic molecules. *Physical Review A*, 83(2):021802, February 2011.

[279] Adrien Dousse, Jan Suffczyński, Alexios Beveratos, Olivier Krebs, Aristide Lemaître, Isabelle Sagnes, Jacqueline Bloch, Paul Voisin, and Pascale Senellart. Ultrabright source of entangled photon pairs. *Nature*, 466(7303):217–220, July 2010.

[280] Abhi Saxena, Yueyang Chen, Albert Ryou, Carlos G. Sevilla, Peipeng Xu, and Arka Majumdar. Improving indistinguishability of single photons from colloidal quantum dots using nanocavities. *ACS Photonics*, 2019.

[281] D. L. Underwood, W. E. Shanks, Jens Koch, and A. A. Houck. Low-disorder microwave cavity lattices for quantum simulation with photons. *Physical Review A*, 86(2):023837, August 2012.

[282] Long Chang, Xiaoshun Jiang, Shiyue Hua, Chao Yang, Jianming Wen, Liang Jiang, Guanyu Li, Guanzhong Wang, and Min Xiao. Parity–time symmetry and variable optical isolation in active–passive-coupled microresonators. *Nature Photonics*, 8(7):524–529, June 2014.

[283] H. A. Haus and W. Huang. Coupled-mode theory. *Proceedings of the IEEE*, 79(10):1505–1518, 1991.

[284] Philip Trøst Kristensen and Stephen Hughes. Modes and mode volumes of leaky optical cavities and plasmonic nanoresonators. *ACS Photonics*, 1(1):2–10, December 2013.

[285] Philip Trøst Kristensen, Rong-Chun Ge, and Stephen Hughes. Normalization of quasinormal modes in leaky optical cavities and plasmonic resonators. *Physical Review A*, 92(5), November 2015.

[286] Miloš Popovic, Christina Manolatou, and Michael Watts. Coupling-induced resonance frequency shifts in coupled dielectric multi-cavity filters. *Optics Express*, 14(3):1208, 2006.

[287] J. D. Joannopoulos. *Photonic crystals: molding the flow of light*. Princeton University Press, Princeton, 2008.

[288] Parag B. Deotare, Murray W. McCutcheon, Ian W. Frank, Mughees Khan, and Marko Lončar. High quality factor photonic crystal nanobeam cavities. *Applied Physics Letters*, 94(12):121106, March 2009.

[289] M. Bayer, T. Gutbrod, J. P. Reithmaier, A. Forchel, T. L. Reinecke, P. A. Knipp, A. A. Dremin, and V. D. Kulakovskii. Optical modes in photonic molecules. *Physical Review Letters*, 81(12):2582–2585, September 1998.

[290] T. Mukaiyama, K. Takeda, H. Miyazaki, Y. Jimba, and M. Kuwata-Gonokami. Tight-binding photonic molecule modes of resonant bispheres. *Physical Review Letters*, 82(23):4623–4626, June 1999.

[291] Kirill A. Atlasov, Karl Fredrik Karlsson, Alok Rudra, Benjamin Dwir, and Eli Kapon. Wavelength and loss splitting in directly coupled photonic-crystal defect microcavities. *Optics Express*, 16(20):16255, September 2008.

[292] Kirill A. Atlasov, Alok Rudra, Benjamin Dwir, and Eli Kapon. Large mode splitting and lasing in optimally coupled photonic-crystal microcavities. *Optics Express*, 19(3):2619, January 2011.

[293] Arka Majumdar, Armand Rundquist, Michal Bajcsy, and Jelena Vučković. Cavity quantum electrodynamics with a single quantum dot coupled to a photonic molecule. *Physical Review B*, 86(4):045315, July 2012.

[294] Mian Zhang, Cheng Wang, Yaowen Hu, Amirhassan Shams-Ansari, Tianhao Ren, Shanhui Fan, and Marko Lončar. Electronically programmable photonic molecule. *Nature Photonics*, 13(1):36–40, December 2018.

[295] Charles Santori, David Fattal, Jelena Vučković, Glenn S. Solomon, and Yoshihisa Yamamoto. Indistinguishable photons from a single-photon device. *Nature*, 419(6907):594–597, October 2002.

[296] Axel Kuhn, Markus Hennrich, and Gerhard Rempe. Deterministic single-photon source for distributed quantum networking. *Physical Review Letters*, 89(6):067901, July 2002.

[297] Wen-Hao Chang, Wen-Yen Chen, Hsiang-Szu Chang, Tung-Po Hsieh, Jen-Inn Chyi, and Tzu-Min Hsu. Efficient single-photon sources based on low-density quantum dots in photonic-crystal nanocavities. *Physical Review Letters*, 96(11):117401, March 2006.

[298] C. Weisbuch, M. Nishioka, A. Ishikawa, and Y. Arakawa. Observation of the coupled exciton-photon mode splitting in a semiconductor quantum microcavity. *Physical Review Letters*, 69(23):3314–3317, December 1992.

[299] D. G. Lidzey, D. D. C. Bradley, M. S. Skolnick, T. Virgili, S. Walker, and D. M. Whittaker. Strong exciton-photon coupling in an organic semiconductor microcavity. *Nature*, 395(6697):53–55, September 1998.

[300] J. P. Reithmaier, G. Sęk, A. Löffler, C. Hofmann, S. Kuhn, S. Reitzenstein, L. V. Keldysh, V. D. Kulakovskii, T. L. Reinecke, and A. Forchel. Strong coupling in a single quantum dot-semiconductor microcavity system. *Nature*, 432(7014):197–200, November 2004.

[301] E. Peter, P. Senellart, D. Martrou, A. Lemaître, J. Hours, J. M. Gérard, and J. Bloch. Exciton-photon strong-coupling regime for a single quantum dot embedded in a microcavity. *Physical Review Letters*, 95(6):067401, August 2005.

[302] T. Fischer, P. Maunz, P. W. H. Pinkse, T. Puppe, and G. Rempe. Feedback on the motion of a single atom in an optical cavity. *Physical Review Letters*, 88(16):163002, April 2002.

[303] Şahin Kaya Özdemir, Jiangang Zhu, Xu Yang, Bo Peng, Huzeyfe Yilmaz, Lina He, Faraz Monifi, Steven He Huang, Gui Lu Long, and Lan Yang. Highly sensitive detection of nanoparticles with a self-referenced and self-heterodyned whispering-gallery Raman microlaser. *Proceedings of the National Academy of Sciences*, 111(37):E3836–E3844, September 2014.

[304] Frank Vollmer and Stephen Arnold. Whispering-gallery-mode biosensing: Label-free detection down to single molecules. *Nature Methods*, 5(7):591–596, June 2008.

[305] Frank Vollmer and Lan Yang. Label-free detection with high-Q microcavities: A review of biosensing mechanisms for integrated devices. *Nanophotonics*, 1(3-4):267–291, January 2012.

[306] Elena I. Smotrova, Alexander I. Nosich, Trevor M. Benson, and Phillip Sewell. Threshold reduction in a cyclic photonic molecule laser composed of identical microdisks with whispering-gallery modes. *Optics Letters*, 31(7):921, April 2006.

[307] Xiaoshun Jiang, Qiang Lin, Jessie Rosenberg, Kerry Vahala, and Oskar Painter. High-Q double-disk microcavities for cavity optomechanics. *Optics Express*, 17(23):20911, October 2009.

[308] Yi-Wen Hu, Yun-Feng Xiao, Yong-Chun Liu, and Qihuang Gong. Optomechanical sensing with on-chip microcavities. *Frontiers of Physics*, 8(5):475–490, October 2013.

[309] Cong Cao, Si-Chen Mi, Yong-Pan Gao, Ling-Yan He, Daquan Yang, Tie-Jun Wang, Ru Zhang, and Chuan Wang. Tunable high-order sideband spectra generation using a photonic molecule optomechanical system. *Scientific Reports*, 6(1):22920, March 2016.

[310] Dario Gerace and Vincenzo Savona. Unconventional photon blockade in doubly resonant microcavities with second-order nonlinearity. *Physical Review A*, 89(3):031803, March 2014.

[311] H. Flayac and V. Savona. Unconventional photon blockade. *Physical Review A*, 96(5):053810, November 2017.

[312] Hyeongrak Choi, Di Zhu, Yoseob Yoon, and Dirk Englund. Cascaded cavities boost the indistinguishability of imperfect quantum emitters. *Physical Review Letters*, 122(18):183602, May 2019.

[313] Iulia M. Georgescu, S. Ashhab, and Franco Nori. Quantum simulation. *Reviews of Modern Physics*, 86(1):153–185, March 2014.

[314] Svetlana V. Boriskina. Spectrally engineered photonic molecules as optical sensors with enhanced sensitivity: A proposal and numerical analysis. *Journal of the Optical Society of America B*, 23(8):1565, August 2006.

[315] Svetlana V. Boriskina and Luca Dal Negro. Self-referenced photonic molecule bio(chemical) sensor. *Optics Letters*, 35(14):2496, July 2010.

[316] Yueyang Chen, James Whitehead, Albert Ryou, Jiajiu Zheng, Peipeng Xu, Taylor Fryett, and Arka Majumdar. Large thermal tuning of a polymer-embedded silicon nitride nanobeam cavity. *Optics Letters*, 44(12):3058, June 2019.

[317] Taylor K. Fryett, Yueyang Chen, James Whitehead, Zane Matthew Peycke, Xiaodong Xu, and Arka Majumdar. Encapsulated silicon nitride nanobeam cavity for hybrid nanophotonics. *ACS Photonics*, 5(6):2176–2181, April 2018.

[318] Steven G. Johnson, M. Ibanescu, M. A. Skorobogatiy, O. Weisberg, J. D. Joannopoulos, and Y. Fink. Perturbation theory for Maxwell's equations with shifting material boundaries. *Physical Review E*, 65(6):066611, June 2002.

[319] K. C. Smith, Y. Chen, A. Majumdar, and D. J. Masiello. *In preparation.*

[320] Qiang Li, Tao Wang, Yikai Su, Min Yan, and Min Qiu. Coupled mode theory analysis of mode-splitting in coupled cavity system. *Optics Express*, 18(8):8367, April 2010.

[321] Mehmet Bayindir, B. Temelkuran, and E. Ozbay. Tight-binding description of the coupled defect modes in three-dimensional photonic crystals. *Physical Review Letters*, 84(10):2140–2143, March 2000.

[322] John Preskill. Quantum computing in the NISQ era and beyond. *Quantum*, 2:79, 2018.

[323] Ehud Altman, Kenneth R Brown, Giuseppe Carleo, Lincoln D Carr, Eugene Demler, Cheng Chin, Brian DeMarco, Sophia E Economou, Mark A Eriksson, Kai-Mei C Fu, et al. Quantum simulators: Architectures and opportunities. *Physical Review X Quantum*, 2(1):017003, 2021.

[324] Richard P Feynman. Simulating physics with computers. *International Journal of Theoretical Physics*, 21(6/7):467, 1982.

[325] Seth Lloyd. Universal quantum simulators. *Science*, 273(5278):1073–1078, 1996.

[326] Daniel S Abrams and Seth Lloyd. Simulation of many-body fermi systems on a universal quantum computer. *Physical Review Letters*, 79(13):2586, 1997.

[327] Daniel S Abrams and Seth Lloyd. Quantum algorithm providing exponential speed increase for finding eigenvalues and eigenvectors. *Physical Review Letters*, 83(24):5162, 1999.

[328] Philipp Hauke, Fernando M Cucchietti, Luca Tagliacozzo, Ivan Deutsch, and Maciej Lewenstein. Can one trust quantum simulators? *Reports on Progress in Physics*, 75(8):082401, 2012.

[329] J Ignacio Cirac and Peter Zoller. Goals and opportunities in quantum simulation. *Nature Physics*, 8(4):264–266, 2012.

[330] Jarrod R McClean, Zhang Jiang, Nicholas C Rubin, Ryan Babbush, and Hartmut Neven. Decoding quantum errors with subspace expansions. *Nature Communications*, 11(1):1–9, 2020.

[331] Earl T Campbell, Barbara M Terhal, and Christophe Vuillot. Roads towards fault-tolerant universal quantum computation. *Nature*, 549(7671):172–179, 2017.

[332] Christian Kokail, Christine Maier, Rick van Bijnen, Tiff Brydges, Manoj K Joshi, Petar Jurcevic, Christine A Muschik, Pietro Silvi, Rainer Blatt, Christian F Roos, et al. Self-verifying variational quantum simulation of lattice models. *Nature*, 569(7756):355–360, 2019.

[333] Iulia M Georgescu, Sahel Ashhab, and Franco Nori. Quantum simulation. *Reviews of Modern Physics*, 86(1):153, 2014.

[334] Iulia Buluta and Franco Nori. Quantum simulators. *Science*, 326(5949):108–111, 2009.

[335] Dieter Jaksch and Peter Zoller. The cold atom Hubbard toolbox. *Annals of Physics*, 315(1):52–79, 2005.

[336] Maciej Lewenstein, Anna Sanpera, Veronica Ahufinger, Bogdan Damski, Aditi Sen, and Ujjwal Sen. Ultracold atomic gases in optical lattices: mimicking condensed matter physics and beyond. *Advances in Physics*, 56(2):243–379, 2007.

[337] Immanuel Bloch, Jean Dalibard, and Sylvain Nascimbene. Quantum simulations with ultracold quantum gases. *Nature Physics*, 8(4):267–276, 2012.

[338] Rainer Blatt and Christian F Roos. Quantum simulations with trapped ions. *Nature Physics*, 8(4):277–284, 2012.

[339] Ch Schneider, Diego Porras, and Tobias Schaetz. Experimental quantum simulations of many-body physics with trapped ions. *Reports on Progress in Physics*, 75(2):024401, 2012.

[340] Alán Aspuru-Guzik and Philip Walther. Photonic quantum simulators. *Nature Physics*, 8(4):285–291, 2012.

[341] Andrew A Houck, Hakan E Türeci, and Jens Koch. On-chip quantum simulation with superconducting circuits. *Nature Physics*, 8(4):292–299, 2012.

[342] Lucas Lamata, Adrian Parra-Rodriguez, Mikel Sanz, and Enrique Solano. Digital-analog quantum simulations with superconducting circuits. *Advances in Physics: X*, 3(1):1457981, 2018.

[343] Jochen Braumüller, Michael Marthaler, Andre Schneider, Alexander Stehli, Hannes Rotzinger, Martin Weides, and Alexey V Ustinov. Analog quantum simulation of the Rabi model in the ultra-strong coupling regime. *Nature Communications*, 8(1):1–8, 2017.

[344] Toivo Hensgens, Takafumi Fujita, Laurens Janssen, Xiao Li, CJ Van Diepen, Christian Reichl, Werner Wegscheider, S Das Sarma, and Lieven MK Vandersypen. Quantum simulation of a Fermi–Hubbard model using a semiconductor quantum dot array. *Nature*, 548(7665):70–73, 2017.

[345] Dingshun Lv, Shuoming An, Zhenyu Liu, Jing-Ning Zhang, Julen S Pedernales, Lucas Lamata, Enrique Solano, and Kihwan Kim. Quantum simulation of the quantum Rabi model in a trapped ion. *Physical Review X*, 8(2):021027, 2018.

[346] Javier Argüello-Luengo, Alejandro González-Tudela, Tao Shi, Peter Zoller, and J Ignacio Cirac. Analogue quantum chemistry simulation. *Nature*, 574(7777):215–218, 2019.

[347] A Imamoğlu, Helmut Schmidt, Gareth Woods, and Moshe Deutsch. Strongly interacting photons in a nonlinear cavity. *Physical Review Letters*, 79(8):1467, 1997.

[348] Philippe Grangier, Daniel F Walls, and Klaus M Gheri. Comment on "Strongly interacting photons in a nonlinear cavity". *Physical Review Letters*, 81(13):2833, 1998.

[349] Kevin M Birnbaum, Andreea Boca, Russell Miller, Allen D Boozer, Tracy E Northup, and H Jeff Kimble. Photon blockade in an optical cavity with one trapped atom. *Nature*, 436(7047):87–90, 2005.

[350] Andrei Faraon, Ilya Fushman, Dirk Englund, Nick Stoltz, Pierre Petroff, and Jelena Vučković. Coherent generation of non-classical light on a chip via photon-induced tunnelling and blockade. *Nature Physics*, 4(11):859–863, 2008.

[351] C Lang, D Bozyigit, C Eichler, L Steffen, JM Fink, AA Abdumalikov Jr, M Baur, S Filipp, MP Da Silva, Alexandre Blais, et al. Observation of resonant photon blockade at microwave frequencies using correlation function measurements. *Physical Review Letters*, 106(24):243601, 2011.

[352] Anthony J Hoffman, Srikanth J Srinivasan, Sebastian Schmidt, Lafe Spietz, José Aumentado, Hakan E Türeci, and Andrew A Houck. Dispersive photon blockade in a superconducting circuit. *Physical Review Letters*, 107(5):053602, 2011.

[353] Andrew D Greentree, Charles Tahan, Jared H Cole, and Lloyd CL Hollenberg. Quantum phase transitions of light. *Nature Physics*, 2(12):856–861, 2006.

[354] Michael J Hartmann, Fernando GSL Brandao, and Martin B Plenio. Strongly interacting polaritons in coupled arrays of cavities. *Nature Physics*, 2(12):849–855, 2006.

[355] Jens Koch and Karyn Le Hur. Superfluid–Mott-insulator transition of light in the Jaynes-Cummings lattice. *Physical Review A*, 80(2):023811, 2009.

[356] T Grujic, SR Clark, D Jaksch, and DG Angelakis. Non-equilibrium many-body effects in driven nonlinear resonator arrays. *New Journal of Physics*, 14(10):103025, 2012.

[357] Markus Greiner, Olaf Mandel, Tilman Esslinger, Theodor W Hänsch, and Immanuel Bloch. Quantum phase transition from a superfluid to a Mott insulator in a gas of ultracold atoms. *Nature*, 415(6867):39–44, 2002.

[358] Christian Gross and Immanuel Bloch. Quantum simulations with ultracold atoms in optical lattices. *Science*, 357(6355):995–1001, 2017.

[359] Leticia Tarruell and Laurent Sanchez-Palencia. Quantum simulation of the Hubbard model with ultracold fermions in optical lattices. *Comptes Rendus Physique*, 19(6):365–393, 2018.

[360] Michael J Hartmann, Fernando GSL Brandao, and Martin B Plenio. Quantum many-body phenomena in coupled cavity arrays. *Laser Photonics Reviews*, 2(6):527–556, 2008.

[361] Changsuk Noh and Dimitris G Angelakis. Quantum simulations and many-body physics with light. *Reports on Progress in Physics*, 80(1):016401, November 2016.

[362] Davide Rossini and Rosario Fazio. Mott-insulating and glassy phases of polaritons in 1d arrays of coupled cavities. *Physical Review Letters*, 99:186401, October 2007.

[363] E. K. Irish, C. D. Ogden, and M. S. Kim. Polaritonic characteristics of insulator and superfluid states in a coupled-cavity array. *Physical Review A*, 77:033801, March 2008.

[364] M. I. Makin, Jared H. Cole, Charles Tahan, Lloyd C. L. Hollenberg, and Andrew D. Greentree. Quantum phase transitions in photonic cavities with two-level systems. *Physical Review A*, 77:053819, May 2008.

[365] Michael J Hartmann and Martin B Plenio. Strong photon nonlinearities and photonic Mott insulators. *Physical Review Letters*, 99(10):103601, 2007.

[366] Martin Leib and Michael J Hartmann. Bose–Hubbard dynamics of polaritons in a chain of circuit quantum electrodynamics cavities. *New Journal of Physics*, 12(9):093031, 2010.

[367] S Schmidt and G Blatter. Strong coupling theory for the Jaynes-Cummings-Hubbard model. *Physical Review Letters*, 103(8):086403, 2009.

[368] Iacopo Carusotto, Dario Gerace, HE Tureci, Simone De Liberato, Cristiano Ciuti, and A Imamoğlu. Fermionized photons in an array of driven dissipative nonlinear cavities. *Physical Review Letters*, 103(3):033601, 2009.

[369] Martin Hohenadler, Markus Aichhorn, Sebastian Schmidt, and Lode Pollet. Dynamical critical exponent of the Jaynes-Cummings-Hubbard model. *Physical Review A*, 84(4):041608, 2011.

[370] Michael J Hartmann. Quantum simulation with interacting photons. *Journal of Optics*, 18(10):104005, 2016.

[371] Kenji Toyoda, Yuta Matsuno, Atsushi Noguchi, Shinsuke Haze, and Shinji Urabe. Experimental realization of a quantum phase transition of polaritonic excitations. *Physical Review Letters*, 111:160501, October 2013.

[372] Alexander Mering, Michael Fleischhauer, Peter A Ivanov, and Kilian Singer. Analytic approximations to the phase diagram of the Jaynes-Cummings-Hubbard model. *Physical Review A*, 80(5):053821, 2009.

[373] Christian Nietner and Axel Pelster. Ginzburg-Landau theory for the Jaynes-Cummings-Hubbard model. *Physical Review A*, 85(4):043831, 2012.

[374] Bogusz Bujnowski, Justine K Corso, Andrew LC Hayward, Jared H Cole, and Andy M Martin. Supersolid phases of light in extended Jaynes-Cummings-Hubbard systems. *Physical Review A*, 90(4):043801, 2014.

[375] Andrew LC Hayward, Andrew M Martin, and Andrew D Greentree. Fractional quantum hall physics in Jaynes-Cummings-Hubbard lattices. *Physical Review Letters*, 108(22):223602, 2012.

[376] Maxime Boissonneault, Jay M Gambetta, and Alexandre Blais. Dispersive regime of circuit QED: Photon-dependent qubit dephasing and relaxation rates. *Physical Review A*, 79(1):013819, 2009.

[377] Alexandre Blais, Ren-Shou Huang, Andreas Wallraff, Steven M Girvin, and R Jun Schoelkopf. Cavity quantum electrodynamics for superconducting electrical circuits: An architecture for quantum computation. *Physical Review A*, 69(6):062320, 2004.

[378] Andreas Wallraff, David I Schuster, Alexandre Blais, Luigi Frunzio, R-S Huang, Johannes Majer, Sameer Kumar, Steven M Girvin, and Robert J Schoelkopf. Strong coupling of a single photon to a superconducting qubit using circuit quantum electrodynamics. *Nature*, 431(7005):162–167, 2004.

[379] R. J. Schoelkopf and S. M. Girvin. Wiring up quantum systems. *Nature*, 451(7179):664–669, February 2008.

[380] Tomoyuki Yoshie, Axel Scherer, J Hendrickson, Galina Khitrova, HM Gibbs, G Rupper, C Ell, OB Shchekin, and DG Deppe. Vacuum Rabi splitting with a single quantum dot in a photonic crystal nanocavity. *Nature*, 432(7014):200–203, 2004.

[381] J Pelal Reithmaier, G Sęk, A Löffler, C Hofmann, S Kuhn, S Reitzenstein, LV Keldysh, VD Kulakovskii, TL Reinecke, and A Forchel. Strong coupling in a single quantum dot–semiconductor microcavity system. *Nature*, 432(7014):197–200, 2004.

[382] Kevin Hennessy, Antonio Badolato, Martin Winger, D Gerace, Mete Atatüre, S Gulde, S Fält, Evelyn L Hu, and A Imamoğlu. Quantum nature of a strongly coupled single quantum dot–cavity system. *Nature*, 445(7130):896–899, 2007.

[383] Serge Haroche and J-M Raimond. *Exploring the quantum: Atoms, cavities, and photons*. Oxford University Press, 2006.

[384] Claude Cohen-Tannoudji, Jacques Dupont-Roc, and Gilbert Grynberg. *Atom-photon interactions: Basic processes and applications*. Wiley, Weinheim, Germany, 2004.

[385] Jorge Casanova, Guillermo Romero, Ion Lizuain, Juan José García-Ripoll, and Enrique Solano. Deep strong coupling regime of the Jaynes-Cummings model. *Physical Review Letters*, 105(26):263603, 2010.

[386] JM Fink, M Göppl, M Baur, R Bianchetti, Peter J Leek, Alexandre Blais, and Andreas Wallraff. Climbing the Jaynes–Cummings ladder and observing its nonlinearity in a cavity QED system. *Nature*, 454(7202):315–318, 2008.

[387] Jacek Kasprzak, S Reitzenstein, Egor A Muljarov, C Kistner, C Schneider, M Strauss, S Höfling, A Forchel, and W Langbein. Up on the Jaynes–Cummings ladder of a quantum-dot/microcavity system. *Nature Materials*, 9(4):304–308, 2010.

[388] Fabrice P Laussy, Elena del Valle, Michael Schrapp, Arne Laucht, and Jonathan J Finley. Climbing the Jaynes-Cummings ladder by photon counting. *Journal of Nanophotonics*, 6(1):061803, 2012.

[389] Caspar Hopfmann, Alexander Carmele, Anna Musiał, Christian Schneider, Martin Kamp, Sven Höfling, Andreas Knorr, and Stephan Reitzenstein. Transition from Jaynes-Cummings to Autler-Townes ladder in a quantum dot–microcavity system. *Physical Review B*, 95(3):035302, 2017.

[390] Matthew PA Fisher, Peter B Weichman, Geoffrey Grinstein, and Daniel S Fisher. Boson localization and the superfluid-insulator transition. *Physical Review B*, 40(1):546, 1989.

[391] J. Raftery, D. Sadri, S. Schmidt, H. E. Türeci, and A. A. Houck. Observation of a dissipation-induced classical to quantum transition. *Physical Review X*, 4(3), September 2014.

[392] H. J. Carmichael. Breakdown of photon blockade: A dissipative quantum phase transition in zero dimensions. *Physical Review X*, 5(3), September 2015.

[393] P Carbonaro, G Compagno, and F Persico. Canonical dressing of atoms by intense radiation fields. *Physics Letters A*, 73(2):97–99, 1979.

[394] Max Wagner. *Unitary transformations in solid state physics*. North-Holland Physics Publishing, 1986.

[395] Jay Gambetta, Alexandre Blais, D. I. Schuster, A. Wallraff, L. Frunzio, J. Majer, M. H. Devoret, S. M. Girvin, and R. J. Schoelkopf. Qubit-photon interactions in a cavity: Measurement-induced dephasing and number splitting. *Physical Review A*, 74(4), October 2006.

[396] D. I. Schuster, A. A. Houck, J. A. Schreier, A. Wallraff, J. M. Gambetta, A. Blais, L. Frunzio, J. Majer, B. Johnson, M. H. Devoret, S. M. Girvin, and R. J. Schoelkopf. Resolving photon number states in a superconducting circuit. *Nature*, 445(7127):515–518, February 2007.

[397] Noam D. Elkies. Sum with binomial coefficients and a square root. Mathematics Stack Exchange.

[398] Markus Aichhorn, Martin Hohenadler, Charles Tahan, and Peter B. Littlewood. Quantum fluctuations, temperature, and detuning effects in solid-light systems. *Physical Review Letters*, 100:216401, May 2008.

[399] D. Jaksch, C. Bruder, J. I. Cirac, C. W. Gardiner, and P. Zoller. Cold bosonic atoms in optical lattices. *Physical Review Letters*, 81:3108–3111, October 1998.

[400] Alexander L Fetter and John Dirk Walecka. *Quantum theory of many-particle systems*. Courier Corporation, 2012.

[401] Max T. C. Wong and C. K. Law. Two-polariton bound states in the Jaynes-Cummings-Hubbard model. *Physical Review A*, 83:055802, May 2011.

[402] Chuan-Zhou Zhu, Shimpei Endo, Pascal Naidon, and Peng Zhang. Scattering and bound states of two polaritons in an array of coupled cavities. *Few-Body Systems*, 54(11):1921–1930, 2013.

[403] Qi-Yu Liang, Aditya V Venkatramani, Sergio H Cantu, Travis L Nicholson, Michael J Gullans, Alexey V Gorshkov, Jeff D Thompson, Cheng Chin, Mikhail D Lukin, and Vladan Vuletić. Observation of three-photon bound states in a quantum nonlinear medium. *Science*, 359(6377):783–786, 2018.

[404] Ofer Firstenberg, Thibault Peyronel, Qi-Yu Liang, Alexey V Gorshkov, Mikhail D Lukin, and Vladan Vuletić. Attractive photons in a quantum nonlinear medium. *Nature*, 502(7469):71–75, 2013.

[405] Camille Aron, Manas Kulkarni, and Hakan E. Türeci. Photon-mediated interactions: A scalable tool to create and sustain entangled states of N atoms. *Physical Review X*, 6(1), March 2016.

[406] Guanyu Zhu, Sebastian Schmidt, and Jens Koch. Dispersive regime of the Jaynes–Cummings and Rabi lattice. *New Journal of Physics*, 15(11):115002, November 2013.

[407] H. P. Büchler, A. Micheli, and P. Zoller. Three-body interactions with cold polar molecules. *Nature Physics*, 3(10):726–731, July 2007.

[408] Pascal Naidon and Shimpei Endo. Efimov physics: A review. *Reports on Progress in Physics*, 80(5):056001, 2017.

[409] Pawel Blasiak, Andrzej Horzela, Karol A Penson, Allan I Solomon, and Gerard HE Duchamp. Combinatorics and boson normal ordering: A gentle introduction. *American Journal of Physics*, 75(7):639–646, 2007.